A STUDY OF THE RELATIONSHIP BETWEEN PRECIPITATE STRUCTURE AND CHEMISTRY ON THE MECHANICAL PROPERTIES OF ALUMINIUM ALLOYS.

P.J.S.WARREN

WOLFSON COLLEGE, OXFORD.

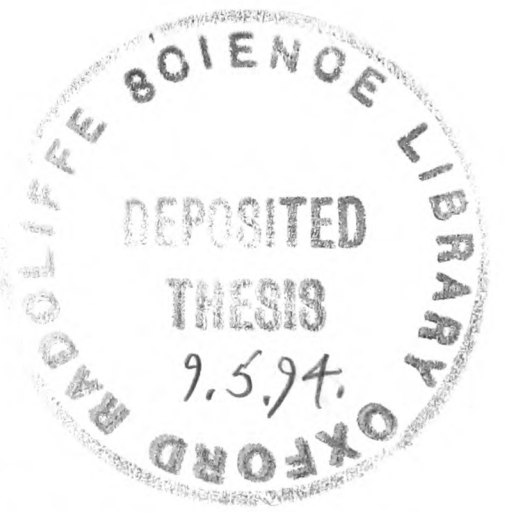

A thesis submitted for the degree of Doctor of Philosophy at the University of Oxford.

Michelmas Term 1993.

Abstract.

A Study Of The Relationship Between Precipitate Structure And Chemistry On The Mechanical Properties Of Aluminium Alloys.

A thesis submitted for the degree of Doctor of Philosophy at the University of Oxford.

P.J.S.Warren, Wolfson College, Oxford, Michelmas Term 1993.

The microstructural chemistry of the commercial aluminium alloy 7150, containing Al, Zn, Mg, Cu and some trace impurities, was investigated in detail. This alloy is a precipitation hardening alloy, deriving most of its strength from the fine distribution of solute rich precipitates formed during thermal processing. At peak strength this alloy suffers from the common problem of stress corrosion cracking, leading to unpredictable premature failure in the presence of a corrosive environment. Failure is mainly intergranular, thus the structure and chemistry of the grain boundary regions is of interest. A large number of previous investigations have failed to correlate any individual parameter with the stress corrosion cracking behaviour.

As the analytical techniques have improved over the last three decades, more complex investigations of the microstructure and the microchemistry have been attempted, in order to more fully characterise the development of this alloy during thermal processing. This thesis presents the results of two of the highest resolution techniques available for microchemical analysis. Scanning transmission electron microscopy X-ray analysis, using a VG-HB501 dedicated scanning transmission electron microscope, enables chemical analysis with a 2nm electron probe, while atom probe analysis, using a VG-FIM100 atom probe with an additional position sensitive detector, enables single atom chemical identification with sub-nanometre spatial resolution.

However, both of these techniques have their own experimental limitations which restrict the accuracy of the results obtainable. A detailed description of the many factors limiting both techniques is presented. Combining these techniques has enabled chemical analysis of all the microstructural features present in this alloy on the nanometre scale. A description of the chemical changes occurring during age hardening of this alloy is given in summary.

Preface.

This thesis reports work conducted by the author in the Department of Materials, Oxford University, during the period October 1990 to October 1993. All of the work is original and where work of others is used or described it has been clearly referenced and acknowledged. No part of this work has been previously submitted for a degree at this or any other university. Some of the work described in this thesis has been published or is in press in the following papers:

i Field Ion Microscope Atom Probe analysis of the effect of RRA heat treatment upon the matrix strengthening precipitates in Al-7150.
P.J.Warren, C.R.M.Grovenor and J.S.Crompton
Surface Science 266 (1992) 342.

ii) Lateral and depth scale calibrations of the Position Sensitive Atom Probe. :
J.M.Hyde, A.Cerezo, R.P.Setna, P.J.Warren and G.D.W.Smith
Proc IFES 1993 to be published in Surface Science.

iii) Comparison of STEM and Atom Probe methods for chemical analysis of grain boundaries in commercial aluminium alloys.
P.J.Warren and C.R.M.Grovenor
Proc Interfaces II (1993) to be published in Materials Science Forum.

Also published,

New Dimensions in Atom Probe Analysis.
A.Cerezo, J.M.Hyde, M.K.Miller, G.Beverini, R.P.Setna, P.J.Warren and G.D.W.Smith
Surface Science 266 (1992) 481

Ultra High resolution chemical analysis by field ion microscopy and position sensitive atom probe techniques.
C.R.M.Grovenor, G.D.W.Smith, A.Cerezo, J.A.Liddle, R.A.D.Mackenzie, P.J.Warren, R.P.Setna, J.M.Hyde, J.Brown, I.Stark and B.A.Shollock.
Ultramicroscopy 47 (1992) 199

I would like to thank both Professor Sir Peter Hirsh FRS and Professor Richard Brook for the provision of laboratory facilities. The work was funded by the SERC in the form of a postgraduate CASE studentship in conjunction with Alcan International. Also, the alloy used was provided by Alcan International. I am grateful to Wolfson College for providing me with pleasant surroundings and company, and also some support for attending conferences.

I sincerely thank Dr Chris Grovenor for his guidance and support and also for his practical philosophy about work. I also would like to thank Dr Jeff Crompton for his initial enthusiasm for this research (wherever he may be) and also Dr Warren Hepples for continuing the industrial liaison.

I also express my thanks to the members of the FIM group past and present who have made work so enjoyable. I am particularly indebted to Alfred Cerezo for designing and developing the POSAP; to Terry Godfrey for making it work and keeping it working; to Ross for enabling me to collect data more rapidly; to Jon for enabling me to analyse the data and generally leading by example; and finally Rohan for being enthusiastic and laudatory throughout my seven years at Oxford.

I would also like to thank the many orienteers who kept me away from the laboratory at the weekends, however it seems unlikely that they will ever read this thesis.

Finally I wish to thank Keyna, for infinite love and support, without whom this thesis would have taken much longer to finish.

Paul J Warren

Department of Materials, Oxford University, October 1993.

Contents

Introduction. **1**
Chapter 1. Literature Review. **4**
1.1. Historical development of alloy 7150. 4
1.2. Microstructure. 5
1.2.1. Precipitation. 5
1.2.1.1. GP zones. 6
1.2.1.2. Transition phase, η'. 6
1.2.1.3. The equilibrium phase, η. 7
1.2.2. Theory of precipitation in Al-Zn-Mg alloys. 7
1.2.3. Effect of heat treatments on precipitation. 10
1.2.3.1. Homogenisation. 10
1.2.3.2. Solution Treatment Anneal. 10
1.2.3.3. Quench. 10
1.2.3.4. Natural Ageing. 11
1.2.3.5. Artificial Ageing - T6 and T73. 11
1.2.3.6. Artificial Ageing - RRA. 13
1.3. Microchemistry. 14
1.3.1. Precipitate Free Zone Chemistry. 14
1.3.2. Grain Boundary Chemistry. 15
1.3.3. Precipitate Chemistry. 16
1.4. Stress Corrosion Cracking - SCC. 17
1.4.1. The dependence of SCC upon hydrogen. 18
1.4.2. Suggested mechanisms occurring in SCC. 19
1.5. The aim of this research. 21
Chapter 2. Material Preparation. **22**
2.1. Choice of specimen heat treatments. 22
2.1.1. Single Step Ageing. 22
2.1.2. Retrogression and Re-Ageing. 22
2.2. Specimen preparation. 23
2.2.1. Heat Treatment of Specimens. 23
2.2.2. FIM Specimen Preparation. 24
2.2.2.1. Non-selective specimen preparation. 24
2.2.2.2. Selective specimen preparation. 25
2.2.2.3. Feature Selection. 26
2.2.3. TEM Specimen Preparation. 29
Chapter 3. Analytical Transmission Electron Microscopy. **30**
3.1. X-ray Chemical Analysis. 30
3.2. Quantification. 32
3.3. Specific Aspects of Quantification. 33
3.3.1. Window definition. 33
3.3.2. Surface Deposition. 34
3.3.3. Statistics. 35
3.3.4. Summary. 36
Chapter 4. Field Ion Microscopy and Atom Probe Methods. **37**
4.1. Introduction to techniques. 37
4.1.1. Field Ion Microscopy. 37
4.1.2. Atom Probe Analysis. 38
4.1.2.1. Principles. 38
4.1.2.2. AP Data Representation. 39
4.1.3. The Position Sensitive Atom Probe. 39
4.1.3.1. Principles. 40
4.1.3.2. POSAP Data Representation. 40
4.2. Previous FIM and Atom Probe Investigations. 42
4.3. FIM of Aluminium 7150. 43
4.4. AP Data Interpretation. 44
4.4.1. Geometrical effects. 44
4.4.2. Detection efficiency. 45

4.4.3. Preferential evaporation effects. 45
4.4.4. Window overlap. 46
4.5. POSAP Data Interpretation. 47
4.5.1. Compositional Information. 47
4.5.1.1. Chemical Identification. 47
4.5.1.2. Spatial Identification. 50
4.5.2. Copper and Zinc. 52
4.5.2.1. Copper Alloy LL-1. 53
4.5.2.2. Zinc Alloy CA-1. 53
4.5.2.3. Summary. 54
4.5.3. Pulse Fraction and Temperature Dependence. 55
4.5.4. Spatial Information. 57
4.5.4.1. Image Compression Factor - ξ. 58
4.5.4.2. Radius Calibration. 58
4.5.4.3. Depth Scale Calibration. 60
4.5.4.4. Application of scale calibrations. 60
4.5.5. Summary of factors affecting POSAP data interpretation. 61
Chapter 5. Precipitate Analysis. 62
5.1. Matrix Precipitate Analysis. 62
5.1.1. T.E.M. Matrix Precipitate Analysis. 62
5.1.2. Atom Probe Matrix Precipitate Analysis. 63
5.1.3. POSAP Matrix Precipitate Analysis. 65
5.1.4. Comparison of AP and POSAP levels detected. 69
5.2. Grain Boundary Precipitate Analysis. 70
5.2.1. TEM Grain Boundary Precipitate Analysis. 70
5.2.2. STEM Grain Boundary Precipitate Analysis. 71
5.3. Precipitate Analysis for Material Aged at 220°C. 73
5.3.1. TEM analysis of 220°C material. 74
5.3.2. AP and POSAP analysis of 220°C material. 74
5.3.3. STEM analysis of 220°C material. 75
5.4. RRA Precipitate Analysis. 76
5.5. Other Precipitate Phases observed. 77
5.6. Summary of precipitation in Al-7150. 78
Chapter 6. Grain boundary Analysis. 81
6.1. Introduction. 81
6.2. Comparison of methods for grain boundary analysis. 82
6.2.1. STEM X-ray analysis. 82
6.2.2. Atom Probe analysis. 83
6.2.3. POSAP analysis. 83
6.2.4. Summary. 84
6.3. STEM Grain Boundary Analysis. 85
6.4. POSAP Grain Boundary Analysis. 90
6.4.1. pjw013 Solution treated material. 90
6.4.2. pgb0101&2 Solution treated material. 92
6.4.3. paul15/3/93 Solution treated material. 92
6.4.4. pgb12010 120°C material. 93
6.4.5. paul3/6/93 120°C material. 93
6.4.6. Compositional information. 94
6.4.7. Grain boundary precipitate compositions. 96
6.4.8. POSAP detection of hydrogen. 98
Chapter 7. Summary and Conclusions. 101
7.1. Introduction. 101
7.2. Summary of techniques. 101
7.3. Summary of results. 102
7.4. Suggestions for further work. 105
References 108

Introduction.

Aluminium alloy 7150 is an Al-Zn-Mg-Cu alloy. This class of alloys evolved from the earlier Al-Zn-Mg alloys and both alloy systems were developed for their combination of high strength, low density and good corrosion resistance, making them suitable for applications in the aerospace industry. The main problem with these high strength alloys is their poor resistance to stress corrosion cracking (SCC) when aged to peak strength. To improve the resistance to SCC it is necessary to overage the material, resulting in a 15-20% loss in strength.

SCC is the premature failure of the material when stressed in a corrosive environment. Failure is usually intergranular, thus it is the grain boundaries that are of interest. A vast amount of time and effort has been spent investigating the possible reasons why material in the as-quenched state is insensitive to SCC, yet during ageing the SCC resistance falls dramatically to an unacceptable level in the peak strength material before recovering again in the overaged material. The structure of the grain boundary region in a precipitation hardened alloy is complex, with many inter-dependent parameters. SCC has been related to parameters such as: precipitate size, spacing and type; precipitate free zone width and slip characteristics; matrix precipitate size, distribution and slip characteristics; solute profiles in the PFZ; and grain boundary segregation. Despite claims to the contrary, there is no single microstructural parameter that has been identified as uniquely controlling the SCC susceptibility[1]. One factor that has been identified as necessary for SCC, but not sufficient cause, is the presence of atomic hydrogen ahead of the crack tip. The chemistry of the grain boundary ahead of the crack tip is likely to affect the interaction of the hydrogen with the material, thus controlling the SCC susceptibility. For this reason a detailed investigation of the grain boundary chemistry in this alloy is required. Workers at Alcan International have used Scanning Transmission Electron Microscopy and X-ray microanalysis to investigate the variations in grain boundary segregation in various treatments[2]. They found segregation of both magnesium and copper to the grain boundaries in aged material. They observed that the grain boundary content of

magnesium steadily increased with ageing, but attributed the improvement in SCC resistance with overageing to a decrease in the copper segregation upon ageing at 160°C.

This thesis is a broader investigation of the microscopic chemistry of this alloy in material aged at various temperatures, and is a direct continuation of Alcan International's investigations of SCC in this alloy. Two techniques were available that had sufficient spatial resolution to be able to investigate the chemistry of the microscopic features of this alloy. STEM X-ray analysis was able to provide chemical information about the grain boundary regions, while Atom Probe analysis was used to provide information about the matrix regions and some analyses of grain boundary regions.

Chapter 1 reviews our current understanding of precipitation in this alloy system, with details of previous microstructural, and also microchemical, investigations. It also gives a selective description of the problem of SCC in this alloy system, while avoiding listing the many individual investigations which have been frequently reviewed elsewhere.

Chapter 2 gives details of the heat treatments and the specimen preparation procedures. In particular, the difficulties in preparation of specimens containing grain boundaries suitable for analysis in the Field Ion Microscope are described.

Chapter 3 provides a brief introduction to Scanning Transmission Electron Microscope X-ray microanalysis, and the factors that affect the accuracy of the results obtained.

Chapter 4 provides a brief introduction to Field Ion Microscopy (FIM), Atom Probe analysis (AP) and Position Sensitive Atom Probe analysis (POSAP). A detailed discussion of all the various factors found to limit the accuracy of the results obtained is described, and the various calibration experiments essential to check the chemical accuracy of this technique are shown.

Chapter 5 gives the experimental results of analysis of the matrix strengthening precipitates, the grain boundary precipitates and an assortment of impurity phase precipitates also observed.

Chapter 6 gives the experimental results of analyses of the grain boundary regions in this alloy.

Chapter 7 provides a summary of the techniques used, as described in Chapters 3 and 4, and an overall description of the development in chemistry of the microstructures analysed in Chapters 5 and 6. A brief discussion of future directions for research is also given.

Chapter 1. Literature Review.

1.1. Historical development of alloy 7150.

Aluminium was first extracted chemically in the mid-nineteenth century, however it was not until the development of the Hall-Herault process of electrolytic extraction from bauxite (1886) that aluminium became commercially viable. Initially, there was still the limitation of a relatively new electricity industry, but by the beginning of the twentieth century aluminium was finding many uses due to properties such as good corrosion resistance, low density, good ductility and good electrical and thermal conduction. Alloying of aluminium with small additions of various solute elements was found to result in the phenomenon of age hardening precipitation, which could greatly increase the strength of the metal.

Aluminium was quickly investigated for its suitability for the new aviation industry, where its high strength-to-weight ratio and good corrosion resistance had major advantages. By the 1930's aluminium alloys were in common use for main structural aircraft components. Much of the early work was done in Germany prior to World War II, making use of home resources due to trade restrictions. One of the main high strength alloys introduced in the 1940's was 7075; an Al-Zn-Mg alloy. This alloy has subsequently proved the most suitable for modification in order to satisfy the continually improving engineering design criteria[3]. The maximum strength has not been greatly improved since it was first introduced. However, changes have been necessary to improve other properties such as the stress corrosion cracking (SCC) resistance, the fatigue life and the processability. It was found that peak aged material (designated T6) had poor SCC resistance. A typical T6 ageing treatment at this time was single-step heating to 120°C for 24 hours. It was found that the SCC resistance could be improved by increasing this temperature to above about 160°C, resulting in overaged material (designated T7) and a 15-20% loss in strength from the peak value. Later, a two stage ageing process was developed that initially used a low temperature (120°C) to produce a fine distribution of precipitates, and then a higher temperature (160°C) in final ageing

to achieve a higher peak strength. Using this two stage process to produce overaged material gave a higher strength for the same acceptable SCC susceptibility (designated T73). This was introduced in the 1960's and rapidly became the normal temper for applications where SCC should be avoided. In the early 1970's a new variation on this alloy composition was developed. Alloy 7050 was specifically designed to be suitable for use in thicker sections where the SCC susceptibility of 7075 was higher, due to the lower quench rates[4]. The specifications of 7075 and 7050 are compared in Table 1.1. The addition of copper reduces the unstressed corrosion resistance, but it substantially improves the SCC resistance. The use of zirconium as the grain refining agent instead of chromium provides similar grain refining properties, however it does not affect the solute levels (forming Al_3Zr as opposed to Al_7Mg_2Cr) and, since it does not act as nucleation sites for subsequent precipitation, it has less effect on the quench sensitivity. Alloy 7150, the material used in this research, is a higher purity version of alloy 7050 developed specifically for use as the upper skins in Boeing 757 and 767 aircraft[5]. The increased purity is mainly a reduction in the levels of iron and silicon, which are common impurities in this alloy system.

1.2. Microstructure.

1.2.1. Precipitation.

The phase diagram for the Al-Zn-Mg system was initially determined by Koster[6]. Subsequent workers determined the phase boundaries with more accuracy and also investigated the effects of additional elements upon the phase diagram. All of this data was collated in a review article by Mondolfo[7]. It is the aluminium-rich corner of the phase diagram which is of commercial interest, making use of the phenomenon of age hardening. This predicts two equilibrium precipitate phases in this region:- $MgZn_2$, the η phase; and $Mg_3Zn_2Al_2$, the T phase. However, in commercially processed material the desired properties are achieved by the precipitation of a number of metastable phases. Loffler [8] reviews the possible decomposition processes occurring in the Al-Zn-Mg system over the composition range of commercial interest. Due to the huge amount of research that has been done on this system (over 1000 references in several review

Alloy	aluminium	zinc	magnesium	copper	other additions
7075	90	5.6±0.5	2.5±0.4	1.6±0.4	0.23±0.05 Chromium
7050	89	6.2±0.5	2.3±0.3	2.3±0.3	0.12±0.04 Zirconium

Alloy 7150 is the same as 7050 except for a lower impurity tolerance level for manganese, iron, chromium and silicon.

Table 1.1. Alloy Specifications (in Wt%)

Structure	a nm	c nm	Reference
Hexagonal	4.96	8.68	Mondolfo 7
Hexagonal	4.96	14.03	Graf 17
Monoclinic	4.97	5.54	Gjønnes & Simensen 18
Hexagonal	4.89	13.74	Auld & Cousland 19
Hexagonal	4.96	14.03	Park & Ardell 21

Table 1.2.

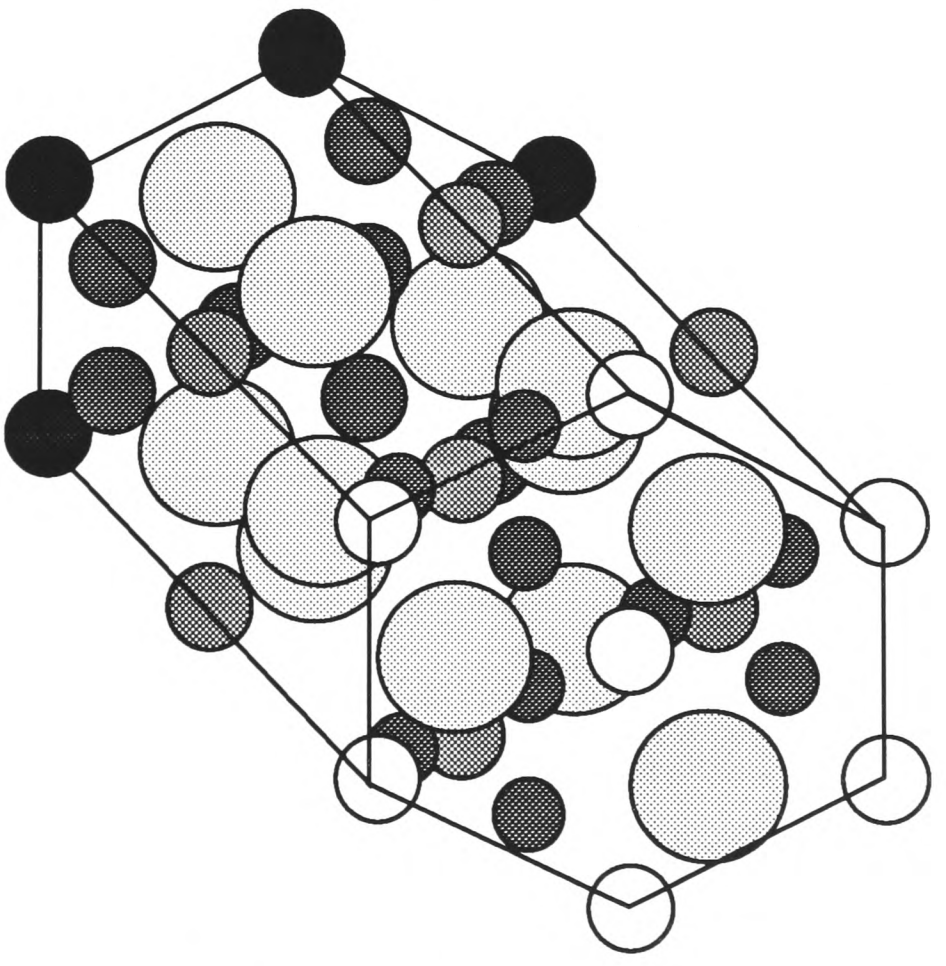

3-D Structure of $MgZn_2$

Figure 1.1

articles), the following description of the precipitation processes is selective, in order to present a picture of the microstructure in the alloy of interest here. Most of the basic research was done on the initial Al-Zn-Mg system, and the description of precipitation in the Al-Zn-Mg-Cu system must be considered as a extension of this. Where there are known differences due to the addition of copper they are described explicitly. Generally the copper is thought to behave in a similar manner to the zinc; however, it will have different kinetics.

1.2.1.1 GP zones.

Evidence for GP zones was first found from X-ray diffraction studies[9,10,11]. Further work suggested ordering of these zones during growth[12,13]. Conventional direct imaging TEM showed small spherical particles of diameter less than 50Å[14]. A high resolution TEM study identified two types of GP zones in low concentration alloys. At lower temperatures (<60°C), GP zones formed on the (001) planes, but above 60°C ordered GP zones, coherent with (111) matrix planes, also formed. These higher temperature zones had a hexagonal structure and were precursors to the η' phase[15]. The chemical composition of GP zones in two alloys has been investigated by FIM/AP showing solute rich planes separated by almost pure aluminium planes[16]. The kinetics of GP zone formation is thought to be controlled by a solute-vacancy interaction but there is contention over whether the process starts by clustering of zinc or whether it is dependent upon magnesium migration.

1.2.1.2 Transition phase η'.

Early X-ray work[9,11,17] suggested the presence of a hexagonal transition phase η'. The existence of plate-like precipitates of η' was confirmed by TEM[18,19]. Various lattice parameters have been suggested, as shown in Table 1.2. Mondolfo[20] gave a probable explanation of these variations, in that it depends which solute rich planes you consider as defining the unit cell, bearing in mind that the η' still contains a large proportion of aluminium and is of the same order of thickness as the unit cell.

The η' plates have the orientation relationship (10.0)η' // (110)Al (00.1)η' // $(1\bar{1}1)$Al [21]

being at least partially coherent on the (111) planes. It is thought that transformation of the hexagonally ordered spherical GP zones is the dominant method of formation of the η' precipitates in the high strength alloys. Nucleation of η' on small vacancy and solute clusters is also likely.

1.2.1.3 The equilibrium phase, η.

The equilibrium phase η is very similar to the intermediate phase η'. The structure is a hexagonal unit cell containing 12 atoms. Figure 1.1 shows a three dimensional representation and Figure 1.2 gives a two dimensional break-down of the layered structure. Various lattice parameters are reported (Figure 1.3), mainly due to the effect of different solute concentrations on the lattice parameter. The Laves[22] parameters are usually used, since these were taken from pure $MgZn_2$.

Nine different orientation relationships have been identified from detailed diffraction analysis of single large precipitates. These have various morphologies (Figure 1.3).

The most commonly observed precipitates during standard commercial heat treatments are those with orientation relationships types 1, 2, and 4 (signified η_1, η_2, and η_4 etc.).

It is thought that the η_2 phase can be formed by transformation of the η' precipitates. The majority of the η phase variants are formed directly from the matrix by nucleation and growth.

1.2.2. Theory of precipitation in Al-Zn-Mg alloys.

The Al-Zn-Mg system was investigated by Lorimer and Nicholson[23] and several deficiencies in the classical model for precipitate nucleation were found. The standard model for solid => solid precipitation was considered as an extension of liquid => solid

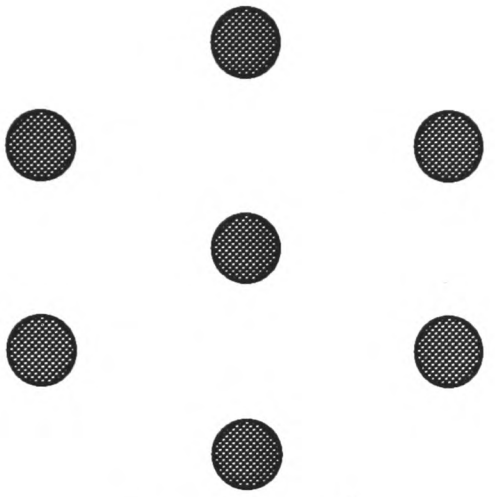

Zinc at 0 Å.

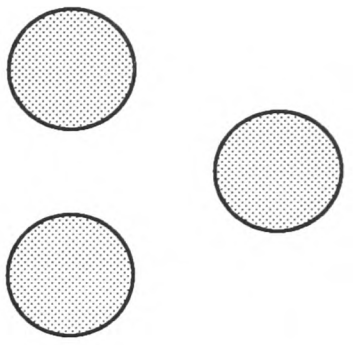

Magnesium at 0.54 Å

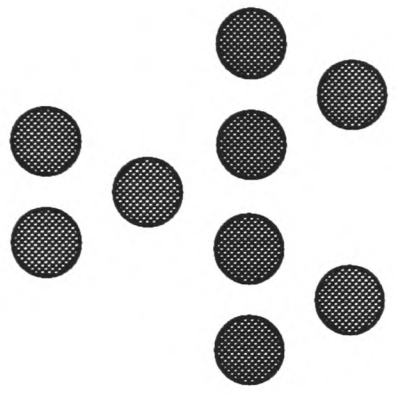

Zinc at 2.15 Å

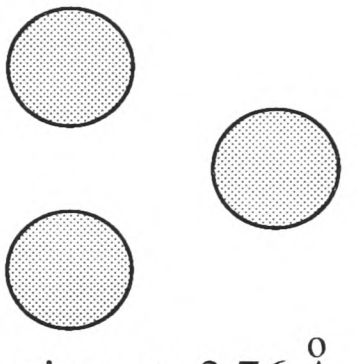

Magnesium at 3.76 Å

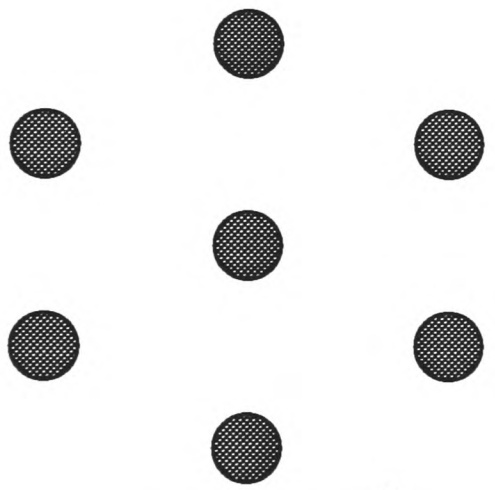

Zinc at 4.3 Å

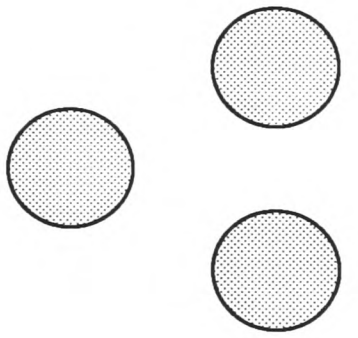

Magnesium at 4.86 Å

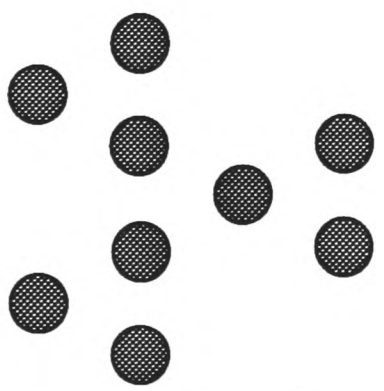

Zinc at 6.45 Å

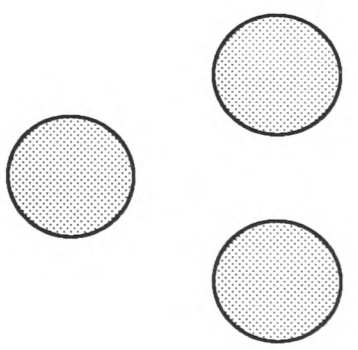

Magnesium at 8.06 Å

Figure 1.2 Crystal Structure of $MgZn_2$

Mg	(1/3,2/3,z)	(1/3,2/3,1/2-z)	(2/3,1/3,-z)	(2/3,1/3,1/2+z)
Zn	(0,0,0)	(x,2x,1/4)	(-x,-2x,3/4)	(x,-x,1/4)
Zn	(0,0,1/2)	(2x,x,3/4)	(-2x,-x,1/4)	(-x,x,3/4)

Structure - hexagonal unit cell with 12 atoms
(C14, P63/mmc from Pearson)
Atom positions where x= 0.83053 z= 0.063 (Hyde & Andersson)

a =b nm	c nm	Reference
5.21	8.60	Laves
5.23	8.57	Graf
5.20	8.62	Schmalzried
5.17	8.50	Tarschisch
5.15	8.48	Mondolfo

Lattice Parameters

Type No	η Al	η Al	Reference
1	(10.0) // (001)	(00.1) // (110)	Schmalzried
2	(00.1) // $(1\bar{1}\bar{1})$	(10.0) // (110)	Mondolfo
3	(00.1) // $(\bar{1}\bar{1}1)$	(11.0) // (110)	Schmalzried
4	$(\bar{1}2.0)$ // $(1\bar{1}\bar{1})$	(00.1) // (110)	Thackery
5	$(\bar{1}2.0)$ // $(1\bar{1}\bar{1})$	(30.2) // (110)	Thackery
6	$(\bar{1}2.0)$ // $(1\bar{1}\bar{1})$	(20.1) // $(1\bar{1}2)$	Thackery
7	$(\bar{1}2.0)$ // $(1\bar{1}\bar{1})$	(10.4) // (110)	Thackery
8	$(\bar{1}2.0)$ // $(1\bar{1}2)$	(00.1) // $(31\bar{1})$	Gjønnes
9	$(\bar{1}2.0)$ // (001)	(00.1) // (110)	Embury

Orientation Relationships

1	6 or 8 sided plates
2	rounded or hexagonal plates
3	hexagonal or triangular plates
4	rods [00.1]//[110]
5	rods at approx 11° to [00.1]//[110]
6	rods at approx 15° to [00.1]//[110]
7	rods at approx 25° to [00.1]//[110]
8	rods along $[1\bar{1}2]$//$[\bar{1}2.0]$
9	plates on (001)

Morphology (Gjønnes & Simensen)

Details of the structure, lattice parameters, orientation relationships and morphology of the nine identified η type precipitates.

Figure 1.3

nucleation theory. The main driving force for nucleation in the classical nucleation theory is solute supersaturation. This model is adequate for some systems, however experimental observations on some age hardening aluminium alloy systems showed that by variations of heat treatment:

i similar supersaturations can give different precipitate distributions;

ii the precipitate distributions formed are inhomogeneous; and

iii the precipitate distributions are dependent upon the quench rate, the time at room temperature prior to ageing, the ratio of heating rate to ageing temperature and trace impurity elements.

It was proposed that a critical vacancy concentration is necessary for nucleation. The nucleation of these precipitates is therefore dependent upon both solute and vacancy supersaturation. The effect of vacancies can only be implied by other experimental observations, since direct observation is not possible; thus the effect of heat treatments upon the precipitate-free-zones around grain boundaries and other vacancy sinks were studied.

Precipitation is now thought to occur by nucleation on solute-vacancy clusters formed during the early stages of the quenching treatment. These clusters can grow slowly at room temperature. There is a distribution of cluster sizes, and only clusters greater than a critical size may act as nucleation sites. Thus the precipitate distribution depends on the time at room temperature. Around a grain boundary there is both solute depletion and vacancy depletion after quenching. If the quench rate is slow then the material is at higher temperatures for longer times during quenching, so the diffusion path is longer and the depletion region is wider. Away from the boundary the longer diffusion path means that the distribution of solute-vacancy clusters will be coarser. After quenching, if the ageing temperature is high, then few clusters are sufficiently large to act as nucleation sites and a coarse distribution of precipitates is formed. If the high ageing temperature is then reduced, before all the smaller clusters have been dissolved, it is possible for many of these smaller clusters to act as nucleation sites at the lower

temperature, giving a second finer distribution of precipitates. If the nucleation of precipitates were dependent upon the concentration of free vacancies, this effect would not be observed because the vacancies would be lost during the ageing at the higher temperature. If the solution treatment temperature is increased, then the number of vacancies retained during quenching is increased, and thus the width of the depleted zone is narrower for a fixed critical vacancy concentration.

Many experimental results[23] point towards the existence of solute-vacancy clusters formed during the early stages of the quench. The size and composition of a critical nucleus must be temperature dependent. Also, these clusters must be fairly stable, since they can survive ageing at a higher temperature in order to act as nuclei later, when the ageing temperature is reduced, and the supersaturation increased. It is possible that stabilisation of the clusters is achieved by vacancies reducing the misfit strain energy associated with the solute atoms. Magnesium is known to have a strong binding force with vacancies[24]. However, this contradicts the observation that Al-Mg alloys do not form age hardening precipitates in this manner. It is possible that the solute-vacancy clusters in this system are stabilised at a size which is too small to act as nucleation sites, for example as simple Mg-V pairing. Since both the Al-Zn and the Al-Zn-Mg system do show fine precipitation, the zinc must be involved with the formation of clusters critical for precipitation. Additions of Ag to the Al-Zn-Mg system have been shown to cause even finer precipitation and elimination of the precipitate-free-zone. The effect of this trace impurity could be to stabilise the initial clusters preventing vacancy and solute migration to the grain boundaries. [Recently there have been FIM investigations of the effect of Ag upon precipitation which suggest that the silver is involved in the formation of initial clusters, which then attract magnesium[25].]

Other workers[26] were reaching similar conclusions working on different systems. These are discussed in the article by Lorimer and Nicholson[27], and so will not be covered here. The review article by Loffler [8] covers many subsequent investigations of the early stages of precipitation in these alloys.

1.2.3. Effect of heat treatments on precipitation.

Having described the possible precipitates in this system, and given a brief description of the basic theory behind their formation, it is now possible to describe the effect on this precipitation of the various stages in current commercial heat treatments.

1.2.3.1 Homogenisation.

The as-processed material must be heated to a high temperature, for a time sufficient to homogenise the large scale segregation of the solute elements due to the processing technique, without affecting the grain structure or causing detrimental liquation of grain boundaries or impurity phases. This is a separate heat treatment process, often quite long and complex, requiring critical temperature control.

1.2.3.2 Solution Treatment Anneal.

This is always the first stage in the main heat treatment process after fabrication. It is necessary to dissolve any age hardening precipitates that have formed. Solution treatment forms a solid solution of age hardening solute elements, homogeneous on the sub-micron scale. Increasing the temperature increases the number of vacancies and hence the supersaturation of vacancies achievable by quenching. If the temperature is raised too high, liquation of the grain boundaries can occur, which can destroy the mechanical properties of the material. However, increasing the solution treatment temperature is found to give enhanced SCC resistance[28] thus, the solution treatment temperature is usually kept just below the temperature at which liquation occurs and careful temperature control is required. A typical treatment used for this material is 1hour at 470°C.

1.2.3.3 Quench.

The rate of cooling from the solution treatment temperature is critical to the final microstructure. The cooling rate must be sufficiently high to cause the retention of a

supersaturated distribution of both vacancies and solute atoms. As mentioned previously, the supersaturated solutions of vacancies and solute must interact to form clusters in order to act as nucleation sites for either GP zones or η' precipitates. A faster cooling rate allows less time for diffusion, resulting in a finer distribution of clusters. The highest rate possible is desirable, but there are practical heat transfer limitations, and at high quench rates cracking can occur in thicker sections due to the internal stresses. A typical central quench rate achieved on Al-7150 commercial $2^1/_2$" thick plate is $100^oC/s$.

1.2.3.4 Natural Ageing.

By holding the newly quenched material at a low temperature (usually room temperature is used, just for ease), the quenched solute-vacancy clusters can slowly grow by diffusion, thus decreasing the solute and vacancy supersaturation. This causes the average size distribution of the clusters to increase with time. By increasing the average size of the clusters, more clusters will be large enough to act as nuclei for precipitation during subsequent ageing. Some Ostwald ripening may also occur, reducing the number of clusters. A balance must be found to maximise the number of precipitates. The typical time used is this case is 24 hours at room temperature. The economics of needing to store large quantities of material for long times during processing are a major factor in the choice of the natural ageing time.

1.2.3.5 Artificial Ageing - T6 and T73.

It is at the artificial ageing stage in the process that heat treatments may vary in order to achieve the different final properties desired. Increasing the ageing temperature can reduce the time taken to achieve peak strength, but it can also cause a reduction in the peak strength achieved. This is initially due to a reduction in the number of clusters being large enough to act as nuclei at the higher temperature, and also due to a reduction in the number of nuclei because of faster Ostwald ripening at higher temperatures. The ageing temperature also affects what type of precipitates form, and this affects the maximum achievable strength due to their different interactions with dislocations during

deformation. Specifically it is the change from dislocations cutting the precipitates, to dislocations looping the precipitates, that is being considered here. The two main commercial treatments are T6, designed to give peak strength, and T73, designed to slightly overage the peak strength material in order to improve the SCC resistance. These treatments may both use two stage ageing with an initial temperature around 100-120°C to form the finest dispersion of GP zones, and then ageing at a higher temperature to increase the speed of growth of these precipitates, either to peak strength, or to cause overageing, with an associated improvement in the SCC resistance.

Much of the early work of characterising the microstructures of this system was done on the early stages of precipitation, but very little work was done on actually characterising the microstructure of the commercial materials. There have been many conflicting reports over the types of precipitates present in these structures. Adler and DeIasi[29,30] attribute peak strength to GP zones they observed in the TEM; however, the means of identification seems to have been by size and morphology. They describe the T73 microstructure as predominantly η'. At the beginning of the 1980's interest in the detailed characterisation of the microstructure of alloys was renewed by the possibility of peak strength and good SCC resistance, as offered by a new ageing treatment called Retrogression and Re-ageing[31]. Rajan, Wallace and Beddoes[32] avoid the issue of precipitate identification by describing the T6 microstructure as the "normal coherent precipitate microstructure" and the T73 microstructure as η' and η precipitates. In a more detailed subsequent investigation[33] the T6 microstructure was again described as containing "a coherent second phase" and also some η' was identified, by the method of indexing of diffraction patterns, as used by DeArdo and Simensen[34]. A concurrent investigation of the microstructure of T6 and T73 materials by Park and Ardell[21] identified the precipitates by the indexing of diffraction patterns[18,35]. They identified the fine strengthening particles present in the T6 microstructure as being η' with some η particles. The T73 microstructure was described as mainly η precipitates. In a further investigation of the effect of RRA (see below) upon the microstructure of the alloy, Park and Ardell[35] compare their results with Dahn et al[33]. and agree with all of the

observations on the effect of RRA, except in the main identification of the type of precipitates (GP zones vs. η'). Dahn et al [36] disagreed and thus Park and Ardell produced a paper specifically reviewing the problem[37]. It is the Park and Ardell version that seems more applicable to the current research.

1.2.3.6 Artificial Ageing - RRA.

The treatment Retrogression and Re-ageing (RRA), for improving the SCC resistance, was initially suggested as a treatment by Cina[31]. A typical RRA treatment would be ageing at 120°C for 24 hours, increasing the temperature for a short time (e.g. 1hour at 180°C) prior to quenching and re-ageing at 120°C for 24 hours again. The effect of this treatment on the properties is shown in Figure 1.4. The effectiveness of this treatment was later confirmed by Rajan et al.[32] although they found that the initial minimum in the hardness, during the retrogression stage, did not correspond to the optimum values of SCC resistance and hardness as previously suggested. Investigation of the scientific reasons behind the improvement in SCC required detailed characterisation of the microstructure, as described above. This description of RRA is the Park and Ardell version.

The T6 microstructure of the matrix consists of a fine dispersion of η' particles with some η particles. Raising the temperature rapidly to the retrogression temperature causes those η' particles smaller than a critical size to start dissolving, while the larger η' grow and transform into η. At the retrogression temperature, it is also possible for η particles to be nucleated and grow; however, during retrogression the total number of particles must be decreasing. The grain boundary precipitates are already identified as η in the T6 structure and retrogression causes coarsening. Re-ageing causes re-growth of partially dissolved η' particles or re-precipitation of η' from the quenched solid solution. Buratti et al[38] have determined a working range for commercial RRA treatments for different temperatures and material thicknesses. They use measurement of %IACS (International Annealed Copper Standard) conductivity as an indicator of SCC resistance, with values greater than 36% representing good SCC resistance.

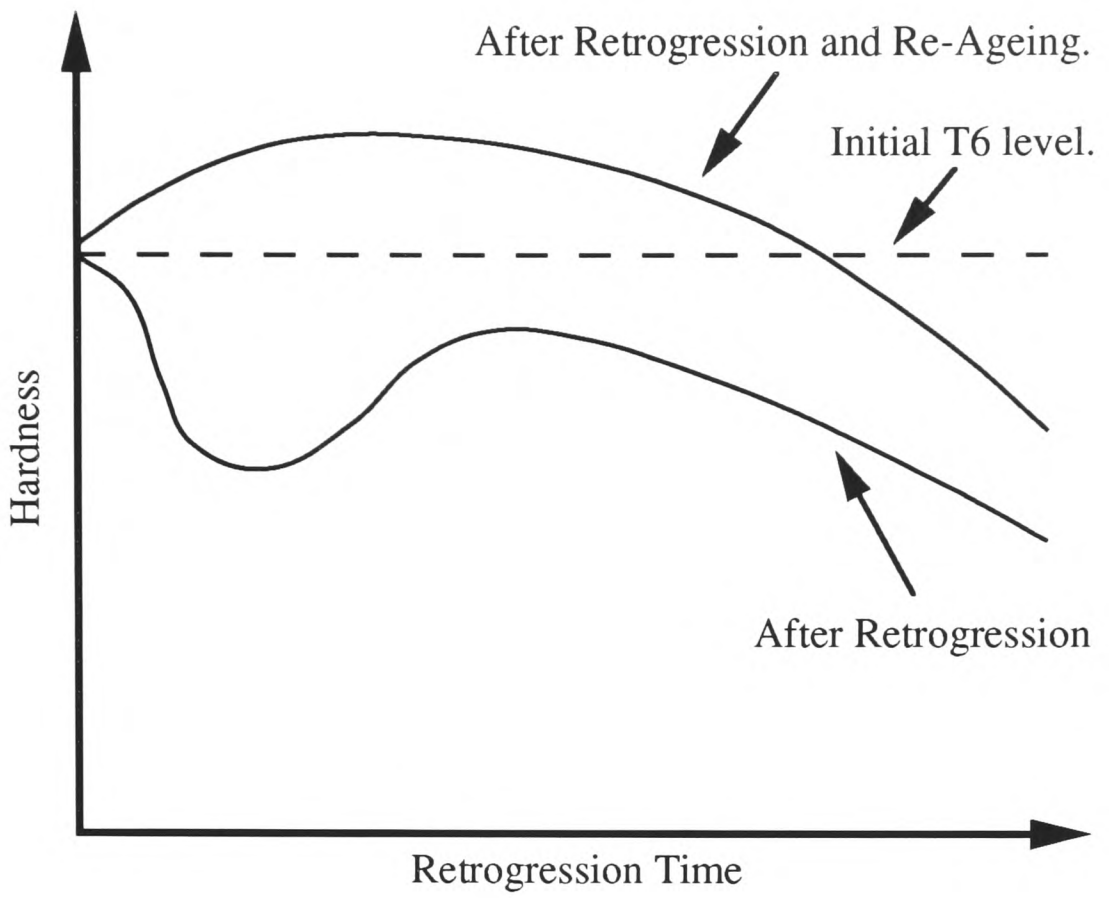

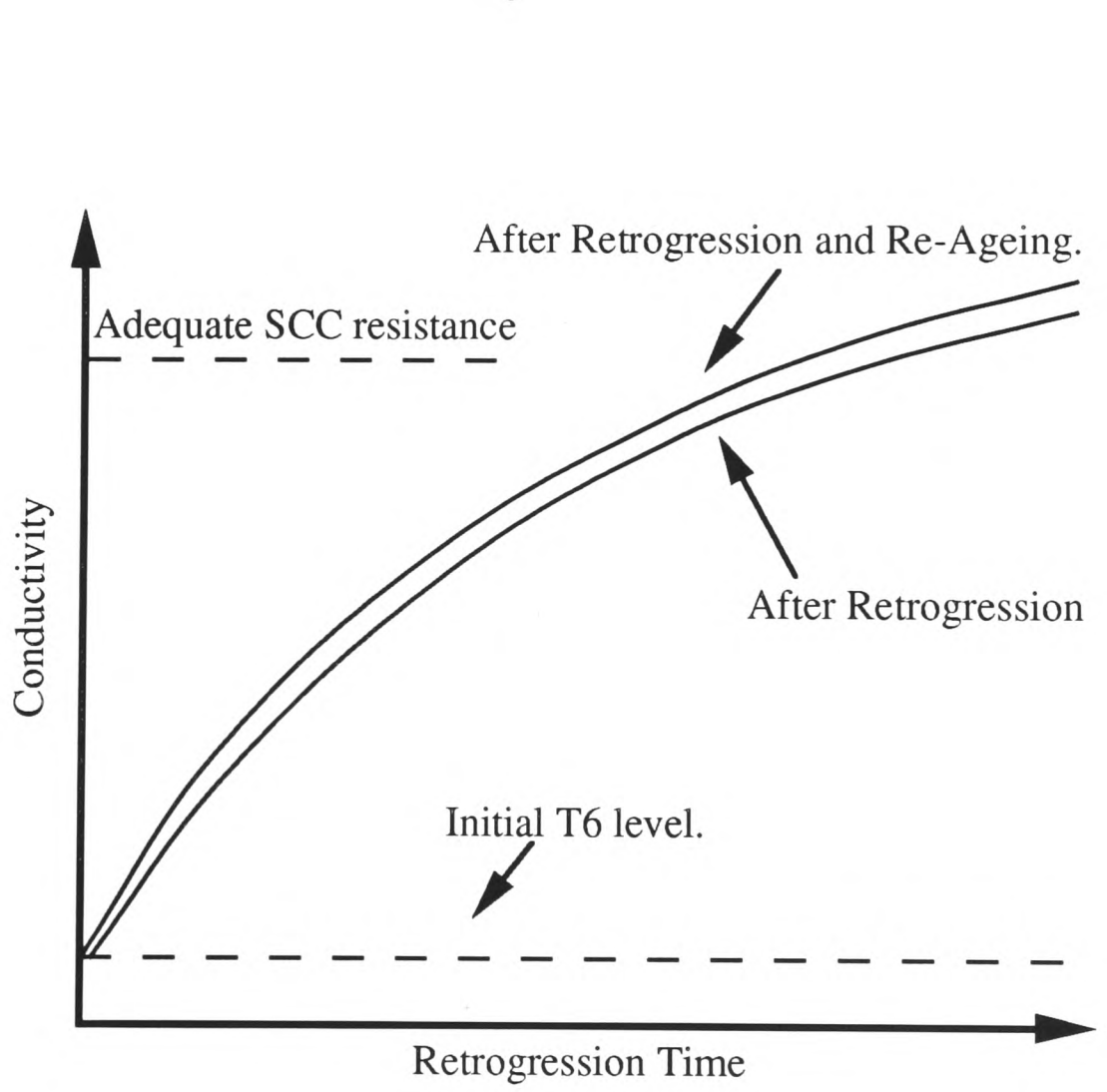

These show the effect of a Retrogression and Re-ageing treatment upon hardness and conductivity which are used to monitor the strength and SCC resistance respectively.

Figure 1.4

Ohnishi[39] has shown that RRA treatment can also improve the fracture toughness contrary to the earlier results of Swanson[40].

1.3. Microchemistry.

The microchemistry of 7000 series alloys has been the subject of much speculation and debate, due to the possible effects this may have on the problem of SCC. It is only during the last two decades that experimental techniques have developed sufficiently to provide data to support theories for possible mechanisms.

The primary limitation upon obtaining this information has always been the scale of the structures. For each of the investigations described here, the spatial resolution of the analyses have been given, in order to show the potential accuracy of the investigations.

1.3.1. Precipitate Free Zone Chemistry.

Much of the early work on the theory of nucleation was based of the phenomenon of the precipitate free zone (PFZ) around vacancy sinks (primarily internal interfaces, but also dislocations). The theory of age hardening precipitation was developed to explain phenomena like the observed dependence of the PFZ width upon solution treatment temperature, but not ageing temperature. Ward and Lorimer[41] monitored the effects of quench rate and ageing time upon the solute profiles around a boundary in an AlZnMg alloy using TEM and Energy Dispersive X-ray analysis (EDX), (EDX~100nm probe). Air cooled material was found to show broad depletion of zinc, after cooling, while no depletion was found in water quenched material until after significant ageing at 180°C. No comment on magnesium was made, presumably due to detection limitations. Doig and Edington[42] used TEM with Electron Energy Loss analysis (EELS) to monitor the magnesium solute profile (~10nm probe). They found that rapid quenching in water caused magnesium pile-up at the boundary, while slower quenching led to magnesium depletion over about 100nm, due to precipitation at the boundary. Later Raghavan[43] monitored the solute concentration as the PFZ developed during ageing, of an air-cooled (250μm thick) specimen, using EDX analysis with a probe size of 40nm. After

quenching, no significant depletion of zinc or magnesium was observed, nor were any precipitates observed. However, upon ageing, both elements became depleted across the whole PFZ width (600nm) due to diffusion, both to the boundary and to the edges of the PFZ. Diffusion to the edge of the PFZ occurs because, after the start of precipitation, the solute in the PFZ is supersaturated with respect to the matrix solute content in equilibrium with the precipitates, yet is unable to precipitate due to the lack of vacancies.

Park and Ardell[44] carried out an investigation of the PFZ chemistry for the three commercial tempers T6, T73 and RRA in 7075 material. The PFZ in these commercial tempers is only about 70nm wide. They quote a 6nm probe width (JEOL 100CX), however this is probably an underestimate, especially after scattering by surface contamination. They did not comment on magnesium segregation probably due to detection limitations, however they compared the zinc and copper levels in the PFZ. Zinc depletion was found to be very strong in the T6 condition, but further ageing to T73 (and RRA) only caused a slight reduction; however, copper depletion in the PFZ was found to increase significantly during further ageing to T73 or RRA. The problem of surface deposition of copper was minimised by keeping the foil thickness greater than 200nm at the point of analysis. However this reduces the spatial resolution further.

1.3.2. Grain Boundary Chemistry.

Viswanadham et al.[24] used Auger electron spectroscopy (AES) to investigate the depth profiles of zinc and magnesium for in-situ fracture surfaces of aged material. This is close to being realistic fracture information, except for the use of liquid nitrogen temperatures to achieve fracture. They found that both zinc and magnesium were segregated to the interface in the as-quenched material. After ageing they found that almost all of the zinc was associated with grain boundary precipitates, while over 50% of the magnesium could be considered 'free'. The segregation mechanism was described in terms of a Mg-V interaction, leading to solute drag. The dependence of this segregation upon solution heat treatment temperature and ageing temperature was

further investigated by Pickens and Langan[28] using the same technique, AES. The lateral resolution of AES was only about 200nm, thus separation of the precipitate and boundary contributions was not possible.

The evidence for magnesium segregation to the grain boundary, and the possible mechanisms for SCC, were reviewed by Scamans, Holroyd and Tuck[45]. Both equilibrium (energetically favourable) segregation and non-equilibrium solute-vacancy-drag mechanisms were developed. Their overall conclusion was that magnesium segregation to internal and external interfaces has various detrimental effects on SCC, but is not sufficient cause for SCC.

Crompton et al[2] subsequently performed a detailed EDX thin foil analysis of the solute content of the grain boundary interface. This used a HB501 STEM with a 3nm probe capable of minimising the contributions from non-grain boundary solute. The material they used was Al-7150 which had significant levels of copper, unlike the alloys in previous investigations. They found that in the as-quenched condition both zinc and magnesium were segregated to the boundary, while copper appeared uniformly distributed. After ageing at 120°C the boundary content of zinc was greatly reduced, by precipitation, and the magnesium content was slightly reduced, with little change in the uniformity of copper. Increasing the ageing temperature to 160°C, and ageing to T6 condition, caused the copper content of the boundary to increase significantly; however, further ageing caused a decrease in the copper content of the boundary and a gradual increase in the magnesium content. This work was the direct precursor to this current research.

1.3.3. Precipitate Chemistry.

Due to the small size of the matrix strengthening precipitates in material aged to near peak strength (matrix precipitates<10nm), there have been no documented attempts to analyse the chemistry of these precipitates. It is not possible to extract these precipitates from the surrounding matrix material due to their small size, and most electrolytes preferentially dissolve the precipitates. Precipitate extraction has only been used

successfully applied in AlZnMg alloys, for the investigation of larger heterogeneous impurity phases[46] such as Al_7Cu_2Fe and Mg_2Si. For this reason the precipitate chemistry in the AlZnMg system is always referred to as $MgZn_2$ which is the stoichiometric description of the equilibrium η phase, towards which the precipitate compositions are heading. For alloys with significant additions of copper, it has been shown that copper is also incorporated into the grain boundary precipitates, which are analysable by STEM EDX analysis; thus the description $Mg(ZnCu)_2$ is appropriate. Rao[47] describes chemical analysis of the grain boundary regions in Al-7075, including the grain boundary precipitates (Zn, Mg and Cu rich), but only describes his results qualitatively due to the large probe size (20nm) and the other general difficulties in quantification. Rao was more interested in the presence of silicon and copper rich precipitation in the overaged material, however Al-7150, as used in the present investigation, has particularly low levels of silicon. He does, however, mention the need for an investigation of the development of the copper content of the precipitates with ageing and this is one of the aims of the current research.

1.4. Stress Corrosion Cracking - SCC.

Since the main driving force for this investigation of phase chemistry in the AlZnMgCu system is the poor intergranular stress corrosion cracking resistance, it is necessary to present a description of the current understanding of this phenomenon.

SCC is the term used to describe the premature fracture of a material when stressed in the presence of a corrosive environment. This is a major problem, because if the strength of a material for a particular engineering application is affected by the environment, great care is needed in the choice of safety margins during design.

SCC can occur in many different materials and has been a problem in aluminium ever since it was first alloyed to improve its strength and other properties. Thus there is a huge amount of literature on SCC in aluminium alloys. There are several theories for describing the possible processes occurring in SCC and the literature has been reviewed regularly to attempt to bring together conflicting data and hypotheses[48,49] Burleigh[50] is

a recent review which goes a long way towards clarifying differences between alloy systems; however, in 7000 series alloys there is still no single microstructural parameter that has been identified as controlling SCC. This is mainly because it is impossible to systematically vary each parameter independently. Also the data is a muddle of alloy compositions, with the effects of commercial factors such as grain refiners, impurities and trace elements often ignored in laboratory investigations.

One feature of SCC in 7000 series alloys is its dependence upon the presence of hydrogen. It is this aspect that I shall concentrate on here although many other conflicting views have been suggested over the years.

1.4.1. The dependence of SCC upon hydrogen.

There are several clear experimental examples of the dependence of SCC upon hydrogen:

i susceptibility can be caused by pre-soaking in water, but has been found to be reversible if the material is then stored in vacuum prior to testing[51] ;

ii hydrogen diffusion was shown to be active in SCC by observing the failure of a tube, notched on the outside, due to the presence of a corrosive solution inside[52] ;

iii hydrogen recombination limiting 'poisons' have been used to show reduced corrosion but enhanced SCC, hence the amount of corrosion is less important than the amount of free hydrogen ions[53];

iv hydrogen has been measured directly by laser probe mass spectroscopy as being enhanced ahead of the crack[54] ;

v dry hydrogen (molecular) has no effect, however, high pressures and electrical discharge in the hydrogen can result in susceptibility (producing atomic hydrogen)[55] ;

vi SCC requires a threshold stress to be exceeded[56] ; and

vii the fracture mechanism seems to be discontinuous[57]

Having determined that atomic hydrogen plays a key role in the mechanisms of SCC, many authors have then gone on to postulate possible mechanisms based on their characterisations of SCC susceptible materials.

1.4.2. Suggested mechanisms occurring in SCC.

1 What happens at the surface?

Crack initiation occurs at the surface. There are surface irregularities. These can trap corrosive solution leading to the formation of local electrochemical cells and corrosion. There is also a protective oxide surface film. This layer can be ruptured mechanically at grain boundaries or slip steps, penetrated by diffusion, or dissolved chemically by the environment. Surface variations in chemistry, notably at grain boundaries, can set up electrochemical cells with the environment, leading to corrosion and anodic dissolution.

2 Where does the hydrogen come from?

The first source to be considered must be internal hydrogen content, present due to the manufacturing processes. Electrochemical reactions of the alloy, with the environment, may also produce hydrogen (via cathodic reactions). Hydrogen may also be present in the environment, but not due to chemical interaction with the material itself.

3 How does the hydrogen penetrate the material?

Entry of hydrogen is associated with the breaking of the protective oxide film, either by chemical or mechanical means. This in itself, however, does not mean that the oxide film is impenetrable to atomic hydrogen. Diffusion is more rapid along linear defects such as dislocations and grain boundaries, and is enhanced by dislocation transport during deformation.

4 Where does the Hydrogen go?

Preferentially, the hydrogen will go to sites of lattice misfit; grain boundaries, dislocations, point defects and solute atoms can all be energetically favourable sites. Hydrogen may react chemically to form hydrides; it is known to have strong interactions with magnesium and also copper and aluminium. Hydrogen could

recombine internally to form gas bubbles. Coarse precipitates could act as traps for hydrogen, thus reducing the concentration of 'free' hydrogen.

5 How does the hydrogen reduce the strength and promote the fracture?

Hydrogen could 'act to reduce the cohesive binding'. This effect would be largest at the regions of highest concentration, such as grain boundaries and precipitates, and the high stress region ahead of the crack tip. It should also be dependent upon the local chemistry. Hydrogen could react to form hydrides which could then fail in a brittle manner. Magnesium hydride formation at grain boundaries has been suggested, but not proven. Hydrogen could recombine and act as sites of high internal stress nucleating microvoids. Hydrogen could increase dislocation mobility, thus enhancing localised ductile fracture in the hydrogen-rich tri-axial stress region ahead of the crack.

As just described there are a multitude of possible mechanisms that have been suggested to explain the mechanism of hydrogen with the alloy. Since the SCC sensitivity develops during the thermal ageing practice required to control the strength, many attempts have been made to correlate the SCC behaviour with particular aspects of the microstructure. In other systems, correlation between grain boundary region chemistry and SCC has been shown to be due to anodic dissolution mechanisms; however, in this system anodic dissolution mechanisms are thought to be less critical than the effects of hydrogen, as discussed above.

Reviews of microstructural investigations[1] describe suggested correlations with: grain boundary precipitate size and spacing; matrix precipitate size, spacing and coherency, affecting dislocation motion; precipitate free zone width; solute profiles or slip characteristics; and grain boundary interface solute segregation.

These will not be documented again here, since they tend to confuse rather than clarify. Further details of previous microstructural investigations, and their bearing on SCC, may be introduced as required, in the discussion of results.

1.5. The aim of this research.

In brief, the aim of this research is to try to characterise the development of phase chemistry of the alloy Al-7150 with different ageing temperatures. From a more detailed understanding of the chemical processes occurring during precipitation, it is hoped that a better description of the factors affecting the SCC resistance of this alloy may be formed.

Chapter 2. Material Preparation.

2.1. Choice of specimen heat treatments.

2.1.1. Single Step Ageing.

The main work presented here used a single-step ageing procedure to cause precipitation. Three main heat treatment temperatures (120°C, 150°C and 180°C) were used with different ageing times chosen to produce material with similar strengths as determined from previous ageing curves[58]. In addition to these main heat treatments, material in the as-solution-treated state and material grossly overaged at a temperature of 220°C were also investigated. The details of these heat treatments are listed in Table 2.1.

The solution treated material was investigated to check for the earliest signs of precipitation or clustering in the as-quenched state, whereas the over-aged material was investigated to determine the shape and composition of the precipitates in this alloy system at equilibrium.

2.1.2. Retrogression and Re-Ageing.

An investigation previously submitted for Part II of my undergraduate degree considered the effect of a Retrogression and Re-Ageing heat treatment on the phase chemistry of matrix strengthening precipitates. In that work the hardness and conductivity were monitored regularly throughout the multiple step RRA process. A selection of nine specimens were observed in the TEM and from these four specimens were chosen for chemical analysis. The heat treatments previously investigated by FIM/AP are listed in Table 2.2.

Work on the RRA treatment was continued at the start of this research by the application of the new POSAP (Position Sensitive Atom Probe) analysis to two of these specimens (RA120 and RRA180). The advantage of POSAP analysis over conventional AP analysis is the ability to spatially select just the precipitate atoms, thus allowing

SOL	Solution treated for 1hour at 470°C and water quenched.
100/120	Solution treated, quenched, naturally aged for 24hours and aged for 100hours at 120°C.
20/150	Solution treated, quenched, naturally aged for 24hours and aged for 20hours at 150°C.
8/180	Solution treated, quenched, naturally aged for 24hours and aged for 8hours at 180°C.
40/220	Solution treated, quenched, naturally aged for 24hours and aged for 40hours at 220°C.

Table of specimen heat treatments.

Table 2.1

SOL	Solution treated for 1hour at 470°C and water quenched.
RA120	Solution treated, quenched, naturally aged for 24hrs and aged for 24hrs at 120°C, quenched, naturally aged for 24hrs, re-aged for 24hrs at 120°C.
RRA150	Solution treated, quenched, naturally aged for 24hrs and aged for 24hrs at 120°C, retrogressed for 2hrs at 150°C, quenched, naturally aged for 24hrs, re-aged for 24hrs at 120°C.
RRA180	Solution treated, quenched, naturally aged for 24hrs and aged for 24hrs at 120°C,retrogressed for 2hrs at 150°C and 4hrs at 180°C, quenched, naturally aged for 24hrs, re-aged for 24hrs at 120°C.

Table of Retrogession and Re-Ageing heat treatments.

Table 2.2

determination of the aluminium content of the precipitates. This information is entirely complementary to the solute fraction information obtained by previous AP analysis.

Comparison of the two specimens from the RRA treatment showed an increase in precipitate size and definition with increasing temperature and due to the two-step nature of the RRA treatment the RRA180 material also showed a bimodal distribution of precipitate sizes in agreement with the theory of RRA.

The RRA material will be referred to in Chapter 5 dealing with characterisation of the chemistry of precipitation.

2.2. Specimen preparation.

2.2.1. Heat Treatment of Specimens.

The material was supplied as a 12 X 12 X 2.5 inch rolled plate of commercial 7150 produced at Kitts Green in Birmingham.[2999501-2 CANADAIR W51 : 27.7%IACS]

The grain structure and uniformity was investigated by both optical microscopy and transmission electron microscopy in the three orthogonal directions with respect to the rolling direction.

RD (plane perpendicular to rolling direction)

ST (plane perpendicular to short transverse direction)

LT (plane perpendicular to long transverse direction)

Figure 2.1 shows the grain structure as observed optically.

It is primarily the high angle grain boundaries that etch to reveal the grain structure. The micrographs show a typical elongated grain structure, due to the rolling, with precipitates on the grain boundaries. The unetched microstucture shows dispersoids also aligned in the rolling plane. These are detrimental to the performance of the material. The material was also found to be cracked intergranularly close to the central rolling plane.

The orientation with respect to the rolling direction is shown as RD. The typical elongated grain structure formed by the rolling process is clearly visible in the planes perpendicular to the rolling direction and perpendicular to the long transverse direction. The top rolling surface, which is perpendicular to the short transverse direction, shows a more equi-axed grain structure as existed before the rolling process. Precipitates along the grain boundaries are also clearly visible on the high angle boundaries formed due to the rolling process. The different contrast between grains is due to the different crystallographic orientations reflecting the light differently.

The left picture shows a micrograph of the unetched microstructure in the plane perpendicular to the long transverse direction. This shows several large dispersoids aligned in the rolling direction with smaller precipitates faintly visible on some grain boundaries.

The right picture shows a micrograph of the central cracked region of the $2^1/_2$ inch plate as supplied. The cracking was severe and clearly intergranular.

Figure 2.1 Optical Micrographs.

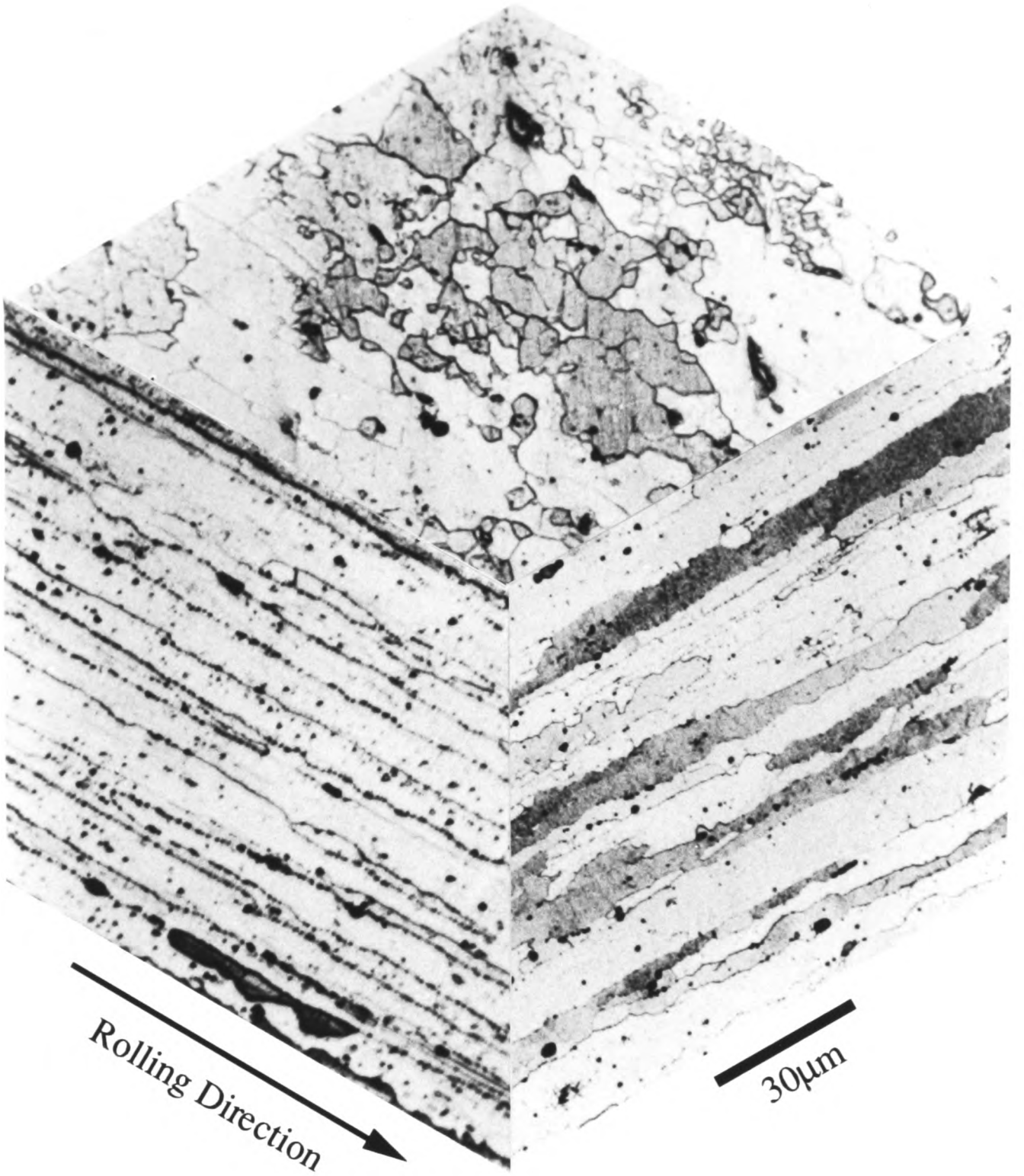
Rolling Direction
30μm

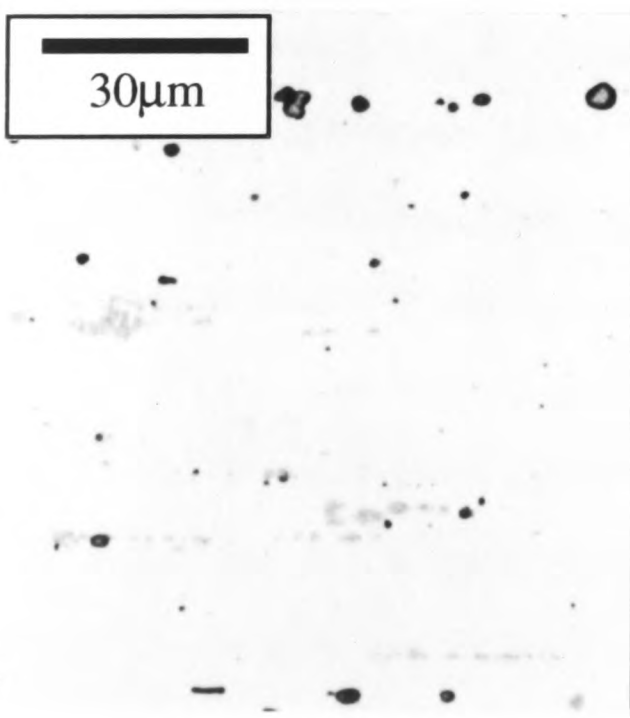
30μm

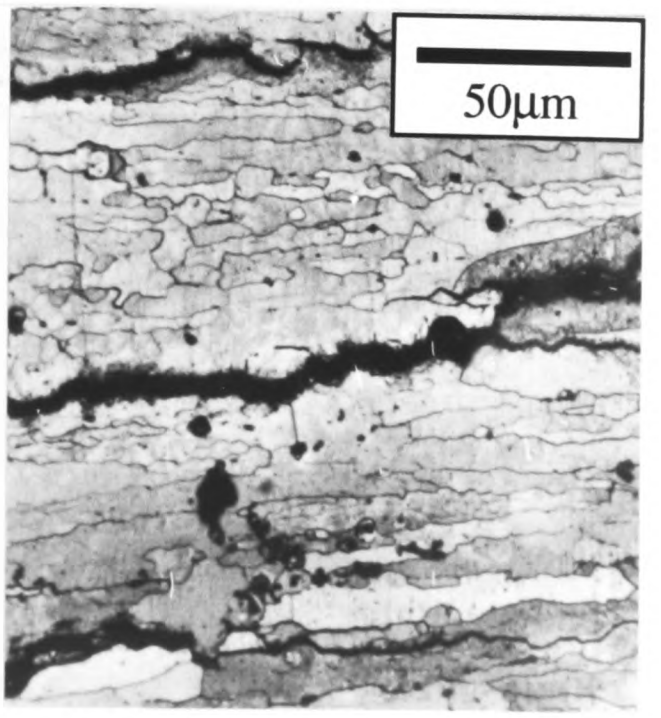
50μm

Observation in the TEM showed the presence of more low angle boundaries in the ST plane segmenting the long elongated grains. Measurement of the grain sizes for the three directions as determined from TEM micrographs showed the grains to be of average size about 6x6x3μm.

Small blocks suitable for laboratory heat treatment were cut from the as-received plate. The dimensions of the blocks were chosen to be a suitable size for preparing FIM specimens. The blocks were all milled to the same size and surface finish in order to give reproducible quench behaviour. They were cut, trying to avoid the central crack, to 27mm (RD) x 25mm (ST) x 16mm (LT).

The blocks were solution heat treated for 1hr at 470°C (not including heating time). The temperature was monitored by a test block containing a thermocouple. Quenching was done by drop-quenching into 1litre of ice cooled water. The test block was found to achieve 220°C/sec quench rate as defined by the cooling rate between 400°C and 290°C.

Room temperature natural ageing for 24hrs was followed by artificial ageing at the appropriate temperatures again monitored by the test block thermocouple.

2.2.2. FIM Specimen Preparation.

2.2.2.1. Non-selective specimen preparation.

Specimen blanks 0.3mm x 0.3mm in cross section were cut from the heat treated blocks using a slow-speed diamond wafering saw. These were then electropolished to a sharp point of end radius less than 50nm. Electropolishing of this material was done using standard Stage I polishing procedure[59] in 25% perchloric acid in 75% acetic acid. The solution was found to be sensitive to contamination by both the electropolishing equipment and also moisture present in the atmosphere. Fresh polishing solution and clean equipment (especially the gold electrode) was found to remove problems of pitting and excess hydrogen bubbling at the specimen surface. If problems persist, the common alternative is to reduce the temperature of the polishing solution below 0°C.

Back-polishing under a stereo microscope was used to produce the final tip and also to reduce the shank taper angle. Back-polishing used a more dilute solution than Stage I since the ratio of electrode surface area to specimen area was much larger. Typically less than 10% perchloric acid in acetic acid was used.

This method of specimen preparation quickly produced very sharp specimens suitable for FIM and atom probe analysis, but it randomly selects the region available for analysis. This method was sufficient for analysis of the matrix strengthening precipitates, since the size of the precipitates was small compared to the volume analysed and they were uniformly densely distributed. Thus, even with random analysis, precipitates were always encountered.

For analysis of features, where the scale of distribution of the features is much larger than the region of analysis, it is necessary to be selective during the specimen preparation procedure.

2.2.2.2 Selective specimen preparation.

In this work, the chemistry of the grain boundary regions is of interest. TEM was used to check the location of the feature of interest within the FIM specimen prior to analysis.

The orientation of the specimen blanks was initially chosen such that the length of the FIM specimen was in the short transverse direction. This meant that the high angle grain boundaries were perpendicular to (and most closely spaced in) the direction of analysis. The disadvantage of this orientation is that it is only possible to analyse across a boundary once. If the specimen is cut with boundaries parallel to the direction of analysis then the chance of finding a boundary is greatly reduced. However, once located, the analysis can proceed along the boundary, thus greatly increasing the amount of data collectable from that interface.

In order to check the FIM specimen for the presence of a grain boundary within the region of analysis a specially modified TEM holder is necessary for the FIM specimen. Various microscopes were available for use during this project. At the beginning of the

project one sample holder modified for FIM specimens already existed for a JEOL 100C microscope. The modified holder is shown in Figure 2.2.a. Initially this was used, but the maximum imaging thickness for 100keV electrons and the generally poor condition of the microscope precluded any successful imaging of grain boundaries in this microscope. A spare sample holder for the Philips microscopes (CM12 and CM20) was found and modified to take FIM specimens. The working distance of this model of microscope was only 3mm compared to 5mm in the JEOL microscope; thus a completely new holder design was required. This is shown in Figure 2.2.b. The new holder was used in both the CM12 and CM20 microscopes, but the advantage of the increased penetration of the 200keV electrons meant that the CM20 was preferred. At the end of the second year of this project a JEOL 200CX microscope was acquired. This then became the preferred microscope because the specimen holder with the larger working distance was much simpler to use.

2.2.2.3. Feature Selection.

More than 50 papers to date report the analysis of grain boundaries by FIM or AP analysis[60]. Early examples were concerned with FIM investigations of the atomic structure of grain boundaries and were often performed using tungsten specimens to facilitate atomic imaging.

Workers in Sweden were the first to repeatedly use electron microscopy to check the surface quality and internal structure of FIM tips prior to use[61]. Electropolishing with short pulses was observed to remove very small amounts of material from the end of the specimen, thus enabling the location of a specific feature within the region of analysis. This technique was later developed by the same group to produce a controlled method of back-polishing used for the AP investigation of long range grain boundary segregation in stainless steels. This increased the available range of data points either side of the boundary by alternating polishing and analysis[62]. For materials where large differences in the electropolishing behaviour of the constituent phases precludes controlled electropolishing, ion beam milling has been used with some success. Further

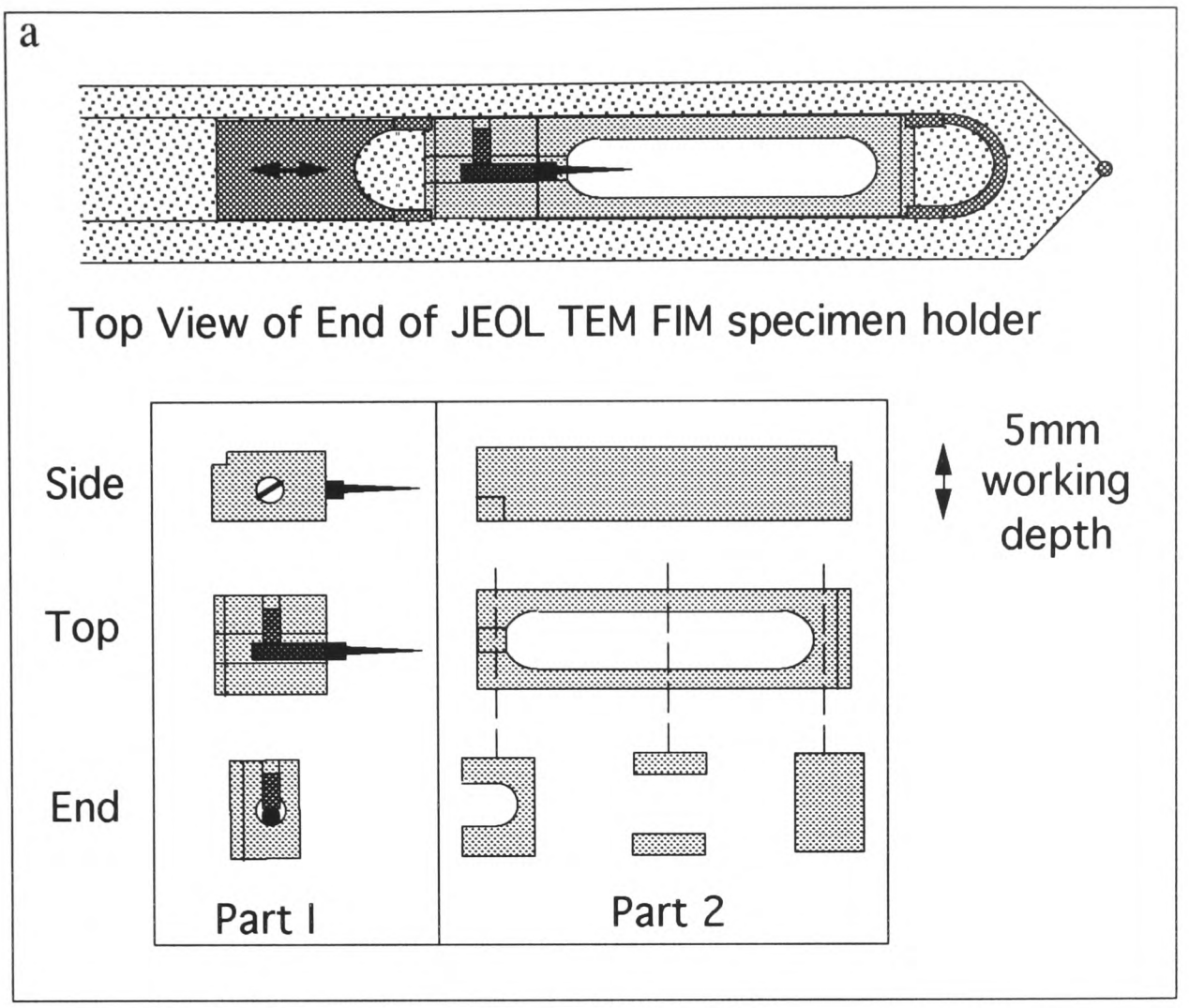

Figure 2.2 Diagrams of the two types of TEM holders modified to take FIM specimens. (Scale x2)
a) existing JEOL holder b) new Philips holder

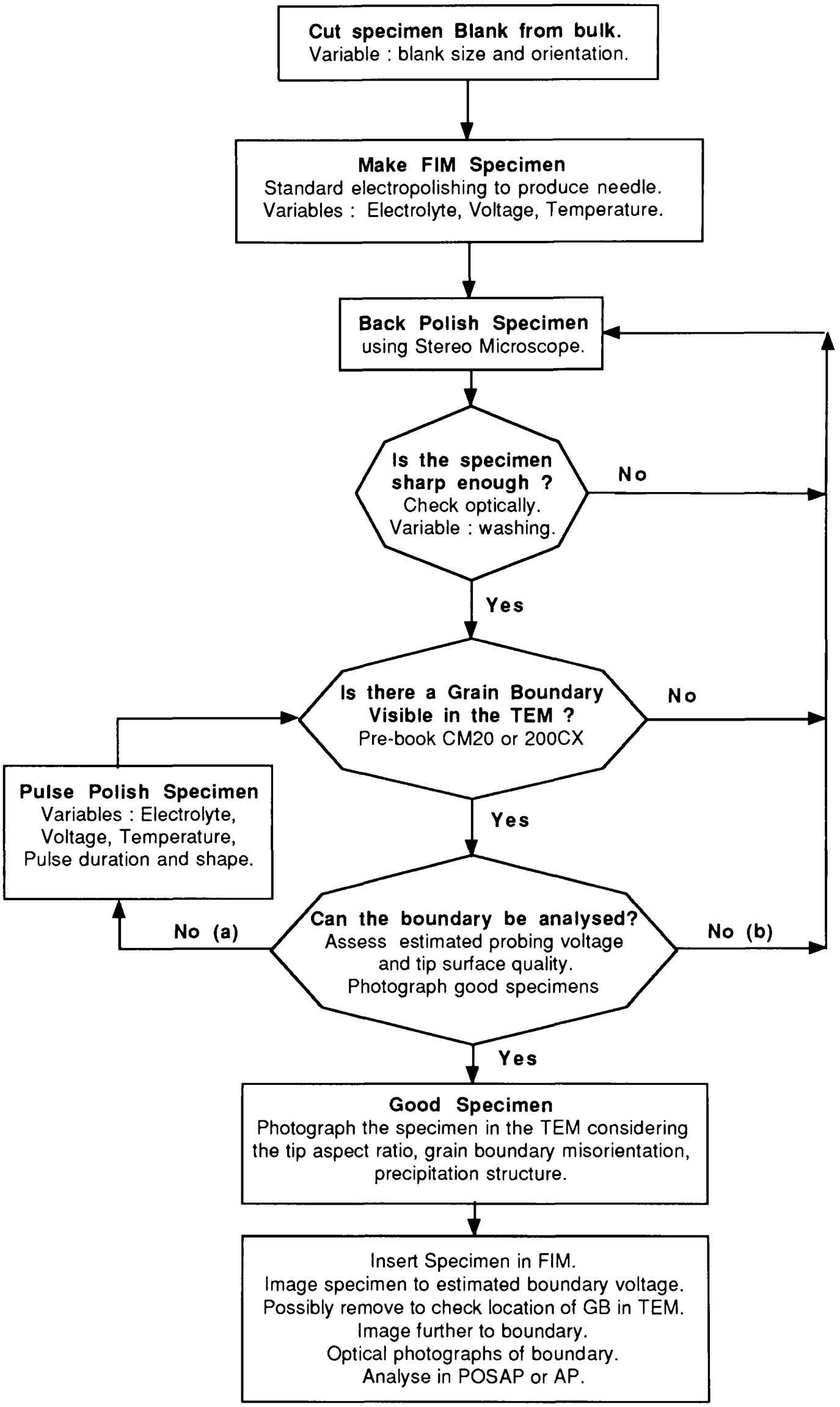

Figure 2.3 Flow Diagram For Preparation of FIM specimen with Grain Boundary.

development of the back polishing technique with the use of higher voltages and shorter pulses was found to cause removal of material from the sides of the specimen causing sharpening without much shortening of the specimen thus extending the analysis range of a specimen[63]. These specimen preparation techniques have been successfully applied to many systems by the Swedish group. These include:-

Austenitic stainless steels, low alloyed steels,

cobalt and nickel based cemented carbides,

nickel, zirconium and titanium.

More recently, workers in America carried out a systematic investigation of the effect of grain boundary misorientation upon segregation of rhenium in molybdenum[64]. They report development of a system for controlled back-polishing with a high success rate. A large amount of boundary characterisation is required prior to back-polishing[65].

In the previous work on grain boundaries in aluminium, there was a notable absence of investigations using the main proponents of this technique. However, recent work by Brenner et al. report the preparation of grain boundary specimens of the same alloy as used in this investigation by back-polishing[66]. They used 2% perchloric acid in 2-butoxy-ethanol (a commonly used solution) for the pulse polishing electrolyte.

Figure 2.3. shows a flow diagram of for the method of grain boundary specimen preparation. Pulse polishing was observed to work for some specimens as shown in Figure 2.4. where both grain boundaries have successfully been brought closer to the specimen tip. However this pulse polishing behaviour was found not to be repeatable or controllable. Figure 2.5. shows a variety of typical problems encountered with pulse polishing.

In this work various solutions were used for pulse polishing. In Stage I, a solution of perchloric acid in acetic acid was used. The material removal during pulsing was too rapid at higher concentrations (25%) so the solution was diluted to 10% and 2% levels. The attack was still too fast and uncontrolled and was also extremely sensitive to moisture which led to preferential attacking of the grain boundaries. After the first

a) shows a TEM dark field micrograph showing the brightly imaging end grain of a FIM specimen after initial back-polishing. The grain boundary is too far away from the specimen surface to be analysed by atom probe analysis. The grain also shows some dislocation contrast with these diffraction conditions.

b) shows a TEM dark field micrograph of the same grain as above however a 4ms 10V pulse in 25% nitric acid in methanol has been applied to remove about 500nm of material from the end of the specimen thus bringing the grain boundary closer to the region of analysis. This specimen was destroyed when a second pulse was applied, due to a layer of surface deposit resisting further electropolishing. The grain boundary as shown here is still outside the region avaialable for analysis.

c) shows a TEM bright field micrograph of a FIM specimen in material aged for 100hrs at 180°C. The location of the grain boundary is clearly visible; however, it is outside the region of analysis.

d) shows a TEM bright field micrograph of the same specimen as above but after two 2ms pulses in 10% perchloric acid in acetic acid. This has brought the grain boundary close enough to the specimen surface for atom probe analysis; however, the grain boundary precipitate is brightly imaging showing that it has been preferentially dissolved by the electrolyte.

Figure 2.4

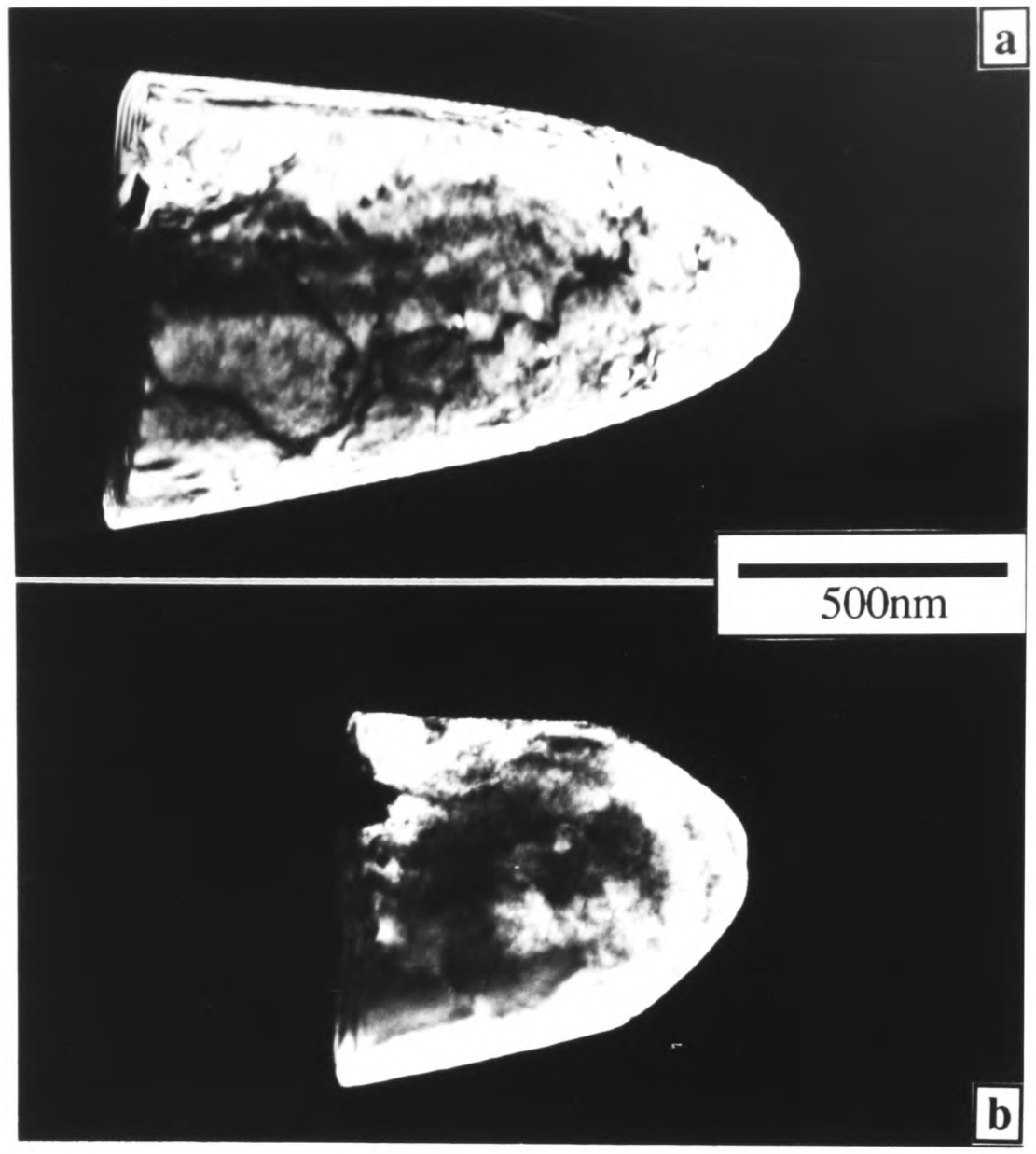
a
500nm
b

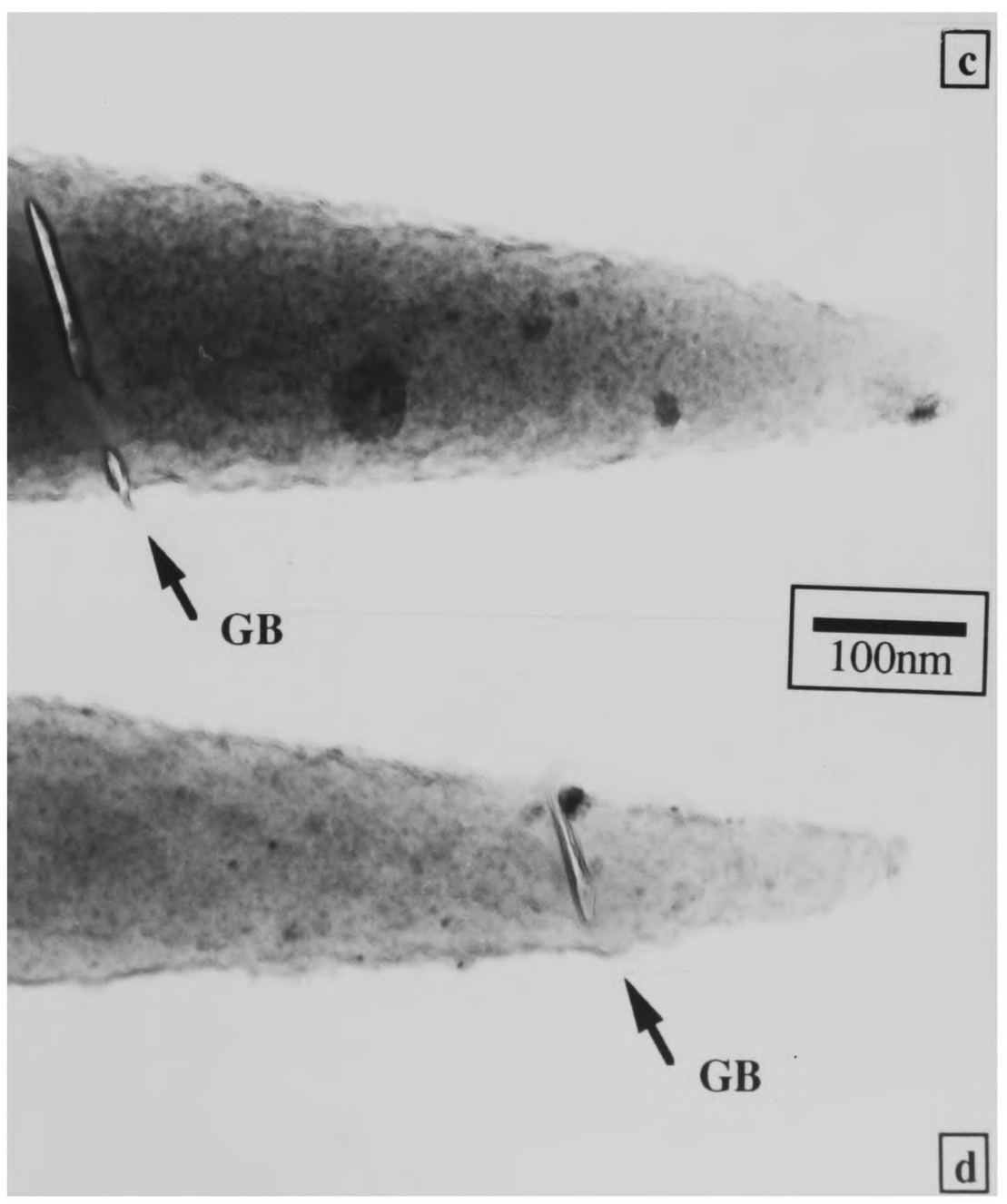
c
GB
100nm
GB
d

a) shows a TEM bright field micrograph of material aged at 180°C. There is severe preferential attack of the grain boundary regions. This attack has occurred on the shank of the specimen well away from the end tip. This specimen would be very likely to fail during imaging.

b) shows a TEM bright field image of a specimen aged at 120°C. There is an aesthetically rather pretty surface deposit that is, experimentally, undesirable. A possible source of such large particles might be grinding emery particles contaminating the methanol wash.

c) shows a TEM bright field micrograph of a single FIM specimen after initial back-polishing. Attached to the surface there is a second mini-tip that has been picked up from the electrolyte. The mini-tip is a by-product of the back-polishing process.

d) shows a TEM bright field micrograph of the same FIM specimen as shown above after washing in contaminated methanol. The methanol has attacked the specimen and penetrated the surface oxide dissolving the aluminium from within to leave a oxide sheath.

Figure 2.5.

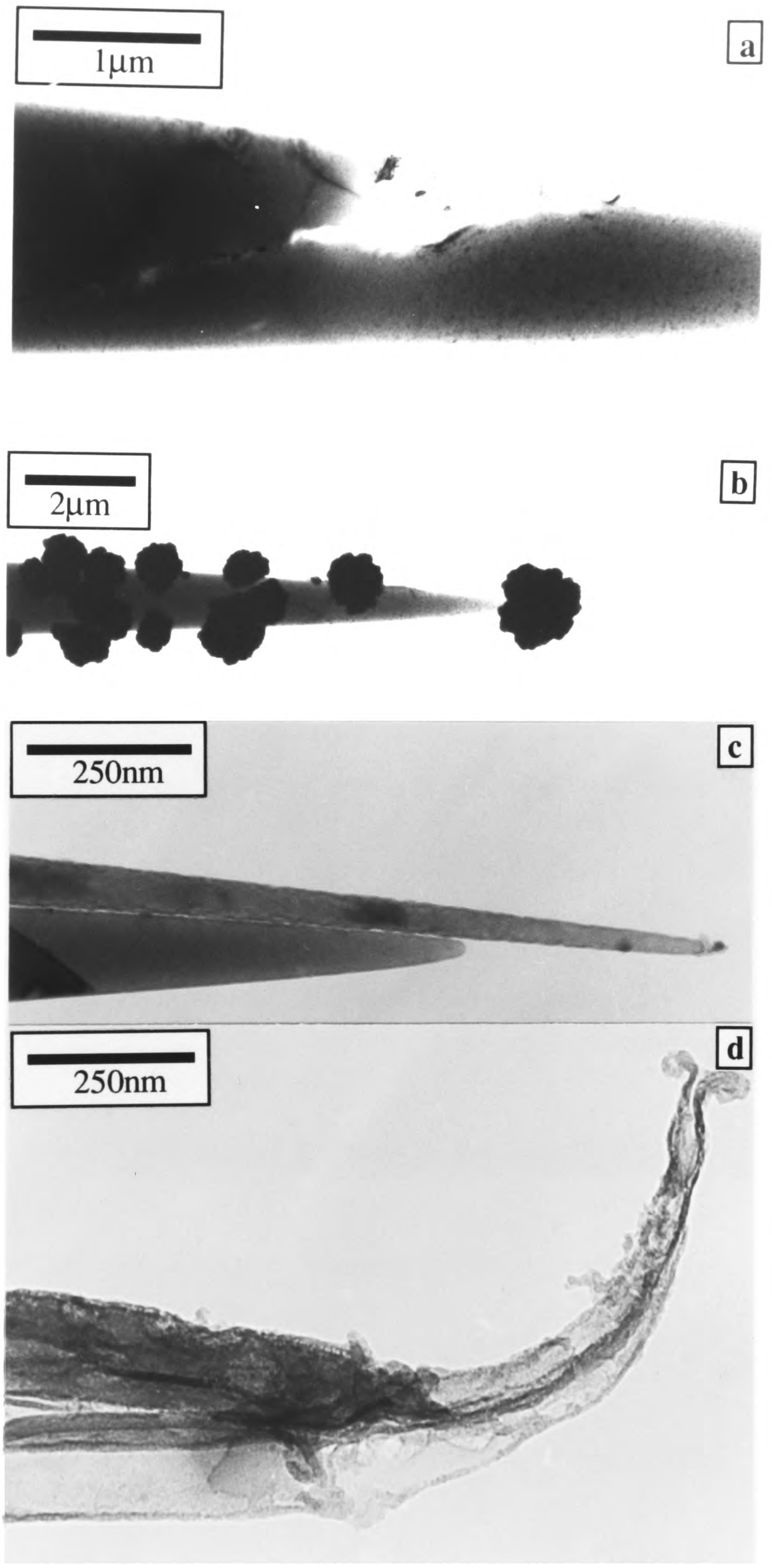
1μm
a
2μm
b
250nm
c
250nm
d

(possibly successful) pulse had been applied, the surface of the tip was often found to be coated with a non-uniform deposit which proved resistant to further pulsing. Increasing the electrolyte concentration or pulse duration to counter the deposit resulted in localised penetration and dissolution of the aluminium from within; thus leaving an outer sheath. Unfortunately, a method of preventing or removing this deposit has not found.

In order to slow the rate of material removal, the solution was changed to 2% perchloric acid in 2-butoxy-ethanol. This was found to leave a thick surface deposit even under standard polishing conditions. No method of washing the tip was successful in removing the deposit. A different solution of 15% nitric acid in methanol was used and found to be much too rapid although producing a good surface finish. Using a more dilute solution and cooling to -60°C and reducing the applied volts to 7V still did not reduce the polishing rate sufficiently for controllable pulse polishing. Yet another problem was the tendency of the pulsing reed to fuse shut; so giving a continuous circuit.

The overall conclusions of my attempts at pulse polishing are

- pulse polishing works for the removal of larger quantities of material by using large pulses; but problems occur when trying to use small pulses for the removal of small quantities of material.

- the use of perchloric acid in acetic acid electrolytes is very sensitive to the presence of moisture.

- the ability to produce uniform polishing is paramount in order to remove small quantities of material .

- a method of successfully washing tips is required.

- a more sophisticated pulser may be required to enable careful monitoring of the pulse shape and the charge applied[65]

Due to the unreliable effect of pulse polishing, specimen preparation was achieved most successfully by repeated back-polishing. Over one year, 70 tips were produced and about 40 of these were put in the FIM with the remainder being destroyed during

polishing or manipulation. Of these 40 specimens only 15 had a boundary within range of either POSAP or AP analysis. Of these 15 specimens, 10 failed during imaging and 5 gave POSAP analyses and one also gave an AP analysis. All specimens flashed eventually either during imaging or during analysis.

2.2.3. TEM Specimen Preparation.

Specimen discs 3mm in diameter were mechanically punched from 0.3mm thick wafers that had been cut from the heat treated blocks using a slow speed diamond saw. These were then ground to 100-150μm and electropolished using commercial Tenupol jet polishing equipment. The electrolyte used was 15% nitric acid in methanol solution with polishing conditions of T<0°C and 15Vdc. This was generally found to produce specimens with large areas suitable for imaging and analysis. Specimens were washed alternately in methanol and ethanol to clean the surface since the quality of very high resolution X-ray analysis is sensitive to surface contamination.

When analysed using Energy Dispersive X-ray analysis (EDX) it was found that the surface of the specimen was coated in a deposit of copper. The formation of surface films during electropolishing is a known phenomenon[67]. The amount of surface deposit may be minimised, but it is not possible to remove it completely. Alternative specimen preparation methods like microtoming and ion beam milling were investigated but microtoming introduced too much deformation and argon ion beam milling removed more aluminium than copper. The implications of this copper-rich surface layer upon quantitative analysis will be discussed later.

Chapter 3. Analytical Transmission Electron Microscopy.

A transmission electron microscope (TEM) simultaneously provides visual, crystallographic and chemical information about the internal microstructure of a thin specimen on the sub-micron scale. The TEM has become well-established as a research tool for the investigation of microstructures in metallic, ceramic and organic materials. The initial usage only for imaging has been advanced by the addition of other detectors to provide quantitative chemical information. When the electron beam passes through the material, there are many possible interactions between the electrons and the specimen. (Figure 3.1.) These can be broadly divided into two categories; elastic events which do not affect the kinetics but do affect the electron trajectories, and inelastic effects which do affect the kinetics.

-Elastic scattering is responsible for electron diffraction and the generation of back scattered electrons.

-Inelastic scattering results in the generation of secondary electrons, Auger electrons, characteristic and continuum X-rays, phonons and plasmons.

This study has concentrated on the use of X-rays for analysis of the development of microstructural chemistry in alloy Al-7150. These features are typically less than 10nm in size.

3.1. X-ray Chemical Analysis.

There are two main methods of generating X-rays by interaction with an electron beam. X-rays can be generated by the decelerating effect of an atom's Coulomb field on a passing electron. The energy lost during deceleration is emitted as X-rays. This produces a continuous spectrum of X-rays up to the energy of the incident electrons. This continuous background radiation, called Bremsstrahlung, should be removed from the total spectrum since it is independent of the composition of the material within the volume of analysis. These background levels can generally be predicted sufficiently accurately to enable their subtraction from the total X-ray signal. However, at the low

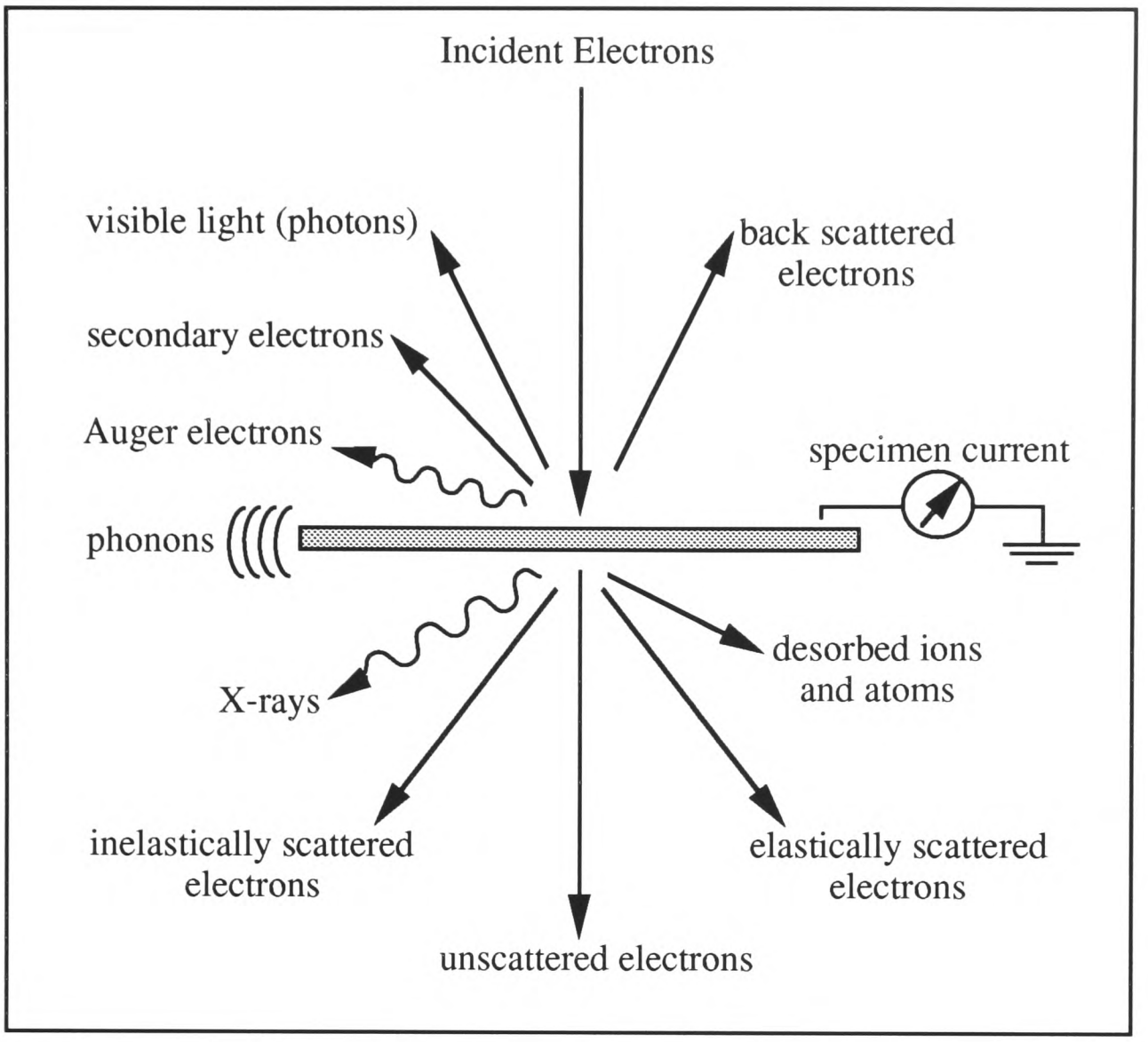

(Courtesy N.J.Long)

Figure 3.1.

Element	Energy keV	Energy keV	Energy keV
Magnesium	K =1.253		
Aluminium	K =1.486		
Copper	Kα=8.04	Kβ=8.804	Lα=0.930
Zinc	Kα=8.63	Kβ=9.570	Lα=1.012
Zirconium	Kα=15.744	Kβ=17.633	Lα=2.124

Table of the characteristic X-ray peak energies for the main elements present in Al-7150. (data from Loretto[105])

Table 3.1

energy end of the spectrum this is not practical since absorption is a strong function of composition (which is unknown). In this case it is necessary to fit empirically the background.

X-rays are also generated when a high energy incident electron hits an atom and ejects a tightly bound inner-shell electron. The atom is left ionised and highly energetic. The atom can lose this energy by emitting an outer-shell electron as a Auger electron or by emitting an X-ray, while an outer-shell electron drops into the gap in the inner-shell. Since the electronic structure of each element is unique, the energies of the emitted X-rays are characteristic of the energy levels of the element. These are thus called characteristic X-rays. Table 3.1. gives the energies of the important characteristic X-rays generated in Al-7150 and Figure 3.2. shows a typical spectrum for this alloy.

Each peak in the X-ray spectrum is described in terms of the electron transition that occurred to generate an X-ray with that energy. For each element $K\alpha$ is the X-ray emitted when an L electron falls into the K shell vacancy. If distinction is made between different L electrons, then the terminology $K\alpha 1$, $K\alpha 2$, etc is used. $K\beta$ is the X-ray emitted when a M electron falls into the K shell, thus a $K\beta$ X-ray always has a higher energy than a $K\alpha$ X-ray from the same element. Similarly, $L\alpha$ X-rays are emitted by an electron dropping from the M shell to the L shell. One particular peak in the X-ray spectrum may be generated by several different elements; however, if that element is really present all of its characteristic X-ray peaks must be present.

If quantitative elemental analysis is required, not only is it necessary to identify the X-rays generated, but it is necessary to know the relative efficiency of generation of the different X-rays for each element. The efficiency of X-ray generation for an atom is affected primarily by the incident electron energy. For a thin foil this is assumed constant through the thickness, although there are actually some losses due to the generation of Bremsstrahlung radiation. Secondly, the efficiency of generation is determined by the probability of Auger electron emission compared to the probability of X-ray emission (and the number of possible ways of returning the ionised atom to the ground state).

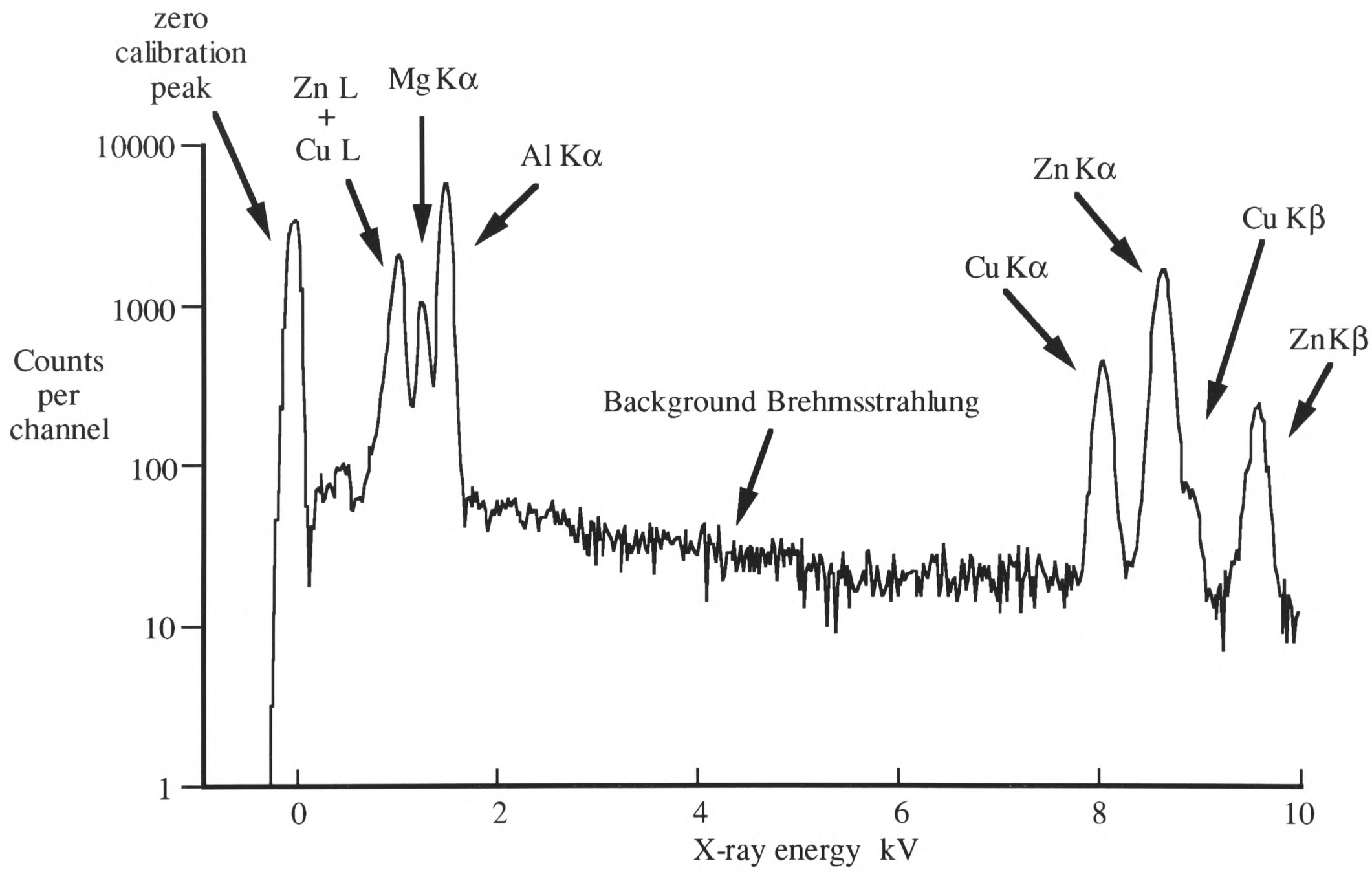

Figure 3.2 A typical X-ray spectrum from this alloy showing the X-ray peaks detected.

Once the X-rays have been generated by the electron beam they must be detected. X-rays are detected by charge generation in a semiconductor device and the signals are sorted by a multichannel analyser to give rapid simultaneous acquisition across the entire spectrum of energies[68]. The energy resolution of a conventional X-ray detector is only about 150eV. This can affect quantification when the peaks are close together; however, there are several standard peak deconvolution programmes available. The usual detector assembly has a beryllium window to protect the detector from vacuum contaminants. The beryllium window will absorb low energy X-rays such as those generated by the light elements up to magnesium. Hence, to maximise the detection of the magnesium X-rays in this system, it is preferable to use a windowless detector. A windowless detector requires a better vacuum and more careful use than the Be window version since surface contamination will affect the detection efficiency. Of the various microscopes available in Oxford with X-ray detectors, only the VG-HB501 had a reliable windowless detector for most of the duration of this research.

3.2. Quantification.

As described above the intensity of X-rays generated (I) is proportional to the incident beam current (i), the number of atoms of the element present (n), the cross-section for ionisation of the atoms by the incident electrons (Q) and the efficiency of that element in producing X-rays (w). Quantification is further dependent upon the efficiency of detection (which varies with X-ray energy) and the attributing of X-rays to each element (windowing and background removal).

$$I \propto i \cdot \Sigma n_j Q_j w_j$$

The number of electrons in the incident beam (i) varies and is usually unknown thus quantification must be achieved by considering relative peak intensities. The ionisation cross-section for an element (Q) is dependent upon the incident beam energy which is assumed to be constant through a thin foil. The detector efficiency varies with the energy of the X-ray and is difficult to determine accurately and can also vary during the lifetime of the detector. Modelling of the X-ray generation and detection efficiencies to

achieve quantification is less accurate than the use of standards which can be checked regularly to detect any changes in the detector operation.

Cliff and Lorimer[69] proposed a method of ratios for relating the X-ray intensities to the compositions whereby

$$\frac{C_A}{C_B} = k_{AB}\frac{I_A}{I_B}$$

The value of k_{AB} is a constant to be determined experimentally, using known standards. Thus, with constant analysis conditions and the appropriate k factors, quantification may be possible.

Other factors of X-ray analysis that need consideration include: spurious X-rays being generated outside the volume of analysis; absorption and fluorescence affecting relative peak intensities; the geometry of the electron beam determining the volume of material excited; the orientation of the specimen with respect to the detector, which can affect the detection efficiency; and the diffraction conditions, which can affect the uniformity of the beam intensity within the excited volume.

3.3. Specific Aspects of Quantification.

This alloy system presents several specific problems which seriously limit the accuracy of any quantitative information that may be obtained by X-ray analysis.

3.3.1. Window definition.

Considering just the Kα X-ray peaks for each element (Figure 3.2) there is significant peak overlap between the magnesium Kα and the aluminium Kα peaks. This is particularly important since the relative elemental concentrations in the alloy are about 93% Al and about 3% Mg. There is also slight peak overlap between the zinc Kα and the copper Kβ peaks. This is less of a problem, due the similar levels of these two solute elements and the wider peak separation. However, if there is significant enhancement of the levels of one element there will also be an apparent slight enhancement of the other due to the peak overlap.

For accurate quantification the background X-rays must be removed (as mentioned above). At the low energy end of the spectrum (<2keV) modelling of the background levels is not accurate due the dependence of the charge collection efficiency of the detector upon energy of the X-rays, which, in turn, is determined by the composition of the material which is still unknown. Incomplete charge collection of aluminium X-rays causes spreading of the aluminium peak towards lower energies thus increasing the overlap with the magnesium peak which is itself spread-out. It is thus necessary to accept that the magnesium content in this work is not accurately quantifiable using X-ray dispersive analysis.

For accurate quantification of the zinc and copper an empirical method of background subtraction can be used. The background contributions to Zn and Cu may be approximated to the background levels observed in a similarly sized adjacent window.

3.3.2. Surface Deposition.

A particular problem of elemental quantification in this system is surface deposition of copper. It has long been known that specimen preparation by electropolishing or ion beam thinning can alter the chemistry of the surface[67]. Several examples of surface deposition (as distinct from spurious x-ray generation elsewhere in the microscope column) have been documented. The deposition results from selective oxidation of the aluminium thus trapping the copper in the amorphous surface oxide layer forming during electropolishing[70]. The surface film and resultant enrichment is uniform. A study of the effects of different surface preparations found that jet polishing produced the best specimens. Sputtering the surface of an aluminium alloy to remove the excess copper has been shown not to produce the desired effect.

Recent work on Al-7150 by Park and Ardell[71] has also observed deposition of copper. They extended the Cliff-Lorimer relation to give the dependence of the relative intensities upon foil thickness.

$$\frac{I_{B_{Total}}}{I_{A_{Total}}} = \frac{I_{B_{Bulk}}}{I_{A_{Bulk}}} + (K-1)\frac{2t^{layer}}{t^{foil}} * \frac{I_{B_{Bulk}}}{I_{A_{Bulk}}}$$

where I's are the X-ray intensities and K is an enrichment factor.

This gives a dependence upon t^{-1} which can be experimentally verified. The appropriate measurements of foil thickness were not done in the present work, however there was ample evidence of the surface deposition of copper and of the variability of the thickness of deposition with position (Section 5.2.2). Unfortunately, the effect of this copper deposition is to make the accurate determination of the copper concentration impossible.

3.3.3. Statistics.

Statistical considerations affect the accuracy of several of the operations necessary to achieve quantification. Often the problem obeys Poisson statistics. This is applicable when the probability of a specific event is very low, but the total number of events is very high; such that observation of the specific event is significant and the event may be treated as part of a continuous distribution.

For example, consider the accuracy with which the number of counts in each energy channel can be determined. Assume a probability (p) of an X-ray with that energy. For a total number of counts (n), the number of counts in that energy channel is np. According to Poisson statistics, if the experiment were repeated many times the average number of counts of that energy would be np and the standard deviation of the distribution of counts would be $(np)^{1/2}$.

Consider the accuracy of detecting a solute element at the 1% level. If n_A solute counts are detected out of N total counts, this has a standard deviation of $(n_A)^{1/2}$ counts. Thus, using the normal distribution 95% confidence limit of $\pm 2\sigma$, the detected composition will be $(n_A/N) \pm 2(n_A)^{1/2}/N$. Thus to measure solute to $1 \pm 0.1\%$ requires $N > 40000$. A similar argument can be used to determine the significance of a peak over a background level, if background subtraction is used.

In this work, calculating a composition from the X-rays generated using a stationary finely focused electron beam (spot analysis), requires a large number of total counts to achieve good statistical significance due to the low solute levels present. There are two

ways of collecting more counts: to increase the volume of excited material; and to increase the counting time. However, increasing the volume of material means increasing the foil thickness, which reduces the spatial resolution (due to beam broadening effects), and increasing the counting time increases the effect of specimen drift and contamination, both of which reduce the spatial resolution. Using a field emission gun STEM increases the beam brightness and decreases the probe size. The ultra high vacuum conditions in this kind of microscope also decrease the contamination rate. All of these effects are beneficial to the statistics of analysis. In a conventional TEM/STEM (Phillips CM20), contamination was found to reduce the already poor spatial resolution to a level where no useful analysis could be attempted on small features, if counting times were increased sufficiently to give statistical significance to the EDX data.

3.3.4. Summary.

Since quantification of magnesium content will be inaccurate due to peak overlap with the aluminium, and quantification of copper content will be inaccurate due to surface deposition, absolute quantification of precipitate compositions in the AlZnMgCu system has not been attempted in this work. For detection of the low solute levels present in this alloy, the statistical accuracy of any analysis must also be kept in mind when interpreting the experimental data.

Chapter 4. Field Ion Microscopy and Atom Probe Methods.

4.1. Introduction to techniques.

4.1.1. Field Ion Microscopy.

The Field Ion Microscope (FIM) was the first microscope to achieve atomic resolution. The basic instrument is surprisingly simple (Figure 4.1). The specimen, in the form of a sharp needle, is cooled below liquid nitrogen temperature in the presence of about 10^{-4} Torr of an inert image gas and a positive voltage is applied to the specimen with respect to a phosphor screen. When the field at the tip of the specimen reaches about 2-4V/Å an image will start to appear on the phosphor screen, due to field ionisation of the image gas. In the high field region near the tip the gas atoms are polarised and attracted to the tip. These atoms then hop about over the surface, becoming thermally equilibrated, to form a surface layer of adsorbed gas atoms. Ionisation of these adsorbed atoms can occur by the process of electrons tunnelling from the atom into the specimen through a potential barrier which is reduced by the presence of the applied field. However, since tunnelling can only occur if there is an unoccupied energy level in the specimen, and if the potential barrier is narrow enough, thus the highest probability of ionisation is located in a narrow region about 4Å above the surface. Hence tunnelling occurs preferentially at surface protrusions (Figure 4.2). The surface of a specimen will initially be rough, but by extension of the concept of field ionisation, it should be clear, that at sufficiently high fields, it is possible for protruding substrate atoms to become ionised and be evaporated from the surface. An artificial distinction is drawn by describing the image gas atoms as being field ionised and the substrate atoms as being field evaporated.

The field ion microscope is thus a microscope for imaging the surface protrusions of a very sharp needle. The surface will be smoothed by the process of field evaporation to an approximately hemispherical end-form, such that the largest protrusions are due to the crystallographic packing of the substrate atoms. Thus, just by viewing the image, it is possible to view point defects (vacancies and impurity atoms), line defects (dislocations) and planar defects (grain boundaries and twins) in the crystal structure.

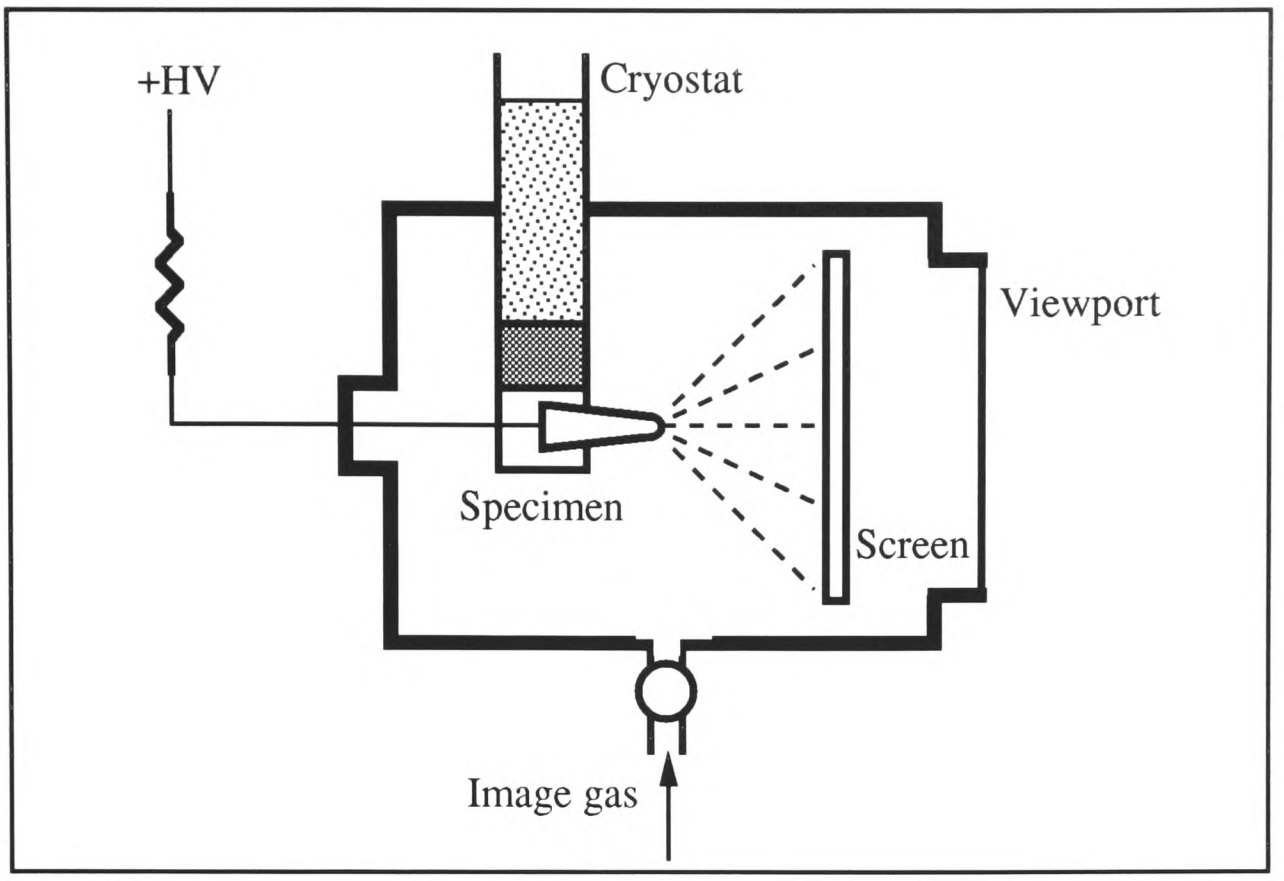

Figure 4.1 Schematic diagram of a field ion microscope.
(courtesy A Cerezo)

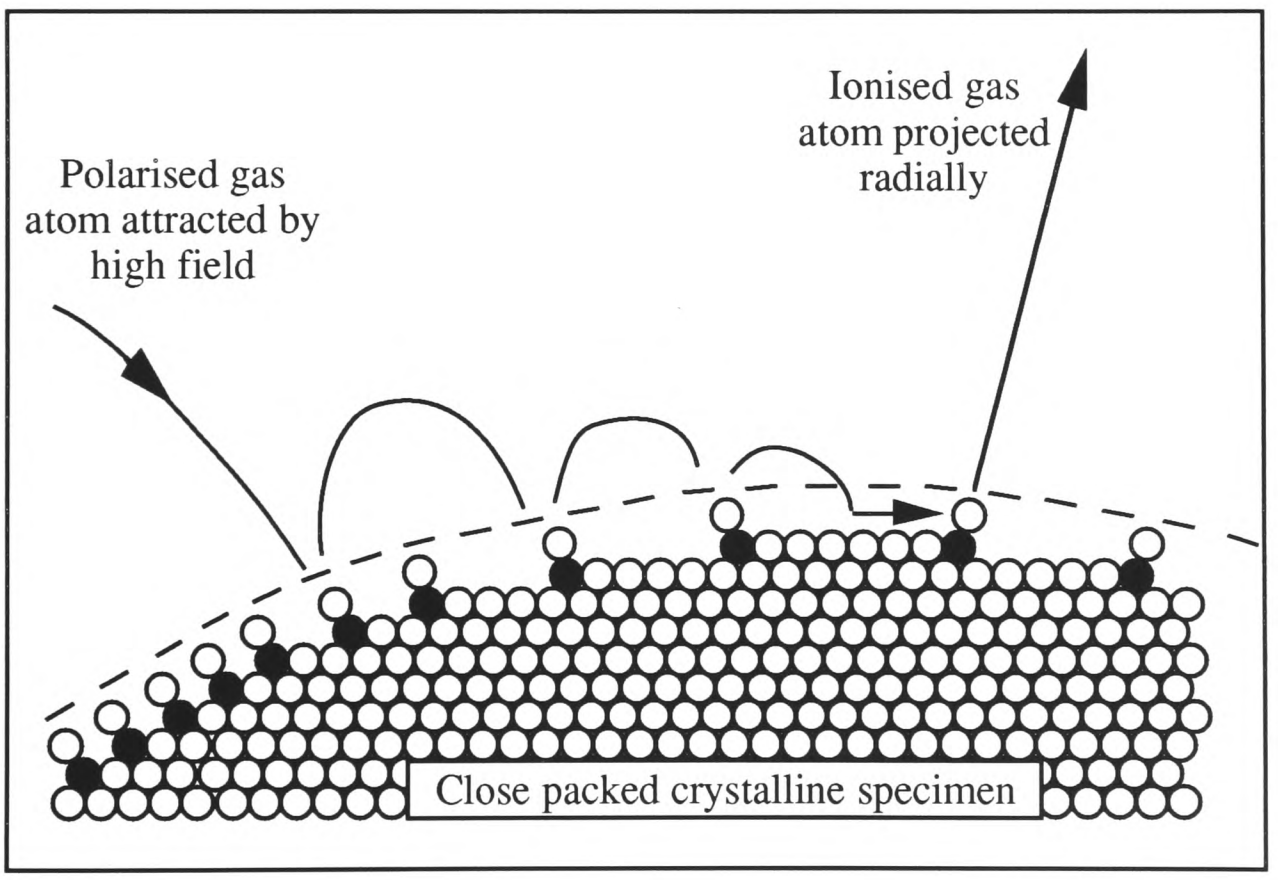

Figure 4.2 Schematic diagram of image formation.

Alloying a material mixes atoms with different work functions and this results in different electron tunnelling rates. For a mixture of elements with sufficiently different imaging characteristics, atomic scale variations in chemistry (such as disordered impurity atoms, ordered structures and second phases) may also be observed in the FIM. For more information about the diversity of applications of the FIM the reader is directed to various comprehensive texts[72,73,74,75].

4.1.2. Atom Probe Analysis.

4.1.2.1. Principles.

Atom Probe analysis is the term used to describe the use of time-of-flight mass spectroscopy, to identify the evaporating species in a field ion microscope. A small hole is made in the phosphor screen of a FIM and the specimen is tilted and rotated such that the image of the feature of interest is aligned over the hole (Figure 4.3.). If the specimen is further evaporated, only atoms from that feature will pass through the hole. These atoms can then be identified by time-of-flight mass-spectrometry.

Initially, the applied voltage is maintained at a level where no field evaporation will occur. Then a short extra voltage pulse is applied, such that field evaporation of some of the surface atoms occurs at a known time. Some of the evaporated atoms then fly through the hole in the imaging screen and are detected, a certain time later, by the single atom detector assembly. Since both the time of evaporation (t_1) and the time of detection (t_2) are known, and the energy gained traversing the flight length (l) is entirely due to the applied voltage V(dc + pulse), a mass-to-charge ratio (m/n) can be determined by using equation 4.1.

$$\frac{m}{n} = \frac{2eV}{l^2}.(t_2 - t_1)^2 \qquad \text{.....4.1}$$

For the VG FIM100 used in this research, the mass resolution was $\Delta m/m > 1/2000$, due to using a Poschenrieder energy compensation system[76,77] .This resolution was sufficient to clearly resolve the different isotopes of copper and zinc at 63, 64, 65, 66, 67 and 68 amu even for the doubly charged ion species.

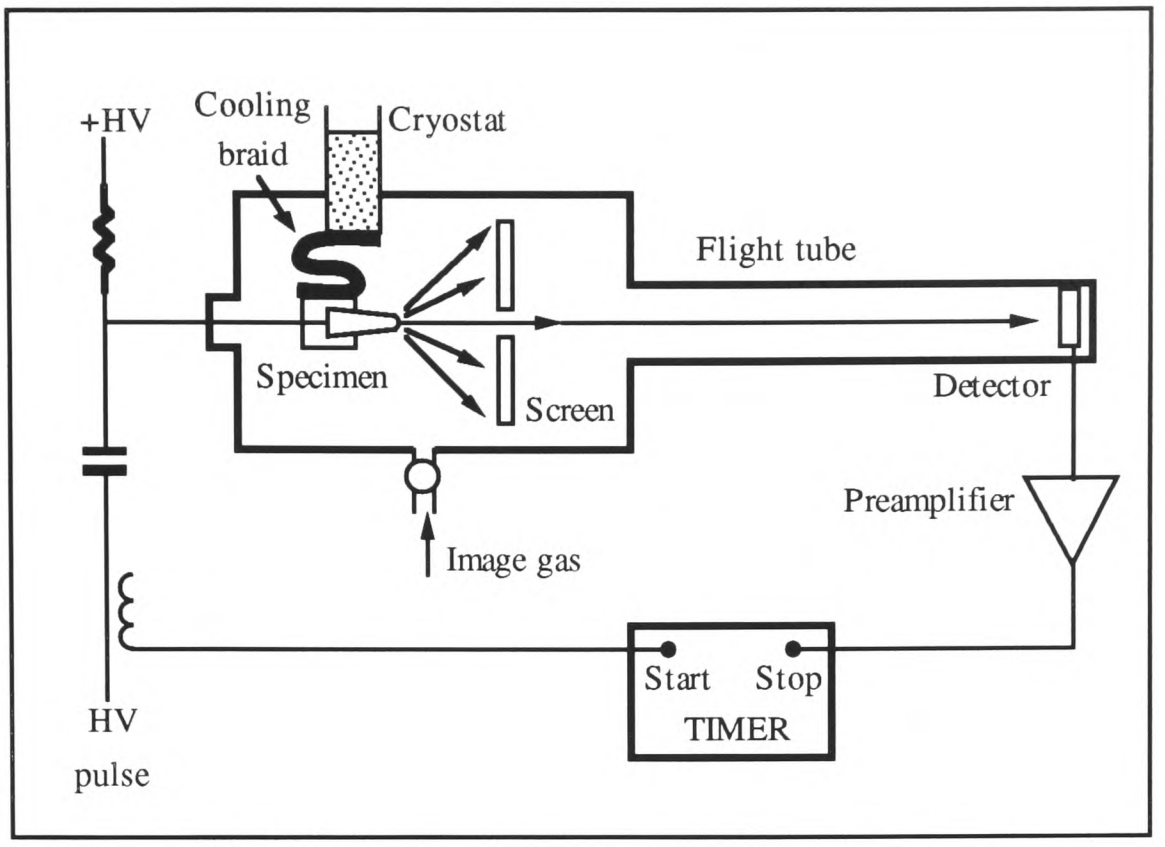

Figure 4.3 Schematic diagram of Atom Probe
(courtesy A.Cerezo)

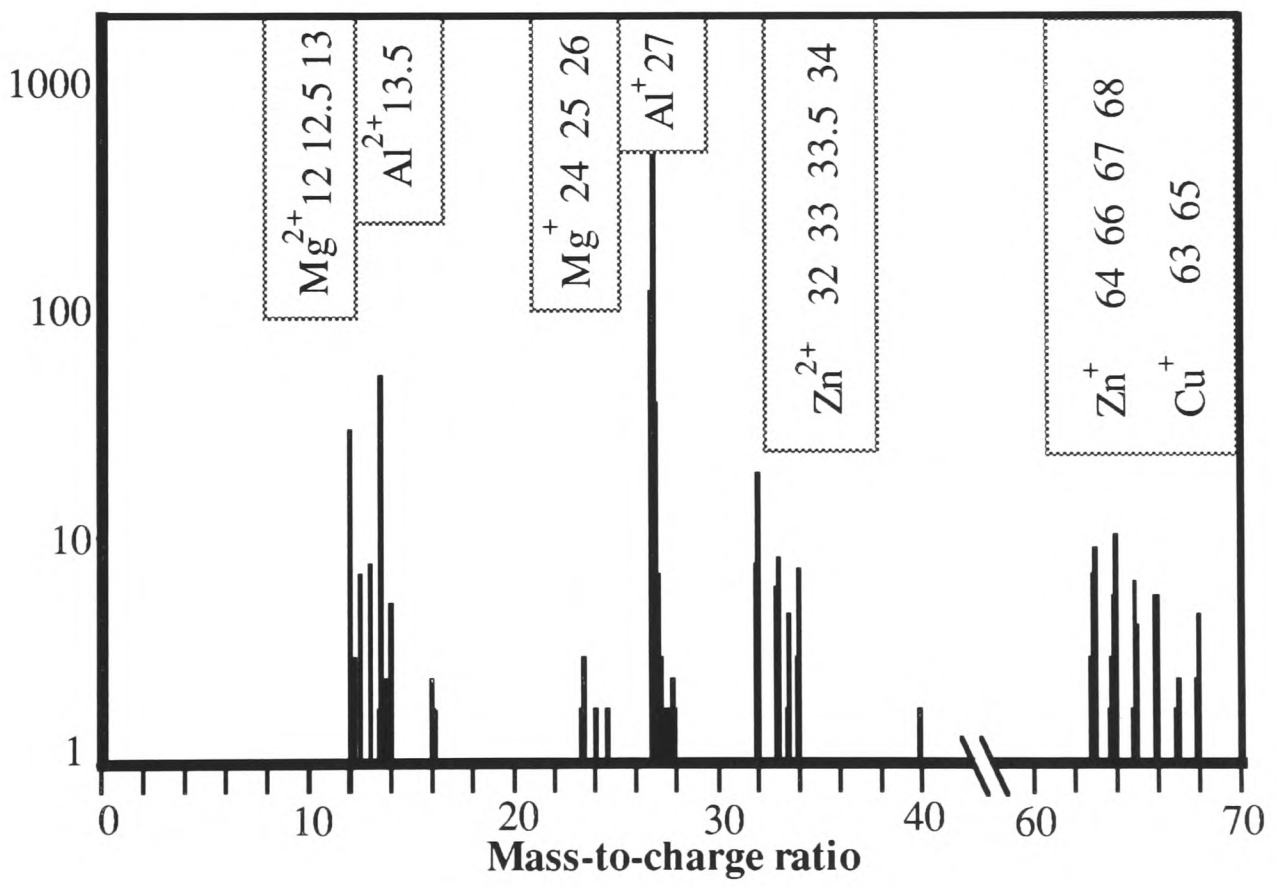

Figure 4.4 Spectrum of ion species detected by AP analysis.
This technique has very clear resolution of species.

4.1.2.2. AP Data Representation.

It is possible to use the AP for single atom identification, particularly of brightly imaging surface atoms; however, analysis is usually more continuous. A series of atoms will be evaporated and the data stored as a sequence of voltages and flight times. These can then be converted into mass-to-charge ratios to enable chemical identification of the ion species being evaporated. Since each element may have different isotopes and also different evaporation species, it is necessary to set up multiple mass-range windows for automatic identification of each element. In alloy Al-7150 the mass windows are very close but there are no peak overlaps; except possibly for hydride formation.

All the atoms may be viewed together as a histogram, showing the number of ions per mass-to-charge ratio. A typical spectrum of mass-to-charge ratios detected for this material is shown in Figure 4.4. From this, the total composition of the analysis may be determined. The data can then be segmented into smaller blocks, to view the variations in composition as the material is sequentially evaporated. This is displayed as a composition profile (Figure 4.5.a). To view the variations over less than 10 atoms, it is more informative to consider the slope of a ladder plot of element A versus element B (Figure 4.5.b). This is particularly useful for small features such as very small precipitates.

4.1.3. The Position Sensitive Atom Probe.

The POSAP is the first of a new generation of detectors designed to combine the positional information of the Field Ion Microscope image with the elemental identification of the Atom Probe[78]. In its present form it still has limitations, however it has stimulated much research into the potential of three dimensional atomic scale chemical analysis and is itself a significant advance in its field.

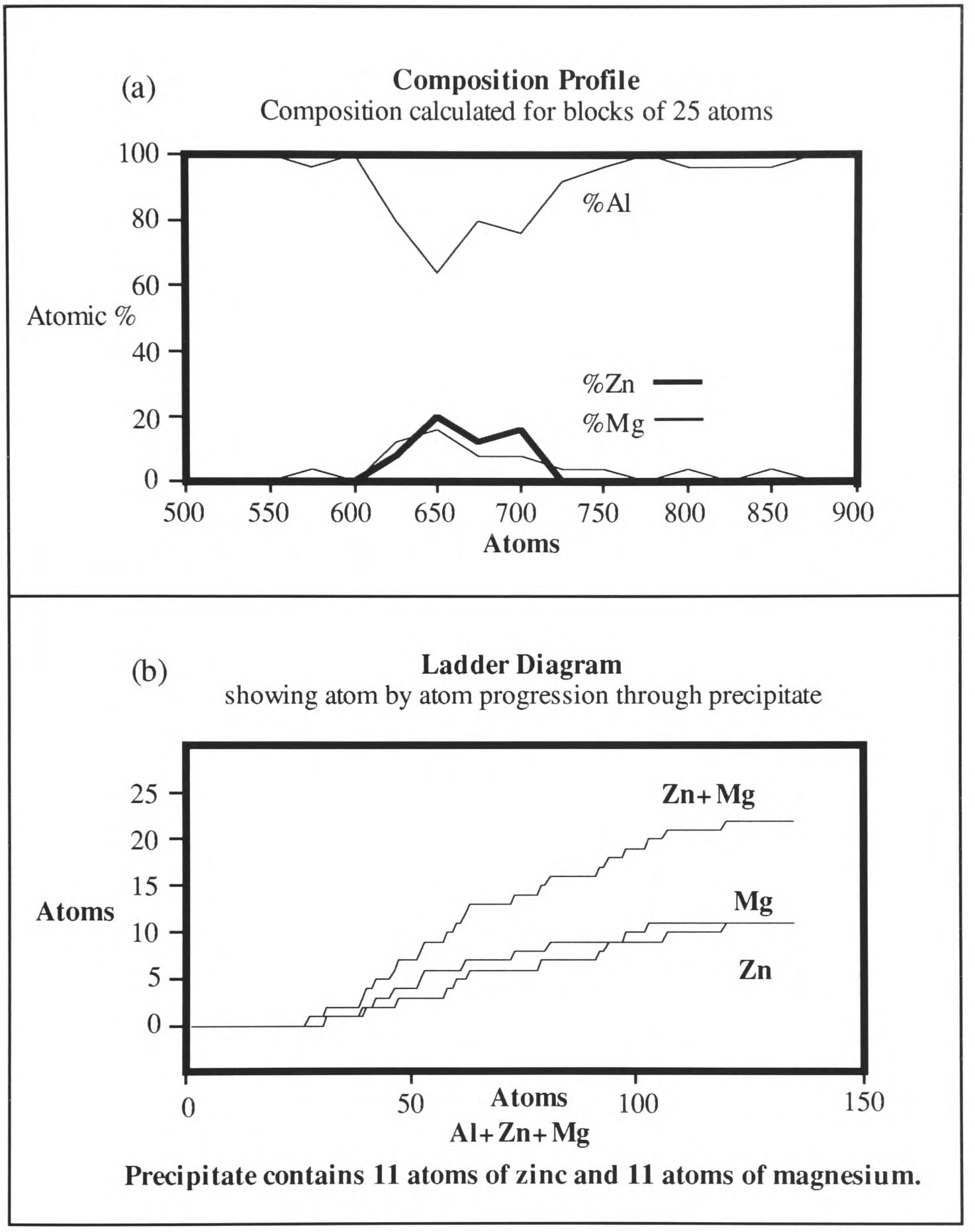

Two methods of representing the composition variations through a small precipitate analysed by AP analysis.
Al-7150 aged at 150°C for 20 hours.

Figure 4.5

4.1.3.1. Principles.

The basic principles are generally the same as for conventional atom probe analysis except that a position sensing detector is used (Figure 4.6). When an atom hits the channel plate detector it generates a cascade of electrons, some of which trigger the timing detector, but most of which are emitted from the channel as a diverging charge cloud. This charge cloud then falls on the positioning detector which divides it between three interlocking anodes (Figure 4.7). The position, which corresponds to the centre of the charge cloud, can be determined geometrically from the ratio of charges detected on the x, y and z anodes. Since the calculated position is a centroid, it is only accurate for single events. This means that accurate positioning requires serial detection, which causes many experimental problems, since the complete avoidance of double and triple ion evaporation events is difficult. This will be discussed further below.

The flight length is determined by the diameter of the detector and the desired diameter of analysis. Since the ion trajectories remain radial (without energy compensation), the flight path to the detector is short. For the POSAP the mass resolution is only about $\Delta m/m \sim 1/70$ compared to $\Delta m/m \sim 1/2000$ for the FIM100 AP. The lateral positioning resolution has been determined by experiment as 95% of atoms lying within 0.2nm of the projected position[79].

4.1.3.2. POSAP Data Representation.

The POSAP detector gives information about the spatial distribution of the elements on the atomic scale. It is necessary to be able to calculate the composition of a small volume of material contained within the larger volume of analysis. In order to select the small volume of interest, it is necessary to be able to view the variations in composition throughout the whole analysis. Since the area of analysis is typically 20nm in diameter, ideally the depth of analysis should be similar. For aluminium there are about 380,000 atoms contained in a cylinder of material 20nm across and 20nm deep, hence powerful computing facilities are needed to be able to manage the data. During this research, data analysis was done on Stellar, Stardent and Silicon Graphics workstations, each

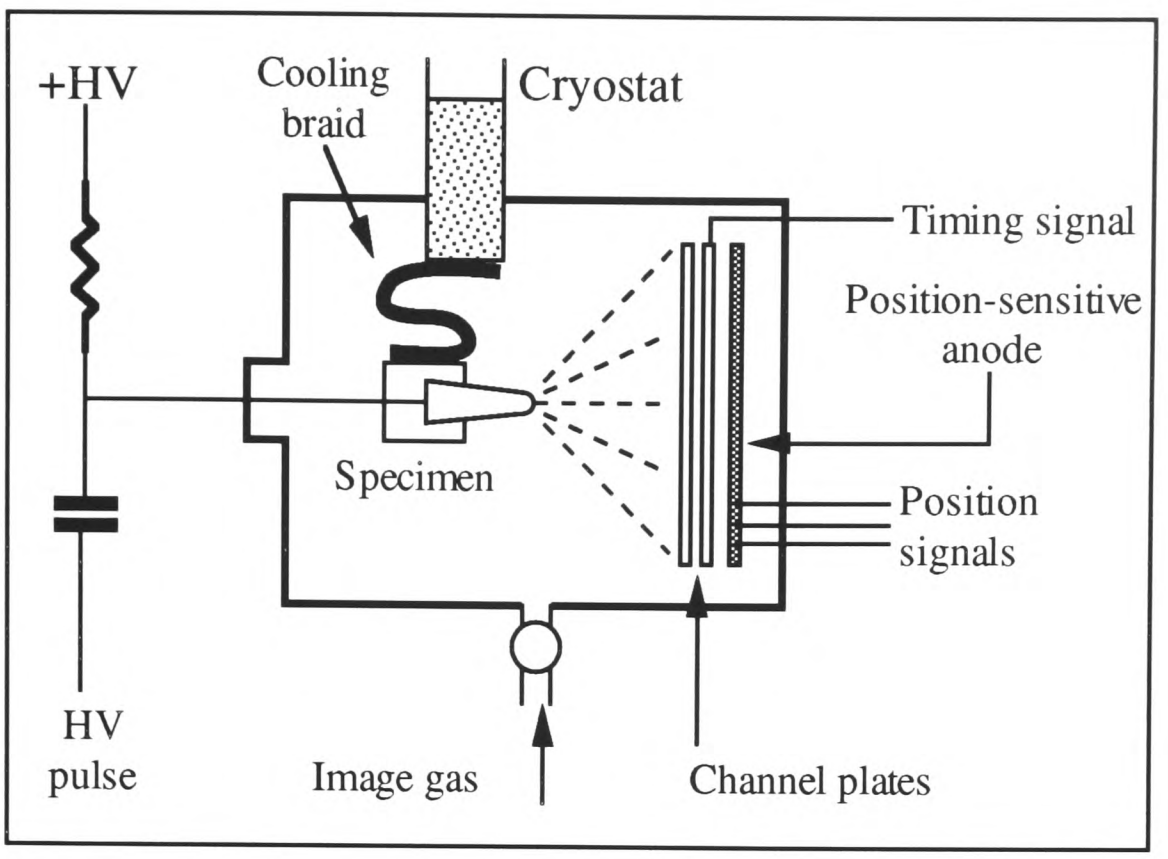

Figure 4.6 Schematic diagram of the POSAP

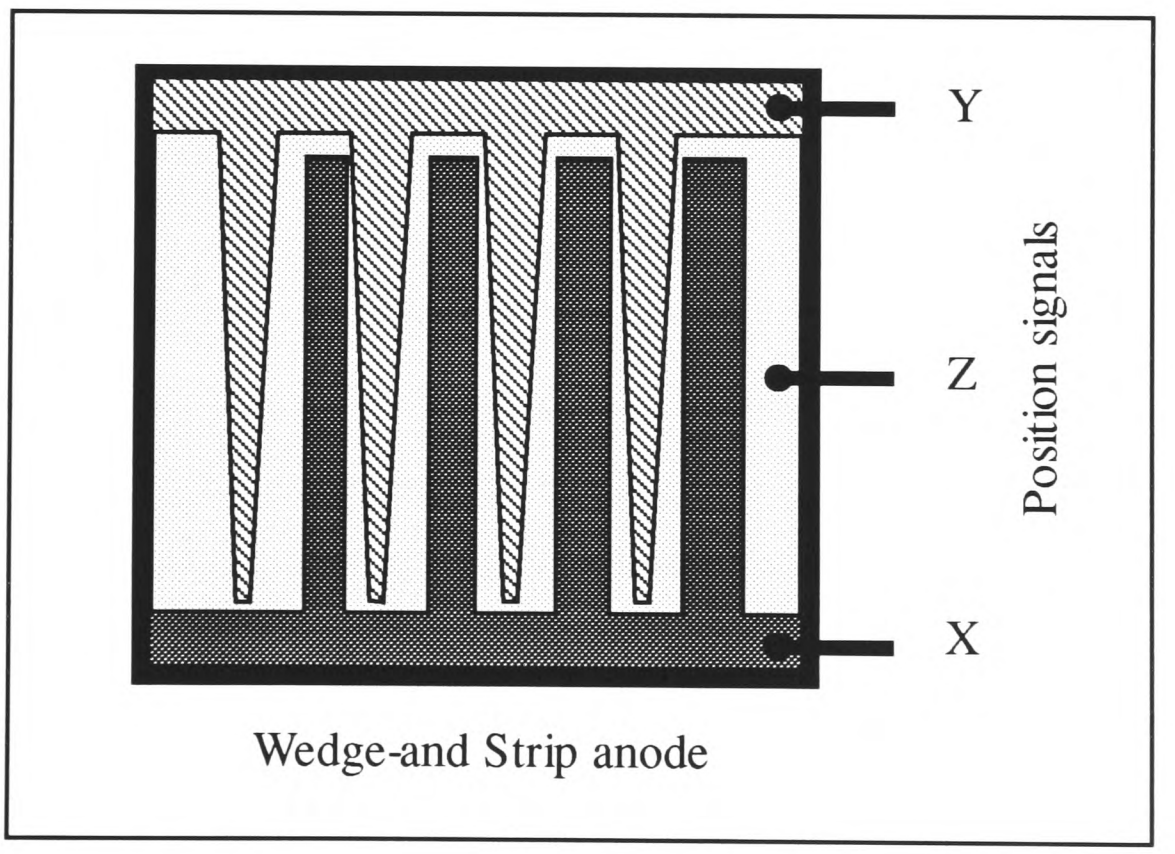

Figure 4.7 Schematic diagram of the position sensitive anode.

supporting the Advanced Visualisation Systems graphics platform, with custom-written modules[80]. These enabled the necessary visualisation of the distribution of elements within the volume analysed. Information displayed as a clear picture may be conveyed much more quickly than numerical data or the written word. Two methods of representation were used.

Atom Positioning

This method of representation marks the location of each atom (Figure 4.8.a). It is possible to choose which atoms are displayed and code the elements by colour. Although the size of mark may be controlled, this method of representation tends to be suited for strong segregation and low solute levels. One problem with this method is that visual artefacts may be introduced, due to non-uniform evaporation characteristics across the region of analysis: this causes variations in the density of positioning within the volume analysed. Non-uniform evaporation characteristics occur most noticeably at low index poles, where evaporation occurs more frequently as double events. Thus, it is usual to avoid analysis near to low index poles.

Isosurface Representation

The effect of variations in density of positioning can be removed by division of the data volume into smaller finite volume elements for which the composition is calculated. However, due to the statistically small number of atoms of each element it is necessary to apply a smoothing routine. Normal smoothing (averaging) removes the fine detail, whereas centre-weighted smoothing retains much of this detail. A surface of constant composition can then be drawn to delineate regions within which a higher concentration of a chosen element has been detected (Figure 4.8.b). Care must be taken in the choice of smoothing and the choice of composition level. This method of representation is more suited for high solute content alloys with large changes in composition (e.g. Cu-Co precipitates or Fe-Cr multilayers) rather than for the present material [81,82].

(a)

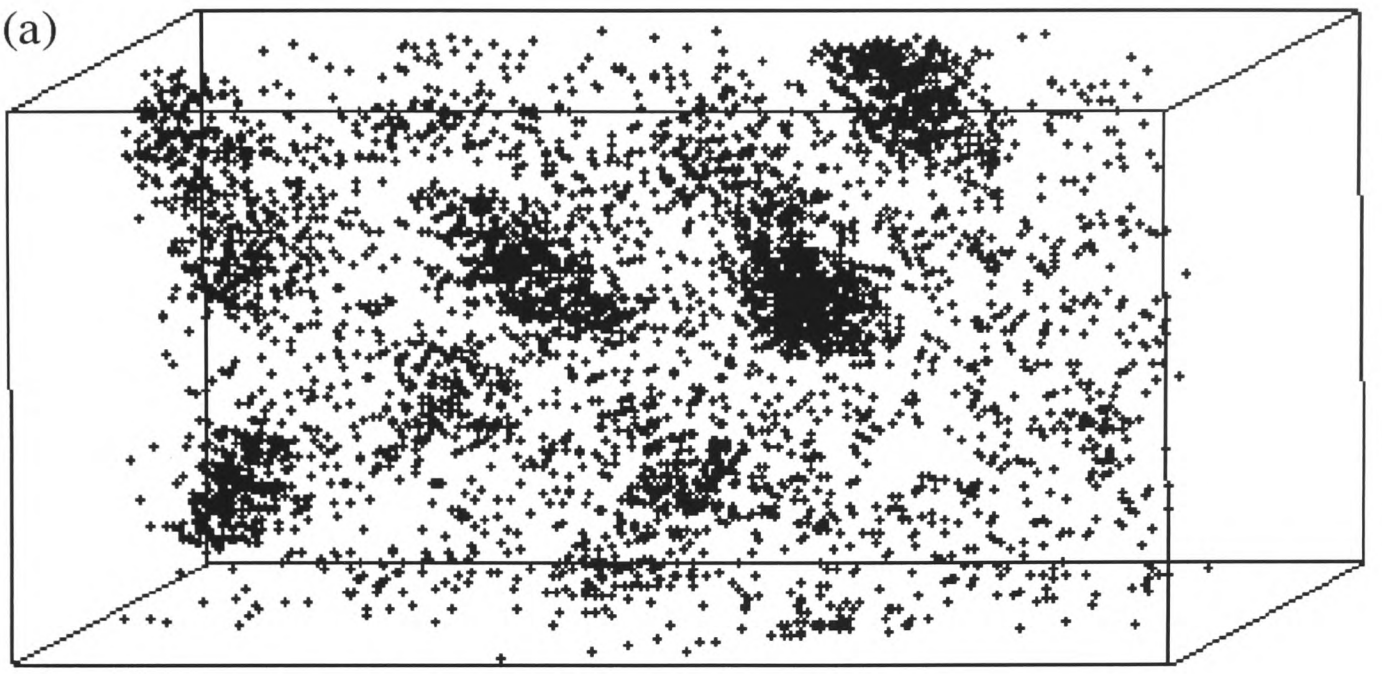

Distribution of Magnesium atoms.

(b)

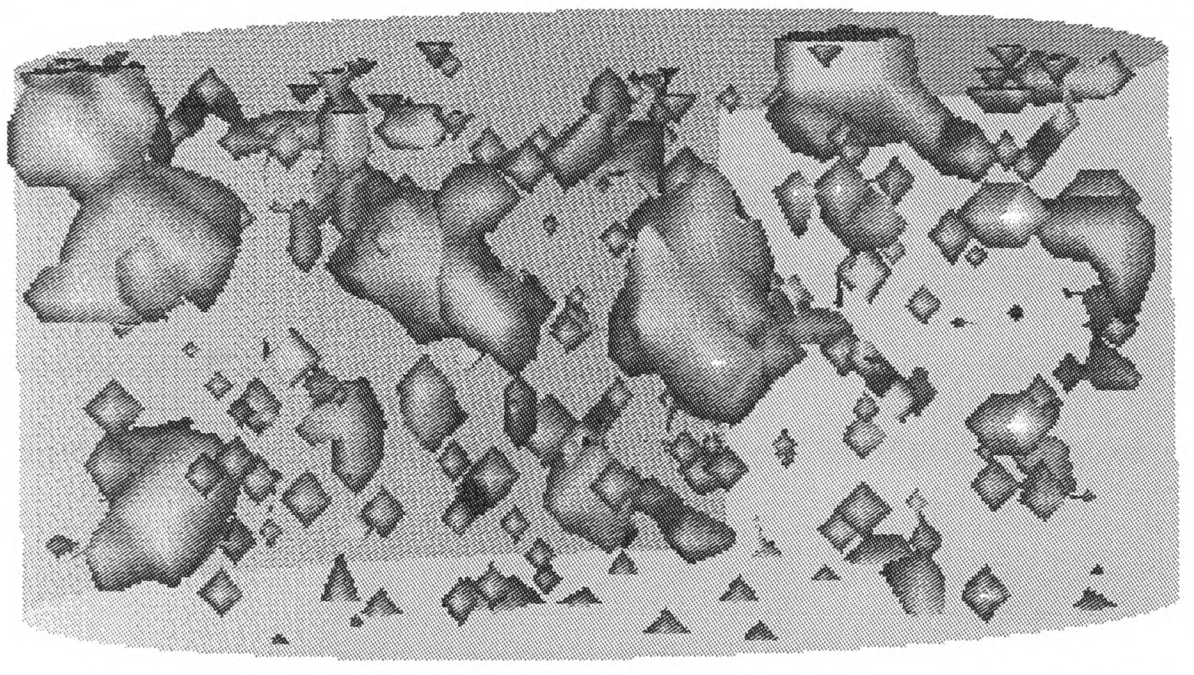

Isosurface showing 10 Atomic% Magnesium level.

(a) and (b) show the two representations of the same view of some material aged at 150°C. Visualisation of the distribution of atoms (a) is preferred as the method for viewing the location of precipitates within the volume of analysis. The isosurface (b) contains some detail which is probably an artefact of the low solute levels and hence high statistical scatter in compositions.

Figure 4.8

4.2. Previous FIM and Atom Probe Investigations.

Aluminium alloys were for many years considered not particularly suitable for FIM analysis due to their low strength (compared to refractory metals) and problems with oxide removal. Also atomic resolution imaging of aluminium requires low temperatures and high fields due to the small spacing of the atoms. Some early FIM imaging was done by Boyes[83] (at Oxford) and he mentions a FIM investigation of the structure of GP zones in an Al-Zn-Mg alloy showing plate-like zones and refers to further work which seems not to have been pursued. Subsequently, most FIM work on aluminium alloys has been done in Japan using equipment specially designed to achieve very low temperatures. This enables atomic imaging of the structure of the GP zones due to the differences in ionisation and evaporation potentials of the solute elements. Some GP zones were analysed by alternate single atom AP analysis and FIM imaging enabling a three dimensional picture of the distribution of the elements to constructed. The work of Japanese groups upon aluminium alloys is reviewed by Hirano and Hono[84]. The structure of the GP zones in the Al-Zn-Mg alloy is described as "unclear", and no work is reported. More recently, work on a variety of alloys has been done by Hono[85] using a new low temperature atom probe. Preliminary results were presented in 1991 and further work on the early stages of precipitation in the Al-Zn-Mg-(Cu) system may be expected.

Grovenor et al. have investigated GP zones in high purity[16] and commercial[86] Al-Zn-Mg alloys by AP analysis. They used high temperatures of 70K for imaging in argon and analysis was done 'blind'. Brenner[66] has studied aluminium 7150 by atom probe analysis, using neon imaging gas and low temperature (≈30K) to aid alignment of the area of analysis over the precipitates of interest. Clear atomic resolution was not achieved even at 30K, although the precipitates were found to be darkly imaging. His work was carried out concurrently with the preliminary work for the current investigation[58] submitted for Part II of my undergraduate degree.

4.3. FIM of Aluminium 7150.

The field ion microscopy of aluminium alloys is quite difficult due to the surface oxide always present on the specimen. Since the oxide has a higher evaporation field than the metal aluminium it can cause large field induced stresses that result in mechanical failure of the specimen. A high temperature (~80K) and an imaging gas with a low ionisation field (argon) were used in this work to allow easy removal of the surface oxide layer. Several different stages of removal were clearly discernible (Figure 4.9).

Initially, large elongated image spots are visible flickering over the surface, as the outer porous oxide growths are removed. Gradually, from the centre, the image becomes more uniform and intense, as evaporation reveals the more compact oxide close to the metal. Further evaporation may be erratic as particles of oxide break away from the tip. When the true metal is reached, it appears as a dark region expanding from the centre of the image as the oxide is peeled away. Initially for a sharp tip the aluminium does not image brightly, however as the oxide is removed further and the area of aluminium increases (and the magnification decreases) the (110) poles appear as diffuse bright regions approximately rectangular in shape. The image of the aluminium is generally much weaker than the oxide image and any bright spots from adsorbed argon atoms. The image is non-uniform due to the crystallographic variations in the work function of the material and possible interaction with image gas leading to faceting of the surface. This means that the low index poles, such as (100) and (111), are flattened and appear dark. Reducing the temperature allows more adsorption of the image gas to prominent sites, thus improving imaging of the crystallography. However, at 70K argon condenses and a different gas such as neon must be used. Unfortunately neon has a much higher evaporation field, thus increasing the stresses on the specimen and chance of failure.

FIM images showing the sequence of evaporation of the brightly imaging surface oxide layers, to reveal the predominantly darkly imaging aluminium alloy. Please refer directly to the main text for a more detailed description of the imaging behaviour.

Figure 4.9.

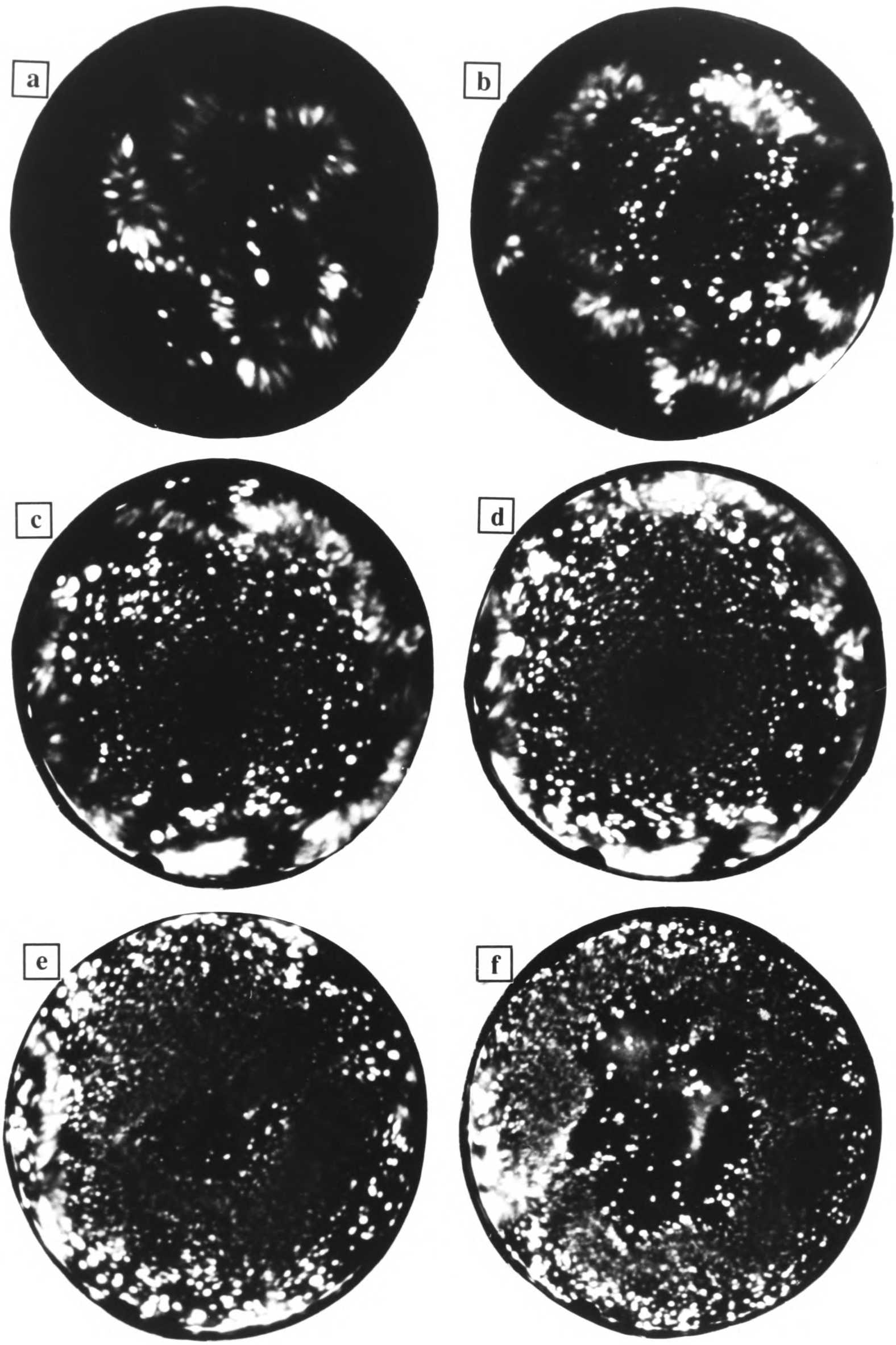
a
b
c
d
e
f

4.4. AP Data Interpretation.

All atom probe investigations in this work were carried out under standard conditions of 70K and 20% pulse fraction as used by previous workers from this group[16].

Since under these imaging conditions small zinc- and magnesium-rich precipitates in alloys 7150 are not visible in the FIM image, it was only possible to choose to analyse a particular precipitate in the over-aged material. For the under-aged material, analysis was done by 'probing blind'. Since the number density of precipitates is very high, a random analysis will soon encounter one. When the data is viewed as a composition profile, it is possible to quickly identify the location of the precipitates and then more detailed analysis enables the composition of both precipitate and matrix regions to be calculated separately. However, before stating the composition, there are several factors affecting accuracy to be considered.

4.4.1. Geometrical effects.

The geometry of analysis has two main effects (Figure 4.10). Firstly the area analysed varies in size during the course of the experiment. The size of the area analysed is dependent upon the fixed size of the aperture hole in the image screen and the variable magnification of the image. The ion trajectories are considered to be effectively radial thus as evaporation occurs and tip radius increases, the area of analysis also increases ($\alpha\ r^2$). For this material about 1000 atoms are detected per nm depth at 10kV dc applied voltage (actually calculated from the POSAP calibration work).

Secondly since the area of analysis is typically 3-7nm in diameter, the feature of interest may not totally cover the area of analysis; thus, the observed composition may be altered by contributions from the surrounding matrix material. **This is very important since it means that usually only an estimate of the solute fraction in the feature can be determined and not the aluminium content.**

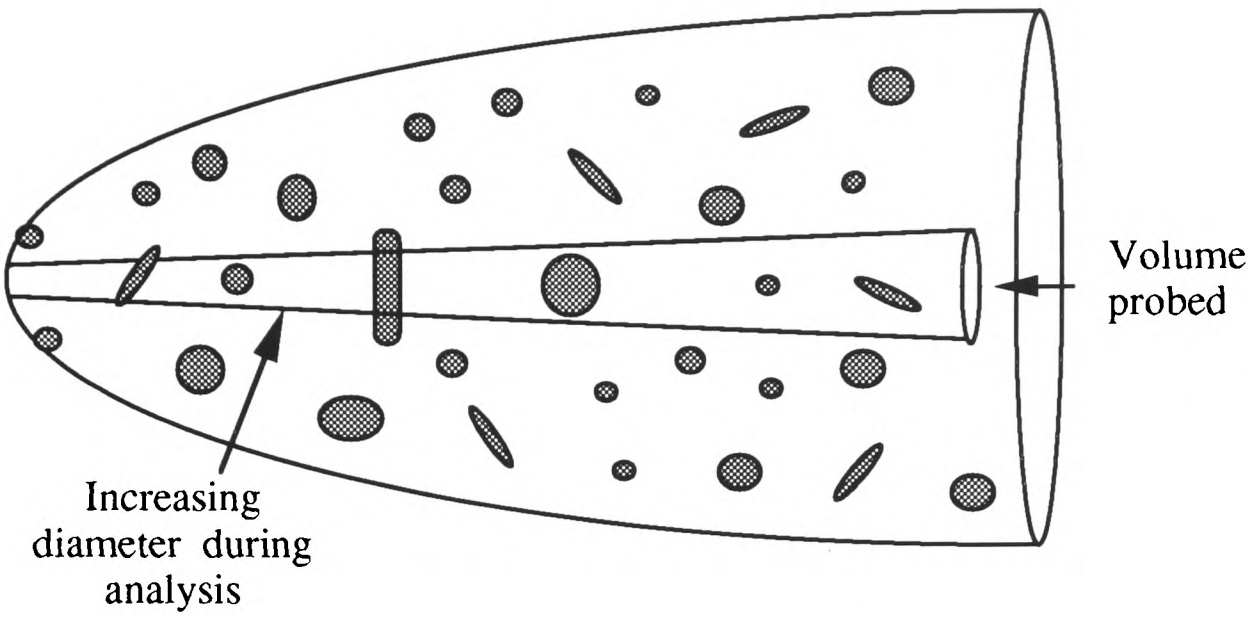

A schematic diagram of the volume analysed through an array of precipitates of various shapes and sizes.

Figure 4.10

Window limits	Ion Species
11.8 - 13.2	Mg
13.3 - 14.8	Al
23.5 - 26.5	Mg
26.7 - 28.5	Al
31.8 - 35.3	Zn
62.5 - 63.5	Cu
63.6 - 64.5	Zn
64.6 - 65.5	Cu
65.6 - 66.5	Zn
67.6 - 68.5	Zn

Table 4.1 AP analysis windows

4.4.2. Detection efficiency.

A microchannel-plate detector has a finite efficiency; thus some atoms are lost from the analysis. Geometrically only about 50% of the detector area is active[87]. The efficiency of the detector is also known to decrease for incident ions of energy less than about 5keV; hence a minimum probing voltage is defined. It is assumed that the detector efficiency is independent of element detected.

4.4.3. Preferential evaporation effects.

Most atom probe experiments are carried out with the assumption that the specimen is held at a steady voltage at which no evaporation can occur and then a fraction of the dc voltage is applied as a short pulse to cause evaporation at a known time. It is also assumed that each element has the same probability of evaporation for a given geometrical configuration. It is necessary to choose a pulse fraction and a temperature such that there are no preferential evaporation effects. This means that the effect of applying the pulse is to change the field, from a level where none of the elements can evaporate, to a level where all of the elements can evaporate equally easily. Previous atom probe investigations of Al-Li alloys[88] have found a particularly strong dependence of the evaporation behaviour of the lithium species upon the temperature of analysis. Analysis at 80K was found to be a factor of two lower than the nominal concentration, while analysis at 20K gave reasonable agreement with the nominal concentration.

The correct analysis conditions can be determined by analysis of solution treated material and comparison of the observed composition with the known composition as determined by other experimental techniques, such as EPMA (Electron Probe Micro-Analysis). Unfortunately, the specimens all failed during AP analysis, before it was possible to collect a sufficiently large number of atoms to remove the statistical scatter due to the low total solute levels in this alloy. However, this aspect of quantification will be considered in more detail in Section 4.5.3. since the POSAP was able to collect a sufficiently large number of atoms. It is thought that preferential evaporation effects do present a problem for the Al-Zn-Mg-Cu system at high temperatures.

4.4.4. Window overlap.

The example of the spectrum in Figure 4.4 (earlier) showed that the AP has sufficient mass resolution to clearly identify all the different species. Identification of the elements from the species detected is straightforward for single atom species, however for clusters there may be several combinations of elements that have the same mass-to-charge ratio. In Al-7150 hydride formation can make absolute determination of the copper concentration difficult [66]. Copper hydride was found to occur mostly as CuH_2^+ species with very little CuH^+. This causes peak overlap with zinc in the 67 amu peak. Figure 4.11 compares the relative isotope abundances for zinc and copper with an example spectrum. The observed isotope abundances may be deconvoluted for the peak overlap at 67amu by assuming that hydride formation is independent of isotope abundance and that only CuH_2^+ species are formed . The windows used are given in Table 4.1. For each file the total window counts of ^{64}Zn, ^{66}Zn and ^{68}Zn are compared to the expected isotope abundances and then the total Zn counts are scaled to compensate for the unwindowed ^{67}Zn and ^{70}Zn species. Also the total window counts of ^{63}Cu and ^{65}Cu are compared and the % hydride formation calculated and the total copper counts corrected for the presence of unwindowed $^{65}CuH_2^+$ species. Selected compositions calculated from the composition profiles are corrected using the same scaling factors. This method of correction becomes less accurate for low peak counts where statistical variations are large. For the example in Figure 4.11 the observed peak counts are closely matched by the corrected peak count values thus showing the model to be accurate.

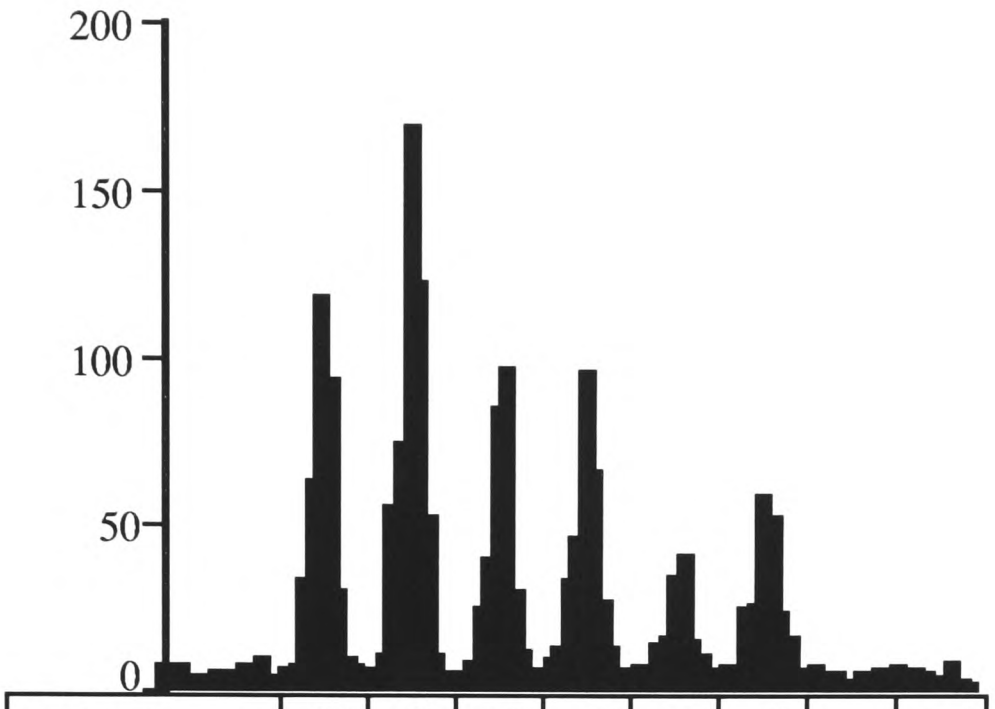

Peak m/n ratio	**63**	**64**	**65**	**66**	**67**	**68**		**70**
Peak counts N	373	510	318	308	—	221		—
%Cu isotopes	69.2		30.8					
%Zn isotopes		48.6		27.9	4.1	18.8		0.62

Peak at 67m/n is not windowed since it contains both Zn species and CuH_2^+ species.

Assume that x% of all copper ions form CuH_2^+species. Solve the equations for $N_{63}$and N_{65} for x.

$$x\% \text{ Hydride Formation} = \frac{0.692\ N_{65} - 0.308\ N_{63}}{0.384\ N_{63} + 0.692\ N_{65}}$$

(x% Hydride = 29%)

Hence calculate correct totals of Zn and Cu given the windowed peak counts.

$$Cu = \frac{0.384\ N_{63} + 0.692\ N_{65}}{0.479} \qquad Zn = \frac{N_{64} + N_{66} + N_{68}}{0.953}$$

(Cu = 758 total counts) (Zn = 1090 total counts)

Using these totals to calculate the expected peak integrals

m/n ratio	**63**	**64**	**65**	**66**	**67**	**68**	**70**
Calculated N	372	531	318	302	45 + 68	205	7

The observed and calculated values compare well numerically and show the model to be accurate.

Figure 4.11

4.5. POSAP Data Interpretation.

The POSAP can provide both compositional and positional information. The factors affecting the accuracy of each type of information are considered separately.

4.5.1. Compositional Information.

Three dimensional representation can give information about the shape and size and distribution of the precipitates. By placing a wire frame box of variable size around the region of interest in a 3-D visualisation, the composition of the positioned atoms within the box may be determined. A composition profile through that region may be calculated in the same way as for conventional atom probe data. Selecting a composition profile through the precipitate can give information about the distribution of elements within and around the precipitate and at the precipitate/matrix interface. Careful positioning of the volume of analysis can exclude contributions from the matrix material to give just the precipitate composition. This is not possible in conventional atom probe analysis. Similar information can be obtained about composition variations at grain boundaries.

The accuracy of the compositional data is determined by two processes:-

a) Selecting the volume of data space corresponding to the feature of interest.

b) Identifying the timing signals that are real atoms which come from that region.

4.5.1.1. Chemical Identification.

The mass range windows are set to identify each ion species detected, but due to the low resolution of the POSAP (compared to the FIM100 AP) there are peak overlaps which limit the accuracy of the chemical identification. Figure 4.12 shows a typical mass spectrum as detected by the POSAP.

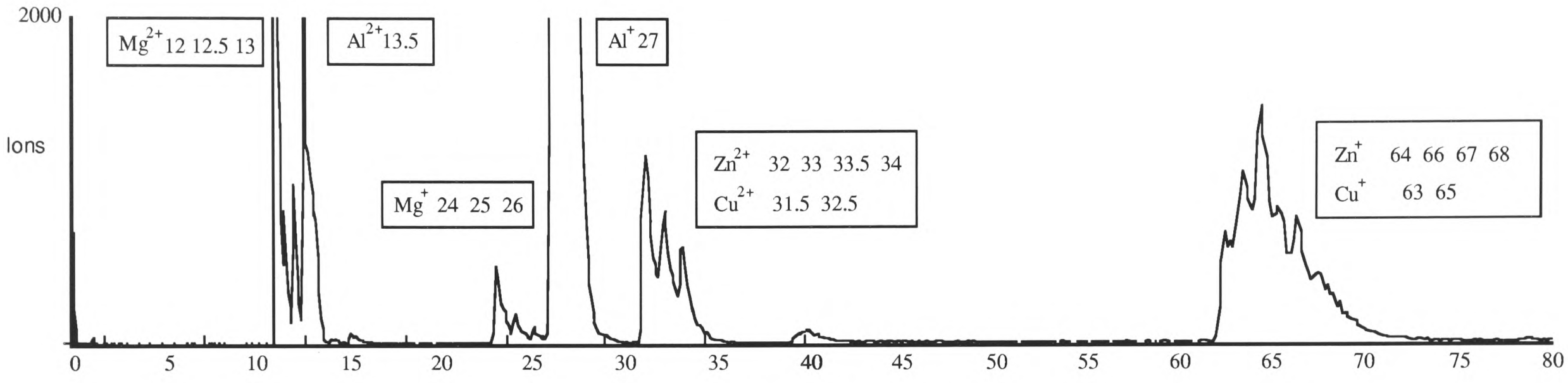

- The expected ions species are listed beside the appropriate regions in the spectrum.
- The alpha scaling factor was set such that the windowed divide at 12.8amu was correct for separating the Mg and Al doubly charged species.
- The Mg single charged species were identified as a separate window "X1" and was used for mapping low field sites.

Element	Range	Species
H	5 - 35	H^+
Mg	11.2 - 12.8	Mg^{2+}
Al	12.9 - 14.5	Al^{2+} AlH
X1	23.3 - 25.8	Mg^+
Al	25.9 - 30.9	Al^+ AlH^+
Zn	31.0 - 37.0	Zn^{2+} Cu^{2+} CuH^{2+}
Zn	62.5 - 72.0	Zn^+ Cu^+ CuH^+

Figure 4.12 Example of a POSAP mass spectrum and the window file used for analysis of all data files

Aluminium.

Aluminium has one isotope with an atomic mass of 27amu. Under typical POSAP analysis conditions this is detected as about 60% Al^+ and 40% Al^{2+}. However, the ratio of the different charge species is actually dependent upon the local field at the surface. In addition, aluminium can form hydride species, but these are not accurately separable from the aluminium peak due to the lower resolution of the POSAP. Hydride formation will be discussed later.

Magnesium.

Magnesium has three isotopes with mass-to-charge ratios 24, 25 and 26 amu. These are normally detected as the doubly charged Mg^{2+} species but there is slight overlap with the Al^{2+} peak thus the setting of the window requires care. At low field sites, the magnesium can occur as singly charged Mg^+ ions.

Zinc and Copper.

These must be considered together for the purpose of POSAP analysis since there is extreme peak overlap due to the reduced mass resolution in the POSAP compared to the FIM100AP. The isotopes are copper at 63 and 65 amu and zinc at 64, 66, 67, 68 and 70 amu. Also copper is known to readily form CuH_2^+ hydrides which directly overlap with the zinc peaks. Quantification of these elements provides further problems as discussed in more detail below.

Zirconium.

Zirconium is present in this material in small spherical grain refining particles. These particles have much higher evaporation fields than the aluminium matrix. The zirconium has isotopes at 90, 91, 92, 94 and 96 amu which are usually detected as doubly and some triply charged species. Triply charged species can lead to peak overlaps with doubly charged zinc/copper.

Hydrogen.

Hydrogen has predominantly one isotope at 1amu. This is detected as about 90% H^+ and 10% H_2^+ ions. The effect of hydrogen detection upon the specimen evaporation rate and the usefulness of data about the distribution of hydrogen on the sample surface will be considered later.

Others species.

Several other peaks were observed in the spectrum which were taken as not originating from the specimen material. The most obvious peak was due to the argon imaging gas Ar^+ at 40amu. Less easily identifiable were peaks at ~16 (Oxygen), ~28 (carbon monoxide overlapping with aluminium and aluminium hydride), ~36-38 (?), ~41-43 (?). The POSAP is particularly susceptible to detecting surface contaminant species originating from the specimen shank or the vacuum due to the low field during evaporation. When analysis commenced at too low a voltage, it was possible that only surface adsorbate was evaporated and detected.

The detection of argon at the start of an experiment was clearly identifiable with the evaporation giving rise to bright spots instead of a uniform image (Figure 4.13.a.). More difficult to spot was the detection of carbon monoxide at 28 which could be easily confused with the aluminium peak. A particular example of a grain boundary analysis affected by the desorption of CO from only one grain is shown in Figure 4.13.b. Incorrectly identifying this adsorbate as aluminium has a large effect on the composition as shown by the composition profile in Figure 4.14. The possibility of more localised desorption of CO from the grain boundary itself or from a particular precipitate is harder to identify; however, it will have an equally detrimental effect on the composition. Checking the spectrum of the selected volume is a simple check for the accuracy of the composition.

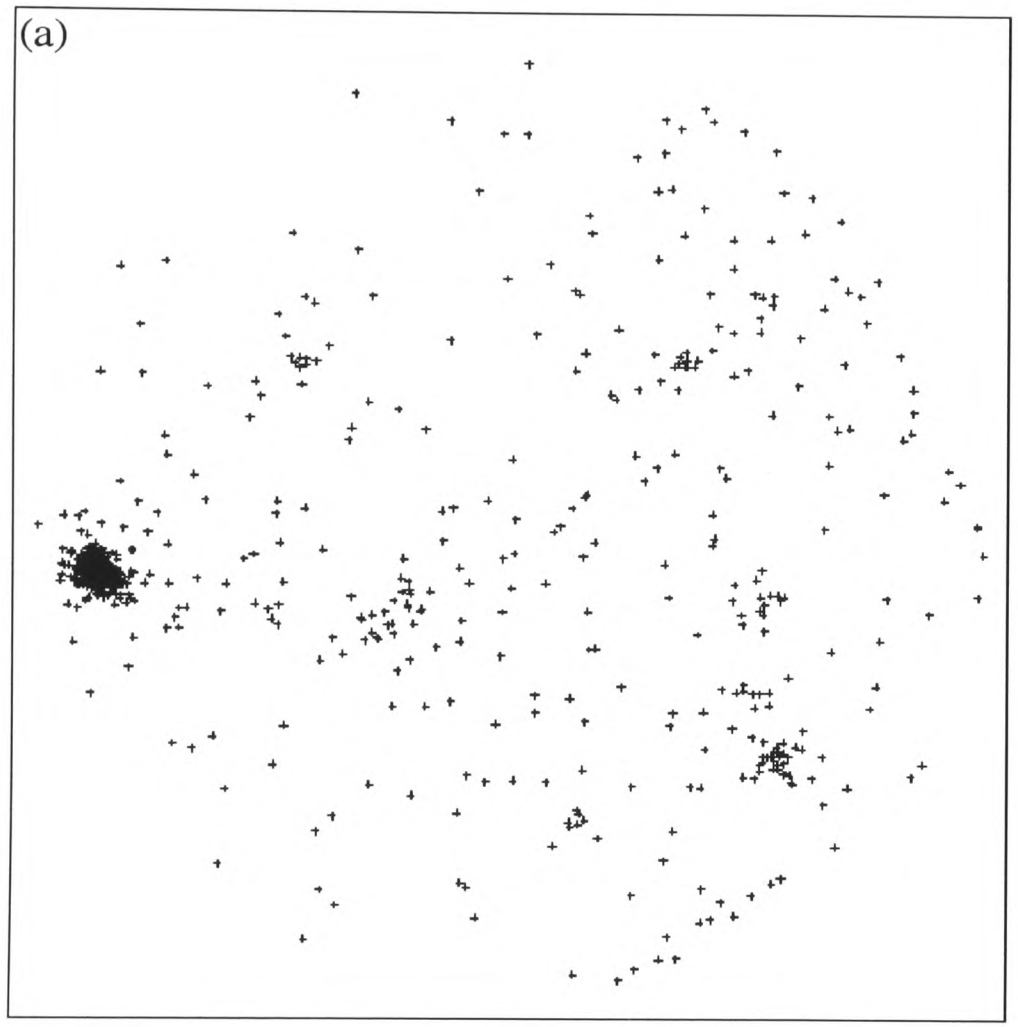

(a) Argon ion species distribution showing bright spots due to localised desorption of argon image gas. Increasing the applied field removes the desorption sites.

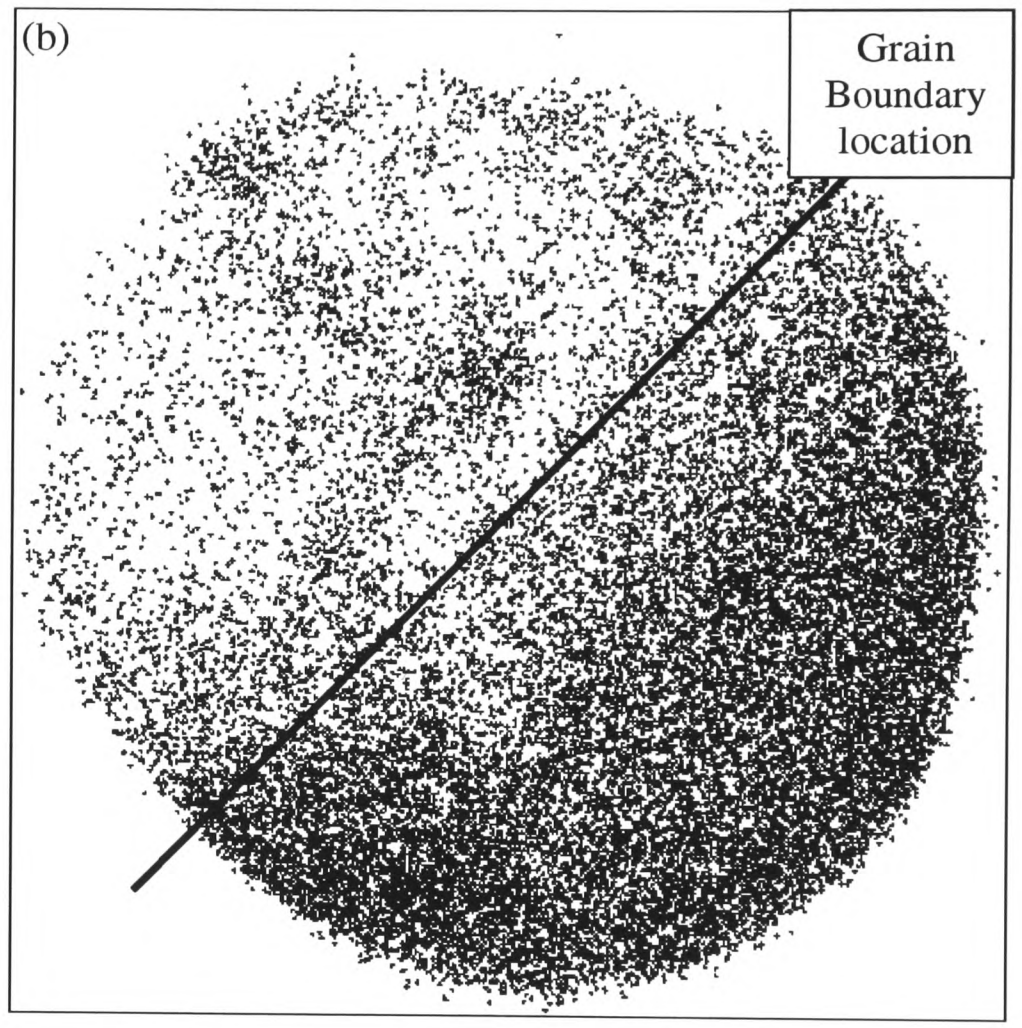

(b) Image of the distribution of ion species at 28amu. This includes some aluminium and some aluminium hydride but it is mostly carbon monoxide adsorbate. The analysis is of a grain boundary region and only one grain is desorbing the CO species. This strongly affects the calculation of compositions.

Figure 4.13

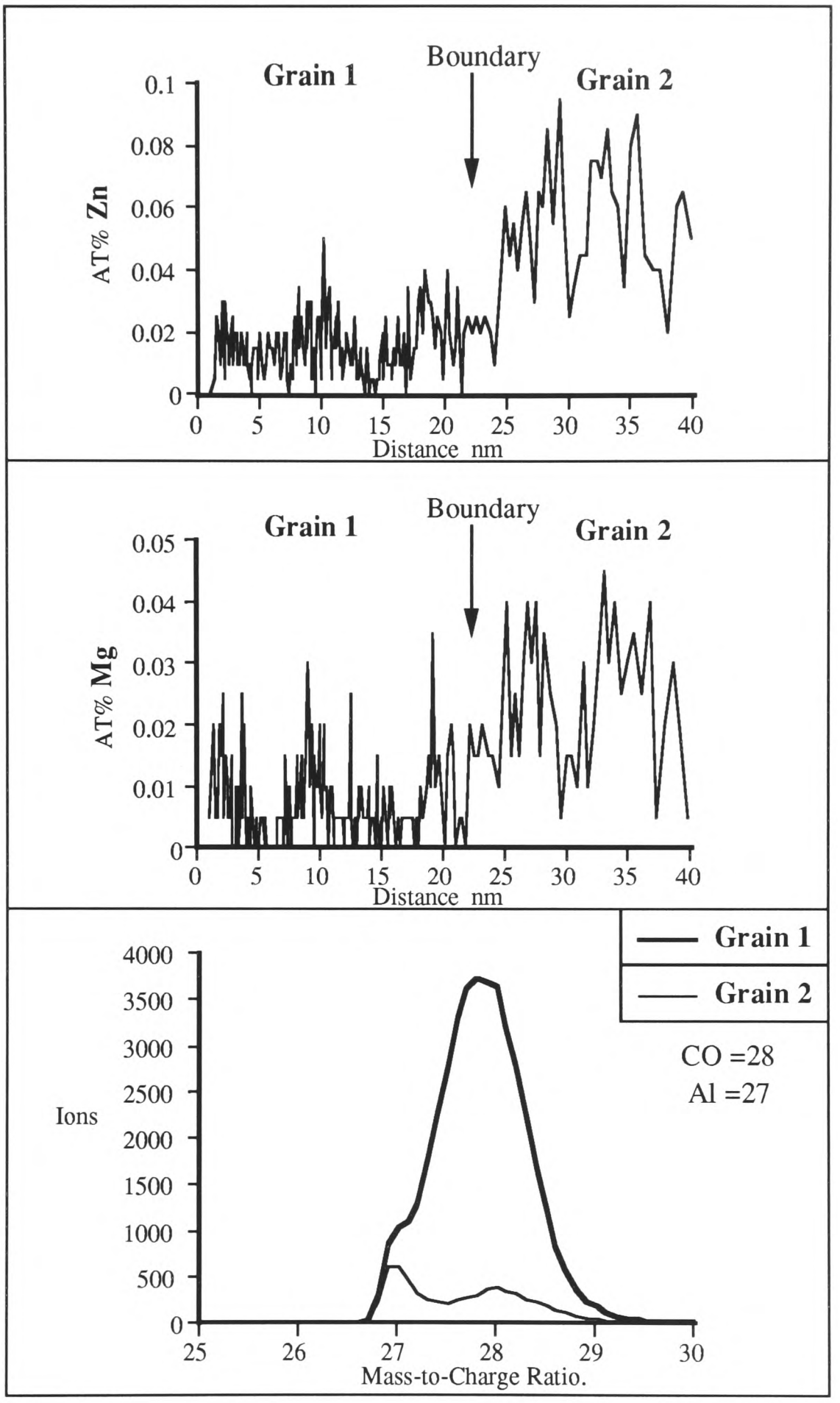

(a) and (b) show the composition profiles of zinc and magnesium across the grain boundary. The difference in solute levels calculated, due to the incorrect identification of CO as aluminium, is evident.

(c) shows the selected spectra for the two grains, showing the relative levels of CO and Al in each grain.

Figure 4.14

Detector Noise

Detector noise has not yet been characterised fully for the POSAP system. During the course of this work, one source of noise in the data was identified as low energy scattered electrons in the system reaching the detector. As a result of this, an aperture was fitted and a small potential applied to remove them. Further work on the identification of other noise signals and their elimination might be beneficial.

4.5.1.2. Spatial Identification.

During a POSAP experiment not all the real timing signals are stored with correct positional information. Since calculating the composition of the volume of space was done just considering the atoms with positional information, a correction for the % positioning for each species is necessary. Information about the % positioning was obtained by analysis of the detection statistics. The main reason for incorrect positional information was due to the occurrence of multiple evaporation events, resulting in two or more ion species reaching the detector on the same pulse signal.

Multiple Events

Figure 4.15. shows the time-gating system used for ion detection. A voltage pulse is applied, then 50ns later the time-of-flight detector looks for an atom in a time window of width 4000ns. When a timing signal has been detected, about 200ns later the position sensing detector samples the charge on the electrodes for 50ns. If there is a multiple event there are several possibilities:

a) If a second ion arrives more than 250ns after the first, then the measured charge is due only to the first ion: thus, the first ion can be positioned whilst the second ion cannot, although both are chemically identified.

b) If the second ion has a similar flight time, such that it arrives within 30ns (the timing detector dead-time) of the first ion, then there is only one timing signal recorded. However, the charge collected by the positioning detector will be approximately double

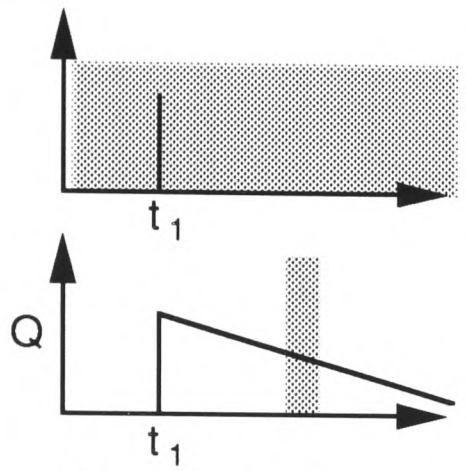

Single timing signal
detected at time = t_1

Single charge decay
sampled at $t=t_1+200ns$

One Correct Time
One Correct Position

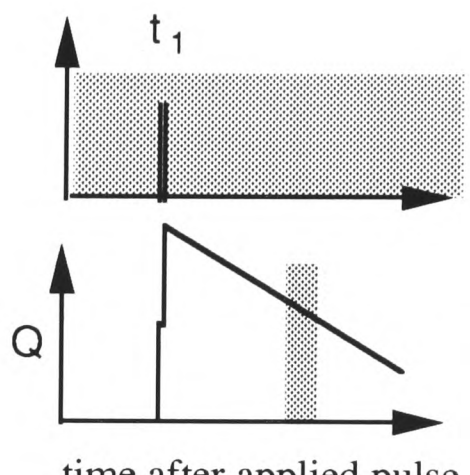

One timing signal
detected at time = t_1

Double charge decay
sampled at $t=t_1+200ns$

Only One Time
No Position(s)

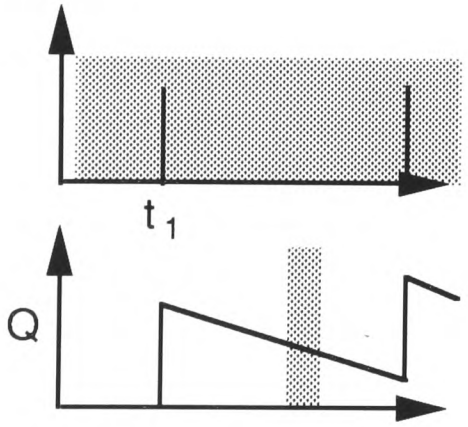

Two timing signals
detected at time = t_1 and t_2

Single charge decay
sampled at $t=t_1+200ns$

Two Correct times
One correct Position

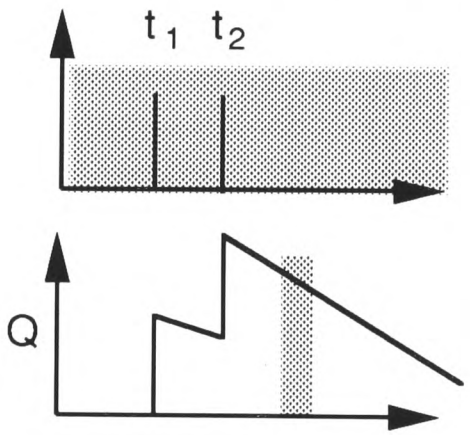

Two timing signals
detected at time = t_1 and t_2

Double charge decay
sampled at $t=t_1+200ns$

Two Correct Times
No Positions

Figure 4.15 showing the four types of multiple events with the available data stated in **bold**.

that generated by a single ion. If the measured charge exceeds the maximum measurable charge it is recorded as a charge overflow and not positioned, but if the measured charge is acceptable then an incorrect centroid position is calculated.

c) If the second ion arrives after the timing detector dead-time of 30ns but before the charge is measured on the positioning detector 250ns later then the second ion's contribution to the charge will be much higher than the first's due to the shorter time for charge decay and this should cause charge overflow on at least one electrode.

Since the accuracy of the centroiding algorithm is better for higher charges, the channel plate gain is set such that there is slight charge overflow on each anode. However, this reduces the overall %positioning. An example of the distributions of the measured charges for each of the electrodes for a whole datafile is shown in Figure 4.16. If one species is found to evaporate as ion pairs, then it is beneficial to apply a threshold to the total charge distribution at about twice the mean charge, in order to reduce the possibility of incorrectly positioning the single-timing-signal, double events[80]. However, for this material the proportion of ion pairs detected was very low, thus this additional charge threshold was omitted during data analysis.

Statistical Analysis of multiple events

Figure 4.17 gives a statistical analysis of the occurrence of the multiple events described above. The main problem is the lack of positioning of the zinc in double events. About 40% of the zinc occurs in double events, and, due to the high atomic mass giving longer flight times, it is usually the second atom detected and thus is not positioned (except when both atoms are zinc). About 30% of the magnesium also occurs as double events; however, since it has a low atomic mass, it is often the first atom to arrive and is positioned correctly. Only about 8% of the aluminium occurs as double events, so there is also a clear preference for the solute elements to evaporate as double events.

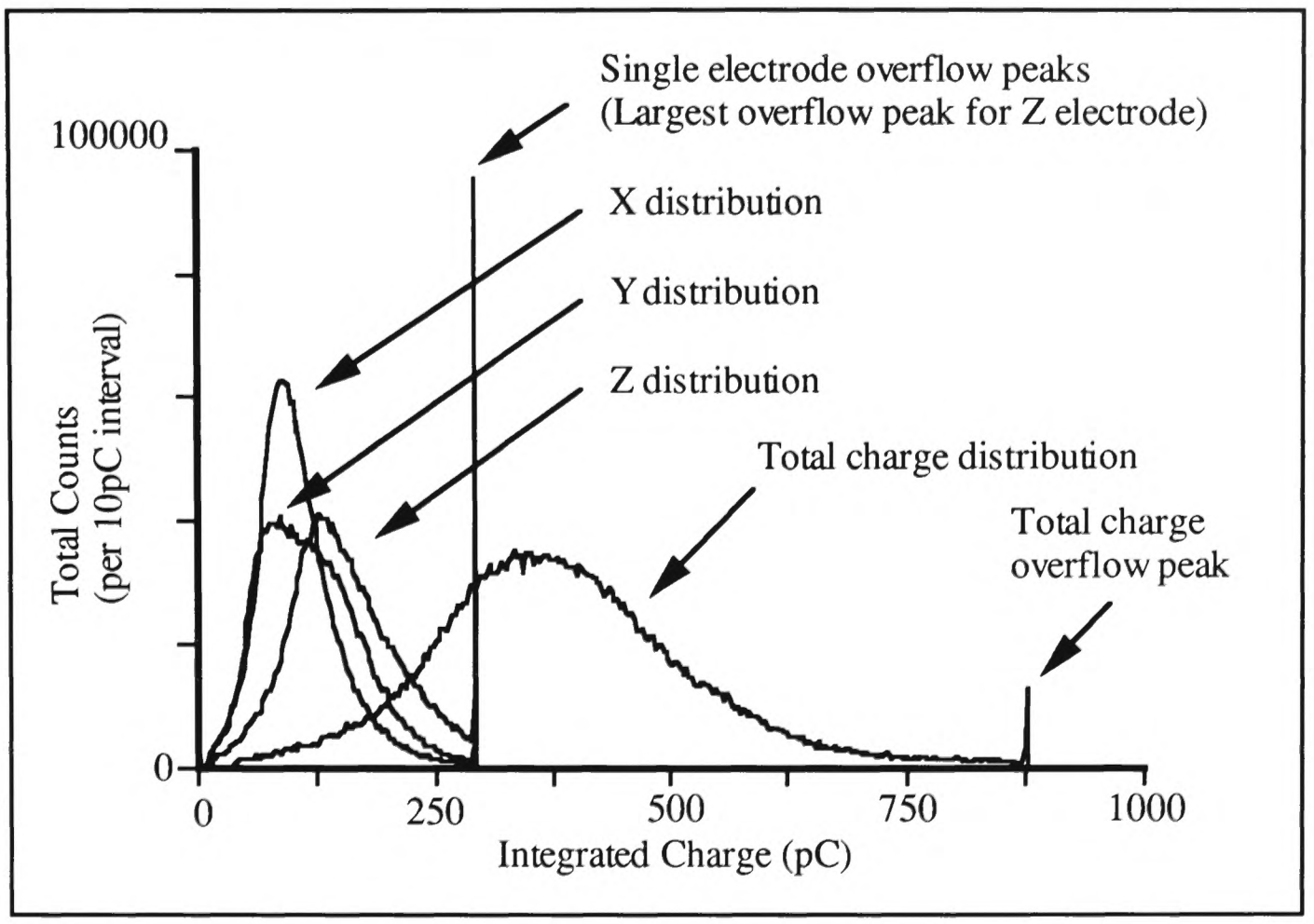

(Charge overflow is much more frequent on the z electrode due to the higher resistance causing slower charge decay.)

Charge Distributions for solution treated material, showing the charge overflow peaks. It was found that there was no obvious second peak in the total charge distribution due to double events; thus no secondary cut-off was introduced (unlike Fe-Cr[8]). This was verified by separating the charge distributions for each of the different elements.

Figure 4.16

Total Atoms Positioned : 176283 Total Windowed Atoms : 191409

Double timing signals break down by element to give

Second Atoms

	Al	Zn	Mg	X1	H	?	Total
Al	5291	1261	0	97	0	792	7441
Zn	0	417	0	0	0	24	441
Mg	767	131	0	42	0	40	980
X1	292	27	0	0	0	10	329
H	78	6	3	0	0	5	94
?	295	36	0	2	0	28	361
Total	6723	1878	3	141	0	899	9646

From these double-timing events the breakdown of the positioning is

Element	1st atom positioned	1st atom not positioned	2nd atom not positioned
Al	5512	1929	6723
Zn	413	28	1878
Mg	820	160	3
X1	18	311	141
H	91	3	0

Single timing events where there is charge overflow indicating the arrival of two ions are also considered.

Element	single time
Al	2911
Zn	55
Mg	69
X1	10
H	0

from this a corrected total composition may be calculated

Element	Pos. Atoms	%	Positioning	Corrected%
Al	169897	96.4	92.1	95.3
Zn	3020	1.7	60.0	2.6
Mg	2752	1.6	90.1	1.6
X1	487	0.3	50.8	0.5
H	127	0.1	97.7	0.1

Figure 4.17 showing a breakdown of the positioning statistics for a file.

The number of double events that register a single timing signal with charge overflow is small due to the low mass resolution of the POSAP. Also a large number of isotopes species (e.g. zinc) reduces this possibility further.

The statistical analysis of positioning shows that there is a problem in calculating the composition of a precipitate by spatially selecting just the positioned atoms. It is possible to correct for this only by assuming that multiple events occur uniformly throughout the data. This is unlikely to be valid assuming double events occur by the evaporation of near-neighbour atoms since that introduces a composition dependence. For example, in a precipitate there will be more Zn-Zn bonds thus the probability of a Zn-Zn double evaporation is higher. It will be possible to test this hypothesis soon with the next generation POSAP instrument currently under development in which multiple events can be detected and positioned unambiguously.

4.5.2. Copper and Zinc.

The atomic masses of the isotopes of zinc and copper are closely interwoven. The mass resolution of the FIM100 AP is sufficient to clearly separate the various isotopes, thus enabling separate quantification. The method for correcting peak overlap due to hydride formation has been discussed in Section 4.4.4. The mass resolution of the POSAP is lower than the AP due to the geometrical constraints of the detector size and the radial ion trajectories thus, as shown in Section 4.5.1.1, POSAP analysis is unable to separate the isotopes. Furthermore in Section 4.5.1.2 it was shown that there are problems with non-positioning of multiple events for the zinc/copper species which tend to be the second ion species to be detected and hence not positioned.

In order to investigate the evaporation behaviour of each element separately, two binary alloys were analysed (Table 4.2.). Both alloys were solution treated and quenched to achieve a random solid solution, such that the POSAP analysis could be representative of the overall composition.

Alloy	Composition (Atomic %)
CA-1	Al-1.52%Zn +trace Si,Fe,Sn,Ti,Ga.
LL-1	Al-0.86%Cu +trace Si,Fe,Mn,Mg,Ni,Zn,Sn.

Table 4.2

1st Atom	2nd Atom	Number	No. of Cu	Percentage
Cu^{+}	-	1341	1341	75.5%
Cu^{2+}	-	120	120	6.7%
Al	Cu^{+}	104	104	5.9%
Al	Cu^{2+}	39	39	2.2%
Cu^{+}	Cu^{+}	78	156	8.8%
Cu^{2+}	Cu^{2+}	8	16	0.9%
Cu^{2+}	Cu^{+}	0	0	0
			1776	100%

Table 4.3

1st Atom	2nd Atom	Number	No. of Zn	Percentage
Zn^{+}	-	735	735	21.1%
Zn^{2+}	-	876	876	25.2%
Al	Zn^{+}	653	653	18.8%
Al	Zn^{2+}	363	363	10.5%
Zn^{+}	Zn^{+}	136	272	7.8%
Zn^{2+}	Zn^{2+}	234	468	13.5%
Zn^{2+}	Zn^{+}	53	106	3.1%
			3473	100%

Table 4.4

Ions	Positioned atoms	Non-pos. atoms	Total atoms	Relative %	Expected %Isotopes
Zn^{64}	453	335	788	44.4	48.6
Zn^{66}	289	222	511	28.8	27.9
Zn^{67}, Zn^{68}	260	215	475	26.8	22.9

Table 4.5

4.5.2.1. Copper Alloy LL-1.

The spectrum showed that for the analysis conditions of 70K and 20% pulse fraction copper was collected as mostly Cu^+ species with only about 6% Cu^{2+} species. Comparing the ratios of Cu^+ peak intensities detected with the known ratio of isotopes of copper showed there to be strong formation of the hydride species CuH_2^+. For this analysis about 60-70% of the Cu^+ species were detected as hydrides. There were too few Cu^{2+} species for determination of the percentage hydride formation.

The statistical analysis (Table 4.3) showed a high percentage of the species are detected as single events and are thus positioned correctly. This showed there to be no serious problem in determining compositions from just the positioned atoms in this alloy. Displaying the positioned copper atoms showed what appeared to be a random solid solution. This was confirmed by a χ^2 test for randomness[89]. Viewing the distribution of the different isotope species, however, showed a non-uniform distribution across the image; suggesting the dependence of hydride formation upon the local field at the surface.

The calculated composition of the volume analysed was 0.90%Cu from the positioned data and 0.94% Cu with the %positioning statistical correction. This compares well with the spark analysis composition of 0.86%Cu and shows that the standard analysis conditions of 70K and 20% pulse fraction does not result in any significant loss of copper by preferential evaporation effects (Section 4.4.3 and Section 4.5.3.).

4.5.2.2. Zinc Alloy CA-1.

For analysis of this alloy (at 70K and 20% pulse fraction again), the spectrum showed the zinc to occur as Zn^+ and Zn^{2+} species in approximately equal proportions.

However the positioning statistics (Table 4.4) clearly showed the serious problem with non-positioning of double events. Only about 46.3% of the total zinc (compared to 64% of the total Al) detected was positioned due to double events of both Al-Zn and Zn-Zn types. Comparison of the ratio of peak intensities with the known ratios of isotopes

showed that there was negligible hydride formation (Table 4.5). It was necessary to consider the contribution of positioned atoms separately from that of the non-positioned atoms, due to the correction applied to the positioned atoms to allow for the difference in flight paths to the detector which slightly shifts and sharpens the spectrum peaks compared to the non-positioned atoms.

The positioned data gave only 0.93% Zn, while after correction for double events this increased to 1.27% Zn. This is only about 80% lower than the spark analysis of 1.52% Zn; however, for this datafile, there was a problem with the channel plate gain, which affected the aluminium composition levels detected. In the next section it will be shown that there is a major problem with preferential evaporation effects leading to a 50% underestimate of the zinc levels actually present. The accuracy of the composition detected in this analysis thus proved to be inconsistent with the levels of under-detection of zinc shown by the many more analyses presented below. This whole section on the accuracy of the detection of zinc deserves more investigation; if only time had permitted.

4.5.2.3. Summary.

Zinc shows a problem with multiple events reducing the positioning, while for copper this is minimal. Copper shows tendency to form hydrides which is not observed for zinc. Both of these effects mean that **it is not possible to separately identify the zinc and copper with the current POSAP detector**. For all POSAP data presented in this thesis "zinc" refers to both the zinc and copper detected unless the copper is specifically mentioned.

In Section 6.4.6 however, a method for qualitatively determining the presence of copper in the absence of zinc is proposed by checking the selected spectrum. But it is necessary to bear in mind that the zinc is less likely to be positioned than the copper; thus the selected spectrum will naturally tend to show the presence of copper more than the presence of zinc. Also only about 30% of the zinc occurs as Zn^+ species which would overlap with the copper species.

4.5.3. Pulse Fraction and Temperature Dependence.

Compositional analysis of a multi-component system can be strongly affected by differences in the evaporation behaviour of the various elements[73]. It is necessary to verify that the temperature and pulse fraction conditions used give the correct composition with no preferential evaporation or retention.

Analyses of solution treated material were performed at temperatures from 30K to 80K and at pulse fractions of 15, 20 and 25% of the dc voltage. Due to the low solute levels in this material, about 60,000 atoms were collected for each set of analysis conditions. It was attempted to reduce the temperature step-wise from 80K to 30K in a continuous analysis with a fixed pulse fraction in order to minimise the effect of other experimental variables. Collecting so many ions for each heat treatment reduced the counting statistics error to less than 0.1% for the solute elements; however, it also involved collecting more than one million ions.

The largest effect of reducing the temperature of analysis was observed in the amount of hydrogen detection during analysis (Figure 4.18.a). Hydrogen detection was observed to increase dramatically upon reducing the temperature of analysis below 50K. This is detrimental to the analysis since the evaporation rate is controlled by the data collection rate and also both aluminium and copper are very prone to hydride formation. When there was lots of aluminium hydride formation the tail of the aluminium peak extended into the Zn^{2+} species window which reduced the accuracy of the compositional information for the zinc.

For calculation of the alloy compositional data, the statistical correction for multiple events was applied and only real metal ion species were considered (thus excluding hydrogen). The results are shown in Figure 4.18.b and 4.18.c.

Magnesium shows clear signs of preferential evaporation at higher temperatures and lower pulse fractions. At 30K, the levels of magnesium detected are only slightly lower than the levels detected by EPMA.

a)

% Hydrogen
(after positioning correction)

Hydrogen detection increases dramatically at 50K and below.

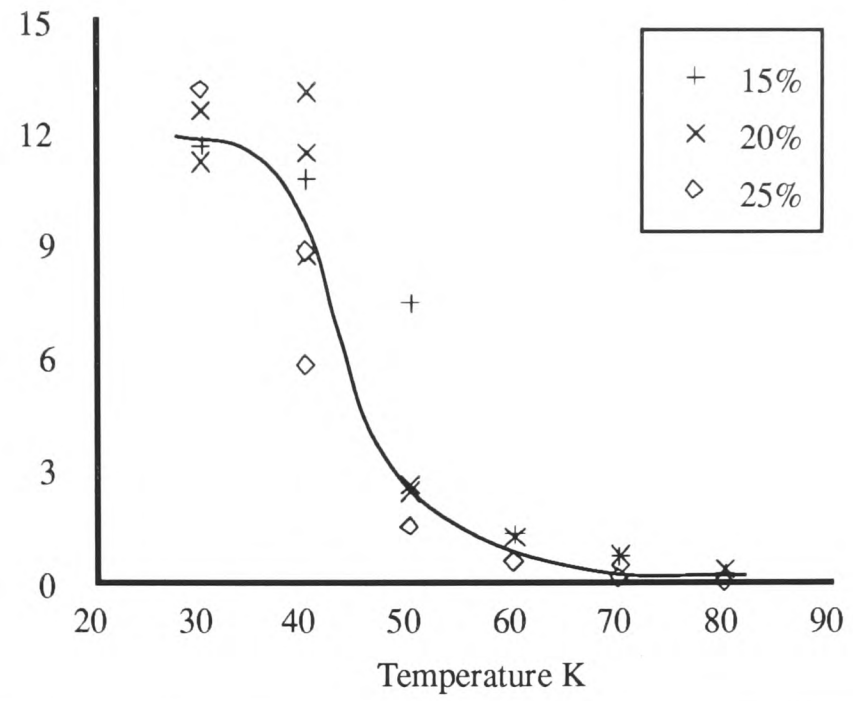

b)

%Magnesium
(after positioning correction)

Magnesium shows clear signs of preferential evaporation at higher temperatures and lower pulse fractions.

+ 15%
× 20%
◇ 25%

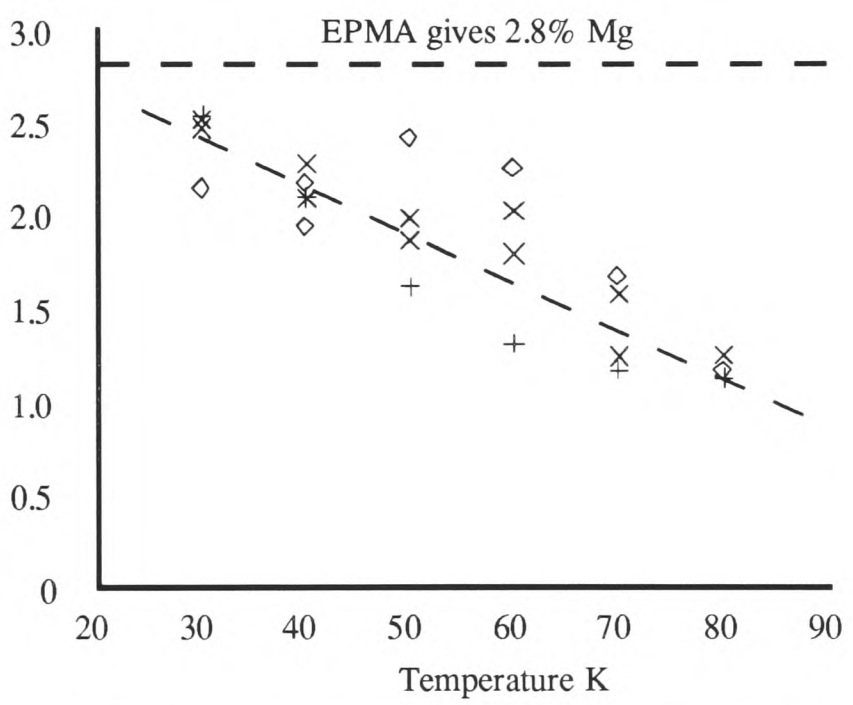

c)

% Zinc/Copper
(after positioning correction)

Zinc/Copper levels detected are lower than expected however there is no clear increase in the levels detected at lower temperatures and higher pulse fractions.

+ 15%
× 20%
◇ 25%

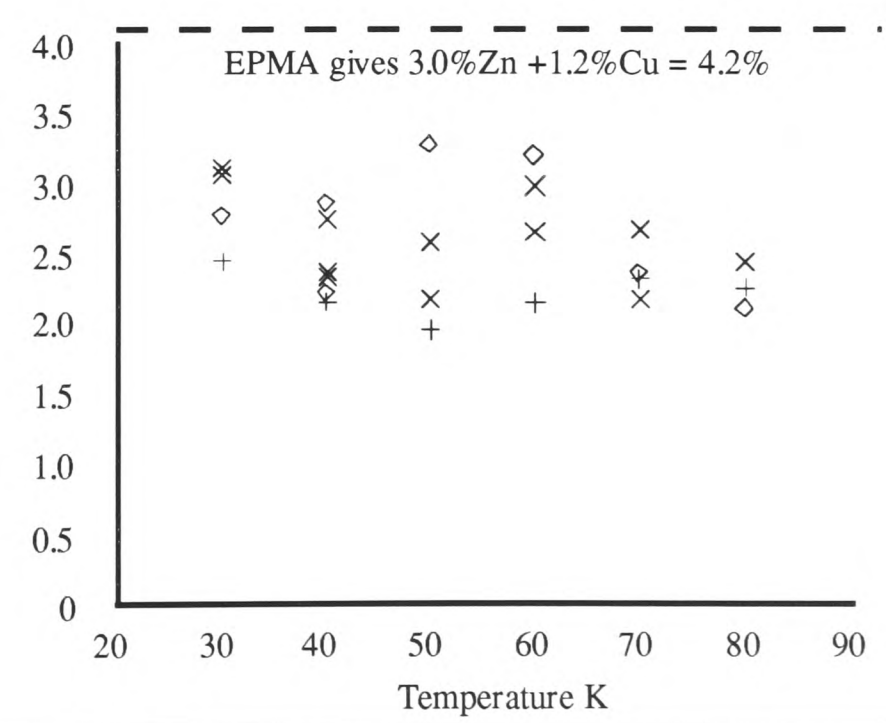

Figure 4.18

Comparison of the levels of Zinc/Copper detected with the levels expected from EPMA analysis show that Zinc/Copper is consistently below the expected level for all temperatures. The data show a wide degree of scatter, with no trend of dependence on either the pulse fraction or the temperature.

In summary:- the solute compositions detected by POSAP analysis were shown to be incorrect for all temperatures used, when compared to the levels detected by EPMA. For magnesium, this was proven to be due to preferential evaporation effects. In order to get the correct magnesium concentration, it is necessary to use a low analysis temperature and a pulse fraction of 20% or more. For the zinc and copper, peak overlap confused matters and ideally these experiments should be redone using the binary calibration alloys to evaluate separately the evaporation behaviour of each of these elements. The use of a low temperature and a high pulse fraction was not observed to be beneficial in this study.

In order to put this investigation into context, it should be noted that all temperatures quoted in this thesis are the temperatures monitored by the temperature controller, rather than the actual temperature of the specimen. It is thought that there is a 14K underestimate of the specimen temperature monitored in this way. The minimum temperature achievable on the FIM100 used for this research was 20K (≈34K). The work on Al-Li preferential evaporation[88] showed that the correct lithium concentration was achieved for temperatures around 20K. The Japanese workers, who have done most of the AP analysis of aluminium, use a special low temperature atom probe[90] capable of achieving a specimen temperature of 20K. The current investigation suggests that this low temperature may be necessary for correct compositional analysis of most aluminium alloys. However, there are other experimental problems in performing analyses at such low temperatures to consider. Hydrogen detection is a problem especially due to the formation of aluminium hydrides, since for alloy systems of technological interest such as AlZnMgCu, as used in this work, and also AlMgSi, as currently under investigation by other workers in this group, peak overlap becomes limiting. Hydrogen is notoriously difficult to remove from vacuum systems. Titanium

sublimation pumps are the most efficient pumps ; however, most of the residual vacuum gas at low pressures (10^{-10}Torr) is hydrogen and vacuum pressure-vessels will continuously be outgassing hydrogen; thus it is difficult to keep the levels low. Other problems associated with analysis at low temperatures are that specimen fracture is more common, and the time necessary for specimen exchange becomes limiting. These factors must all be addressed if accurate compositional information is to be obtained by atom probe analysis.

Even though the FIM100 used in this research is incapable of the lowest temperatures necessary to give really accurate compositional information it can provide spatial information on the nanometer scale about the early stages of precipitation in this alloy and by comparing analyses of different heat treatments it is still possible to detect trends in the compositional development of precipitates during the precipitation process.

4.5.4. Spatial Information.

For each atom detected, the POSAP records the time-of-flight and the position of impact on the detector. In order to reconstruct the data to give a three dimensional representation, it is necessary to know how large an area on the specimen is being analysed and how many atoms are detected in a known depth of analysis. This is of most importance when information on the scale and morphology of the features analysed is required .

The detector area is fixed, however, as a specimen is evaporated during analysis the magnification of the projection decreases. The local magnification (η) of a region of the projection is determined by the local radius of curvature (r_1) and the screen-to-specimen separation (R) (see Eq. 4.2). The radius of curvature is usually assumed to be constant over the whole area of interest thus approximating the end of the specimen to a hemisphere. With this assumption it is then possible to relate the evaporation field (F) at the specimen surface to the applied voltage (V) and the radius of curvature (Eq. 4.3).

$$\eta = \frac{R}{\xi r_t} \quad \ldots 4.2 \qquad\qquad F = \frac{V}{k r_t} \quad \ldots 4.3$$

The voltage can be monitored during an analysis, so, with suitable calibration, it is possible to calculate the change in the area of analysis throughout an analysis.

4.5.4.1 Image Compression Factor - ξ.

Equation 4.2 contains the image compression factor, ξ. The primary cause for image compression is the deflection of evaporated ions, early in their trajectory, due to field distortions introduced by the specimen shank. Assuming this effect to be radially linear, it can be quantified from measurement of the field ion image. The image compression factor is defined as the observed angle of the image over the geometrical angle of image.

From Figure 4.19 it can be seen that $\xi = 1.31$. Determination of ξ for other materials showed the value to be almost constant, given similar specimen preparation methods.

4.5.4.2. Radius Calibration.

Equation 4.3 requires the determination of the radius of curvature for a known voltage. The radius can be determined directly from the field ion image by a method developed by Dreschler and Wolf [91]. The method is shown schematically in Figure 4.20. Consider the image of a specimen showing two poles and some ring structure. Assuming the surface of the specimen to be locally spherical the radius of curvature is given by

$$r = \frac{nd_{hkl}}{(1-\cos\theta)} \quad \ldots 4.4$$

It is useful to consider the errors associated with this equation.

a) The number of rings can only be described to an accuracy of n $\pm 1/2$. This error is particularly large for this system where usually only about four rings are visible.

b) The measured diameter of the rings is generally only accurate to $\pm 10\%$ due to non-circular ring structure.

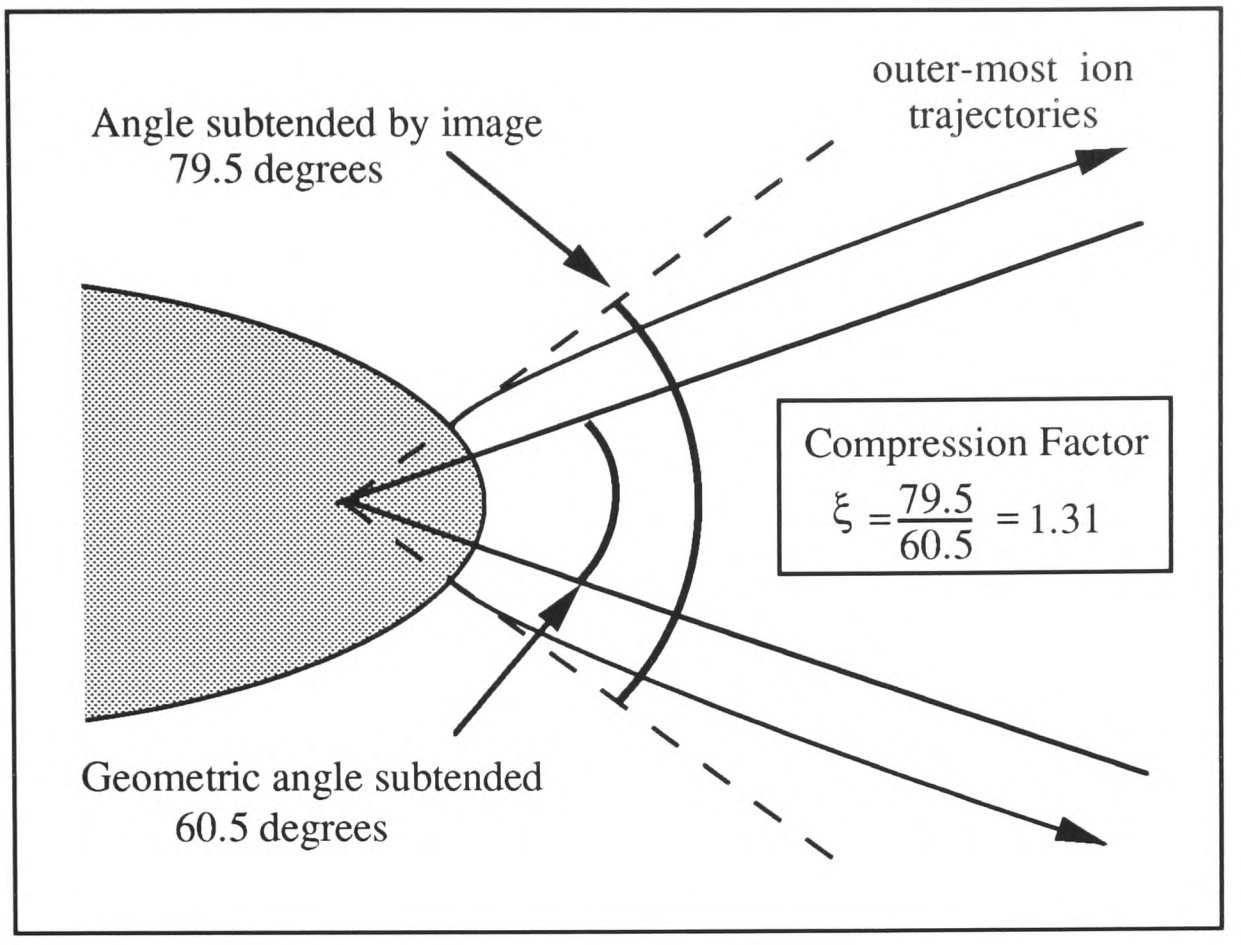

Figure 4.19 Schematic diagram showing the calculation of the image compression factor

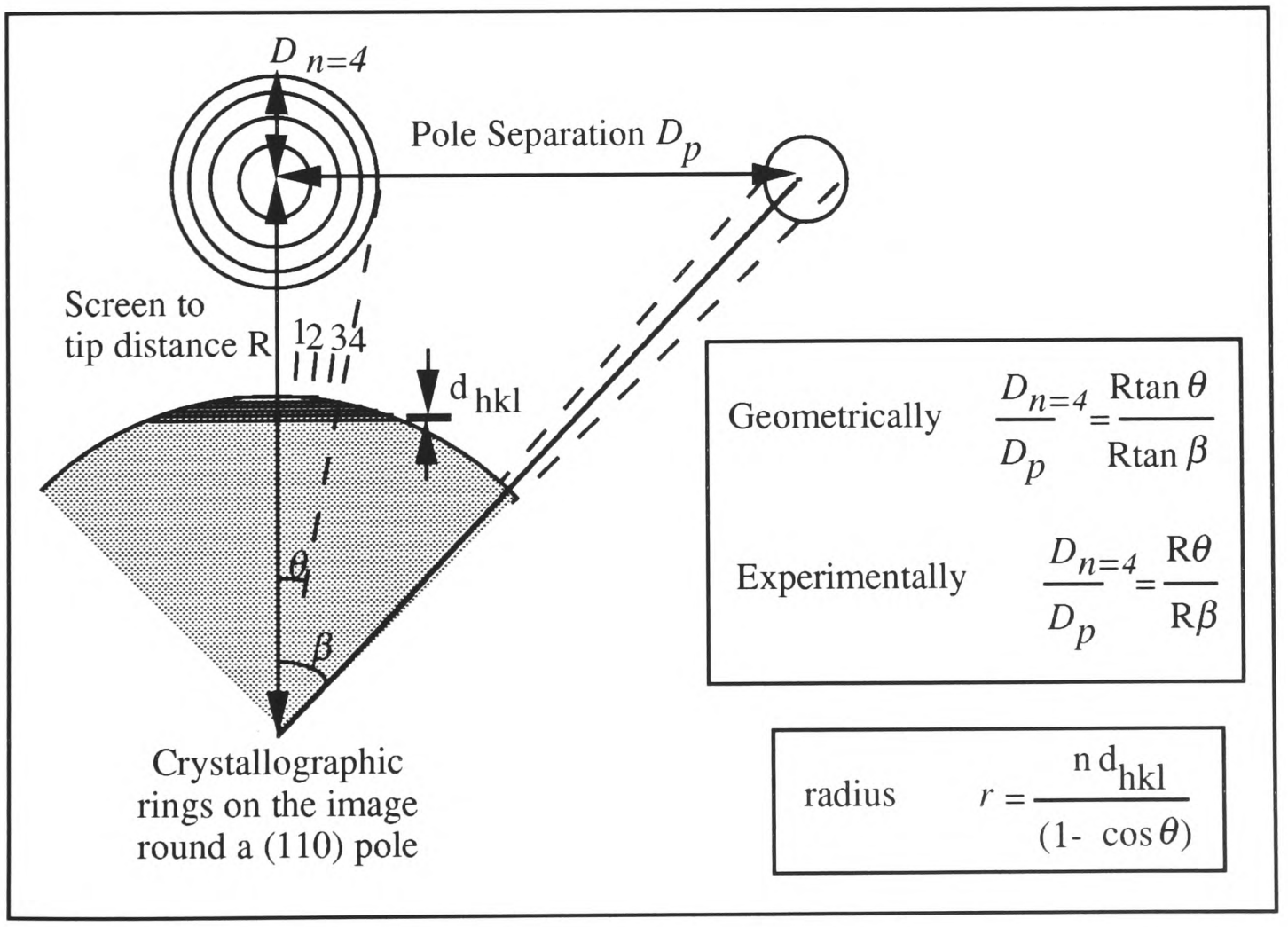

Figure 4.20 The Dreschler-Wolf method for calculating the radius of a specimen from the image of the crystallography.

c) The $(1-\cos\theta)$ dependence makes the equation very sensitive to the value of θ used. The $D = R\theta$ dependence used here is an experimental observation taken from Wilkes[92] and not the geometrical $D = R\tan\theta$

d) This equation determines the radius of curvature around the pole. Since the specimen tip is crystallographically anisotropic and also probably geometrically asymmetrical the local radius of curvature varies across the specimen.

An alternative method of determining the radius of curvature of a specimen is to calculate the average radius of curvature for the whole tip from TEM images of the end-form (Figure 4.21). This ignores crystallographic local variations in curvature, but the observed curvature macroscopically fits well the approximation to a hemisphere. The radii of several different specimens determined by TEM are plotted against the applied imaging voltage in Figure 4.22. This shows a reasonable agreement with equation 4.3 and generally good consistency between specimens; thus confirming the applicability of a calibration calculation to different specimens of the same material. The graph also shows a good agreement with the values calculated by the Dreschler and Wolf method.

Having determined the radius of the specimen, the area of analysis at a known voltage can be calculated by geometry. However, care should be taken in determining the value of the voltage ,V. It was found that the change in voltage in going from imaging (70K, 10^{-4} Torr argon, steady dc voltage) to probing (70K, 10^{-10} Torr argon, dc voltage plus 20% pulse fraction) required a increase in V of approximately 30%, although no change in the specimen occurred.

Uncertainty in the definition of the imaging voltage and the probing voltage can also lead to errors. The imaging voltage used was close to the 'best imaging voltage' ±3% with little or no evaporation, whereas the probing voltage was determined by extrapolating back from the steady-state probing regime, visible in a plot of Voltage vs Ions. Doubling the data collection rate was observed to increase the dc probing voltage by about 4% and dropping the temperature by 10K was observed to increase the dc



Figure 4.21 Example TEM image of a specimen after POSAP analysis.

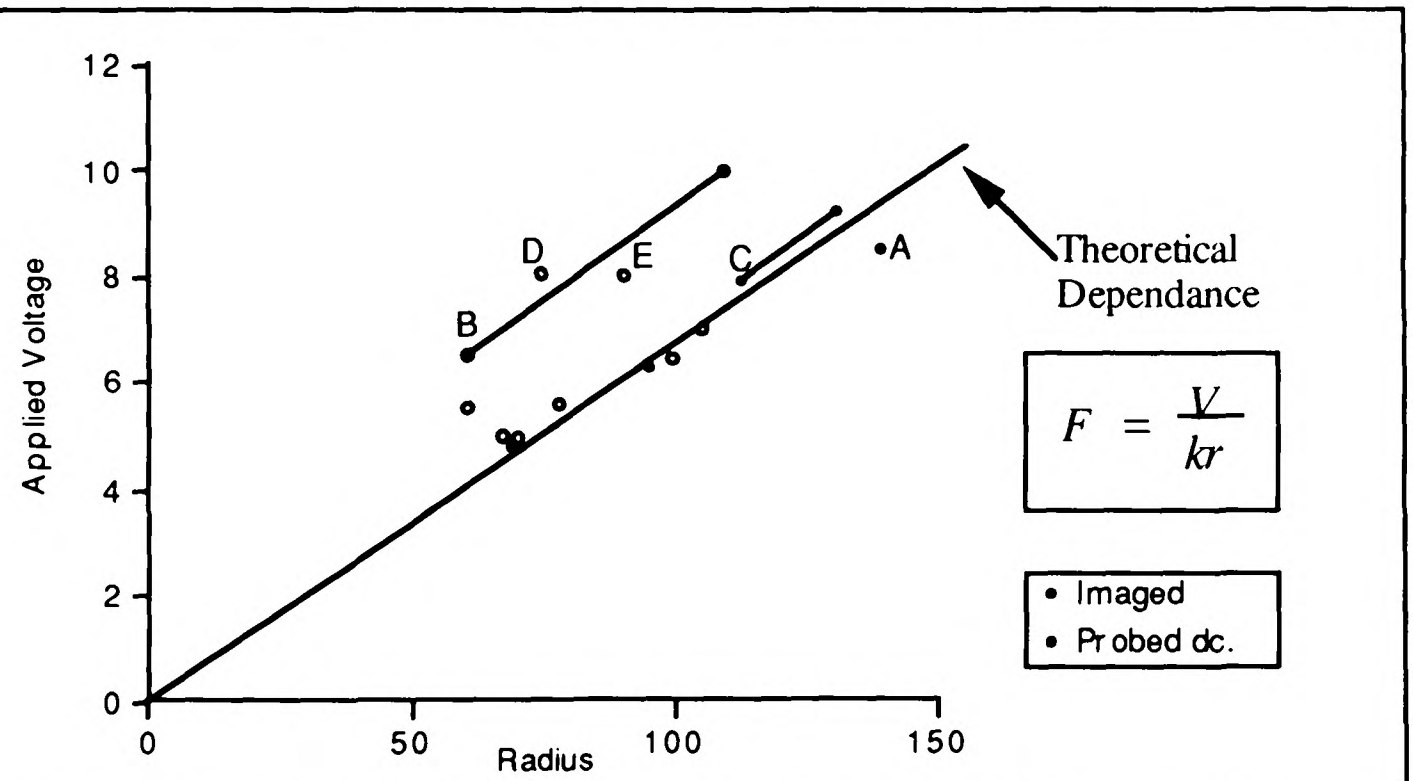

A -radius measured for largest cross-section of non circular tip over-estimating r.

B - two measurements on an extremely sharp tip with non equilibrium end form.

C - two measurements on the same tip showing good correlation of gradient.

D - Zirconium precipitate present causes overestimate of the equilibrium voltage.

E - Voltage determined after imaging in the TEM thus overestimated due to oxide.

Figure 4.22 Graph of Tip Radius measured by TEM against applied Voltage.

probing voltage by about 3% although this effect was reduced at the lower temperatures once detection of vacuum hydrogen effectively reduced the evaporation rate.

4.5.4.3. Depth Scale Calibration.

The easiest and most generally applicable method for calibrating the depth scale is by analysing the material along a low index pole direction in order to observe the ring collapse similar to imaging. For low index poles, the ring spacing is high; thus, sectioning the data shows the ring structure and the number of atoms detected per atomic plane can be calculated (see also Figure 6.29.). For Al-7150 the (110) pole, used for the radius calibration in imaging, was not sufficiently clear in probing, so the (111) pole was used. Figure 4.23 shows a 3000 atom slice through the volume analysed, in which 10800 atoms were detected per plane.

4.5.4.4. Application of scale calibrations.

Before reading the data into the analysis package the radius calibration and the depth calibration are set by entering the radius, the compression factor, and the number of atoms detected per nm depth all at a dc probing voltage of 10kV. These values are critical to the three dimensional representation of the data and were found to differ widely between alloy systems[79]. The values used are described in detail in Figure 4.24.

An estimate of the accuracy of the calibrations for a particular analysis may be judged by calculating the number of atoms detected per nm^3 and comparing this with the theoretical value of 60 atoms/nm^3 for this alloy. Typically an experimental value around 30 atoms/nm^3 was found which suggests a detector efficiency of around 50% which is close to that estimated by previous workers[87]. If the experimental conditions were different to those used during calibration, the effect of this difference shows up rapidly by this method and the radius input value may be altered accordingly.

Since the applied voltage is used to determine the scale of the volume of analysis, it was useful to check how the voltage changed throughout the analysis. Under ideal analysis



Cross section of depth scale analysis at 30K. The image contains 3000 atoms but there are 10800 atoms per plane. The ring structure of the (111) pole is clearly visible.

Figure 4.23

Figure 4.24 Calculation of Scale Calibrations.

Radius calibration from FIM image.

Separation of (110) poles on image =48.6mm

Radius of 4th (110) ring on image = 6mm

Hence angle subtended on image = 7.4 degrees.

Hence radius is 137nm (12% error) for imaging in argon at 70K total BIV of 7330V.

Depth Scale calibration.

Voltage vs Ions plot gave 7500Vdc steady state evaporation voltage.

Ions detected per (111) plane gave 10800.

Analysis was in vacuum at 30K with 20% pulse fraction.

Hence atoms/nm detected = 46765 (7500Vdc, 20%,30K,vacuum)

Scale to fixed conditions of 10kV Total Voltage probing in vacuum at 70K.

Effect of argon image gas going to vacuum is V=> 1.3 V. (no change in radius of tip).

Effect of temperature going 70K=>40K is V=> 1.12V. (no change in radius of tip)

Hence radius calibration gave r=137nm for imaging in argon at 70K total BIV of 7330V

Removing argon gas gives r=137nm for vacuum at 70K and 9529V total voltage.

Scaling to 10kV total voltage gives r=144nm (vacuum, 70K, 10kVtotal)

Hence depth calibration gave 46765atoms/nm (7500Vdc, 20%,30K,vacuum)

Increasing temperature 40K=>70K V=> V/1.12 V=6696Vdc (no change in tip radius)

Scaling to total voltage of 10kV changes tip radius and hence area of analysis.

Atom/nm = $46765(10/6.696 \times 1.2)^2$ =72432. (vacuum, 70K, 10kV total)

Compare these values to the calculable atoms/nm for a radius of 144nm.

D=rwk r=144, w=0.307^c, k=1.31. thus D=58nm. Hence area of analysis =2642nm^2.

Unit cell contains 4 atoms in $(0.4)^3 nm^3$. Atoms/nm^3=60.

Real number of atoms /nm for a tip of r=144 give A/nm=158525.

The detector efficiency is thus ε= 72432 / 158525 = 46%.

This is within the range of the accuracy of the radius calibration.

Specific input for the scale calibration number in AVS.

Ideally the scale calibration in AVS should be dealing with the total voltage. It does not.

At the moment there is an approximation that the increase in voltage on removing the imaging gas approximately cancels with the decrease in voltage when using the dc voltage.

The input numbers used for AVS should be the numbers calculated above for a total voltage of 10kV. Hence use the numbers r = 144nm A/nm = 72432.

conditions, the applied voltage should steadily increase in order to maintain the evaporation rate. Voltage monitoring proved effective at detecting anomalies in evaporation conditions which occurred during the analysis; so providing a guide to the quality of the datafile.

Figure 4.25 shows some possible anomalies in the development of voltage during analysis and Figure 4.26 shows the effect of changing analysis conditions upon the applied voltage.

4.5.5. Summary of factors affecting POSAP data interpretation.

The preceding sections have described in detail the various factors affecting the interpretation of POSAP data. The POSAP can provide good chemical and 3-D spatial information about the distribution of elements on the nanometer scale. However, in order to do so accurately, it is necessary to calibrate the scale of analysis and also to examine in detail the evaporation behaviour of the alloy.

For Al-7150 it has been found that;

i) Zinc and copper are inseparable due to peak overlap.

ii) Both zinc and magnesium evaporate as multiple events. This is a problem for zinc since it is always the second ion to be detected and is thus not positioned.

iii) The levels of magnesium detected (and probably zinc/copper) are affected by preferential evaporation effects thus giving inaccurate total compositions.

iv) The scale calibration of the POSAP is essential to enable true visualisation of the ion species distributions.

All these factors tend to complicate POSAP analysis of this alloy system and should be borne in mind during the following Chapters when discussing the results obtained.

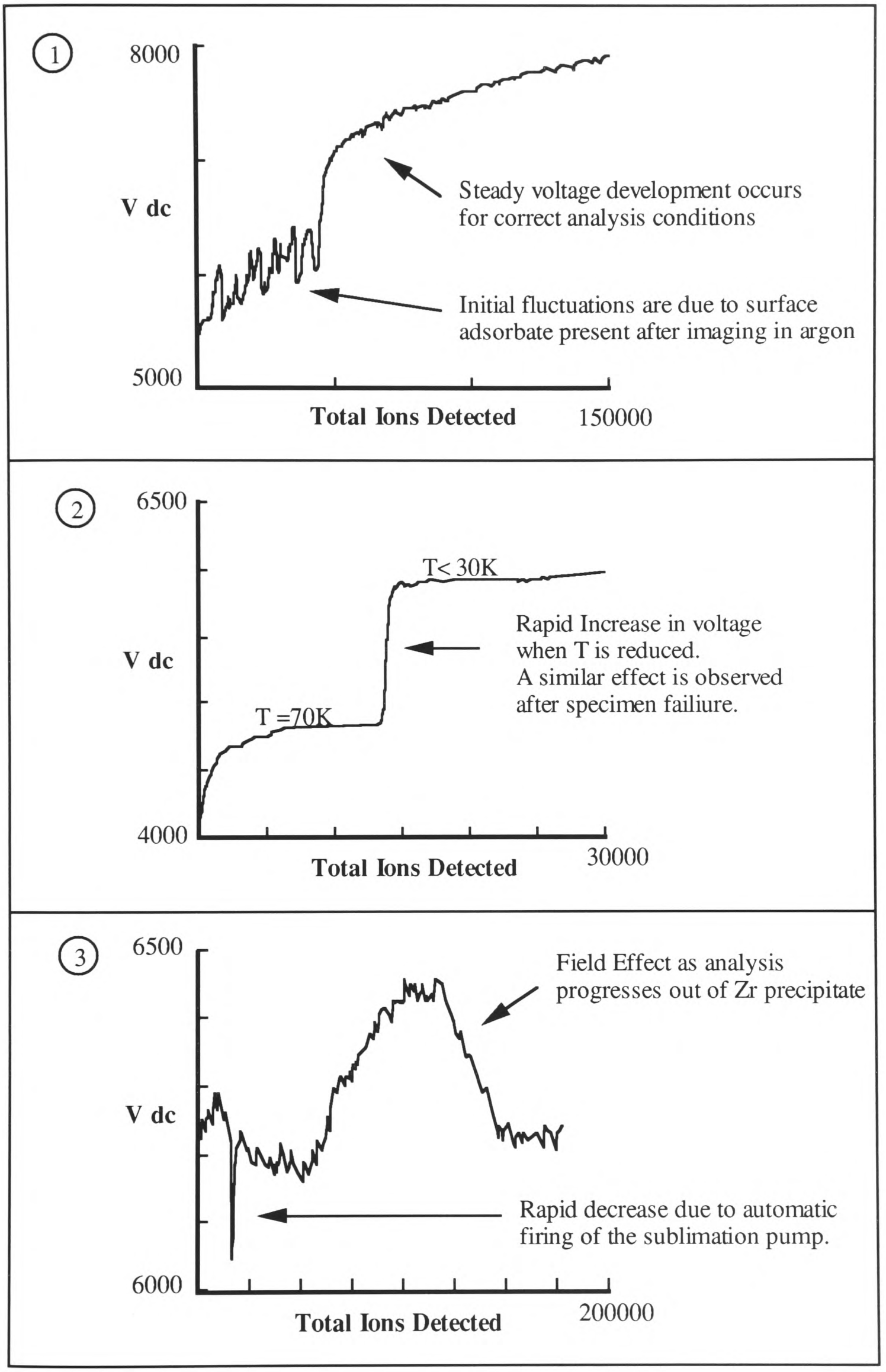

Figure 4.25 Some observed anomalies in voltage development during analysis.

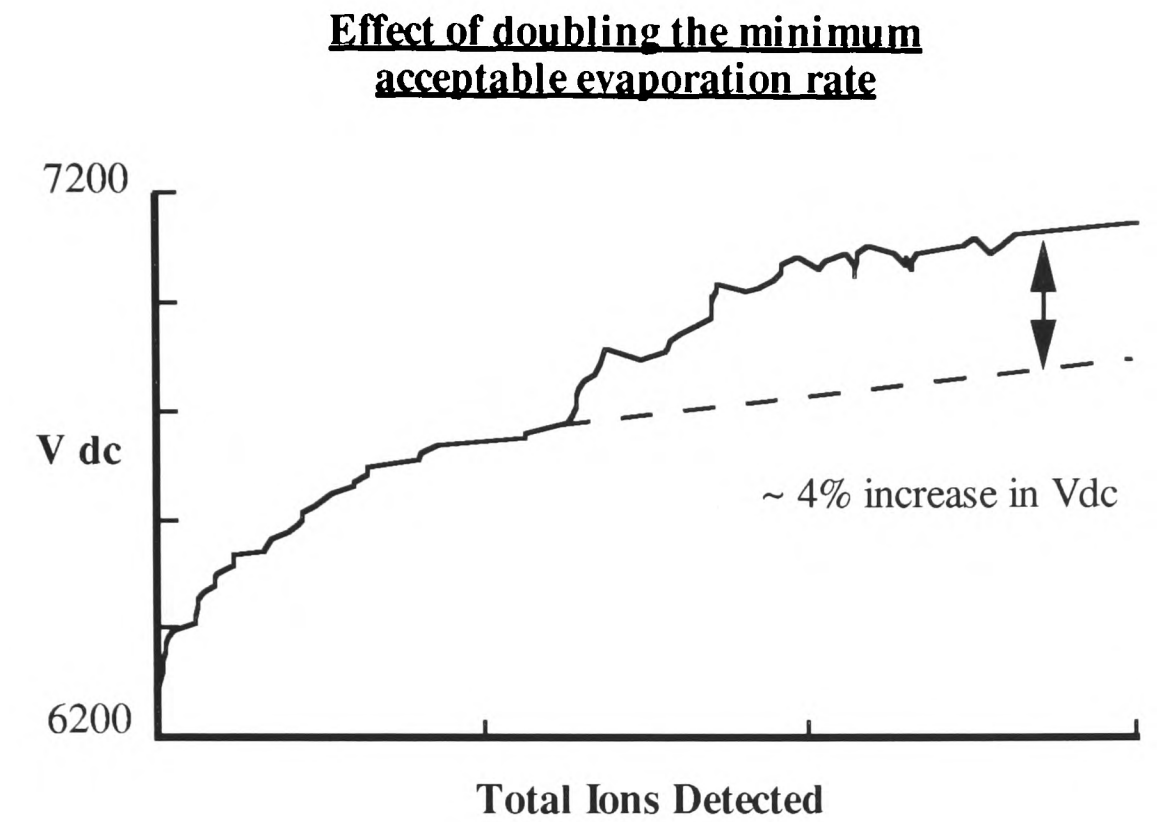

Figure 4.26 The effect of varying the analysis conditions upon the applied dc voltage can be observed easily. Decreasing the temperature by 10K requires a 2-3% increase in voltage while doubling the evaporation rate requires a 4% increase in voltage.

Chapter 5. Precipitate Analysis.

5.1. Matrix Precipitate Analysis.

The strength of this alloy is derived primarily from the interaction of matrix precipitates with dislocations produced during deformation. In material aged to peak strength these precipitates are very small. TEM images have been used to show the development of these precipitates during the ageing process[2]. These images can give quantitative information about the size, distribution and morphology of the precipitates. Analysis of the diffraction patterns can give information about the crystal structure of the precipitate phases[93]. From this information much can be inferred about the atomic scale processes occurring during precipitation. Analysis of the development of the chemistry of the precipitates, at this early stage in the precipitation process, presents the problem of separating the precipitates from the surrounding matrix. Even the highest spatial resolution X-ray analysis, in a dedicated STEM, as used in this work, is limited by both the size and also the separation of the precipitates, due to signal integration through the specimen thickness. The matrix strengthening precipitates in all of the heat treatments were too closely spaced for STEM analysis (except the grossly overaged 220°C material, which will be considered separately in Section 5.3). Atom probe analysis is currently the only technique which can provide chemical information about the matrix strengthening precipitates at near peak strength.

5.1.1. T.E.M. Matrix Precipitate Analysis.

Figure 5.1. shows TEM images of precipitation in each of the heat treatments analysed in this section. Qualitative analysis of the TEM images of the material, aged at 120°C, 150°C and 180°C, shows the expected trends in microstructural development. As the ageing temperature was increased, the number density of precipitates decreased, the size of the precipitates increased and the shape of the precipitates became more defined.

The approximate sizes of precipitates, as measured from these images are:-

120°C ~2-5nm 150°C ~3-8nm 180°C ~5-15nm

a) shows matrix precipitation in material aged for 100 hours at 120°C.
Precipitates 2-5nm in size.

b) shows matrix precipitation in material aged for 20 hours at 150°C.
Precipitates 3-8nm in size.

c) shows matrix precipitation in material aged for 8 hours at 180°C.
Precipitates 5-15nm in size.

Figure 5.1

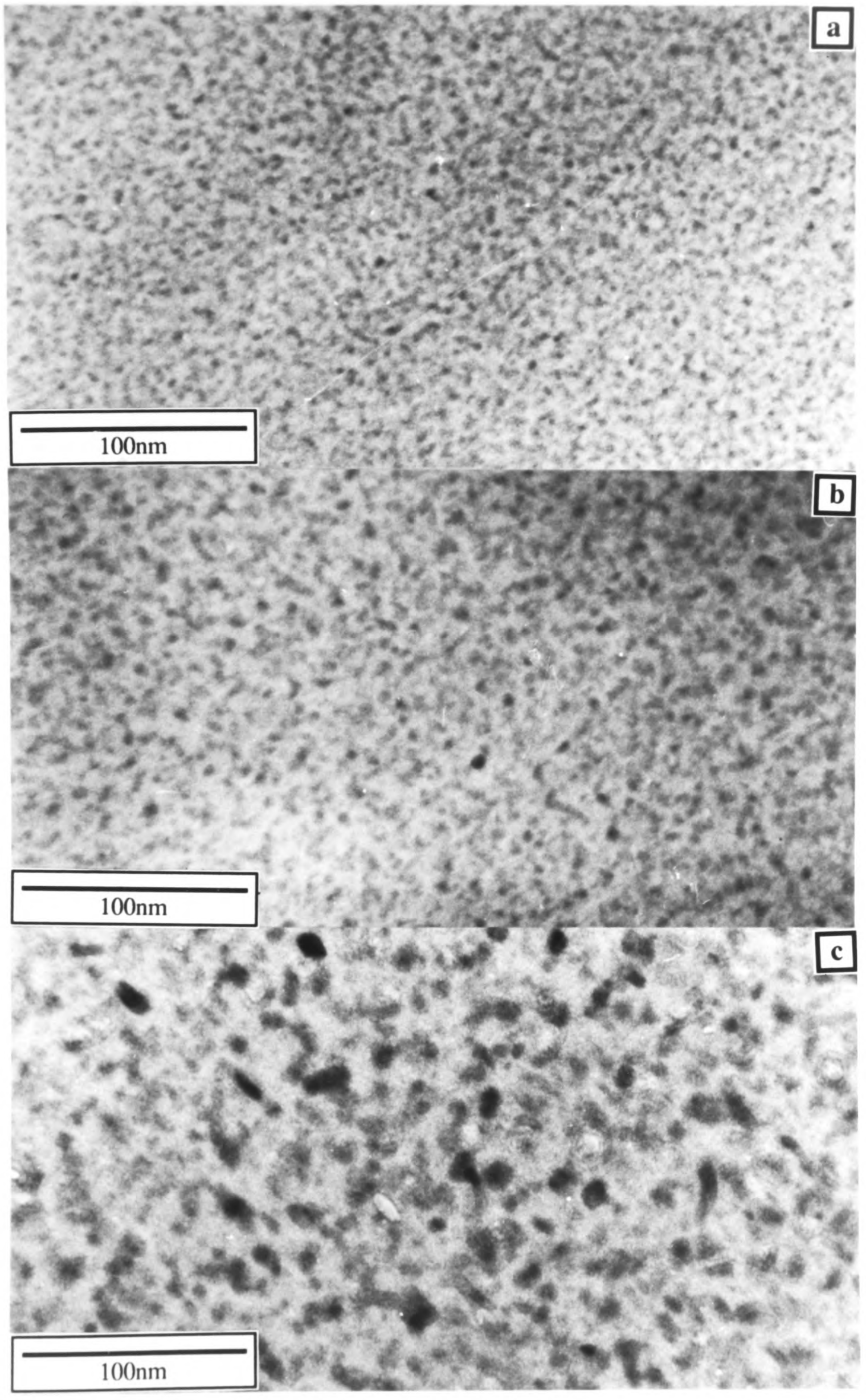
a
100nm
b
100nm
c
100nm

In order to determine the number density of these precipitates, it is necessary to know the foil thickness. Accurate quantification of the number density of precipitates was not attempted due to time constraints, however, qualitatively the number density of the precipitates was seen to decrease with increasing ageing temperature.

The precipitates in material aged at 120°C show no clear morphology; possibly because they are visible more due to atomic/strain contrast in the matrix than diffraction from the precipitate phase. In the material aged at 150°C it is possible to recognise plate-like, rod-like and more generally rounded morphologies. In the material aged at 180°C these are seen to become more clearly defined.

Diffraction characterisation of the precipitation in this alloy system was described in previous work[58] (Part II thesis). The treatments used here produced similar diffraction patterns, suggesting the presence of mainly η' precipitates in the 120°C aged material, but the presence of mainly η precipitates in material aged at 150°C and 180°C.

5.1.2. Atom Probe Matrix Precipitate Analysis.

The technique of atom probe analysis was described earlier in Section 4.1.2. Each heat treatment was analysed and a composition profile was used to define the regions of precipitate and matrix. The compositions were then corrected for the peak overlap due to copper hydride formation, as described in Figure 4.11.

Table 5.I compares the total compositions detected, for each heat treatment, by atom probe analysis; with the average composition as detected by EPMA (which was within the alloy specification). For the material aged at 120°C and 150°C, the scale of the composition fluctuations due to precipitation is smaller than in the material aged at 180°C, thus integrating over both matrix and precipitate regions, in long AP data blocks, is likely to be more accurate. This table shows that the solute levels observed for the 120°C material, analysed by atom probe analysis, are generally about 70-80% of the solute levels detected by EPMA, and the solute fractions observed by AP analysis compare well with the expected EPMA values. The copper solute fraction was relatively rather low and the zinc solute fraction was proportionately higher.

	Ions	%Zn	%Mg	%Cu	SFZn	SFMg	SFCu
EPMA	-	3.0	2.8	1.2	42.9	40	17.1
120°C	126419	2.4	2.15	0.8	44.8	40.1	15.0
150°C	87123	2.64	2.24	0.82	45.8	38.9	15.1
180°C	150147	2.81	2.75	0.86	43.8	42.9	13.4

Table 5.1 Compositions in atomic %.

Ppt.	%Al	%Zn	%Mg	%Cu	SFZn	SFMg	SFCu
120°C	89.1	5.75	4.12	1.0	52.9	37.9	9.2
150°C	88.3	5.9	4.5	1.3	50.3	38.4	11.3
180°C	66.8	15.6	13.6	3.74	47.3	41.2	11.3
Total	%Al	%Zn	%Mg	%Cu	SFZn	SFMg	SFCu
120°C	94.6	2.4	2.15	0.80	44.8	40.1	15
150°C	94.2	2.6	2.2	0.87	45.9	39.0	15.2
180°C	93.6	2.8	2.75	0.86	43.8	42.9	13.4
Matrix	%Al	%Zn	%Mg	%Cu	SFZn	SFMg	SFCu
120°C	96.0	1.57	1.64	0.76	39.4	41.3	19.2
150°C	96.4	1.4	1.42	0.71	39.6	40.2	20.1
180°C	97.2	1.05	1.26	0.46	37.8	45.4	16.6

Table 5.2 Compositions in atomic %.

It should be noted, that these detected compositions compare much more favourably with the real compositions than did the previous atom probe experiments upon the same alloy. During the previous work, it was found to be extremely difficult to get long analyses before specimen failure. For most of the duration of this work similar conditions prevailed and atom probe analysis, although attempted periodically, proved unsuccessful. Finally, the atom probe detector was checked thoroughly and as a result the detector gain was increased to optimise detection efficiency, and the signal threshold was decreased such that some noise was present in the spectrum, but fewer real ions were lost. Also, to ensure prolonged life of the specimen, the analysis conditions were set to give a slow evaporation rate (>1atom /1000pulses). The results of these changes were that specimens could be analysed longer before failure and the compositions detected corresponded much better with the known alloy composition.

For each treatment, the average composition of all the precipitate regions is given in Table 5.2; this is compared to the total composition and also the matrix composition. The matrix composition was calculated as the remainder of the total atoms detected minus the precipitate regions. This method of calculating the matrix composition will give a slight overestimate of the solute contents, due to small contributions from precipitates just clipped by the cone of analysis. However, it has better statistical accuracy than the smaller regions of matrix carefully chosen from the composition profile. Due to the unknown proportions of matrix and precipitate material within the area of analysis, the absolute levels of aluminium in the precipitate are not determinable by atom probe analysis (Section 4.4.1). Thus, it is the solute fractions of the precipitates that are of interest. The solute fractions of zinc, magnesium and copper, for each precipitate, may be plotted upon a ternary composition field. These are shown in Figures 5.2-5.4.

The precipitates in the 120°C material show less variation in solute fractions than those from the higher temperature ageing treatments. All of the precipitates consistently have a lower copper solute fraction than the total composition solute fraction of copper. This means that the precipitates at this stage are much more enriched in zinc and magnesium

A ternary composition field showing the solute fractions for each of the precipitates analysed in material aged at 120°C compared to the solute fraction of the all the ions detected for this heat treatment.

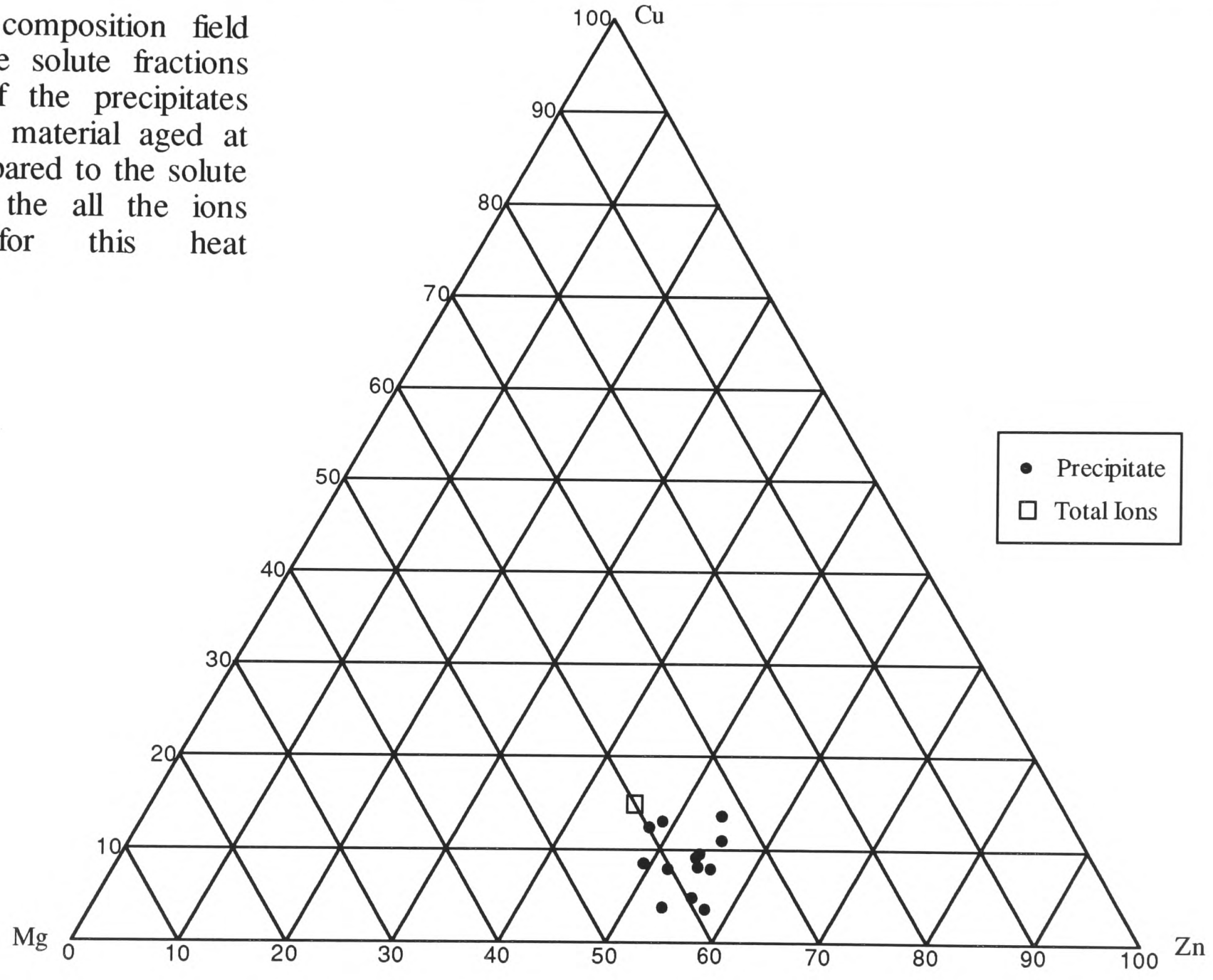

Figure 5.2

A ternary composition field showing the solute fractions for each of the precipitates analysed in material aged at 150°C compared to the solute fraction of the all the ions detected for this heat treatment.

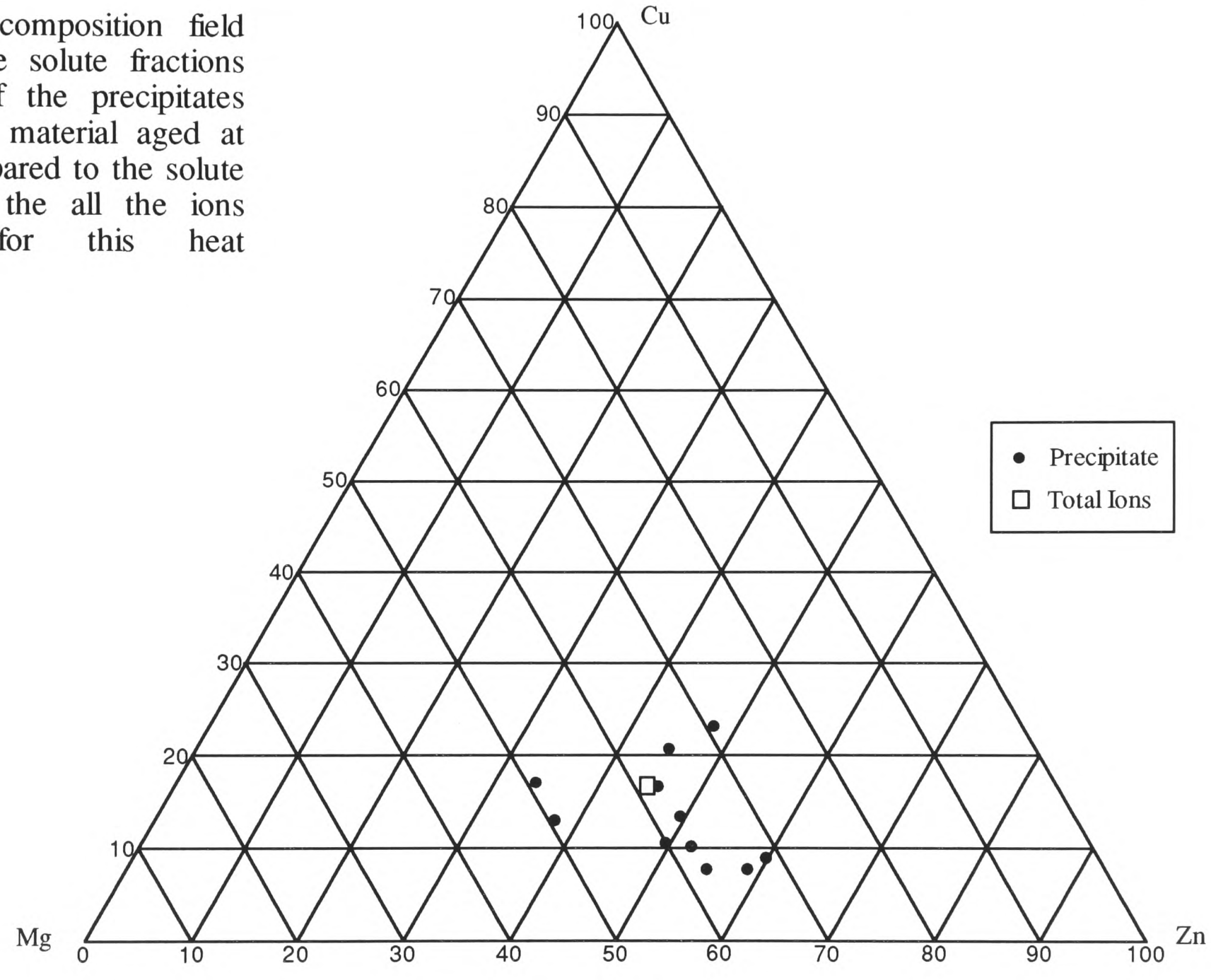

Figure 5.3.

A ternary composition field showing the solute fractions for each of the precipitates analysed in material aged at 180°C compared to the solute fraction of the all the ions detected for this heat treatment.

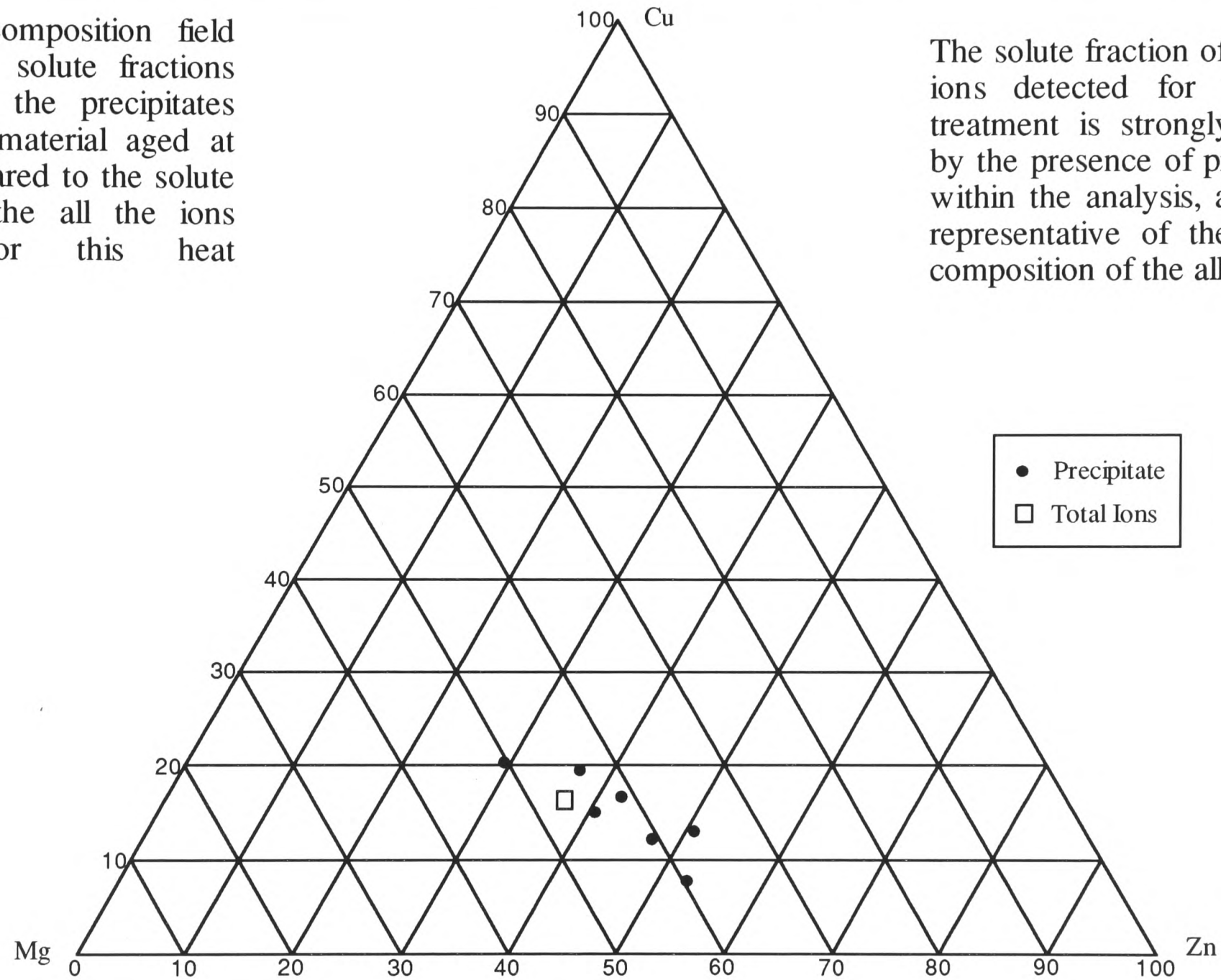

The solute fraction of all of the ions detected for this heat treatment is strongly affected by the presence of precipitates within the analysis, and is not representative of the average composition of the alloy.

Figure 5.4.

than copper. However, upon ageing at 150°C and 180°C the scatter of precipitate solute fractions increases. The precipitate compositions are scattered around the total average composition, but the average of the precipitate compositions shows an increase in the fractions of both magnesium and copper. For these larger precipitates, the proportion of solute in the precipitate is much greater than the proportion of solute in the matrix, and thus the average solute fractions of the precipitates must tend towards the average total solute fractions.

In summary, the copper solute fractions of precipitates aged at 120°C was found to be lower than in material aged at 150°C and 180°C. This agrees with the overall conclusion of previous work, that copper becomes more mobile at temperatures around 150°C. This temperature is also associated with a change in precipitate phase from η' to main η precipitates. These conclusions will be discussed in more detail in Chapter 7.

5.1.3. POSAP Matrix Precipitate Analysis.

POSAP analysis was described earlier in Section 4.1. Material from each of the heat treatments was analysed by POSAP analysis. The distribution of each solute species within the datablock was visualised in 3-D, and from this, it was possible to position a wire-frame box within the data to select just the volume of space corresponding to the precipitate, thus removing the solute contribution to the matrix solid solution. The composition of the precipitate can then be calculated by taking the average composition of the atoms positioned in that volume; or a profile of the variation of composition within the box may be calculated. POSAP analysis has the advantage of determining the aluminium content of the precipitates more accurately than AP analysis, but the disadvantages of lower mass resolution and reduced compositional accuracy, as described in Section 4.5.

Figures 5.6-5.8 show the total distributions of the solute species for each of the treatments analysed. The approximate size of the precipitates in each of the images is shown. The factors affecting the scale calibration of POSAP data have been discussed in detail in Section 4.5.4. These images obtained by POSAP analysis compare well

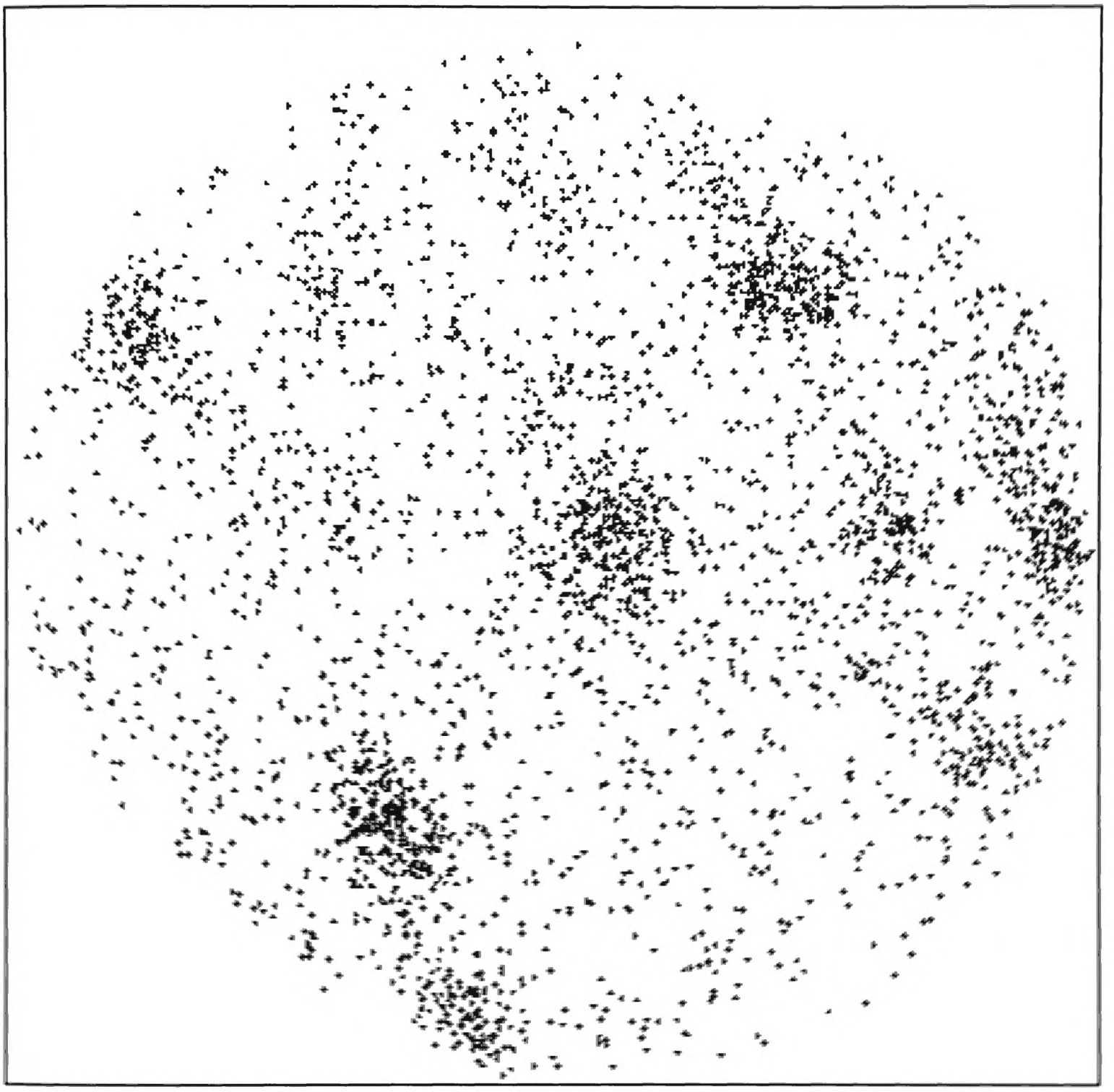

Distribution of all the solute ion species detected for an analysis of material aged at 120°C.

Figure 5.6

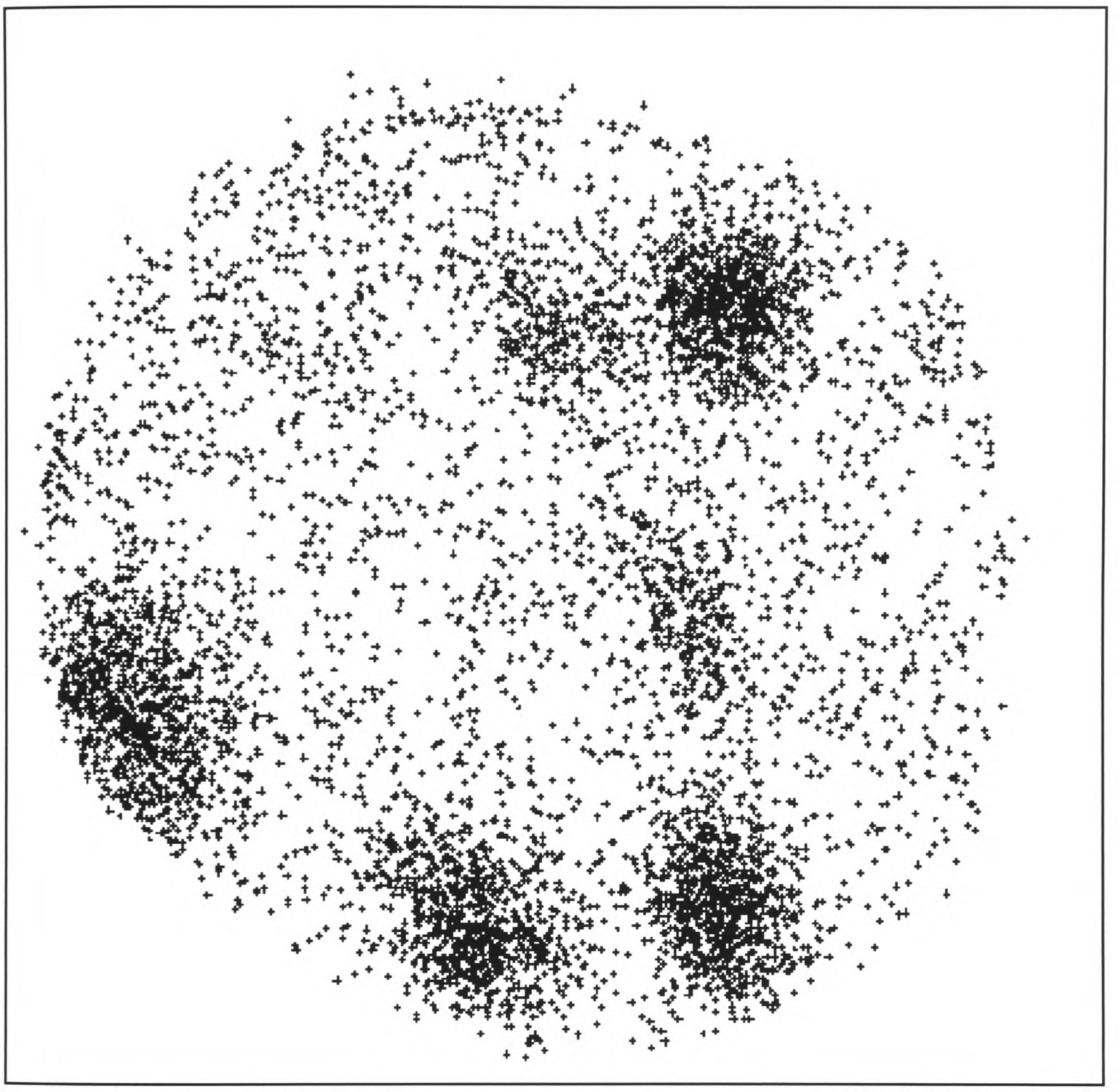

Diameter of area of analysis =25nm Depth of view =6nm

Precipitates are about 3.7–5.5nm

Distribution of all the solute ion species detected for an analysis of material aged at 150°C.

Figure 5.7

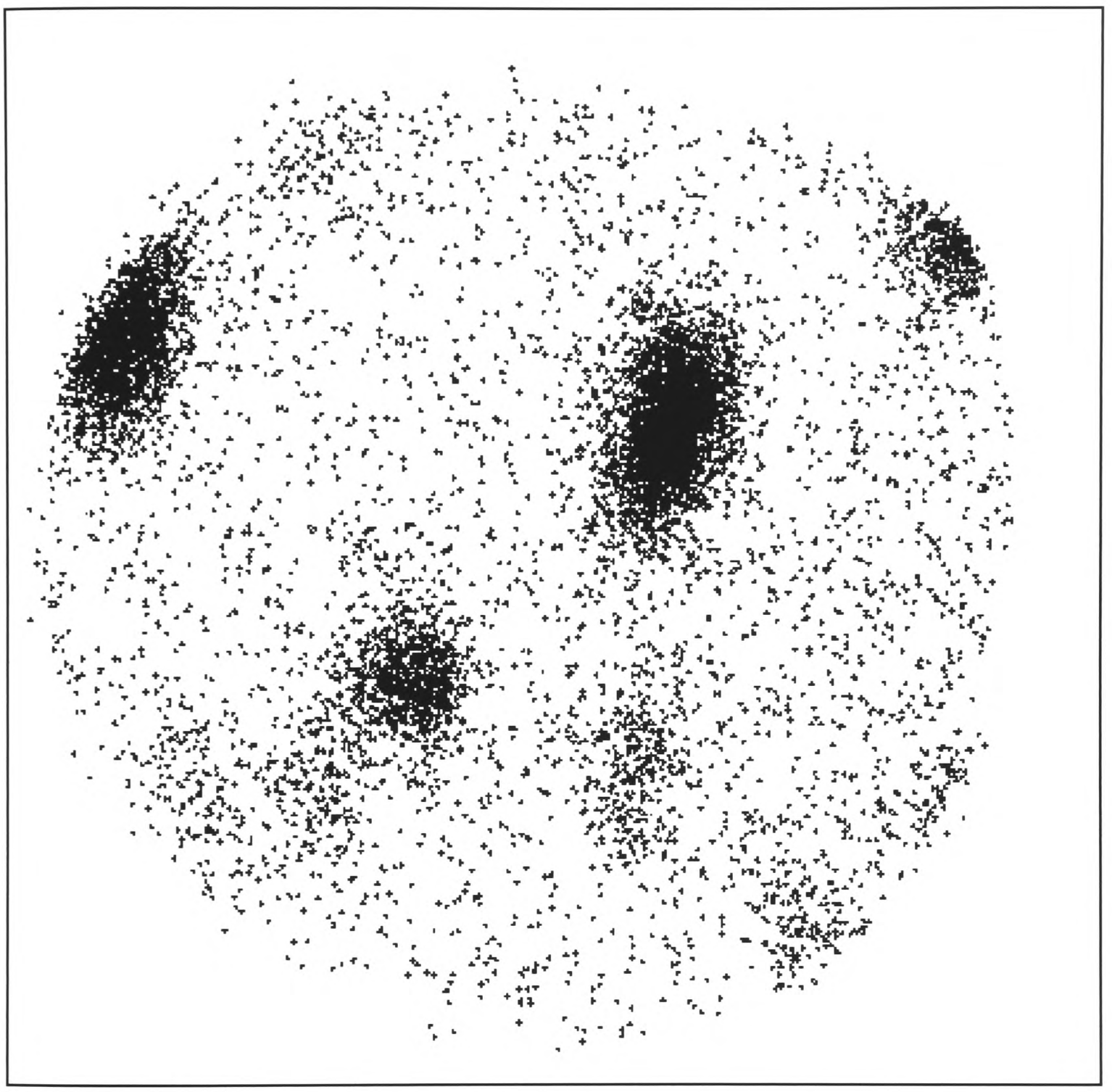

Diameter of area of analysis = 41.5nm Depth of view =6nm

Precipitates are about 4.6–9nm

Distribution of all the solute ion species detected for an analysis of material aged at 180°C.

Figure 5.8

with the TEM images of the same materials, shown in Figure 5.1, and the measured size of precipitates is very similar.

The distribution of different ion species (Mg^{+}, Mg^{2+}, Zn/Cu^{+}, Zn/Cu^{2+}) detected may be viewed separately, to show up quickly any differences in segregation behaviour. Figure 5.9 shows the separate solute ion species distributions for the 150°C material shown in Figure 5.7. To the first approximation, these images are very similar, each showing the presence of the precipitates in a matrix solid solution. It is not accurate to interpret compositional variations from just the images, due to variations in positioning density across an image.

In addition to any experimental factors that may affect the accuracy of the compositional information obtained, there is the conceptual difficulty of defining the composition of a precipitate on the atomic scale. The precipitates at this stage in the ageing process are metastable, and they do not have a precise stoichiometric composition. The early stage precipitates aged at 120°C do not show any crystallographic morphology in TEM, which suggests that they do not have a clearly defined interface with the matrix. The later stage precipitates aged at 150°C and 180°C both show signs of distinctive morphology, consistent with a semi-coherent or incoherent interface. The composition of a precipitate should ideally be the composition of the total precipitate, in order to avoid errors due to internal variations in composition, and also to maximise the statistical accuracy of the composition. Selecting all the precipitate but avoiding contributions from the surrounding matrix requires the definition of a precipitate interface. As described briefly in Section 4.1.3.2, the difference in solute levels between the precipitate and matrix regions are too low, and the scale of precipitation is too small, for accurate determination of the concentration isosurface of a precipitate. Calculating the composition of the atoms selected by a wireframe box is limited by the orthogonal geometry of the volume selected. If all the solute atoms associated with the precipitate are contained within the box, then a significant proportion of the surrounding matrix is also sampled. This means that the solute content may be quite accurate, but the aluminium content will be overestimated. If the selected volume is placed entirely within

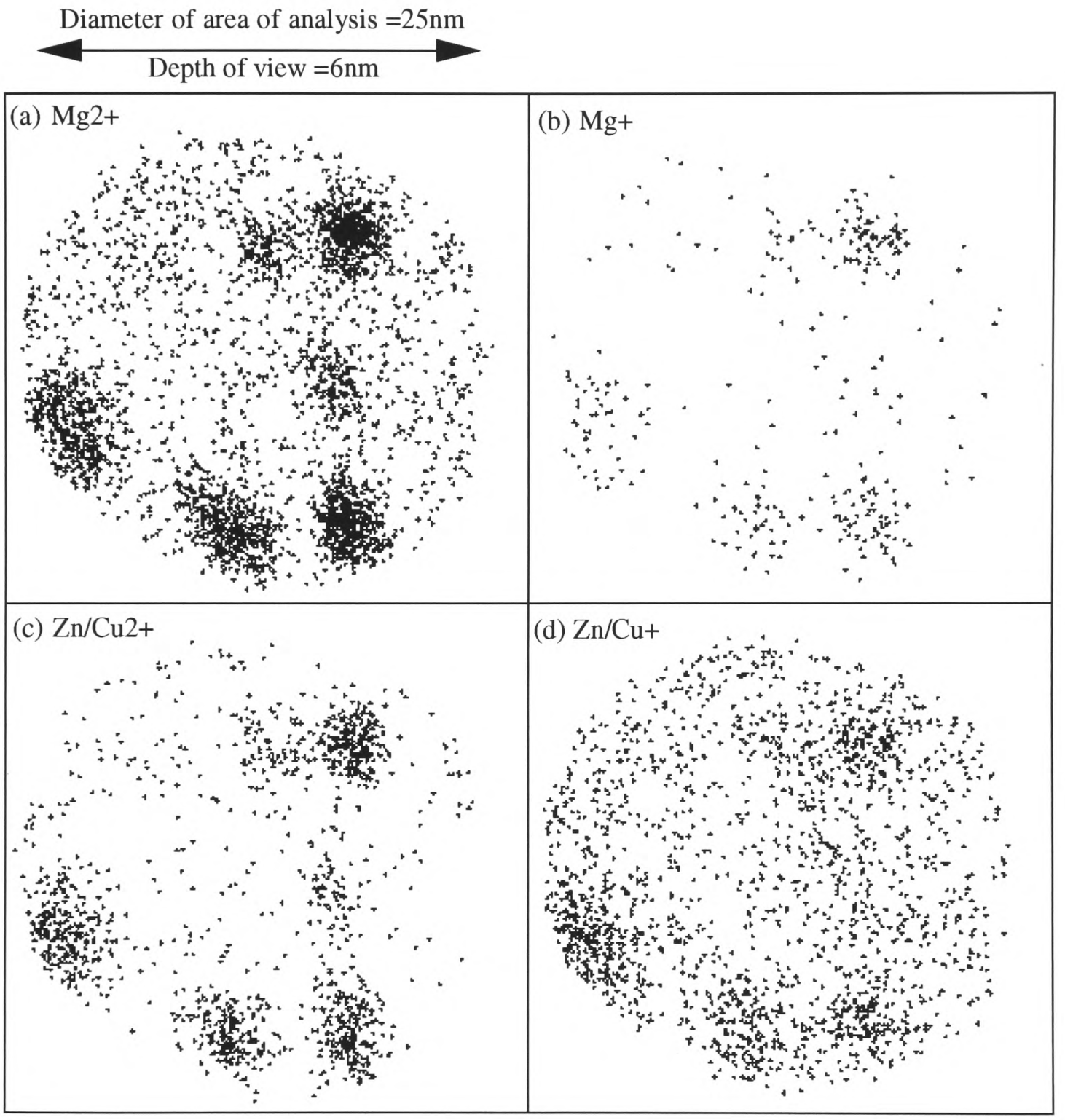

Atom distributions of the separate solute ion species detected.
(a) Mg2+ ions (b) Mg+ (c) Zn/Cu2+ (d) Zn/Cu+

Figure 5.9

the precipitate then the aluminium concentration of the precipitate may be determined quite accurately, but the solute content will only be representative of the whole precipitate if the composition is uniform. This all means that the size and position of the selected box can strongly affect the composition measured. Figure 5.10 shows the variation in compositions measured for one of the precipitates in Figure 5.7. An alternative method for determining the composition of a precipitate is to set the selected box to imitate conventional atom probe analysis and calculate a composition profile through the precipitate (Figure 5.11). The direction of the profile, and the area of the profile, may be controlled to ensure that the profile passes quickly from being totally in the matrix, to being totally in the precipitate. This is a good method in that it can show up clearly any interface segregation (which for these precipitates is negligible). However, only a small fraction of the precipitate atoms detected are sampled by this method and it does not necessarily give the total solute composition accurately. The three dimensional data should contain more information about solute distribution within the precipitate, but representing it clearly is a problem. Until better spatial resolution enables correlation of the 3-D data with the crystallography, extracting information about local variations in composition within a precipitate remains liable to error.

For analysis of the precipitates in each of these heat treatments, the solute content is defined in terms of the total solute fractions of (Zn/Cu) and Mg in the precipitate. The aluminium content of the precipitate is defined as the average aluminium content in the centre of the precipitate, thus giving a measure of the solute enrichment.

The composition of the selected volume can only be calculated from the positioned atoms. As discussed in Section 4.5.1, the relative lack of positioning of the (zinc/copper) means that the calculated composition will be too low. This can be corrected by assuming uniform %positioning through the volume of analysis. Table 5.3 shows the effect of correction of the composition, to take into account the total % positioning of the datafile.

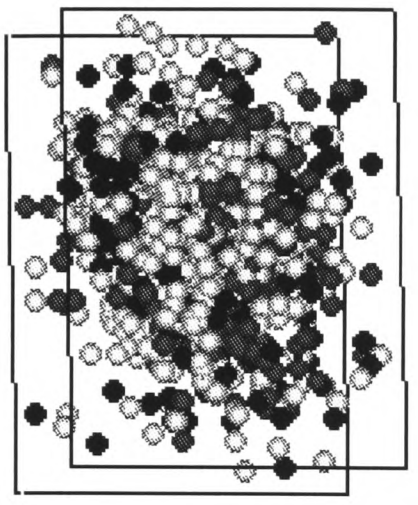

Atoms contained		Composition atomic%		Zn/Mg
3167	Al	80.5	Al	
374	Zn	9.5	Zn	0.76
494	Mg	12.5	Mg	

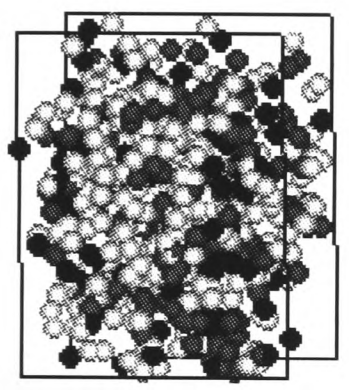

1627	Al	69.3	Al	
313	Zn	13.3	Zn	0.77
407	Mg	17.3	Mg	

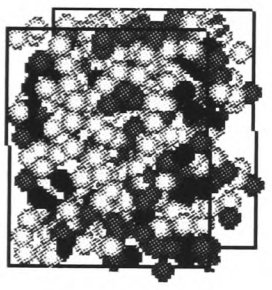

837	Al	63.9	Al	
144	Zn	11.0	Zn	0.44
329	Mg	25.1	Mg	

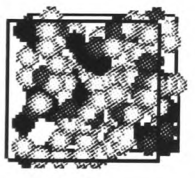

121	Al	43.2	Al	
63	Zn	22.5	Zn	0.66
96	Mg	34.3	Mg	

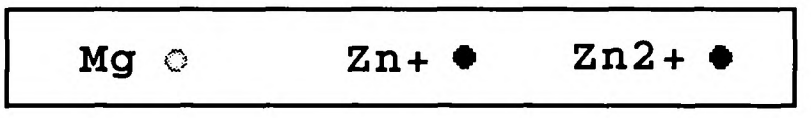

Figure 5.10 showing the method of calculation of the composition of a precipitate. The composition shown here is calculated from just the positioned atoms. The precipitate is more magnesium rich in the centre.

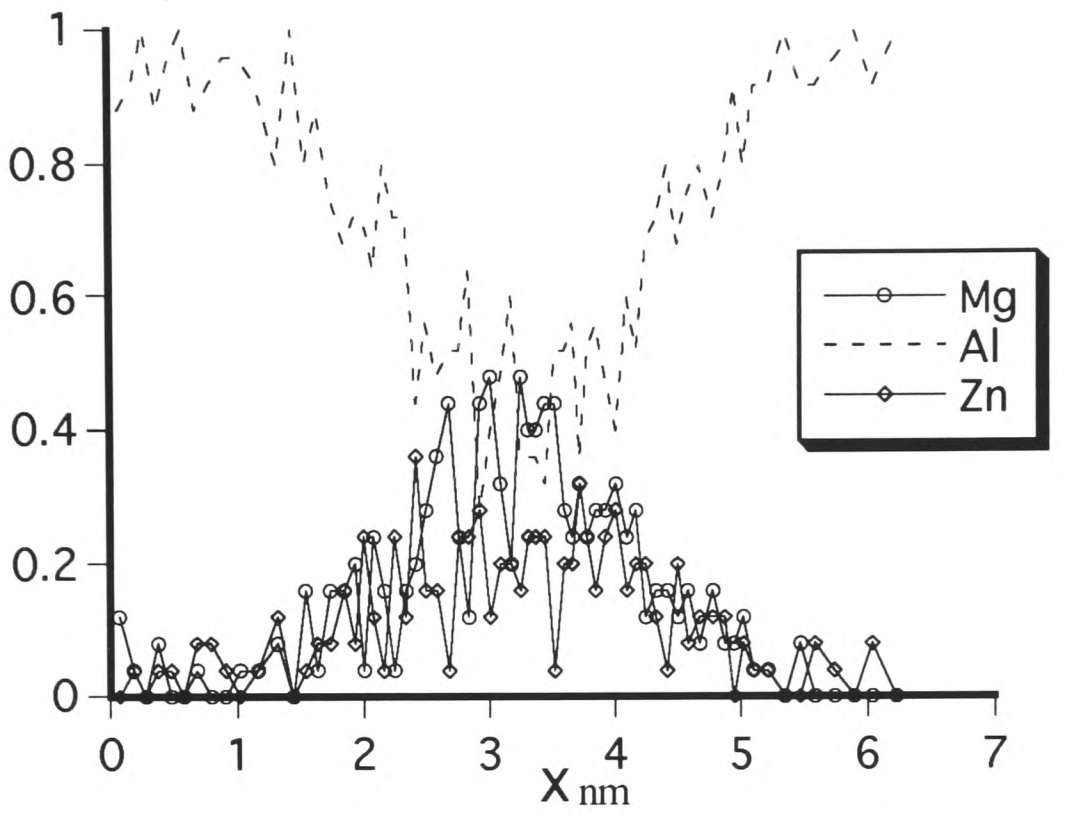

Figure 5.11.showing the composition profile aligned through the precipitate.

Atoms	Box 1	Box 2	Box 3	Box 4
Al	3167	1627	837	121
Zn	374	313	144	63
Mg	494	407	329	96
%Composition	Box 1	Box 2	Box 3	Box 4
Al	0.78	0.69	0.63	0.43
Zn	0.09	0.13	0.10	0.23
Mg	0.12	0.17	0.25	0.34
	Positioning	Statistics		
	Al	0.847		
	Zn	0.557		
	Mg	0.781		
Corrected %	Box 1	Box 2	Box 3	Box 4
Al	0.74	0.64	0.59	0.38
Zn	0.13	0.19	0.15	0.30
Mg	0.12	0.17	0.25	0.32

Table 5.3 showing effect of correction for positioning statistics.

Figures 5.12-5.14 shows the ternary composition fields for the precipitates in each of the heat treatments. The compositions are calculated using the central %Al and the total solute fractions of Zn/Cu and Mg.

This shows that there is a general densification of the precipitates upon ageing at higher temperatures but there is no obvious change in the ratio of zinc to magnesium.

Considering the variation of solute distribution within the precipitates it can be seen from Figure 5.10 (previously) that as the size of the box is decreased there is a decrease in the zinc to magnesium ratio. This was observed to be true for almost all of the precipitates analysed, in all heat treatments. For each treatment, Figure 5.15 shows the Zn:Mg ratio at the centre of the precipitate divided by the Zn:Mg ratio of the total precipitate, plotted against the %Al at the centre. The values obtained were consistently less than unity. This suggests that there is relatively more magnesium at the centre of the precipitate compared to the zinc/copper. This can be explained by a variety of theories.

i It could be an ion trajectory effect of local magnification at the precipitate. The zinc species are slower to accelerate away from the specimen, thus they may be deflected more by local field variations. If this were true, then the spreading of the zinc should only be perpendicular to the probe direction; however, analysis of this effect, both parallel and perpendicular to the probe direction, showed no obvious difference.

ii It could be a positioning effect, whereby the zinc at the centre of the precipitate is more likely to occur as double events, due to a higher proportion of Zn-Zn bonds.

iii It could be a real effect, that magnesium is slightly cored to the centre of the precipitate, or alternatively, that there is zinc or copper at the edge of the precipitate. The problem of not being able to separate the copper and zinc species makes this rather confusing.

Since there are many possible explanations for what is a small but repeatable effect, I shall leave it to further work to decide the real reason for this effect.

A ternary composition field showing the solute fractions for each of the precipitates analysed by POSAP analysis in material aged at 120°C.

The solute fractions have been calculated by taking the minimum aluminium content at the centre of the precipitate and the ratio of the total solute content Mg: (Zn/Cu).

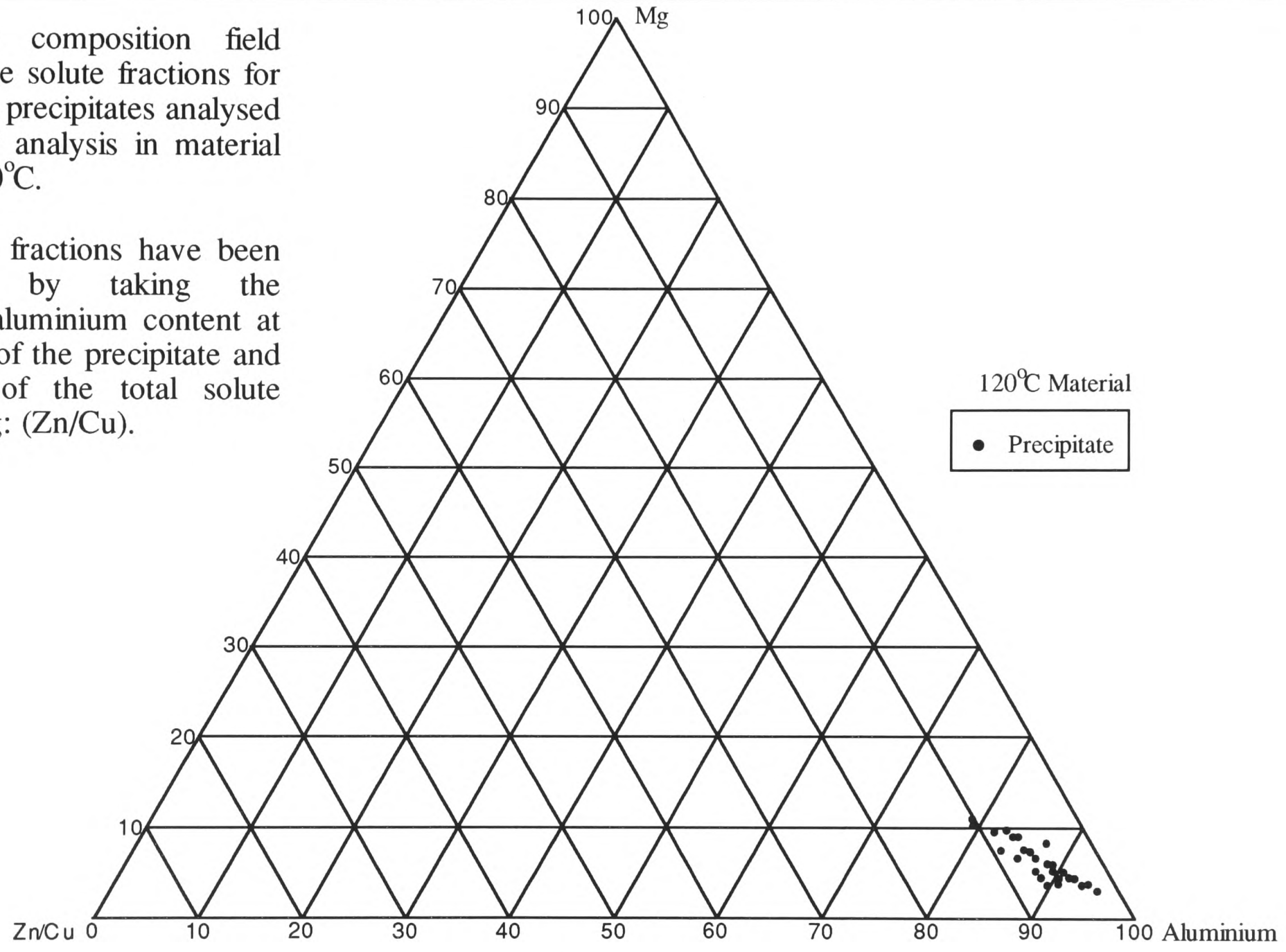

Figure 5.12

A ternary composition field showing the solute fractions for each of the precipitates analysed by POSAP analysis in material aged at 150°C.

The solute fractions have been calculated by taking the minimum aluminium content at the centre of the precipitate and the ratio of the total solute content Mg: (Zn/Cu).

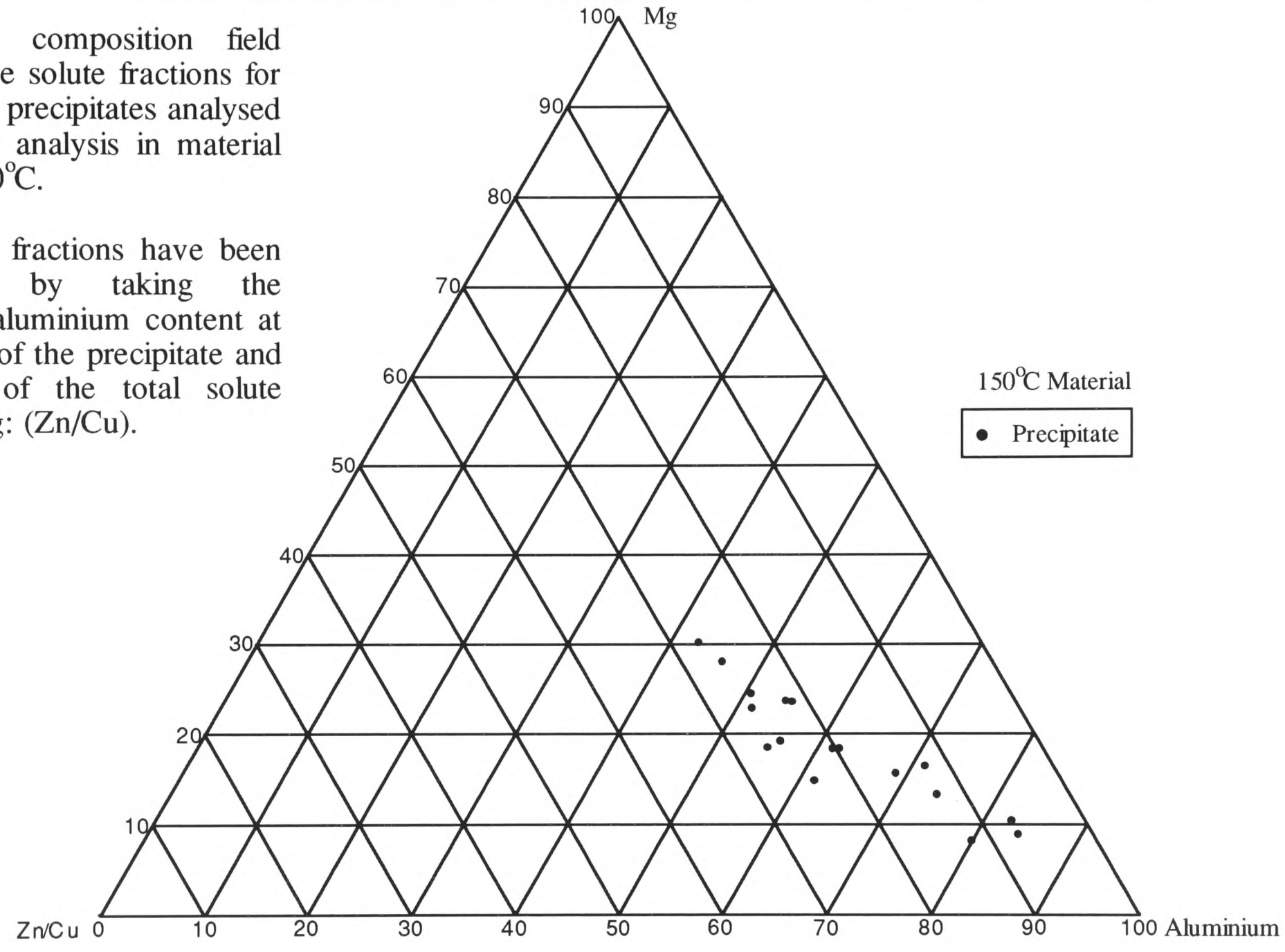

Figure 5.13

A ternary composition field showing the solute fractions for each of the precipitates analysed by POSAP analysis in material aged at 180°C.

The solute fractions have been calculated by taking the minimum aluminium content at the centre of the precipitate and the ratio of the total solute content Mg: (Zn/Cu).

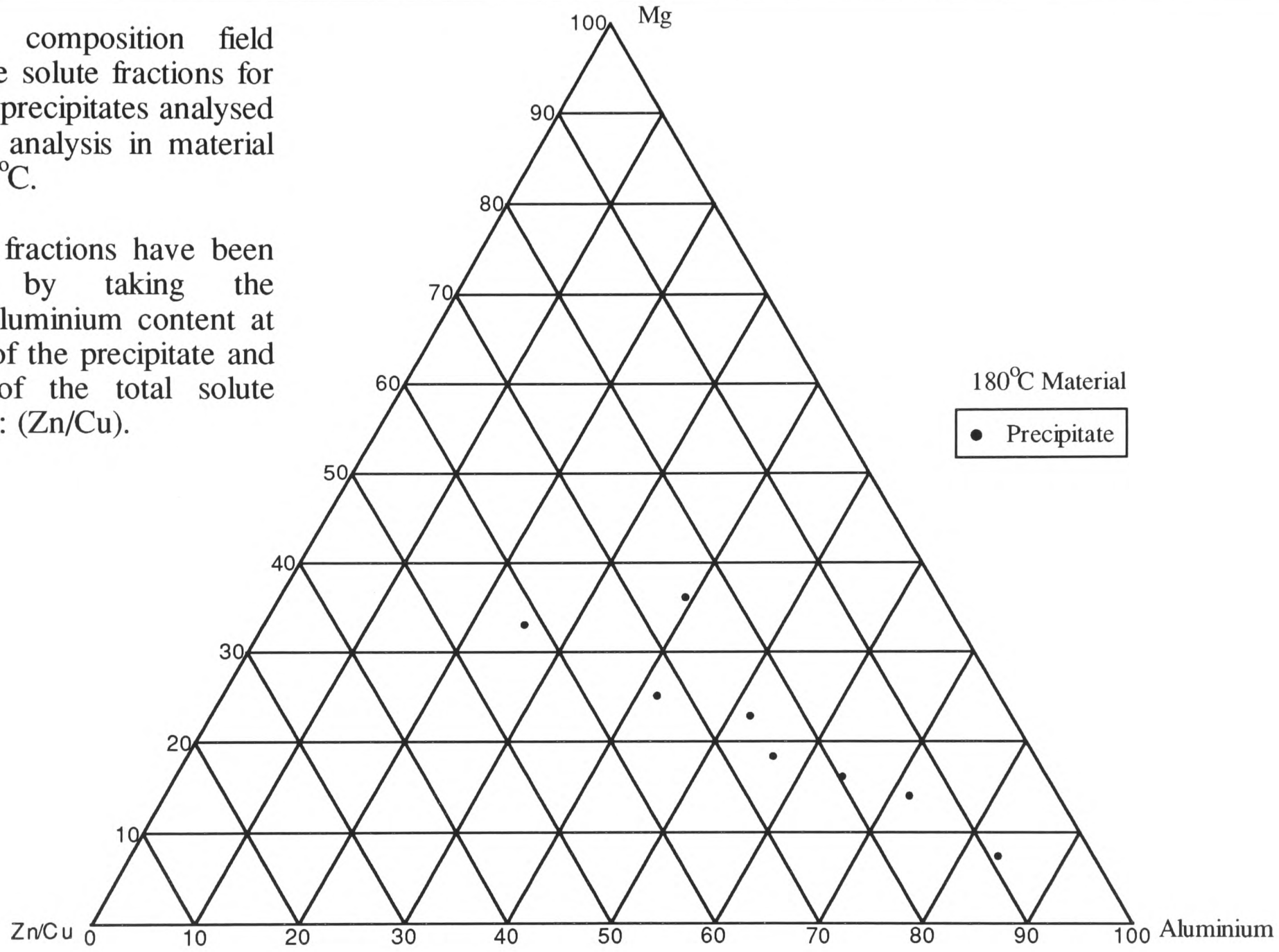

Figure 5.14

a) plot showing coring of magnesium at the centre of the precipitates in material aged at 120°C.

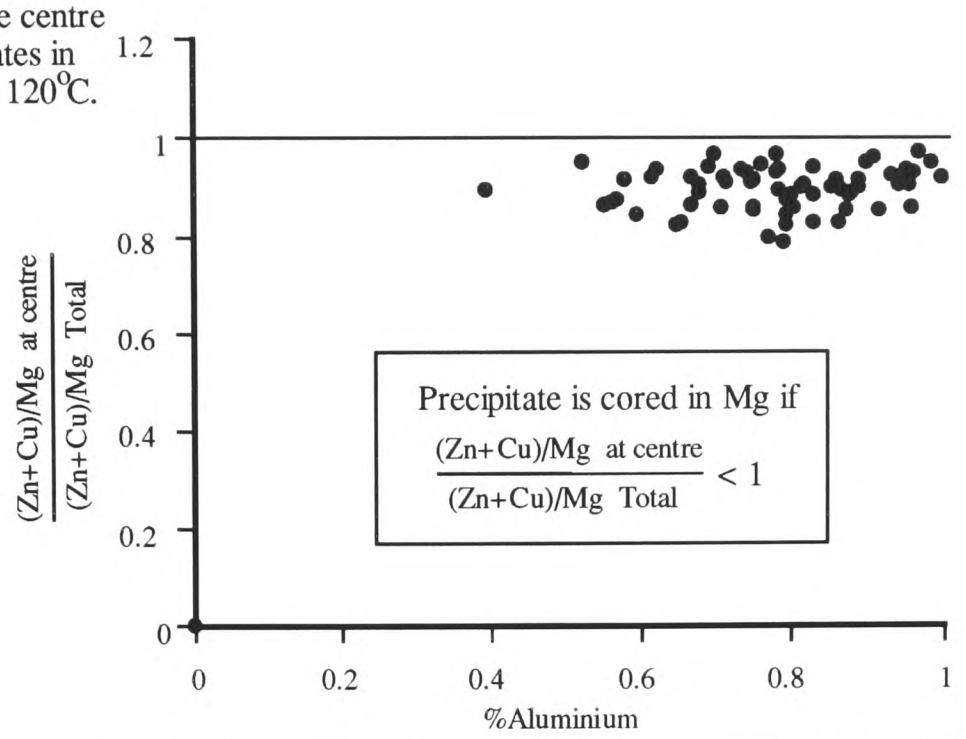

b) plot showing coring of magnesium at the centre of the precipitates in material aged at 150°C.

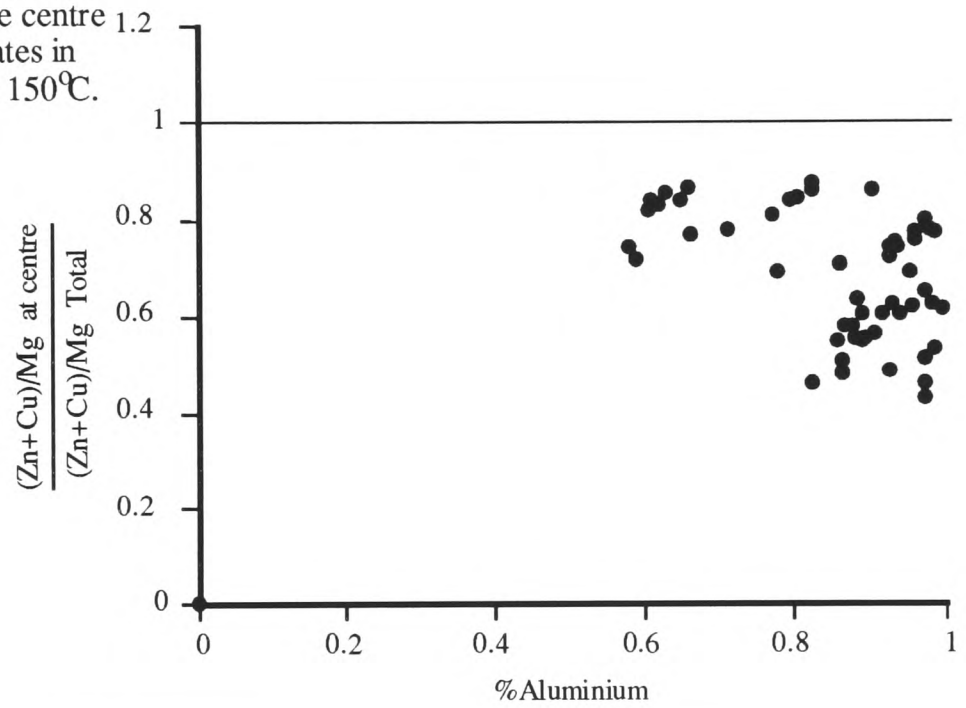

c) plot showing coring of magnesium at the centre of the precipitates in material aged at 180°C.

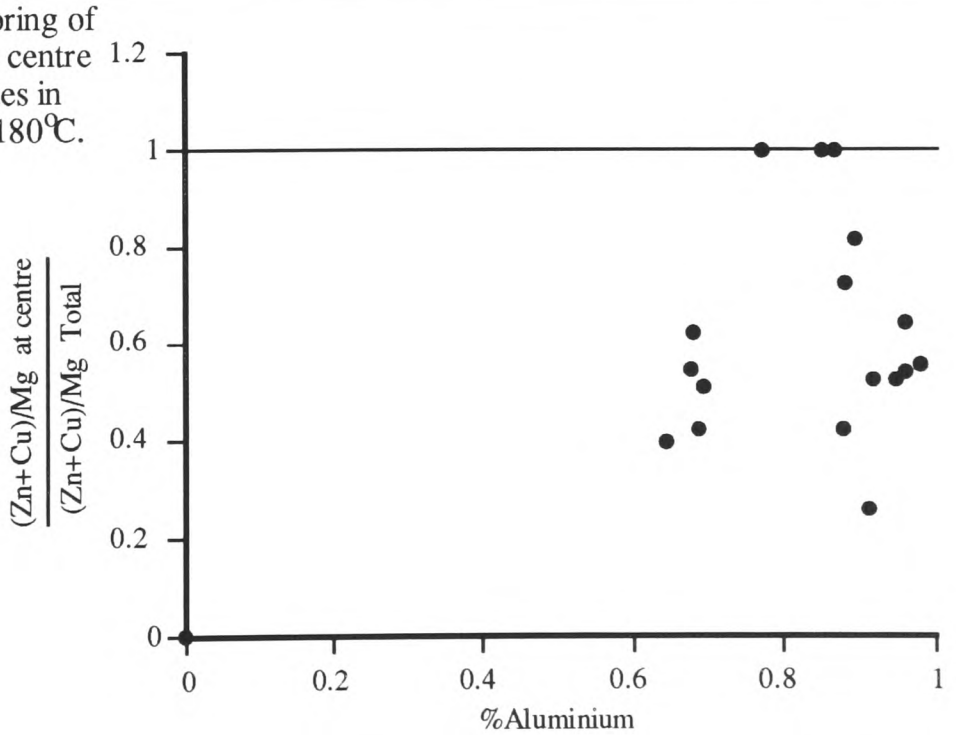

Figure 5.15

Conclusions

Visual comparison of the distribution of solute for each treatment compares well with the TEM images. The precipitates in the material aged at 120°C appear diffuse, and have a low solute content without clear morphology, whilst the precipitates in the material aged at 150°C and 180°C are larger and more clearly defined and some of them show specific morphologies.

The precipitates show a clear increase in total solute content with increasing ageing temperature, however there seems to be no change in the Zn/Cu to Mg ratio (in agreement with the AP data). The precipitates all seem to show slight enrichment of magnesium at the centre of the precipitate relative to the zinc/copper. This effect is very slight and subject to much scatter and there is a significant possibility that it is an experimental artefact.

5.1.4. Comparison of AP and POSAP levels detected.

Let us first consider the absolute levels of solute detection by AP and POSAP analysis techniques. The atom probe compositions were found to be about 80% of the specification values, which suggests that atom probe analysis conditions of 70K and 15% pulse fraction do not seem to result in gross underestimates of solute content, as found for the Al-Li system[88]. Unfortunately, this contradicts the findings of POSAP investigations of accuracy of solute detection described in Section 4.5.3, which found that both zinc and magnesium concentrations for analyses at 70K and 20% pulse fractions, after positioning correction, were still about 50% too low due to preferential evaporation effects. The difference in evaporation rate between POSAP and AP analyses should not be sufficient to account for this discrepancy. A possible explanation for the higher composition levels detected in atom probe analysis might lie in the higher than usual noise counts, often occurring as multiple detection events on a single pulse.

(Subsequently this was traced to secondary electron generation around the AP detector resulting in noise time correlation so the absolute composition levels are dubious.)

5.2. Grain Boundary Precipitate Analysis.

The strength of Al-7150 is derived mostly from the interaction of dislocations with the matrix strengthening precipitates, however as discussed in Chapter 1 the primary cause of failure at peak strength is intergranular Stress Corrosion Cracking. Many diverse theories have been postulated for the reason why peak aged grain boundaries are sensitive to SCC, while overaged grain boundaries are insensitive. The chemistry of the grain boundary regions (precipitate, grain boundary and PFZ) must be different in the different treatments, and to date, no microstructural parameter has been proven to control the SCC susceptibility. Thus accurate information about the chemistry of grain boundary regions is highly desirable, either to show a clear dependence of SCC upon a particular change in local chemistry, or to provide chemical information which enhances our knowledge of the atomic scale processes occurring at a grain boundary during ageing of 7150.

This section presents the results of chemical analysis of the grain boundary precipitates after heat treatments at 120°C, 150°C and 180°C. Due to the difficulty of locating a grain boundary within the region available to atom probe analysis (Section 2.2.2), too few analyses were achieved to enable comparison of grain boundary precipitate chemistry between the different heat treatments. Therefore the atom probe grain boundary analyses will be presented in the section on grain boundary chemistry in Chapter 6.

5.2.1. TEM Grain Boundary Precipitate Analysis.

Figure 5.16 shows TEM micrographs of the grain boundary regions in each of the heat treatments. Other workers have failed to correlate precipitate shape, size, number per unit area or type with the SCC susceptibility[94]. The grain boundary structures were found to vary widely within the same material, however high angle grain boundaries did tend to have cap-like precipitate morphologies ,like the precipitate in figure 5.16.c, rather than clearly rod- or plate-like morphologies oriented at an angle to the boundary.

a) Grain boundary region in material aged for 100hours at 120°C.

b) Grain boundary region in material aged for 20hours at 150°C.

c) Grain boundary region in material aged for 8hours at 180°C.

Figure 5.16.

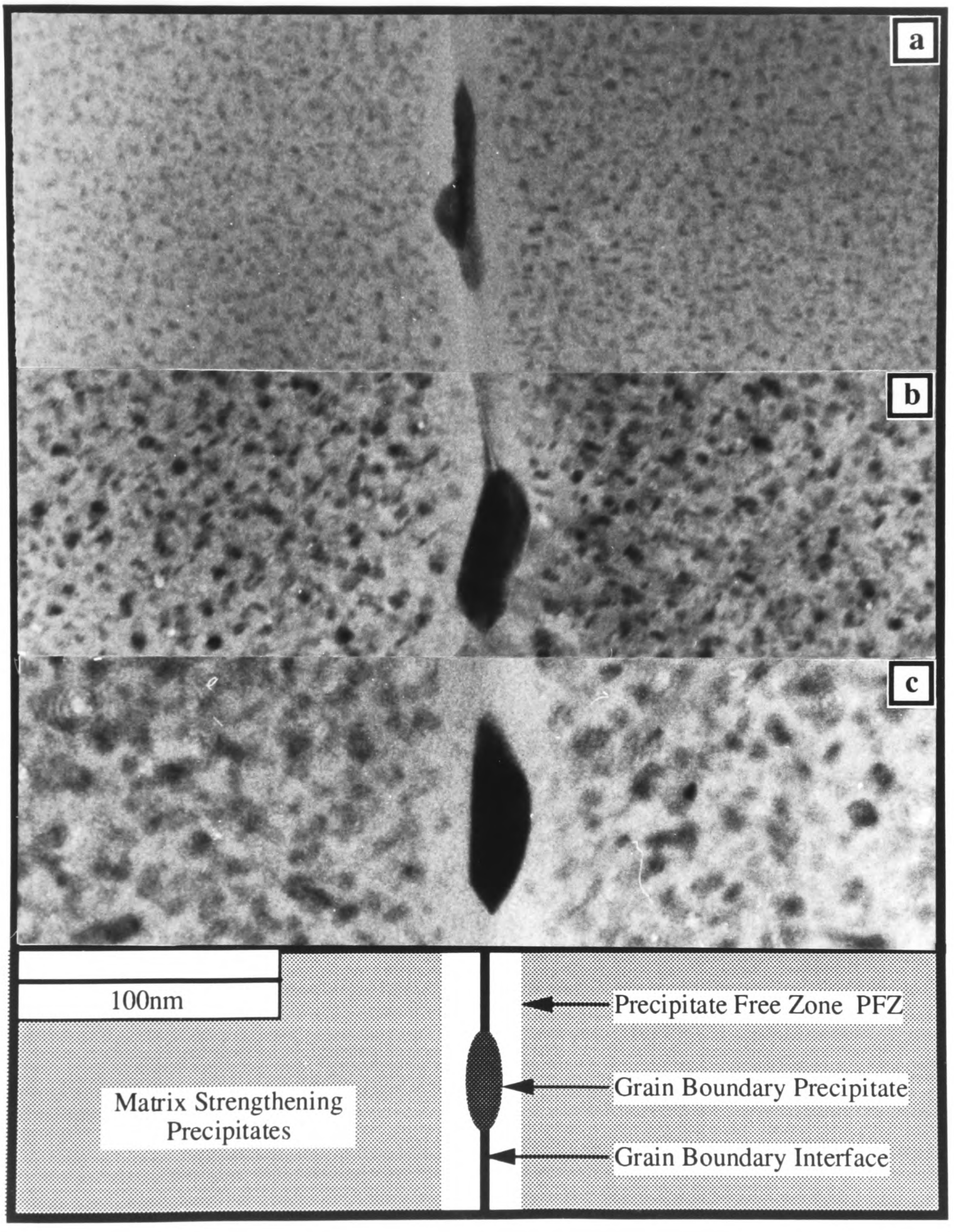
a
b
c
100nm
Precipitate Free Zone PFZ
Grain Boundary Precipitate
Grain Boundary Interface
Matrix Strengthening
Precipitates

5.2.2. STEM Grain Boundary Precipitate Analysis.

For X-ray analysis of precipitates simple spot analyses were taken by placing the probe directly over the image of a precipitate. This generates X-rays from both the precipitate and the matrix. Since the foil thickness varies and the precipitate sizes vary, it is not possible to separate the contributions from precipitate and matrix. A method of precipitate analysis is given by Lorimer et al.[95]

Lorimer Method

Analysis is by integration through the foil thickness and any exposed precipitates are preferentially dissolved during specimen preparation, thus it is not possible to analyse precipitates in this material without a contribution from the surrounding matrix. Lorimer pointed out that the resultant composition will lie on a line between the actual precipitate composition and the actual matrix composition. If the matrix material is pure A, and the precipitate contains A, B and C, then with enough analyses, the ratio of precipitate to matrix becomes irrelevant. If the %B and %C is plotted against the %A for many different precipitate analyses, then extrapolation can be used to give the possible stoichiometric equilibrium phase compositions (eg. ABC, A_2BC_3). This involves several assumptions. Firstly, the matrix material should contain a negligible concentration of the solute elements involved in the precipitate. Secondly, the precipitate is assumed to be an equilibrium phase, such that all of the precipitates analysed have the same composition, and it is only the contribution of the matrix that is complicating matters.

For this alloy system, predicting a precipitate stoichiometry for the early stages of precipitation is not really applicable, since the precipitates are known to be non-equilibrium. Also the matrix material is known to contain significant levels of solute at this early stage in the precipitation. Figure 5.17 shows the plots for the grain boundary precipitate analyses. The 180°C data shows a quite good fit to the model, but the 150°C and 120°C data show progressively worse scatter, due to the effect of higher matrix

a) 180°C Material. The precipitate data fits this method of representation well.

b) 150°C Material. The precipitate data shows slightly more scatter for this material especially in the copper due to thicker surface deposition.

c) 120°C Material. The precipitate data for this material shows a lot of scatter especially in the copper. The contribution from the precipitates is smaller in comparison to the contribution from the surface deposition.

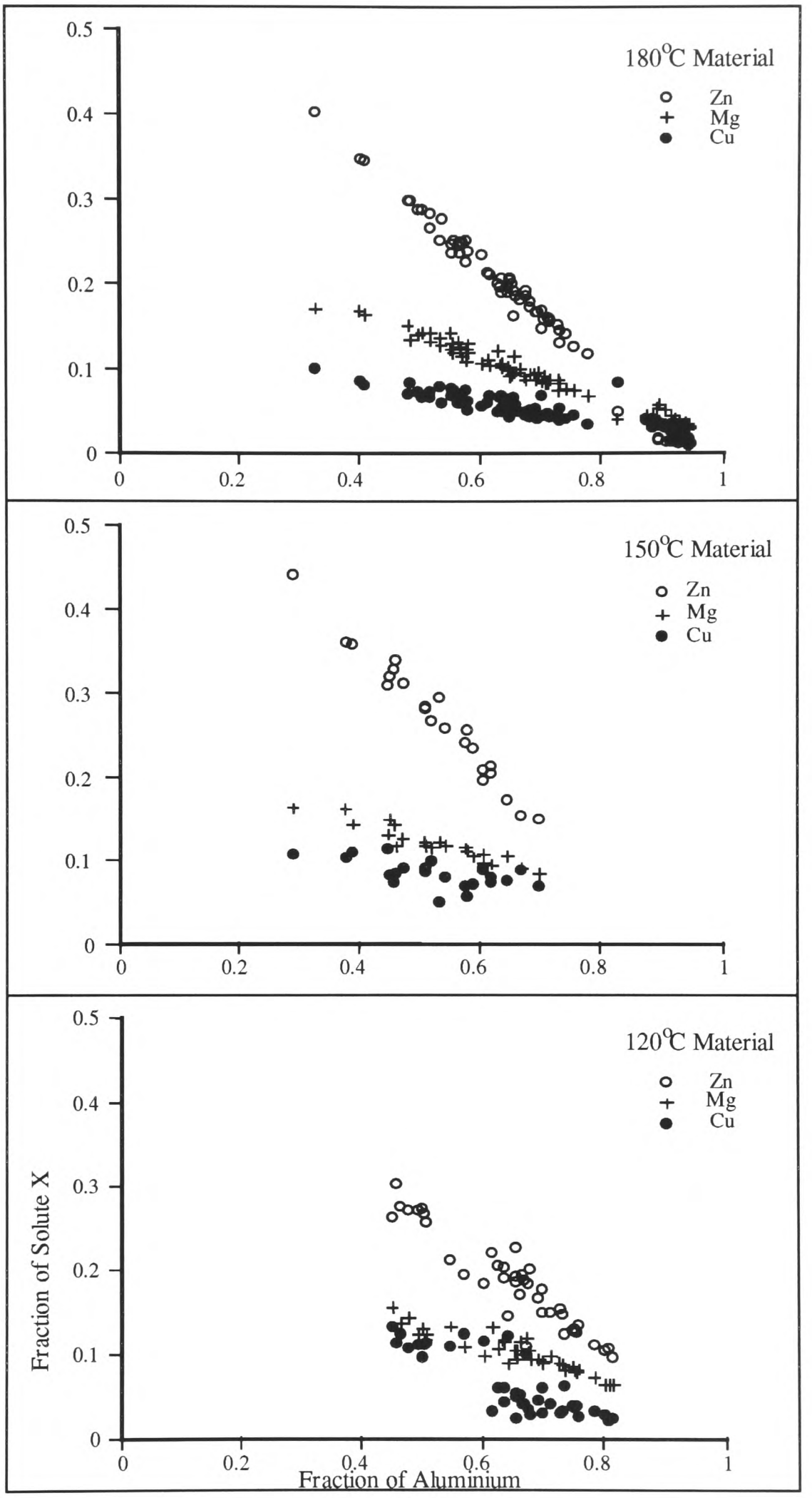

The Lorimer method of plotting the solute levels against the total aluminium content for all the precipitates to give the precipitate stoichiometry.

Figure 5.17

solute and lower precipitate solute levels causing this method of representation to become confused. Figure 5.18 shows the similar plot for solution treated material; the effect of the surface deposition of the copper is very clear. The surface copper will greatly increase the scatter of copper levels detected in the grain boundary precipitates. The absolute levels of solute detected are also subject to errors, as discussed in Chapter 2 thus the extrapolation of the lines will not be very accurate. One useful bit of information that can be estimated from this representation, is that the precipitates are likely to contain more than 30% aluminium, since none of the analyses observed contained less than 30% aluminium.

Ternary Composition Fields.

An alternative representation of compositional information from the precipitates is to remove the major effect of the aluminium content, varying with precipitate size and foil thickness, by calculating the solute fractions for each solute element. Again it is necessary to assume negligible solute concentrations in the matrix material. Since there are three solute elements, the compositional data may be most easily represented on a ternary composition field diagram.

Figure 5.19 shows the ternary composition field for solution treated material. This clearly shows the effect of copper surface deposition. The additional point shows the composition as actually measured using EPMA, which was within the limits of the alloy specification. The amount of copper present deposited on the surface of the specimen far outweighs the total solute content for this specimen. The difference between the position of the extrapolation of the STEM data, and the more accurate EPMA, can be explained by the combination of peak overlap effects increasing the Mg content observed, and also the lack of use of the Cliff-Lorimer correction factors.

Figures 5.20-5.22 show the ternary composition fields for the grain boundary precipitates for material aged at 120°C, 150°C and 180°C. Material aged at 120°C has smaller grain boundary precipitates surrounded by a high matrix solute content, thus the scatter of the solute fractions is larger. Figure 5.23 compares the PFZ and GB

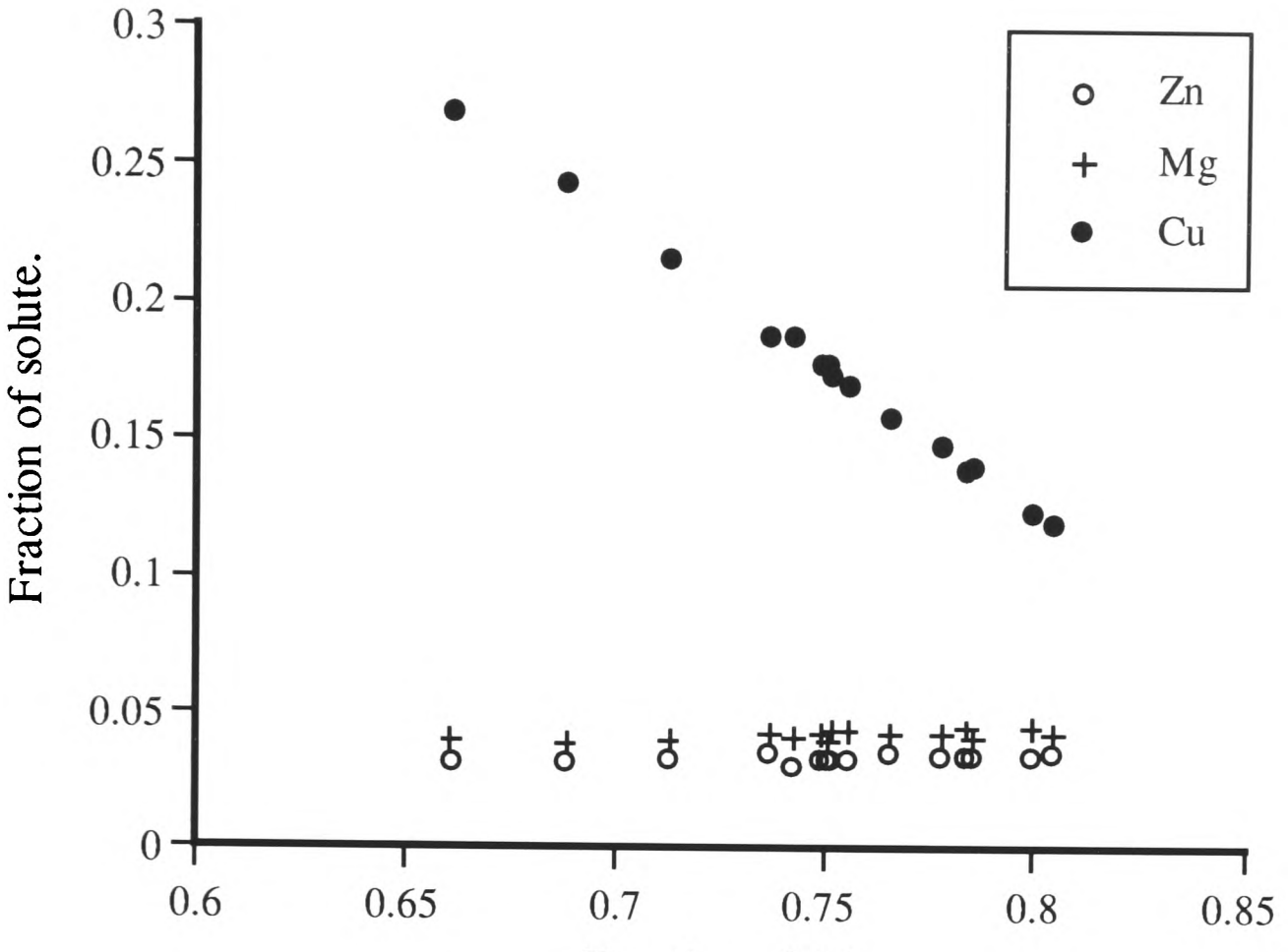

Plot of analyses of solution treated material by the Lorimer method. This clearly shows the effect of surface deposition of copper on the calculated compositions. The specimen thickness was not determined for each analysis position however the higher copper levels correspond to the thinner regions of the specimen such that the relative effect of the surface deposition is greater.

Figure 5.18

A ternary composition field showing the solute fractions for each of the solution treated material analyses.

Clearly the contribution of the surface copper greatly exceeds the true solute levels as detected by Electron Probe Micro- Analysis.

The extrapolation of the line through the analyses shows that there is relatively more magnesium detected than zinc. This is due to the lack of peak overlap correction and lack of Cliff-Lorrimer factor corrections as discussed in Chapter 3.

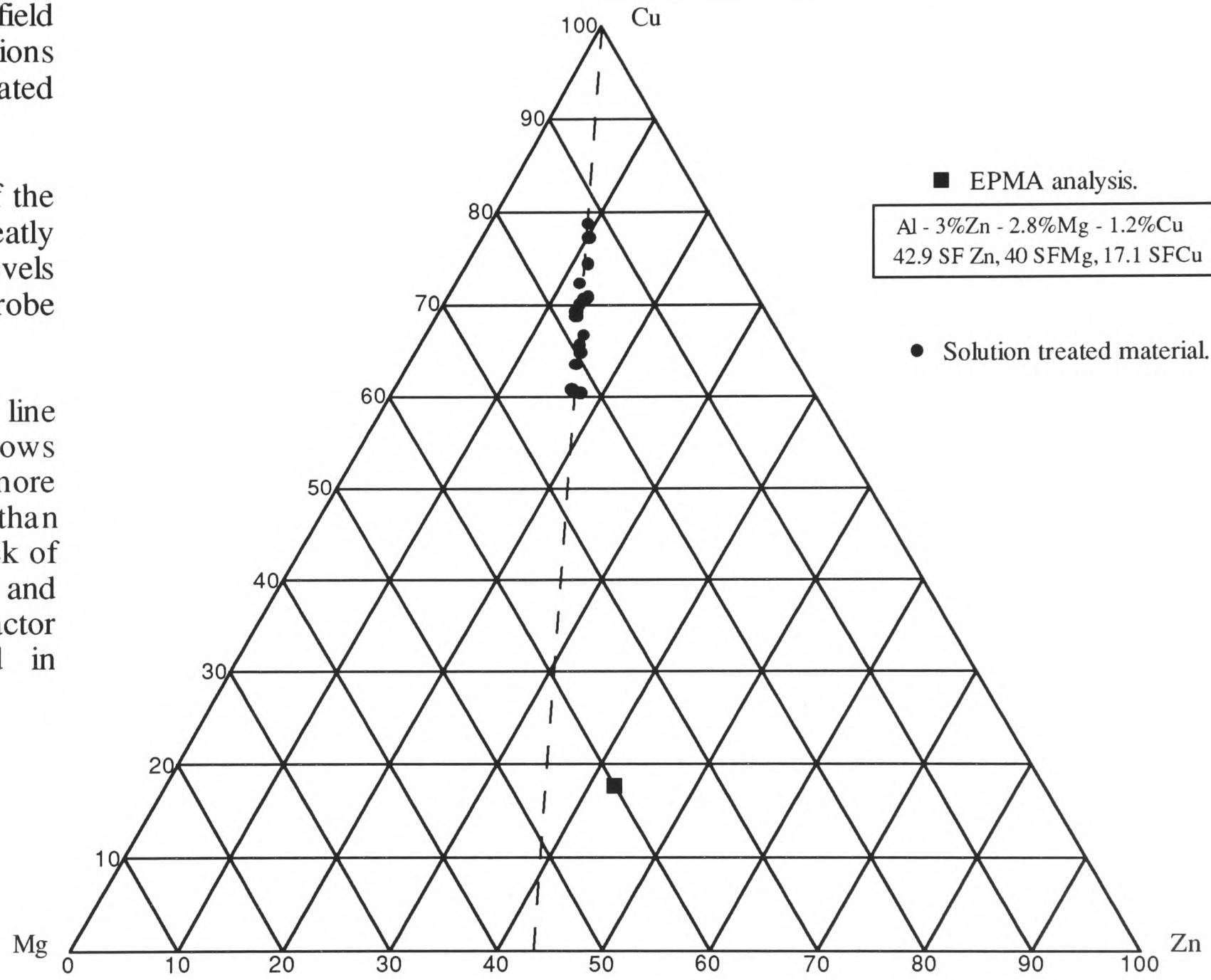

Figure 5.19

A ternary composition field showing the solute fractions for each grain boundary precipitate analysed in 120°C material.

There is a large scatter in the solute fractions detected. This scatter in mostly a variation in copper levels detected mainly due to the effect of surface deposition of copper.

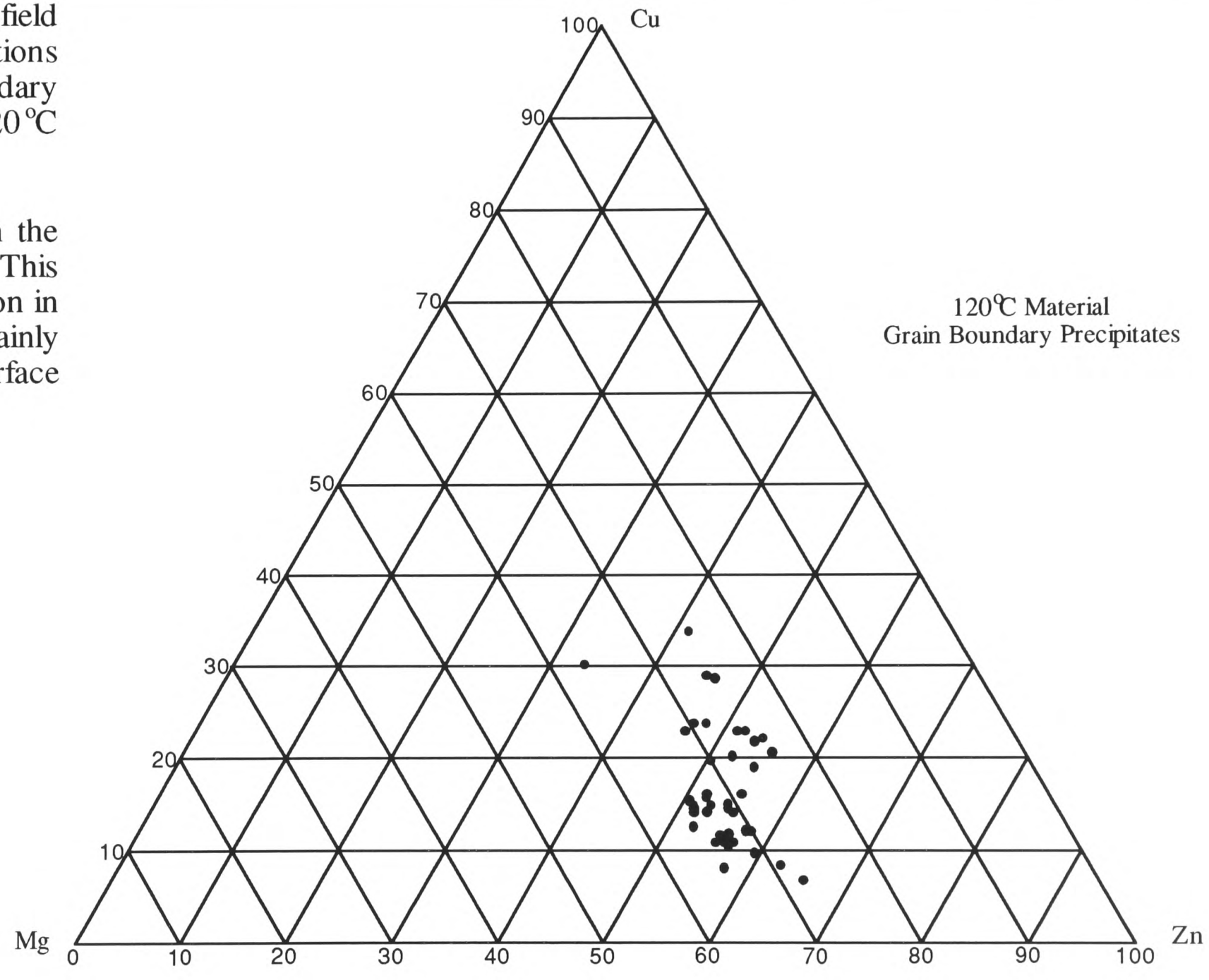

Figure 5.20

A ternary composition field showing the solute fractions for each grain boundary precipitate analysed in 150 °C material.

There is less scatter in the solute fractions detected than in the 120 °C material data however the scatter in still mostly a variation in copper levels detected.

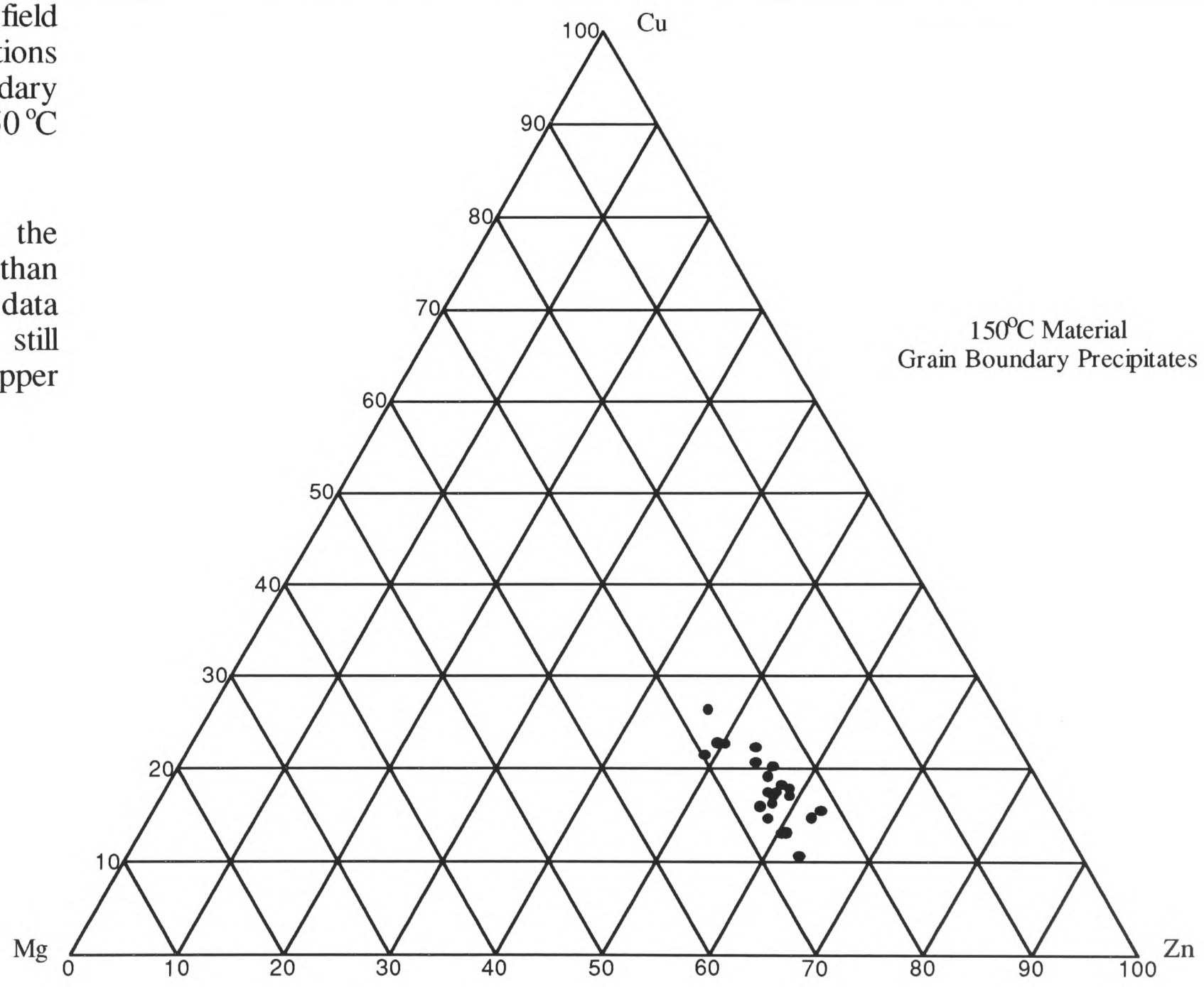

Figure 5.21

A ternary composition field showing the solute fractions for each grain boundary precipitate analysed in 180 °C material.

There is very little scatter in the solute fractions detected.

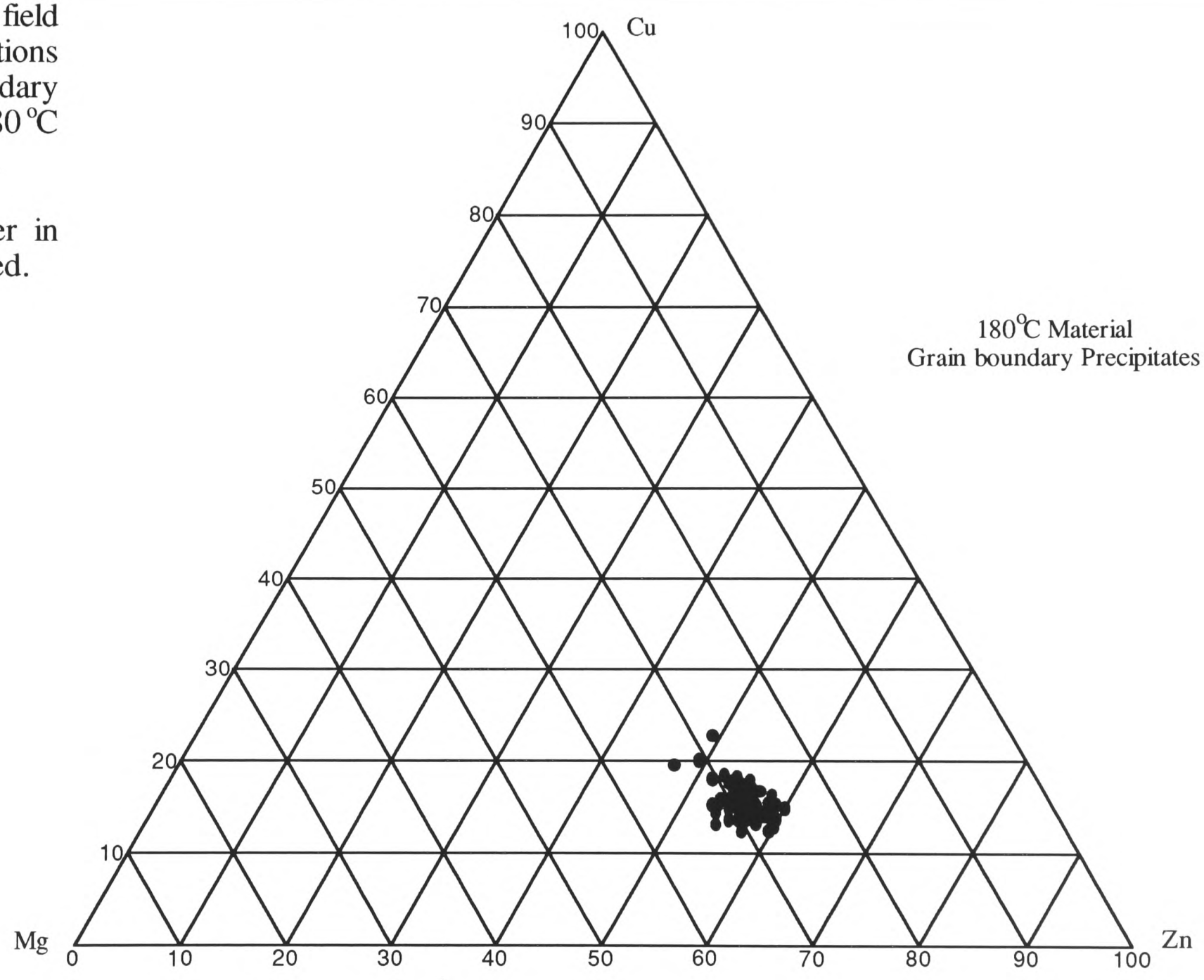

Figure 5.22

A ternary composition field showing the solute fractions for two grain boundary precipitates from each material analysed with the adjacent PFZ levels for each precipitate.

Also shown is the approximate solute enhancement calculable by subtracting the PFZ composition from the precipitate composition.

	GB Precipitate				PFZ			
	Al	Zn	Mg	Cu	Al	Zn	Mg	Cu
120	78.4	11.1	7.3	3.2	91.7	1.5	4.0	2.8
120	74.9	12.8	8.5	3.8	92.7	1.2	3.9	2.2
150	38	33	16.5	12.4	80.6	3.6	3.5	12.3
150	54.5	26	11.7	8.0	84.1	3.3	3.6	9
180	55.6	25.1	11.9	7.4	93.3	1.5	3.4	1.9
180	56.2	24.6	13.2	5.9	94.2	1.1	2.9	1.8

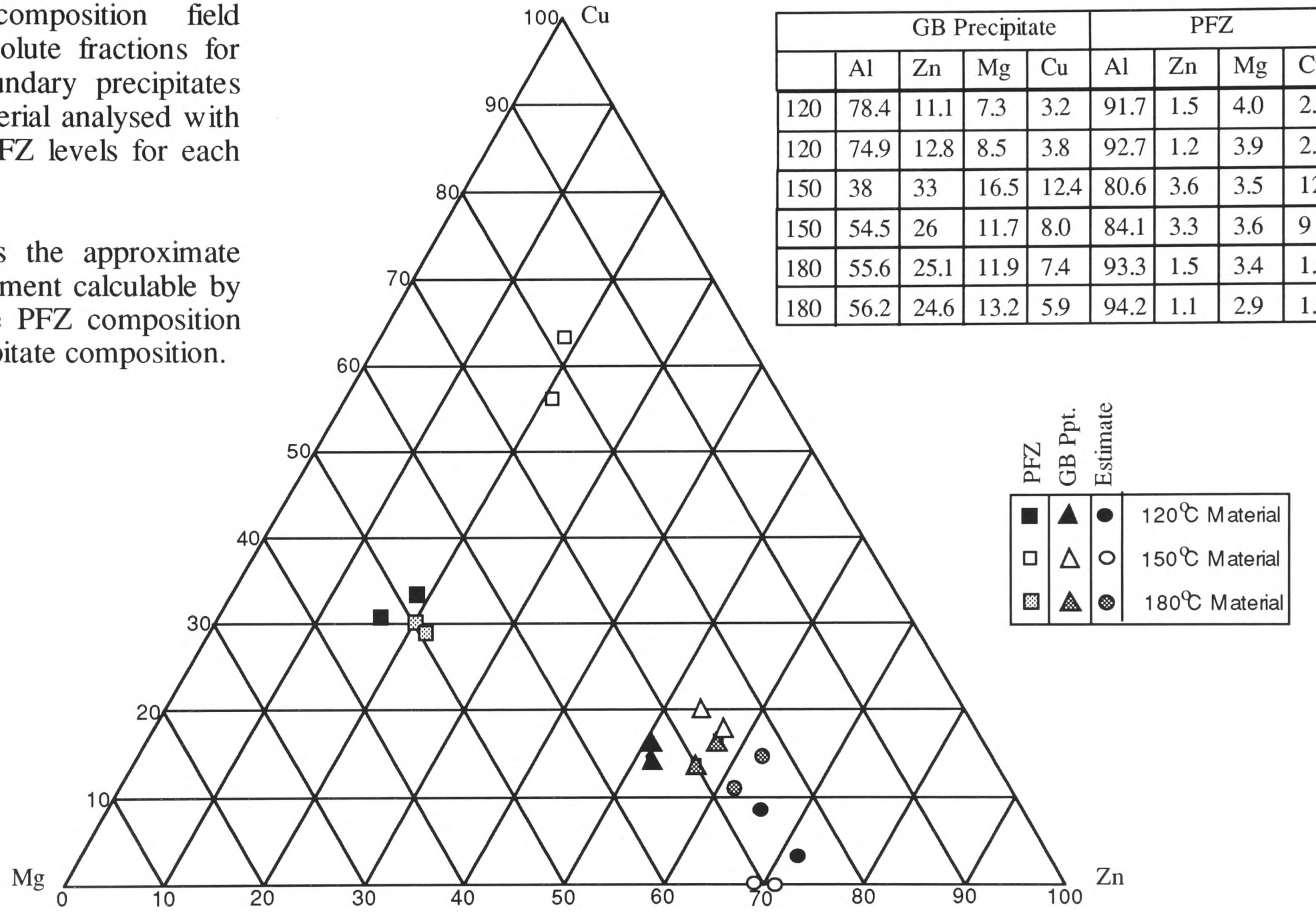

Figure 5.23

precipitate solute fractions for the three treatments. This shows the PFZ to be generally more depleted in zinc than magnesium; and the effect of copper surface deposition strongly affects the observed solute fractions for the PFZ analysis. If the degree of solute enhancement in the precipitate is considered, then the maximum solute enhancement may be approximately calculated, by subtracting the solute detected in the adjacent PFZ, from the solute detected in the precipitate. This is very sensitive to the levels of copper surface deposition, and for the 150°C example, the surface deposition of copper dominates, and there is no observable enhancement of copper in the precipitate. The surface copper thus precludes any realistic attempt to correct the precipitate compositions detected for solute contributions from surrounding matrix.

Considering that Figures 5.20-5.22 are comparing different size precipitates contained in different thickness foils, on different boundaries within each of the different treatments, the overall solute fractions are remarkably similar. There is no clear trend in the solute fraction of the precipitates with different ageing temperatures. The only obvious difference is the increase in precipitate size with increase in total solute content; although this effect is masked by the contribution of the surrounding matrix. The densification of the precipitates is more clearly visible in the POSAP data, which allows removal of the surrounding matrix.

5.3. Precipitate Analysis for Material Aged at 220°C.

As mentioned in Section 5.1, some material was aged for 40hrs at an excessive temperature of 220°C. This was done in order to see what the precipitates aged at the lower temperatures were developing towards, in terms of both the phase structure and the phase composition. It is possible that the precipitates in this material are actually different phases compared to the material aged at lower temperatures, however other workers also use 220°C for a short retrogression step in a multiple step RRA heat treatment[35].

5.3.1. TEM analysis of 220°C material.

Figure 5.24 shows TEM micrographs of matrix and grain boundary regions. The precipitates clearly show a mixture of precise morphologies. The precipitates could be categorised as platelets (D≈125nm T≈25nm), spheres (D≈20nm), and rods of various aspect ratios. These precipitate sizes are huge in comparison to the 5-10nm precipitate sizes in the other heat treatments analysed. A significant feature is that precipitation is so advanced, that the width of the PFZ has increased from the 25-40nm observed in the lower temperature treatments, to being 150-250nm in this heat treatment. The PFZ width is initially determined by the as-quenched vacancy depletion preventing precipitation, but for this temperature and ageing time, the diffusion path is sufficiently large that Ostwald ripening and solute migration to the grain boundary has broadened the PFZ width.

5.3.2. AP and POSAP analysis of 220°C material.

Figure 5.25.a. shows a TEM micrograph of a FIM specimen. The specimen was field evaporated in the FIM to bring the precipitate, as marked, into the field of view. Since the precipitates in this material were very large, and the matrix contained virtually no solute, the FIM image clearly showed the location of the precipitates (Figure 5.25.b). The (110) pole structure of the aluminium matrix was also clearly visible. This photograph was used for the radius calibration of the POSAP, as described in Section 4.5.4.2. Figure 5.26 shows a FIM image of the orientation of the specimen prior to POSAP analysis (with the AP aperture visible at the centre). Figure 5.27.a shows the distribution of the solute detected by POSAP analysis, corresponding perfectly to the FIM image. Due to the very high solute levels in the precipitate, and the very low levels in the matrix, this analysis is suitable for the isosurface representation, as mentioned in Section 4.1.3.2. (Figure5.27.b). The solute species peaks in the spectrum are sufficiently distinct, that an approximate attempt at determining the separate compositions of zinc and copper in the precipitate is possible. Table 5.5 shows the composition levels detected for the precipitate. The precipitate contains 20% aluminium

a) shows a bright field TEM micrograph of matrix precipitation in material aged for 40 hours at 220°C. The precipitates are very large in comparison to the earlier stage precipitates analysed previously. There are clear precipitate morphologies visible; platelets, rods and spheres. As usual any precipitates intersecting the surface of the specimen have been preferentially dissolved by the electropolish and hence they image brightly.

b) shows a bright field TEM micrograph of a typical grain boundary region in material aged for 40hours at 220°C. The width of the PFZ has increased to about 150nm due to the large scale of precipitation and high mobility of solute at this ageing temperature. The PFZ is generated by depletion of vacancies around the boundary during quenching inhibiting precipitate nucleation. In the lower temperature heat treatments precipitation occurs right up to the edge of the vacancy depleted region however at this temperature the solute is sufficiently mobile that coarsening of the matrix precipitates and solute migration to the grain boundary increases the apparent width of the PFZ.

Figure 5.24.

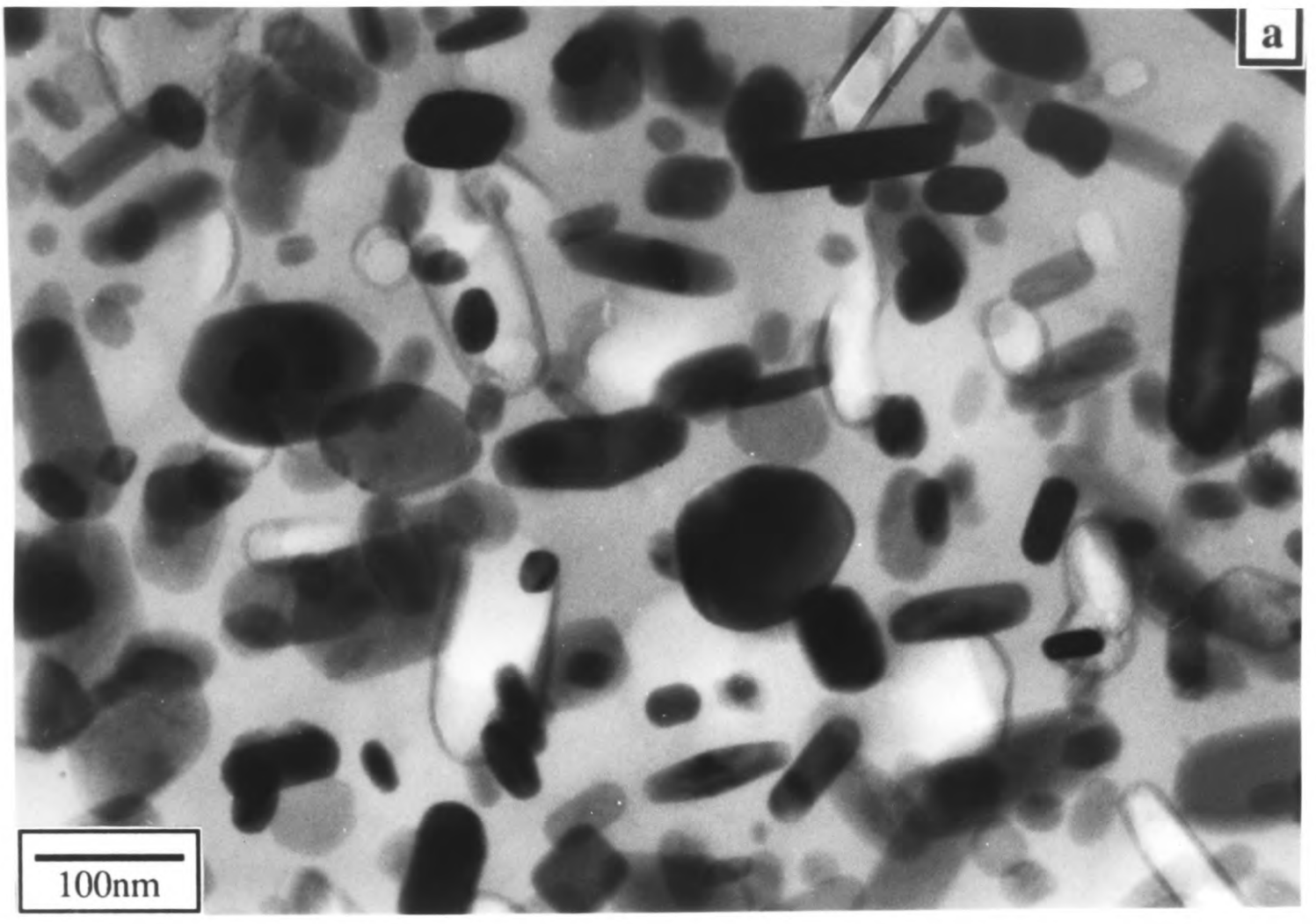
a
100nm

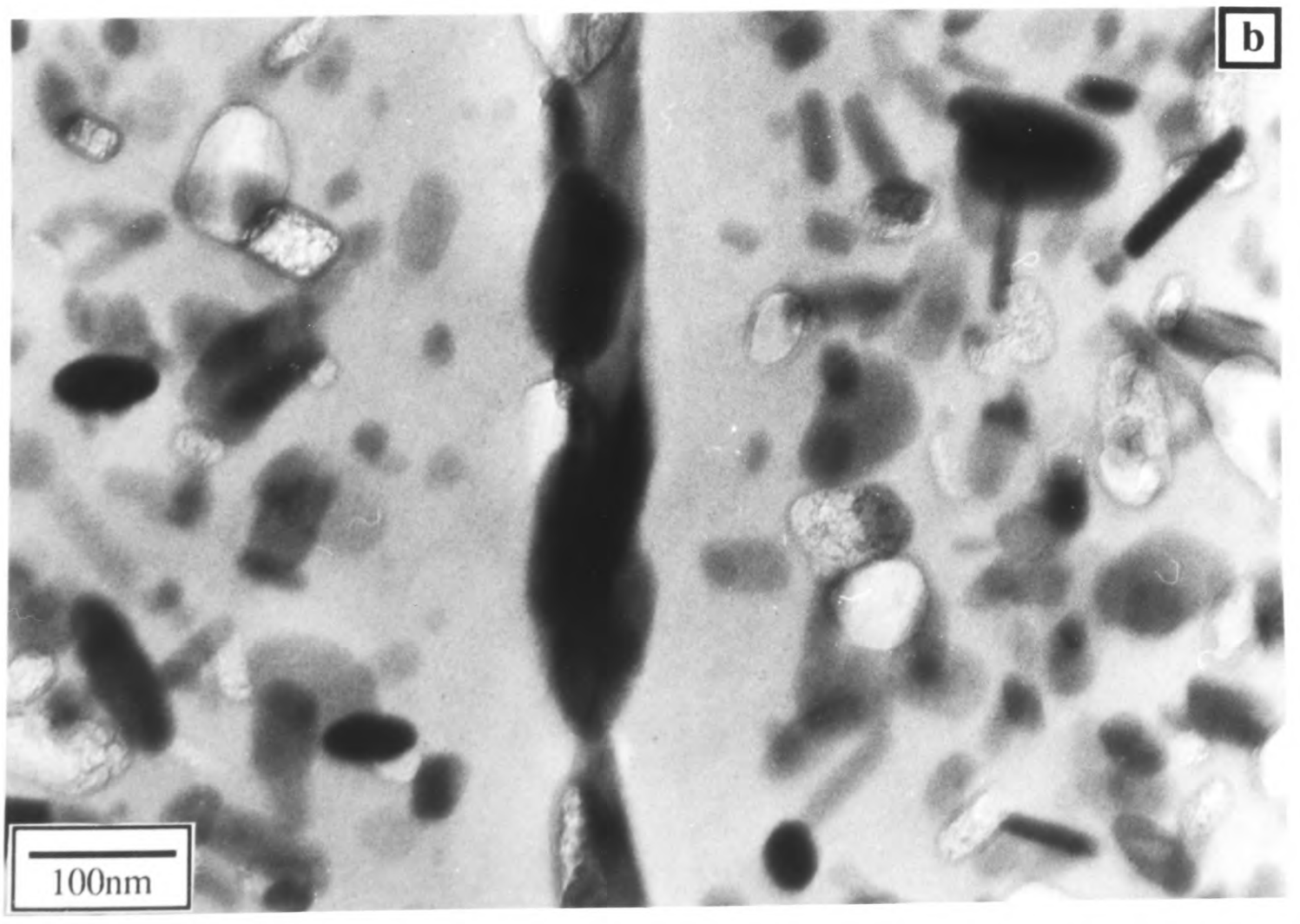
b
100nm

a) shows a TEM bright field image of a FIM specimen containing the large precipitates formed by ageing at 220°C.

b) shows a FIM image of the same specimen imaged to 6.5kV. This image shows very clearly the ring structure of the (110) crystallographic poles. It also shows two brightly imaging large precipitates.

From a knowledge of the radius of curvature of a tip imaged to 6.5kV (section 4.5.4.) it is possible to mark on the TEM image of the specimen the approximate position of the evaporation surface at 6.5kV. From this it is possible to see which precipitates should be visible in the FIM image.

Figure 5.25

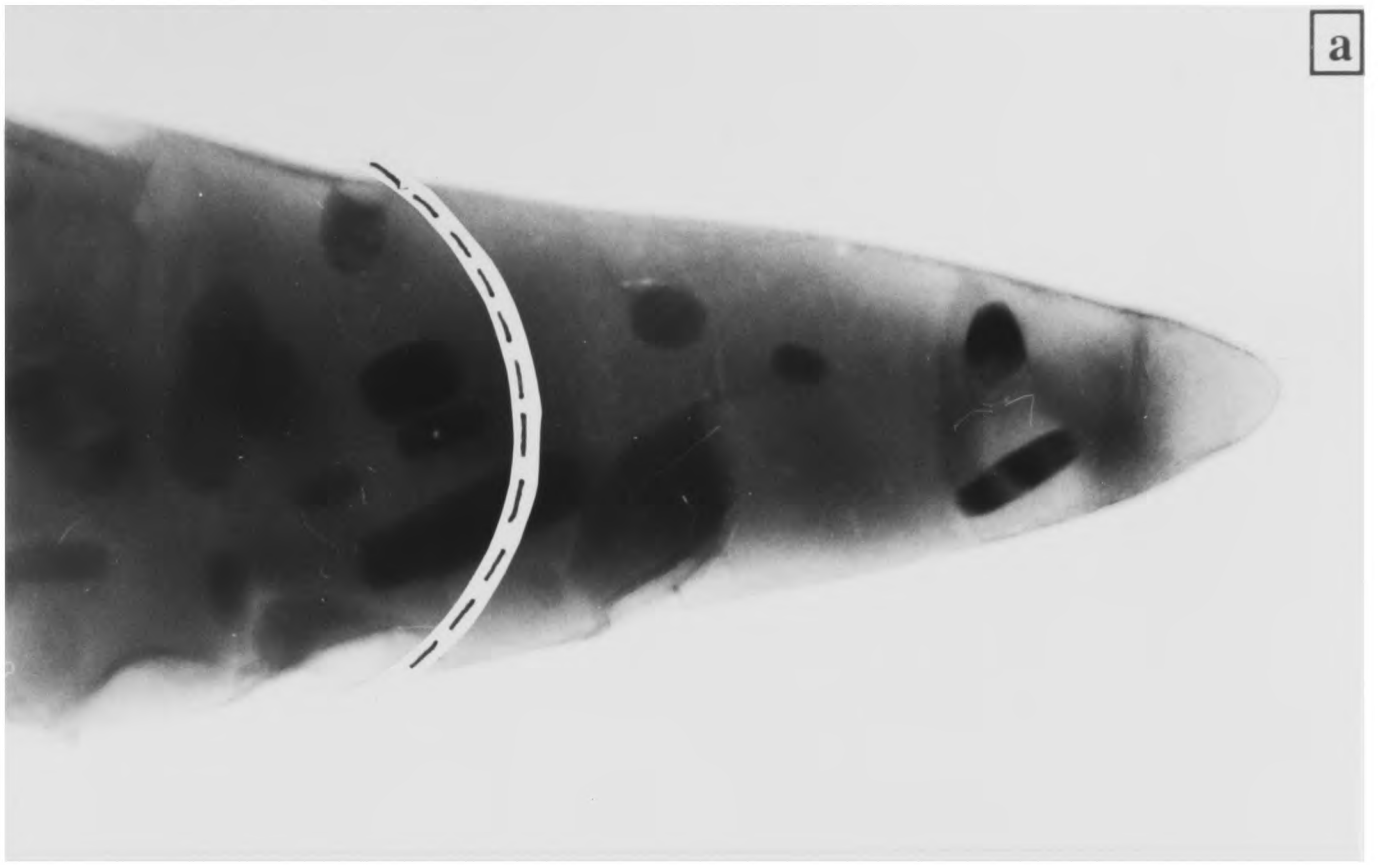
a

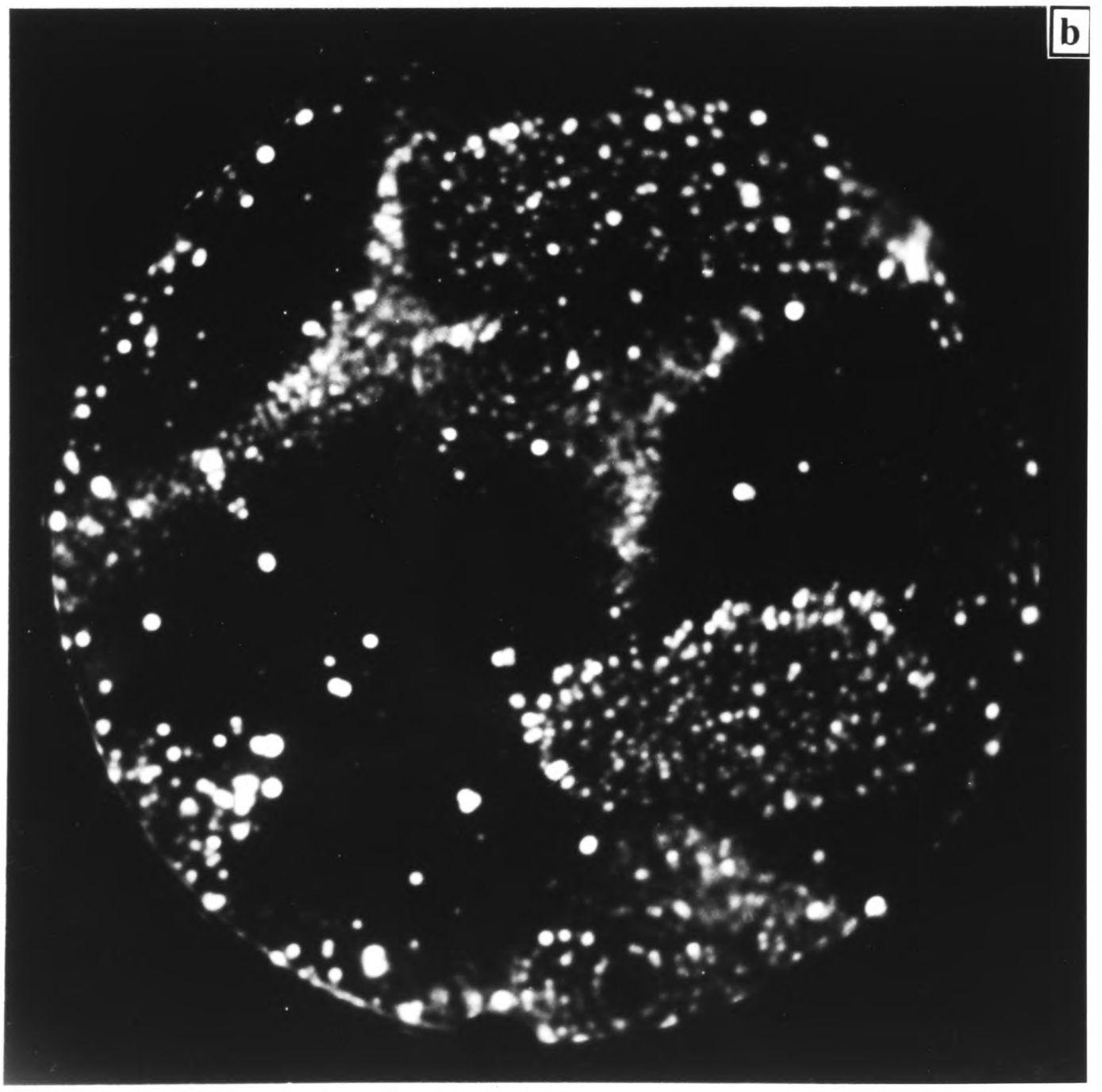
b

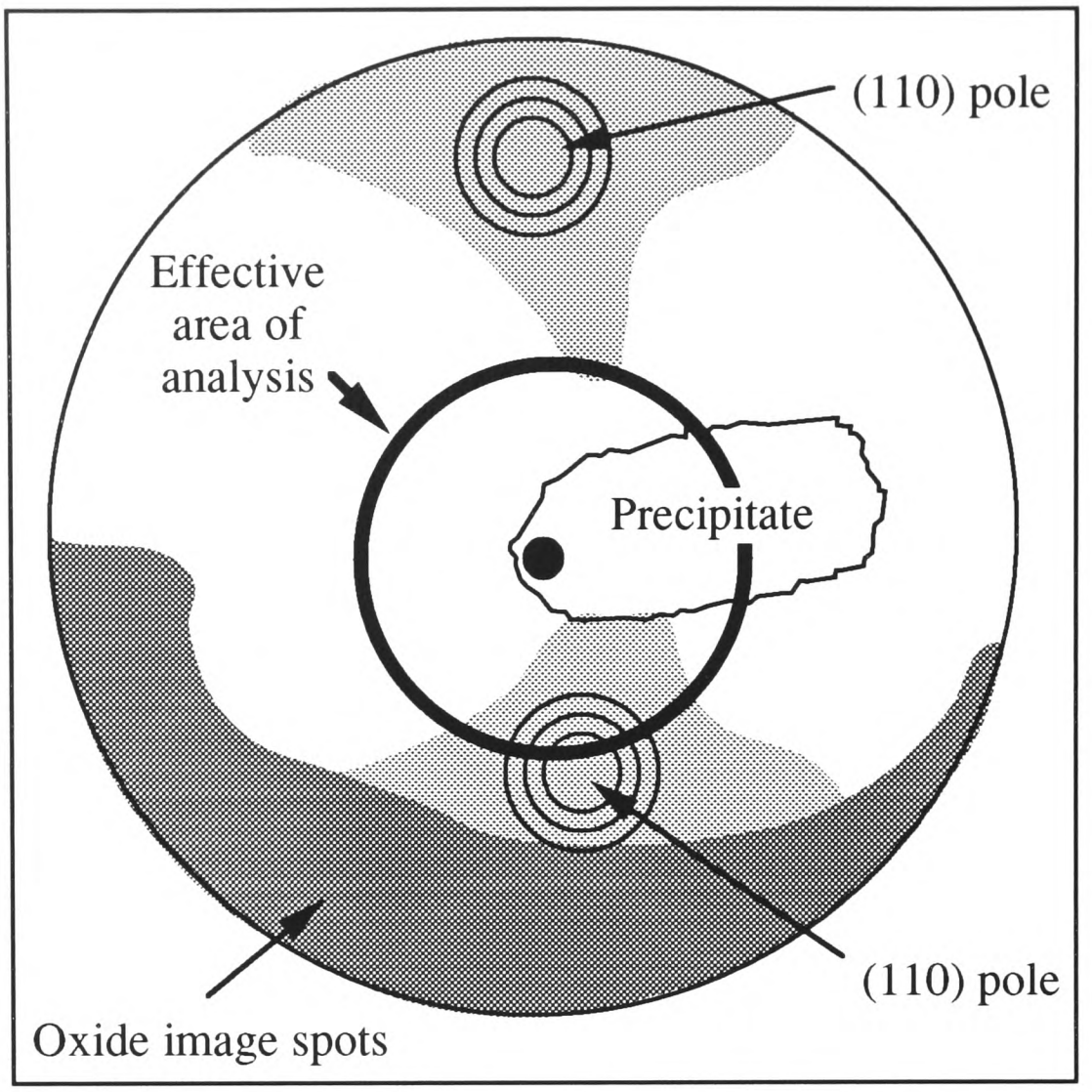

Schematic of FIM image in figure 5.26

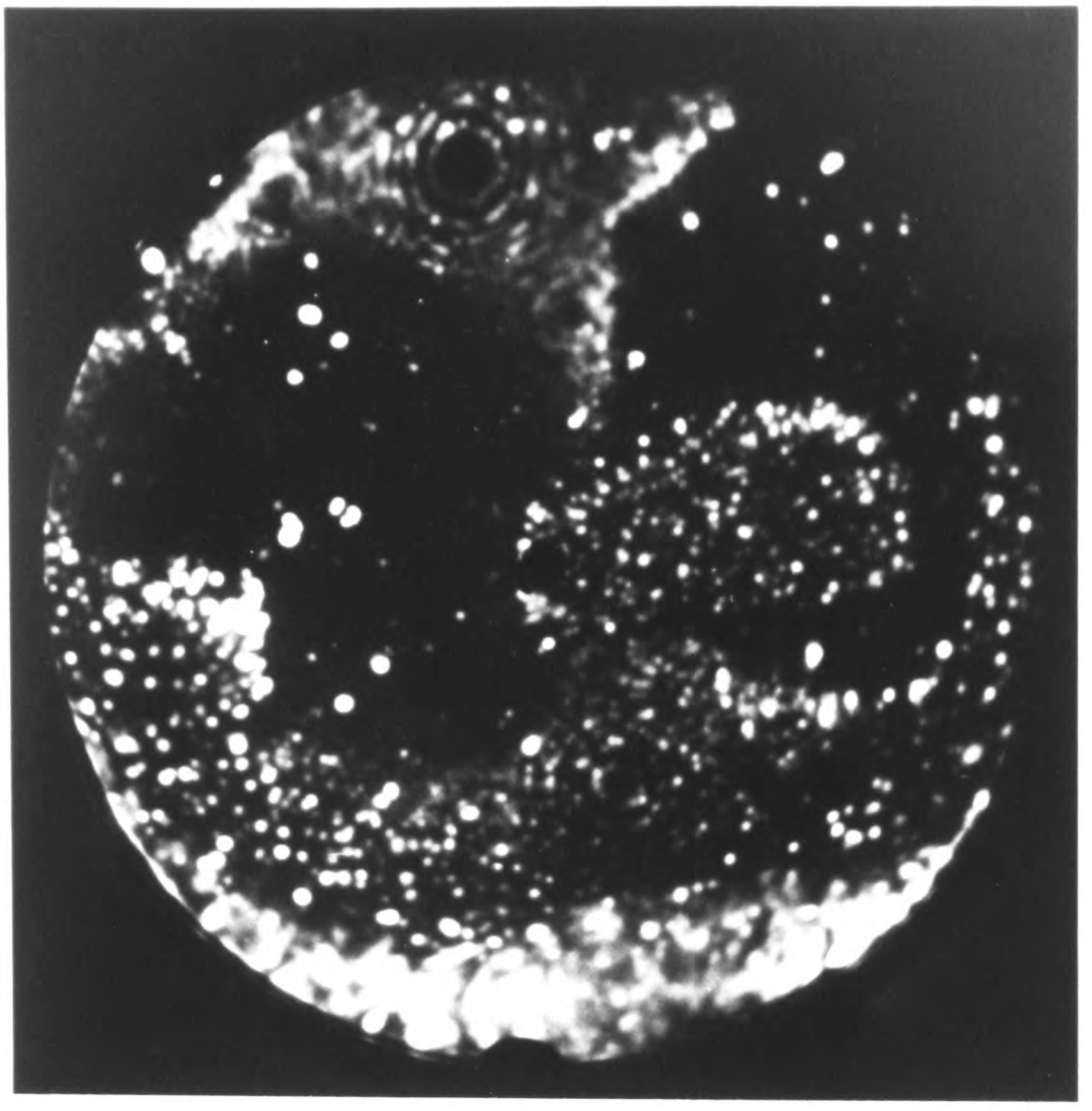

FIM image of precipitate aligned for analysis.

Figure 5.26.

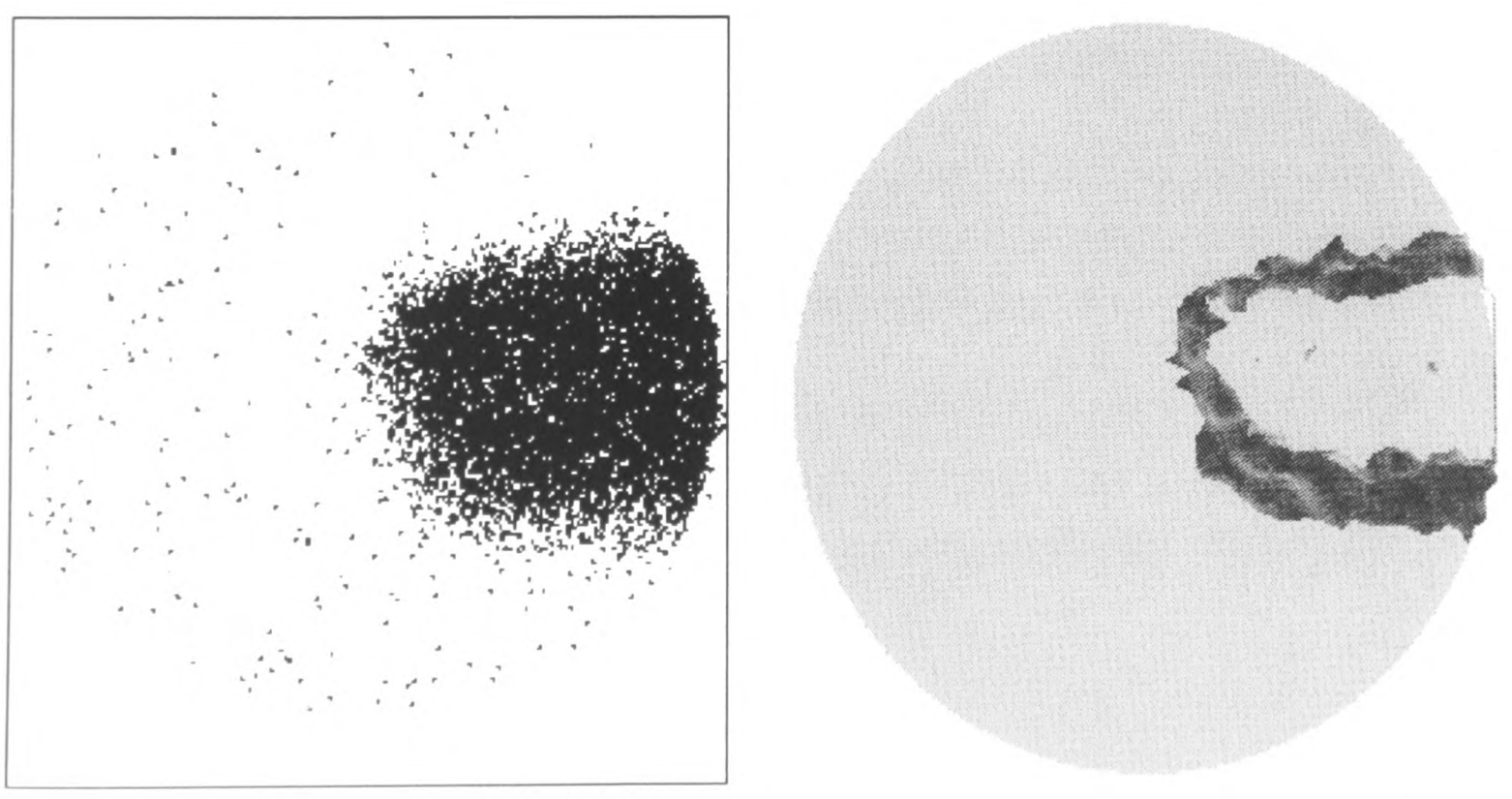

(a) Atom distribution of Zinc species (b) Isosurface drawn at the 10% zinc level (2 point smoothing)

The two methods of representation of POSAP data for 220°C material. The precipitate appears hollow since it intersects the top and bottom of the data file.

Figure 5.27

Ion species	Total % Pos.	Selected atoms	Corrected
Al 2+	90.4	562	622
Al +	92.6	3539	3822
Mg 2+	76.3	5130	5869.6
Mg +	87.4	706	925.3
Zn 2+	68.0	2802	4120
Cu 63+	64.3	528	762
Zn 64+	50.4	693	1375
Cu 65+	59.1	979	1656.5
Zn 66+	50.6	533	1053
Zn 68+	53.3	331	621

element	Atoms	%	%Solute	EPMA	%Solute
Al	4444	20.6	Fraction	93.0	Fraction
Zn	7319	33.9	42.9	3	42.9
Mg	6795	31.5	39.9	2.8	40.0
Cu	3004	13.9	17.5	1.2	17.6

This shows the calculation of the composition of the precipitate in Figures 5.26 and 5.27. The number of atoms in each windowed ion peak are given with the %positioning for the whole file for that windowed peak from which the corrected number of selected atoms is calculated. The zinc and copper are then deconvoluted using the formulae in Figure 4.11 to give the total number of atoms of each species in the precipitate. Fitting this to the normally quoted stoiciometry of $Mg(ZnAlCu)_2$ gives the precipitate composition as $Mg(Zn_{0.5}Al_{0.33}Cu_{0.17})_2$. This was then compared to the EPMA composition which showed unbelievably good agreement. The ratio of solute fractions perfectly match the EPMA total composition solute fractions.

Table 5.5

and the solute fractions of the precipitate perfectly match the total solute fractions of the alloy, as determined by EPMA. The close match must be an accident, because there are other phases with different compositions that are present in this heat treatment, and also the accuracy of the POSAP in determining compositions is not that good, as discussed in Section 4.5. However, the fact that the precipitate contains solute in exactly the same ratio as the total alloy is perhaps to be expected at this stage in the precipitation process, because almost all the solute is contained in the precipitates. No internal crystallographic structure was discernible in the precipitate and there was no interface segregation. Conventional atom probe analysis of this precipitate was attempted in order to directly compare the levels of solute detected by each method, however, as was often the case, the specimen flashed under the more severe analysis conditions of AP analysis, and the detector was suspect as mentioned previously.

5.3.3. STEM analysis of 220°C material.

This heat treatment is good for STEM analysis because, as shown in Figure 5.24, the matrix strengthening precipitates are sufficiently widely spaced that spot analysis of individual precipitates is possible. (All compositional data is given in atomic %.)

Figures 5.28 and 5.29 show the ternary composition fields for the matrix strengthening precipitates and the grain boundary precipitates, respectively. Since the grain boundary precipitates contain more solute (being larger and probably more solute rich), the scatter in compositions is less than that observed for the matrix precipitates. The matrix precipitates appear to contain more copper and less zinc than the grain boundary precipitates. It is possible that the copper enhancement is due to the greater surface contribution. This may be checked by considering the amount of copper present in a matrix (solution) analysis. Figure 5.30 shows the effect of the matrix upon the real precipitate composition, and it is obvious that the shift in solute fractions due to the matrix solute content is much smaller than the observed difference between the matrix strengthening, and the grain boundary, precipitates thus, **the copper enhancement is real.** This can be explained by the presence of AlCuMg precipitates along the

A ternary composition field showing the solute fractions for each matrix strengthening precipitate analysed in 220°C material.

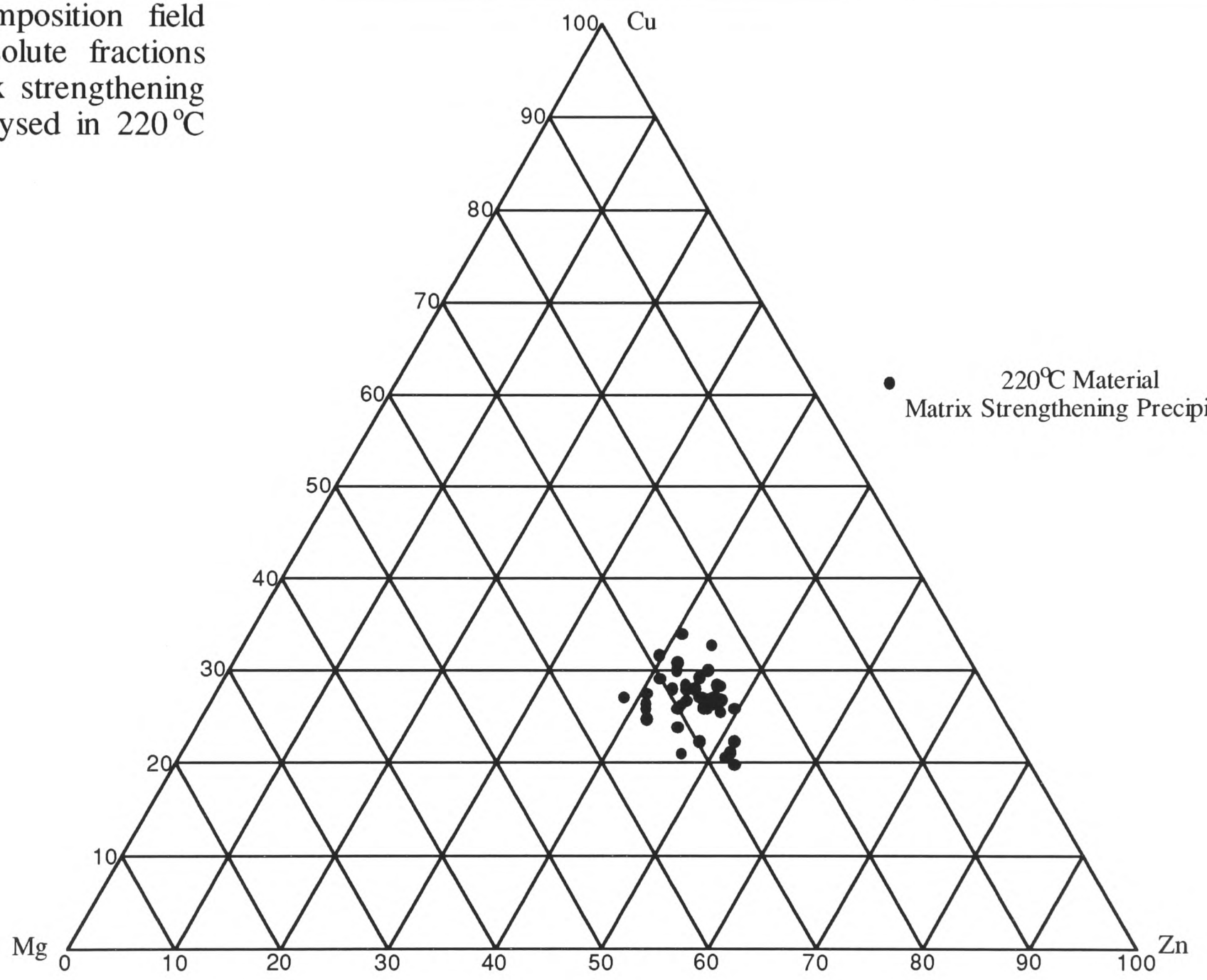

Figure 5.28

A ternary composition field showing the solute fractions for each grain boundary precipitate analysed in 220 ℃ material.

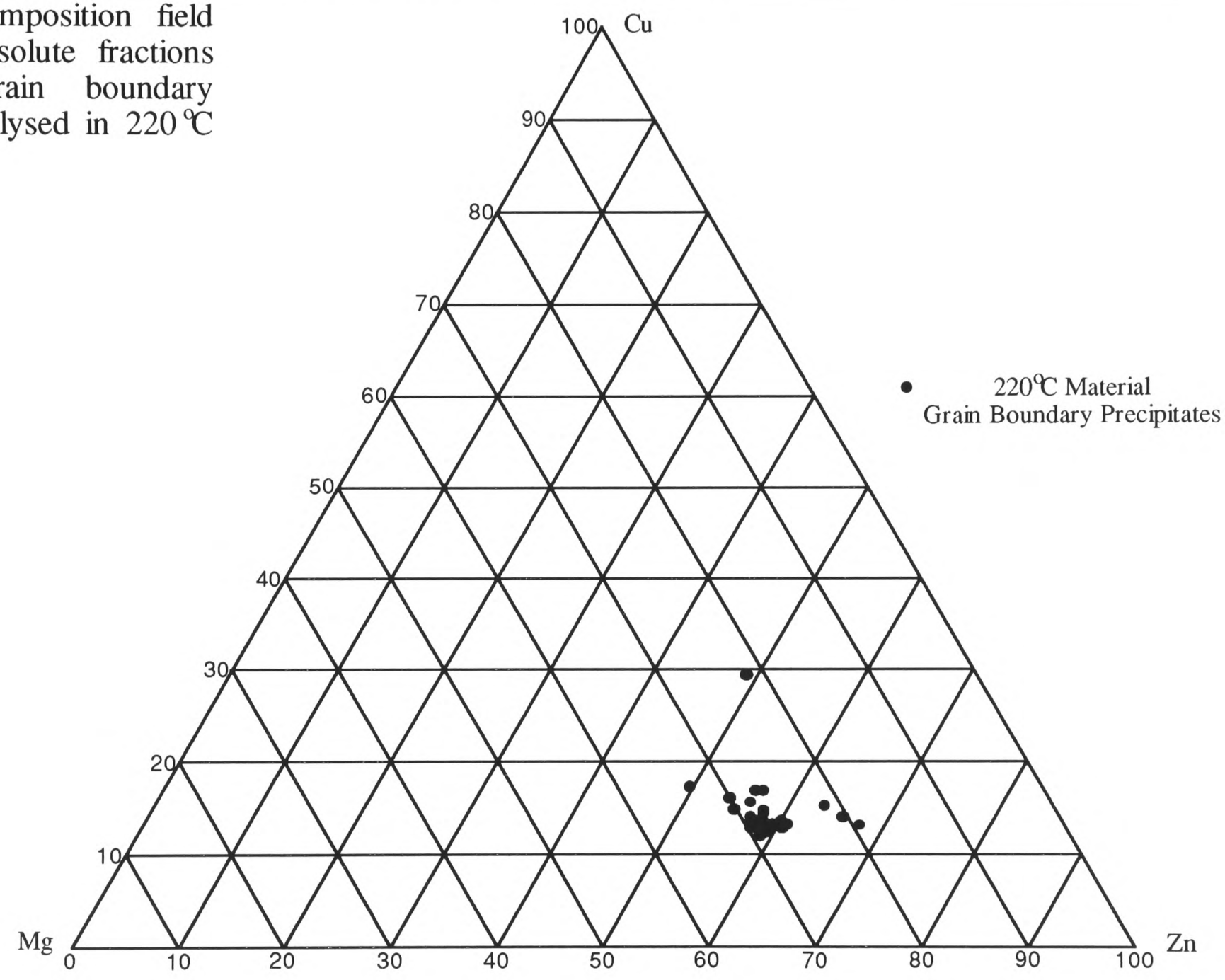

Figure 5.29

A ternary composition field showing an estimate of the effect of copper surface deposition on an example of both a grain boundary precipitate and a matrix strengthening precipitate in material aged at 220℃.

The estimate has been calculated by assuming that the precipitate actually contains no aluminium, thus the detected precipitate composition minus sufficient matrix composition to give zero aluminium content gives an estimate of the maximum possible effect of solute contribution from the surrounding matrix (or PFZ).

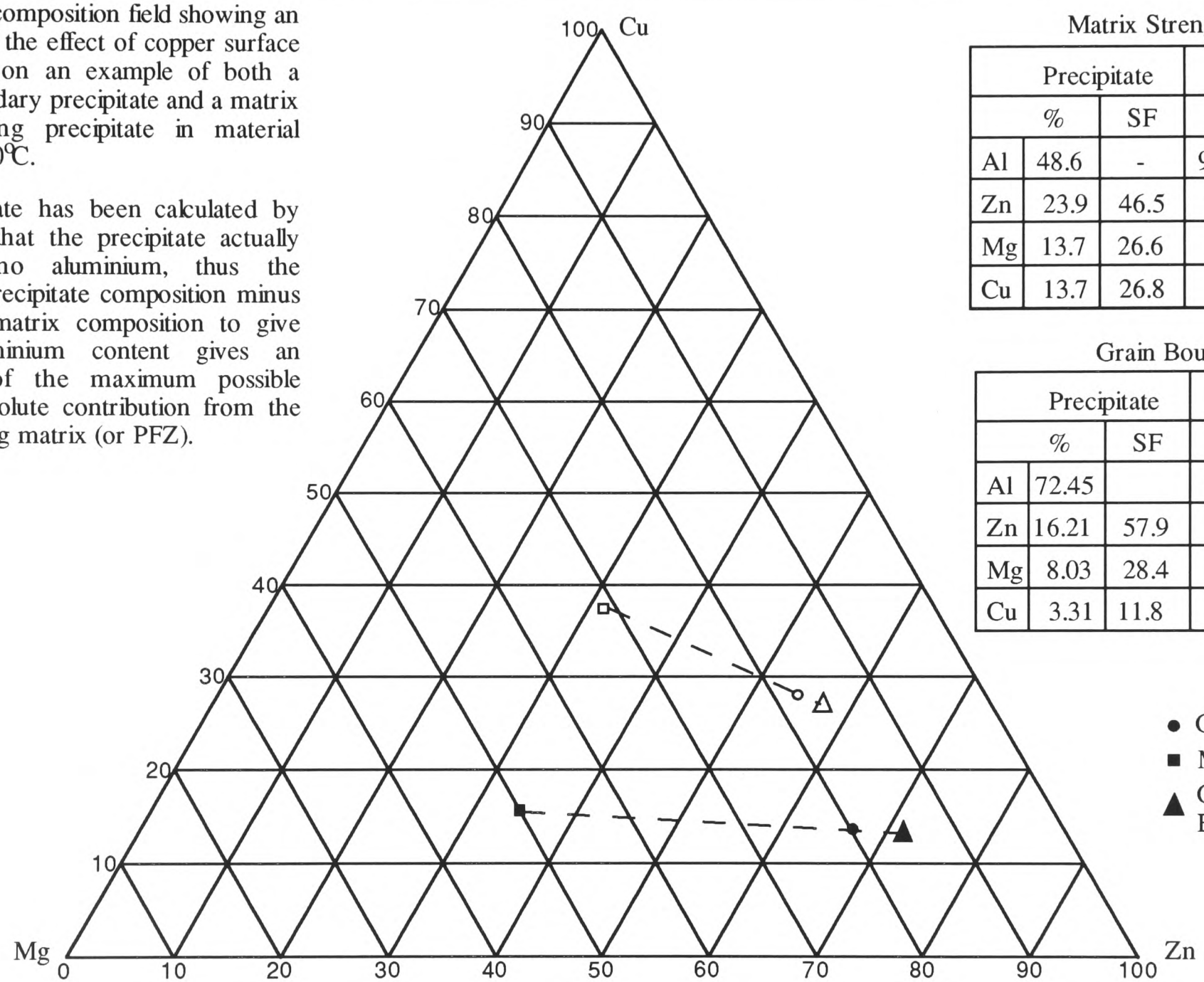

Matrix Strengthening Precipitate data

	Precipitate		Matrix		Estimate	
	%	SF	%	SF	%	SF
Al	48.6	-	91.3	-	0	-
Zn	23.9	46.5	2.1	24	22.78	48.9
Mg	13.7	26.6	3.1	36	12.0	25.8
Cu	13.7	26.8	3.5	40	11.8	25.3

Grain Boundary Precipitate Data

	Precipitate		Matrix		Estimate	
	%	SF	%	SF	%	SF
Al	72.45		94.75		0	
Zn	16.21	57.9	1.38	26.2	15.15	64.4
Mg	8.03	28.4	3.11	59.1	5.65	24.0
Cu	3.31	11.8	0.77	14.6	2.72	11.56

Figure 5.30

A ternary composition field showing the solute fractions for each AlCuMg precipitate analysed in 220℃ material.

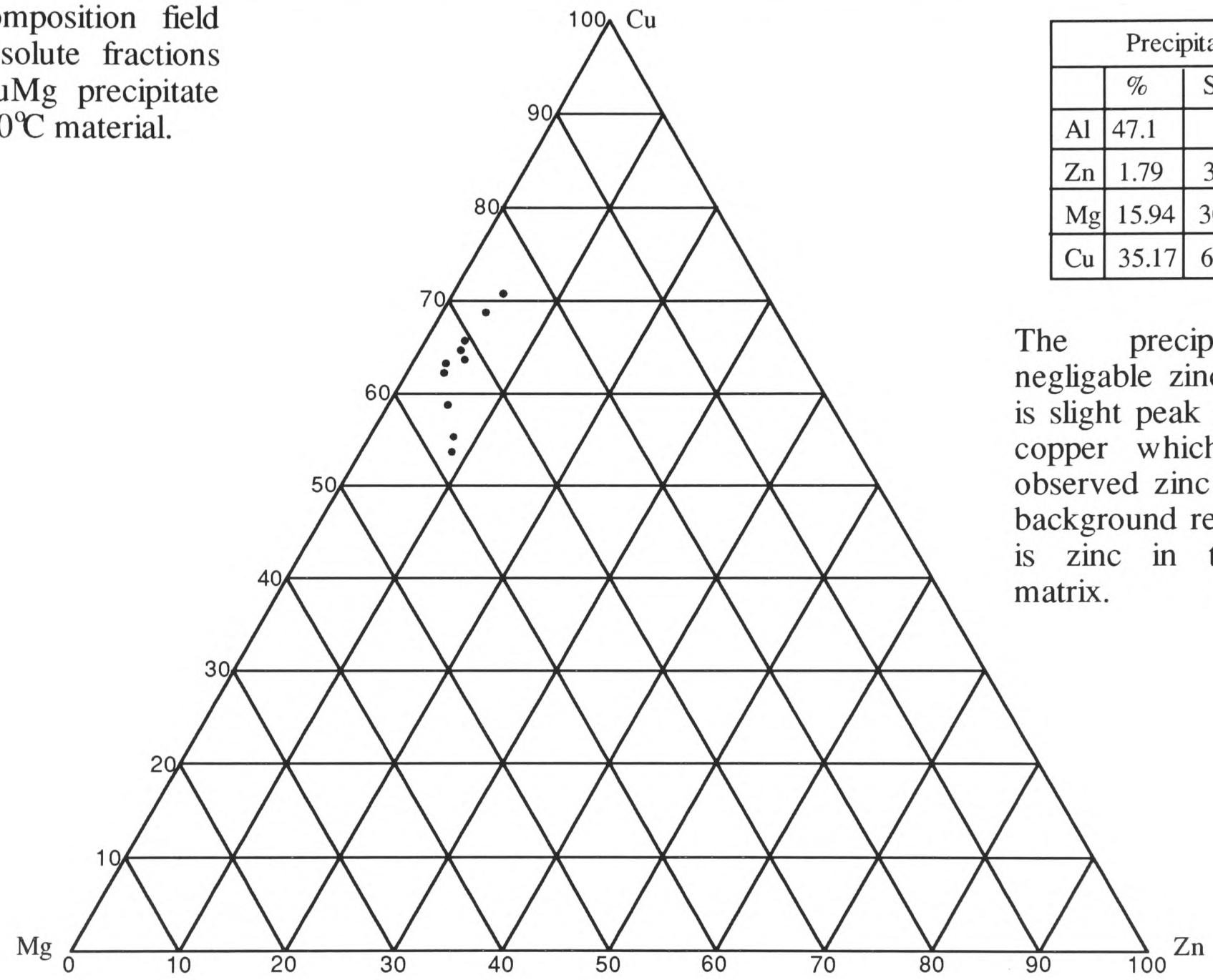

	Precipitate		Matrix	
	%	SF	%	SF
Al	47.1		92.22	
Zn	1.79	3.4	1.87	24.1
Mg	15.94	30.1	3.24	41.6
Cu	35.17	66.5	2.67	34.3

The precipitate contains negligable zinc content. There is slight peak overlap with the copper which enhances the observed zinc and there is no background removal and there is zinc in the surrounding matrix.

Figure 5.31

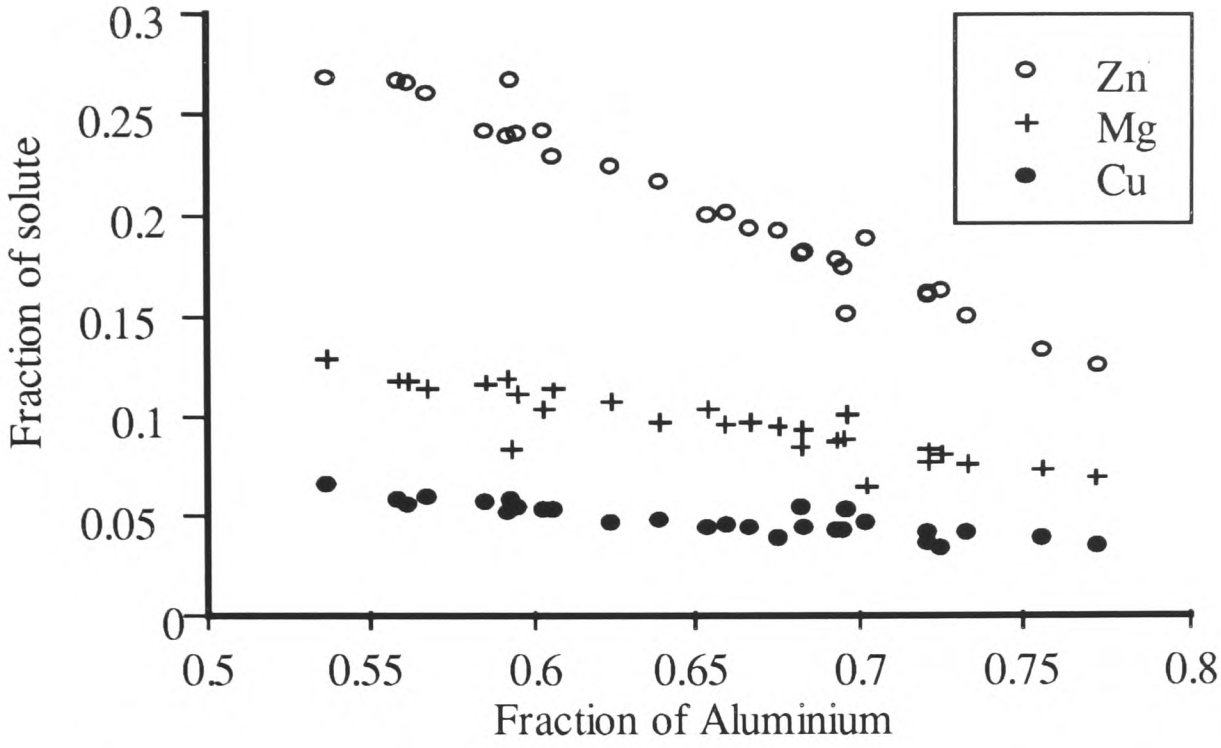

a) Plot of the grain boundary precipitate compositions by the Lorimer method. Since the solute levels in the PFZ are low the data fits this method of representation well.

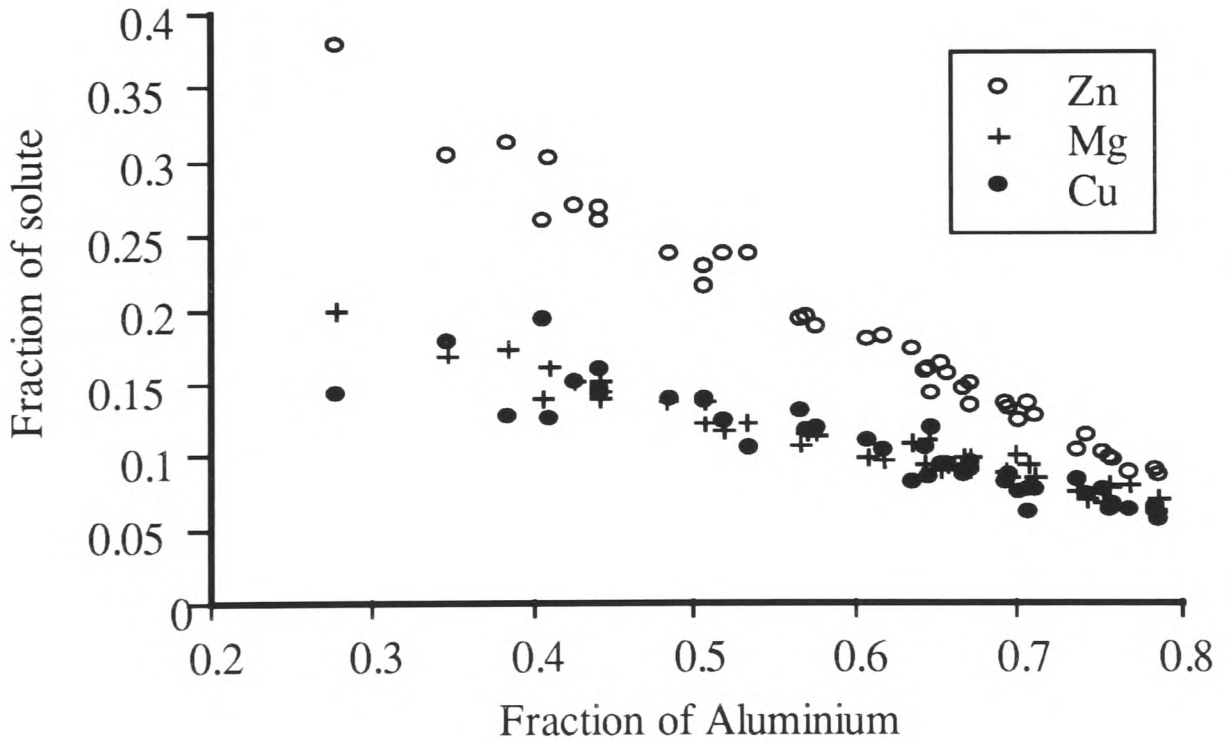

b) Plot of the matrix strengthening preciptates by the Lorimer method. This also shows up the difference in the copper content of the matrix strengthening precipitates compared to the grain boundary precipitates. The greater effect of surface deposition of copper on the lower solute content of the precipitates shows up as greater scatter in the compositions.

Figure 5.32

boundary and the presence of the grain boundary itself, both of which may act as sinks for copper and magnesium. This would result in a relative enhancement of the zinc, and depletion of copper solute fractions of the grain boundary precipitates, as observed.

The grain boundary precipitates shown in Figures 5.28-5.29 are just the AlMgZnCu precipitates. There were also a significant number of AlCuMg precipitates present on the grain boundaries. Figure 5.31 shows the solute fraction composition field for these copper rich precipitates. Both the copper precipitates and the grain boundary interface contain a significant fraction of the grain boundary region copper content. In the matrix, neither of these sites are available, so the copper segregates to the AlZnMgCu precipitates instead. The AlCuMg precipitates are likely to be nucleated at a strongly segregated boundary interface, rather than on existing AlMgZnCu precipitates, since the zinc content of the AlCuMg precipitate is negligible.

The precipitates in this heat treatment are so large, and the matrix solute levels are so low, that the Lorimer method of removing the aluminium contribution to the precipitates works very well. Figure 5.32 shows the plots of solute against aluminium content for analyses of the matrix strengthening precipitates in the material aged for 40hrs at 220°C. As expected, scatter is largest in the copper, due to the surface deposition; however, the agreement with the theory is still good. Since both the copper and magnesium are over-estimated, and hence the zinc and aluminium are underestimated, extrapolation of the best-fit lines is not very accurate. However, it is possible to say that the precipitates, at this stage in the ageing, contain about 20-30% aluminium. This is in agreement with the POSAP results.

5.4. RRA Precipitate Analysis.

The results of atom probe analysis of matrix strengthening precipitates in material which had been retrogressed and re-aged[96] were presented for Part II of my undergraduate degree. The heat treatments used were described previously in Section 2.1.2, and this work was finished at the start of this project by the application of POSAP analysis to

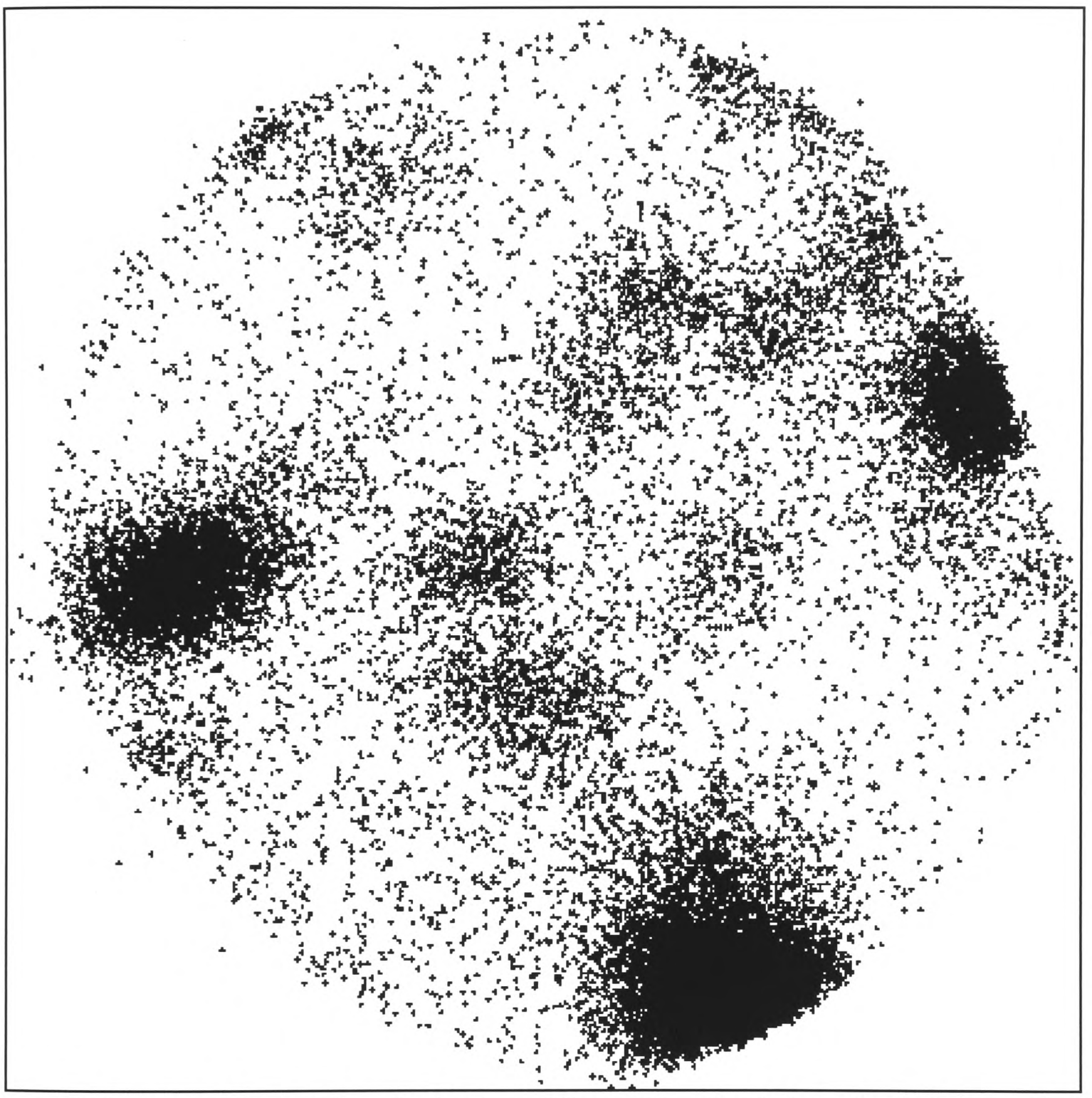

Distribution of all the solute ion species detected for an analysis of RRA180 material. This shows the two sizes of precipitates.

Figure 5.33

a) Ternary composition field showing the composition of the precipitates in the RRA120 material

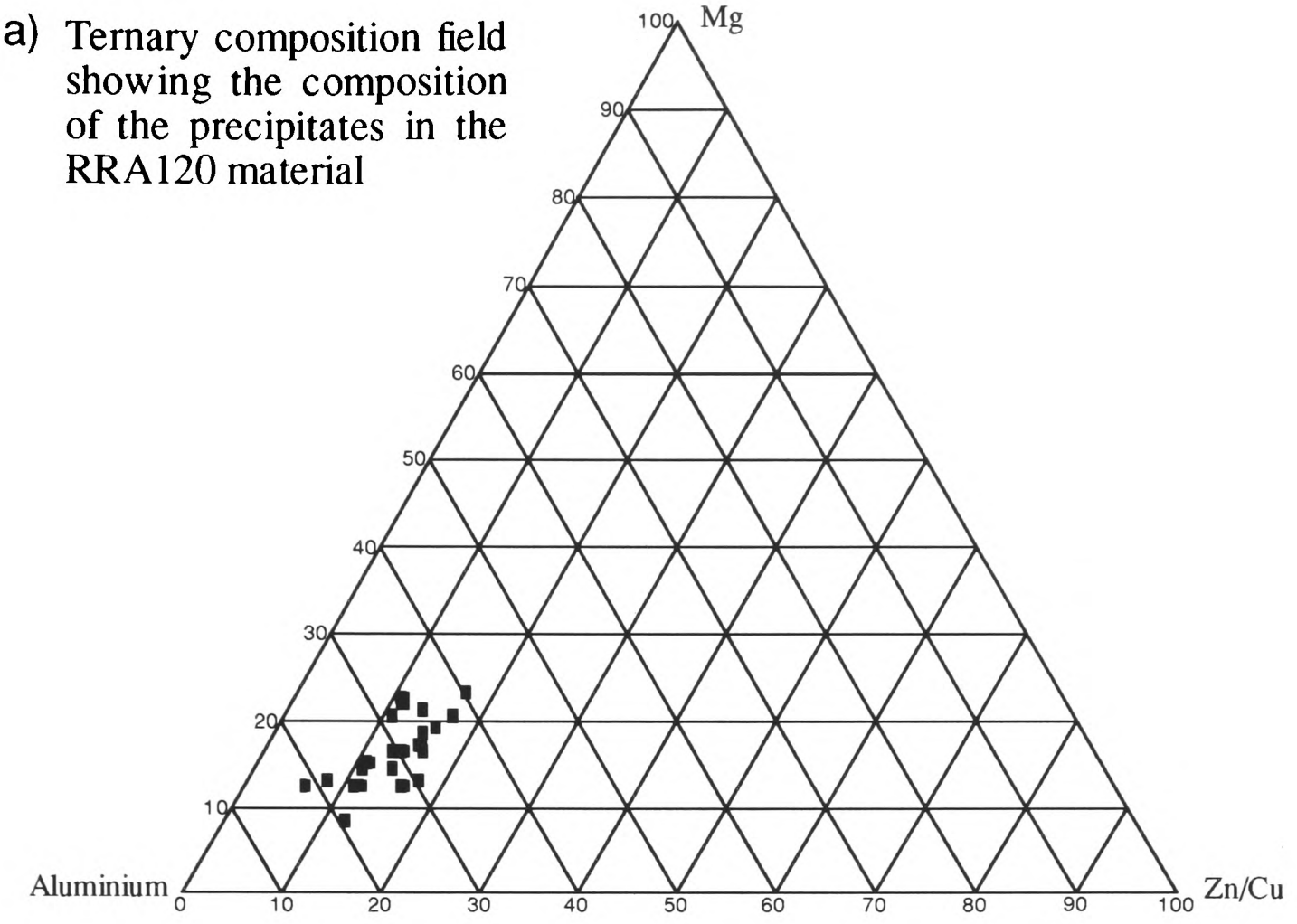

b) Ternary composition field showing the composition of the precipitates in the RRA180 material

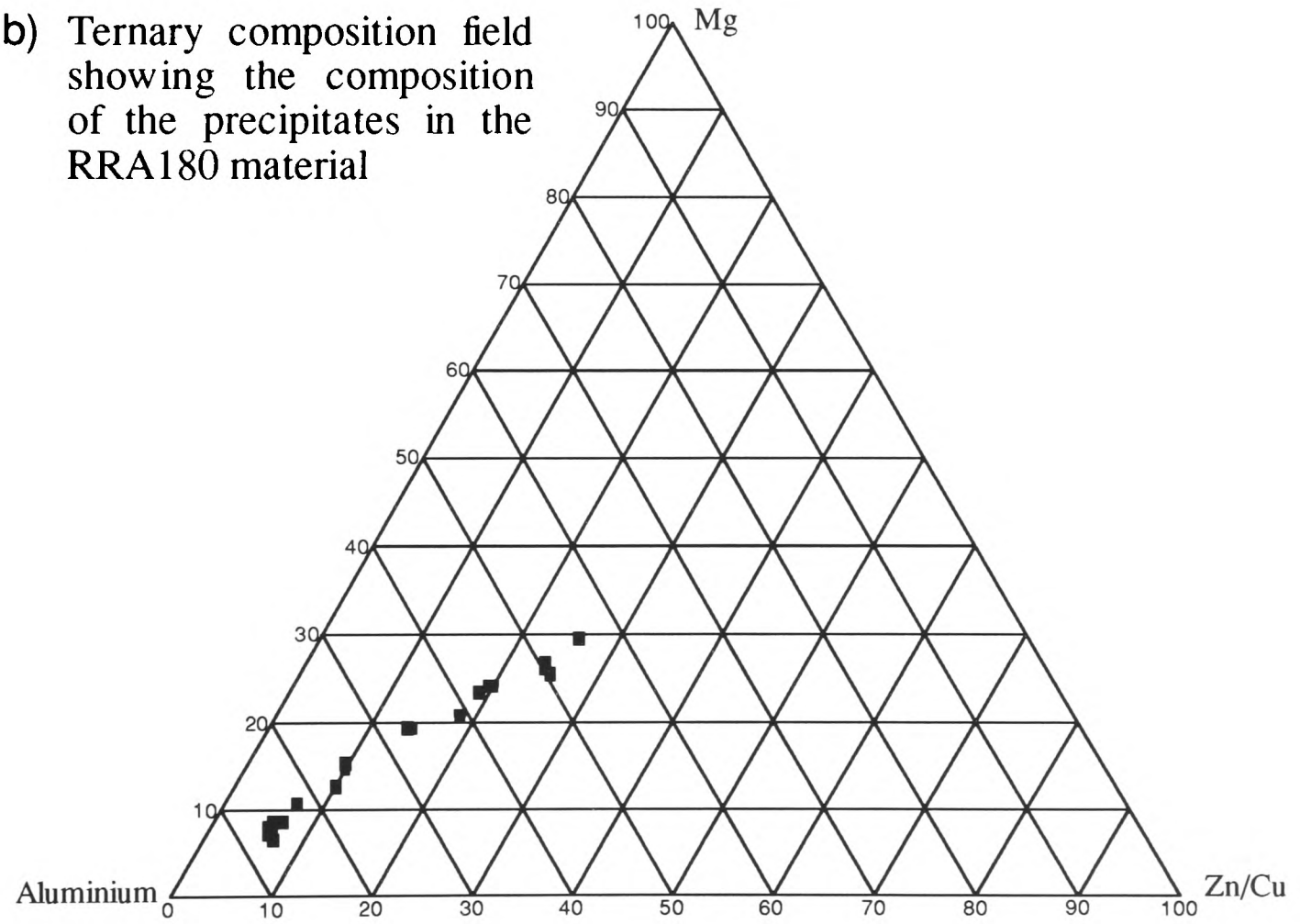

The effect of the RRA treatment is to produce a bimodal distribution in preciptiate sizes.

Figure 5.34

selected heat treatments. Figure 5.33 shows the distribution of solute atom species in some RRA180°C material. Given that all the precipitates shown are totally contained within the volume of analysis, this image shows the bimodal nature of the precipitate distributions after retrogression and re-ageing heat treatment. Between the large precipitates that have grown during retrogression, there is a distribution of smaller precipitates that have grown during the re-ageing heat treatment. These analyses were done using the POSAP Mark I detector, which had a lower mass resolution than the POSAP Mark II detector, which was used for the majority of this project. Due to this lower mass resolution, there is no chance of separating the zinc and copper species. Calculation of the compositions of the precipitates showed, that after retrogression and re-ageing, there was a greater range of precipitate aluminium contents, associated with the bimodal precipitate distribution (Figure 5.34). The POSAP Mk.I also had limitations on the size of data files and rate of acquisition, that meant that the quality of data obtained was less accurate due to the discontinuous nature of the analysis. The image in Figure 5.33 is a composite image of nine consecutive analyses. These results were written up for publication at the end of the first year of this research[96].

5.5. Other Precipitate Phases observed.

The main precipitate phase, upon which the desirable properties of this alloy are based, is the AlZnMgCu phase.

Zirconium is added to this alloy to act as a grain refining agent. This produces a dispersion of spherical precipitates, about 25nm in diameter, present in all ageing treatments. STEM X-ray analysis showed these to contain aluminium and zirconium with very little of any other solute species. TEM diffraction analysis confirmed these to be Al_3Zr phase, as identified by other workers[97]. In the FIM, this precipitate phase has a much higher evaporation field than the aluminium, thus there is severe distortion of the ion trajectories and local magnification effects. This made compositional analysis by the POSAP unreliable, however, the analysis did prove very graphical. Figure 5.35 shows composition maps of slices through an analysis of an Al3Zr precipitate, clearly

Diameter of area of analysis about 25nm.

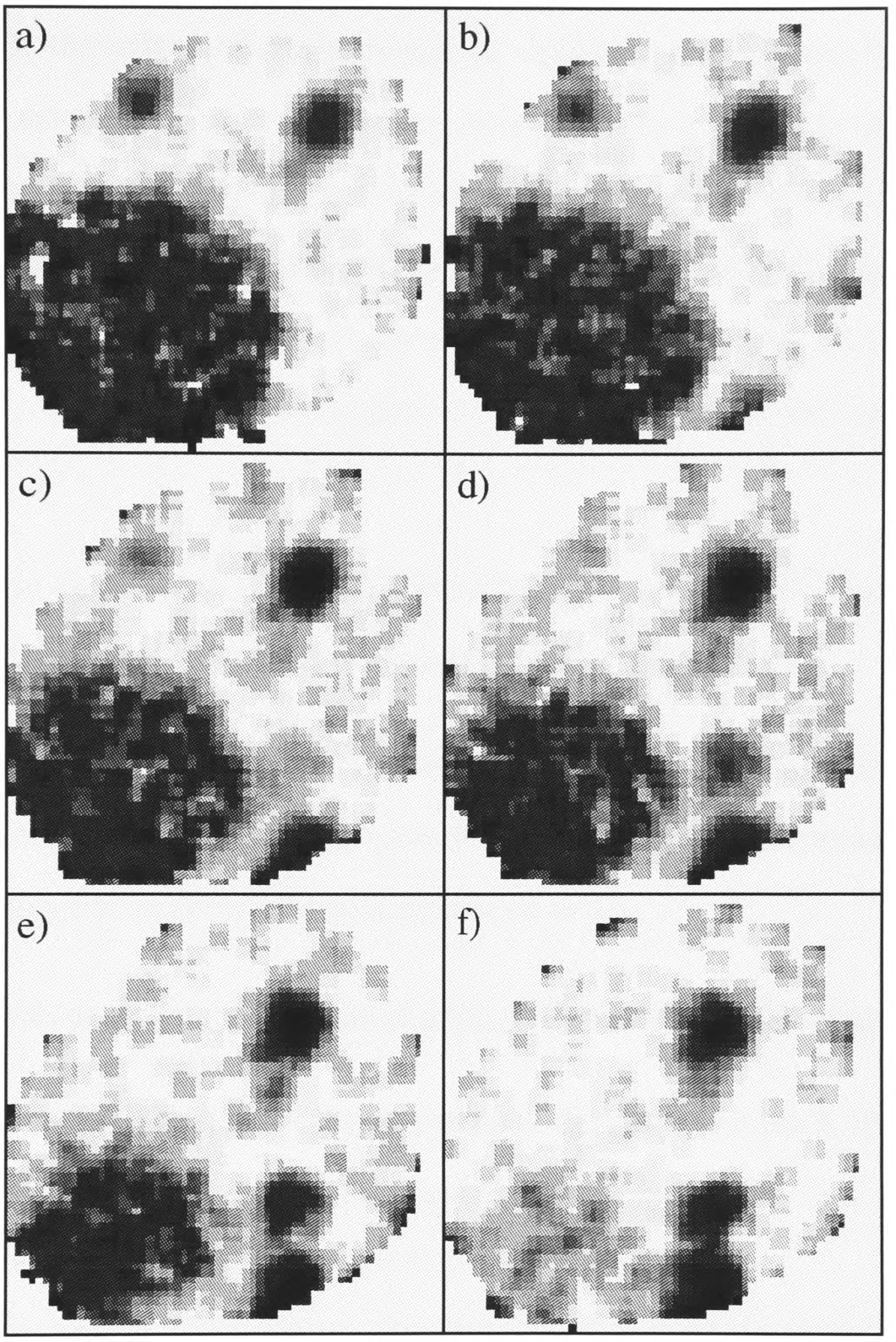

a) to f) show a sequence of composition maps (all solute species) slicing through the datafile showing the shape of the Al_3Zr precipitate as being clearly spherical. There are also some rod precipitates in the surrounding matrix which remain throughout the analysis. These precipitates are observed to move towards the Al_3Zr particle as it shrinks. This is due to a reduction in the local magnification effects as the precipitate evaporates. This sequence of images is the same as would be observed in the FIM image during evaporation except there is more chemical contrast. The scale calibration is inaccurate due to the local field effects.

Figure 5.35

showing the precipitate morphology. Some platelets of the same phase, Al_3Zr, were also observed at grain boundaries (Figure 5.36.c).

In Section 5.3.3, the effect of the presence of AlCuMg phase grain boundary precipitates was discussed. These precipitates, although mainly found in the 220°C material, were also found in small numbers in lower temperature heat treatments. TEM showed them to have a noticeably different morphology to the AlZnMgCu precipitates (Figure 5.36.b). They were also more prone to preferential dissolution. In FIM they showed up clearly, due to the different evaporation potential and also to the high copper content.

TEM analysis also came across an unidentified TiMg phase, and a CuFe rich phase, indexed as Cu_2FeAl_7; both with platelet morphologies (Figure 5.36.a.&d.).

Optical microscopy noted the presence of large precipitates strung along the rolling plane. EPMA found these to be 1-10microns in size and copper rich (probably also combined with other unwindowed elements such as Fe or Si).

Atom probe analysis observed the presence of a Mg_2Si phase in the 220°C material.

Generally, the number of these other phases present in this alloy was small. Due to the small volumes of analysis of all the techniques used in this work, few of these precipitates were encountered, except for the Al_3Zr grain refining phase.

5.6. Summary of precipitation in Al-7150.

Matrix strengthening precipitates.

TEM showed that as the ageing temperature increased:- the number density of precipitates decreased; the size of precipitates increased; the shape of the precipitates became more defined; and previous work showed that the precipitate structure changed from η' to η phase.

a) shows a large platelet precipitate in material aged at 120°C. The precipitate was found to be a MgTi rich phase. This phase was not identified as a known phase from its diffraction pattern or composition.

b) shows a very large grain boundary precipitate of a AlCuMg phase. The morphology of this phase is distinctively different to that of the usual $Mg(AlZnCu)_2$ precipitates. Precipitates of this phase were particularly common in the material aged at 220°C however some precipitates of this phase were found in all the aged materials analysed.

c) shows a Al_3Zr precipitate with plate-like morphology on a grain boundary in material aged at 120°C. This is unusual since most of the zirconium is present in the spherical grain refining particles.

d) shows a large platelet of Al_7Cu_2Fe phase. This was identified from the diffraction patterns obtained.

Figure 5.36

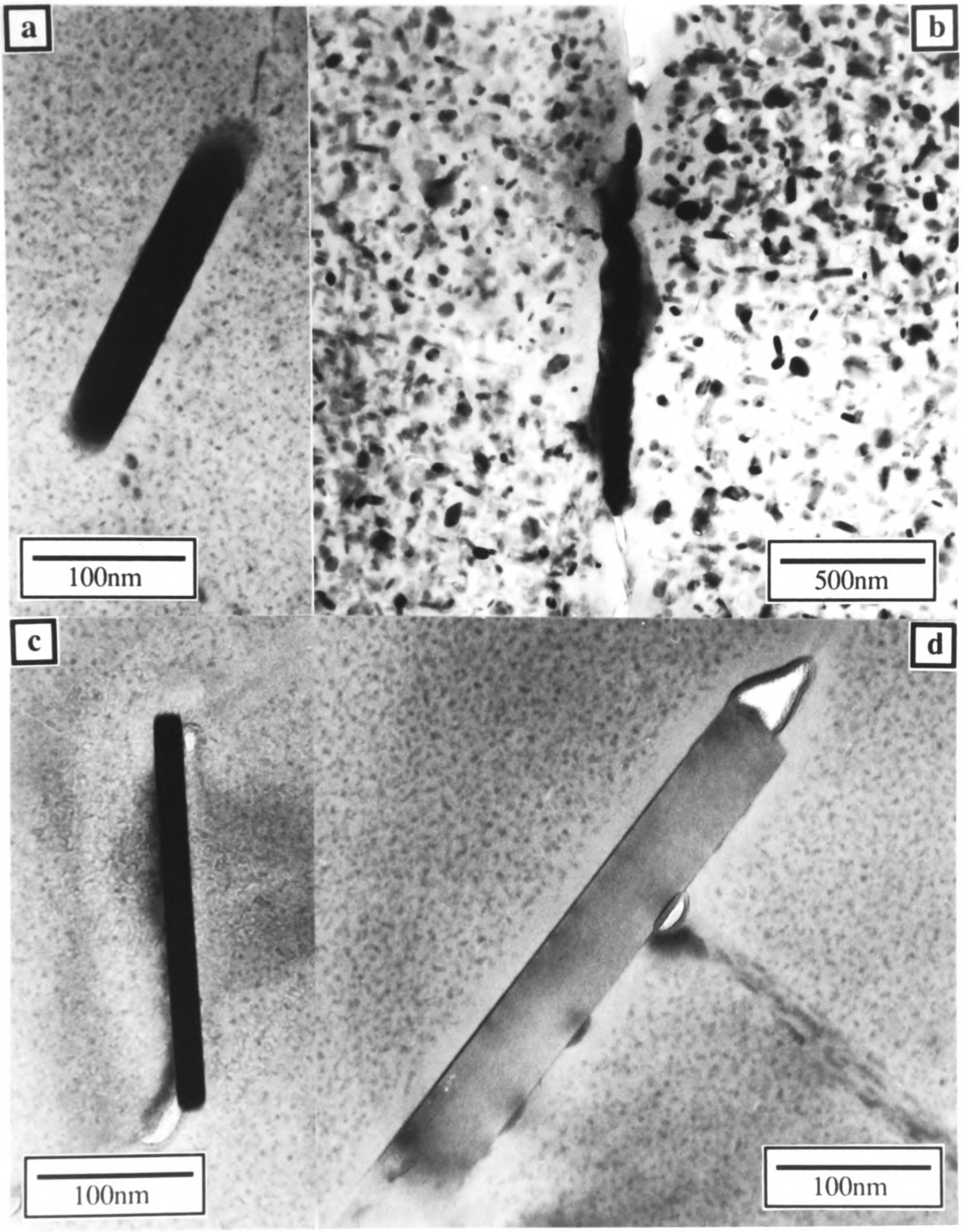
a
100nm
b
500nm
c
100nm
d
100nm

AP analysis was in agreement with the TEM observations of increasing precipitate size and spacing, with ageing temperature. In material aged at 120°C, the precipitates were found to be predominantly clustering of zinc and magnesium. For material aged at 150 and 180°C, the precipitates were found to be significantly enhanced in copper, as well as in zinc and magnesium. Also, as ageing proceeded, the total solute content of the matrix decreased, and thus the precipitates became relatively more enriched with magnesium, since most of the zinc was already associated with the precipitates from the early stages of precipitation.

POSAP 3-D analyses showed good visual comparison with the observations of TEM. Also, as the ageing temperature increased, the total solute content of the precipitates was observed to increase from 5-20% total solute in material aged at 120°C, to 20-50% total solute in material aged at 150°C, and upto 75% total solute for precipitates aged at 180°C. A wide range of scatter in the Zn/Cu : Mg ratio was found, but no dependence upon precipitate size or ageing temperature was observed. The precipitates all appeared to have a higher fraction of magnesium at their centres, although the reasons for this were unclear. This effect was not observed in the atom probe data; thus, it is suggested that it is an artefact of the POSAP data.

STEM analysis was inappropriate due to the close spacing and small size of the precipitates.

Grain Boundary Precipitates.

TEM showed that the microstructure of the grain boundaries varied widely, within each heat treatment and even along the same grain boundary, as the misorientation changed.

Due to the experimental difficulties of grain boundary analysis by atom probe techniques, only four precipitates in total were analysed; these analyses are presented in Chapter 6. There were insufficient analyses to draw any comparisons between heat treatments.

STEM analysis of the grain boundary precipitates showed no discernible change in the Zn/Cu : Mg ratio at different heat treatment temperatures. Considering all of the different grain boundary precipitates analysed, in all of the different specimens, there were remarkably small differences between the solute ratios observed.

220°C Material

The matrix strengthening precipitates in material aged at 220°C were sufficiently widely spaced for STEM analysis, which enabled comparison of the solute ratios from both matrix and grain boundary precipitates. This showed that the matrix strengthening precipitates contained relatively more copper and magnesium than the grain boundary precipitates.

Other Phases.

Several other precipitate phases were observed and identified. The most important type are the AlCuMg precipitates, since these affect the main alloying solute elements. These were observed in all heat treatments, although they were much more prevalent in the grossly overaged 220°C material, especially at the grain boundaries. They could partly account for the relatively lower levels of Cu and Mg in the grain boundary precipitates. Other phases observed included Al_3Zr, Al_7Cu_2Fe, Mg_2Si and a TiMg-rich phase.

Chapter 6. Grain boundary Analysis.

6.1. Introduction.

Much of the work on the alloy 7150 has been motivated by its poor SCC resistance at peak strength. SCC resistance may be improved, but only at the expense of strength. Chapter 1 contains a review of the current state of knowledge on the mechanisms of SCC. Since failure is usually intergranular, the microstructure and chemistry of grain boundary regions is thought to strongly affect the SCC susceptibility of this material. Several authors have used STEM X-ray analysis to investigate this hypothesis. The presence of hydrogen is necessary, but not sufficient cause, for SCC. The mechanism by which hydrogen interacts with the material to promote SCC is currently unknown.

The high strength of this material has been optimised by reducing the scale of the microstructure. The width of the precipitate-free zone has been reduced to approximately 35nm; and precipitates are densely distributed along the boundary. Figure 6.1 shows TEM micrographs of the grain boundary microstructure after each of the heat treatments used in this study. The grain boundary itself, is the region of misfit between the two crystals, and is known to be only one or two atomic spacings in width:- less than 0.5nm. Obtaining chemical information from the interface and surrounding regions, on this scale, presents extreme experimental difficulties.

The structures of different grain boundaries, within material having undergone the same heat treatment, vary widely. It must therefore be assumed that the properties of such boundaries, including the susceptibility to SCC, also differ. Mechanical failure occurs by the easiest path; thus it is the most susceptible boundaries that determine the bulk strength. Since a simple description of what controls the susceptibility is not available, it is not possible to select a particularly susceptible boundary for analysis. In order to conclude that the observed differences in chemistry actually correspond to the observed differences in properties, a large number of boundaries must be analysed and their differences clearly characterised. This has not proved possible in the 3 year project reported on here, due to many experimental difficulties. This investigation does,

a) Grain boundary region in material aged for 100hours at 120°C.

b) Grain boundary region in material aged for 20hours at 150°C.

c) Grain boundary region in material aged for 8hours at 180°C.

Figure 6.1.

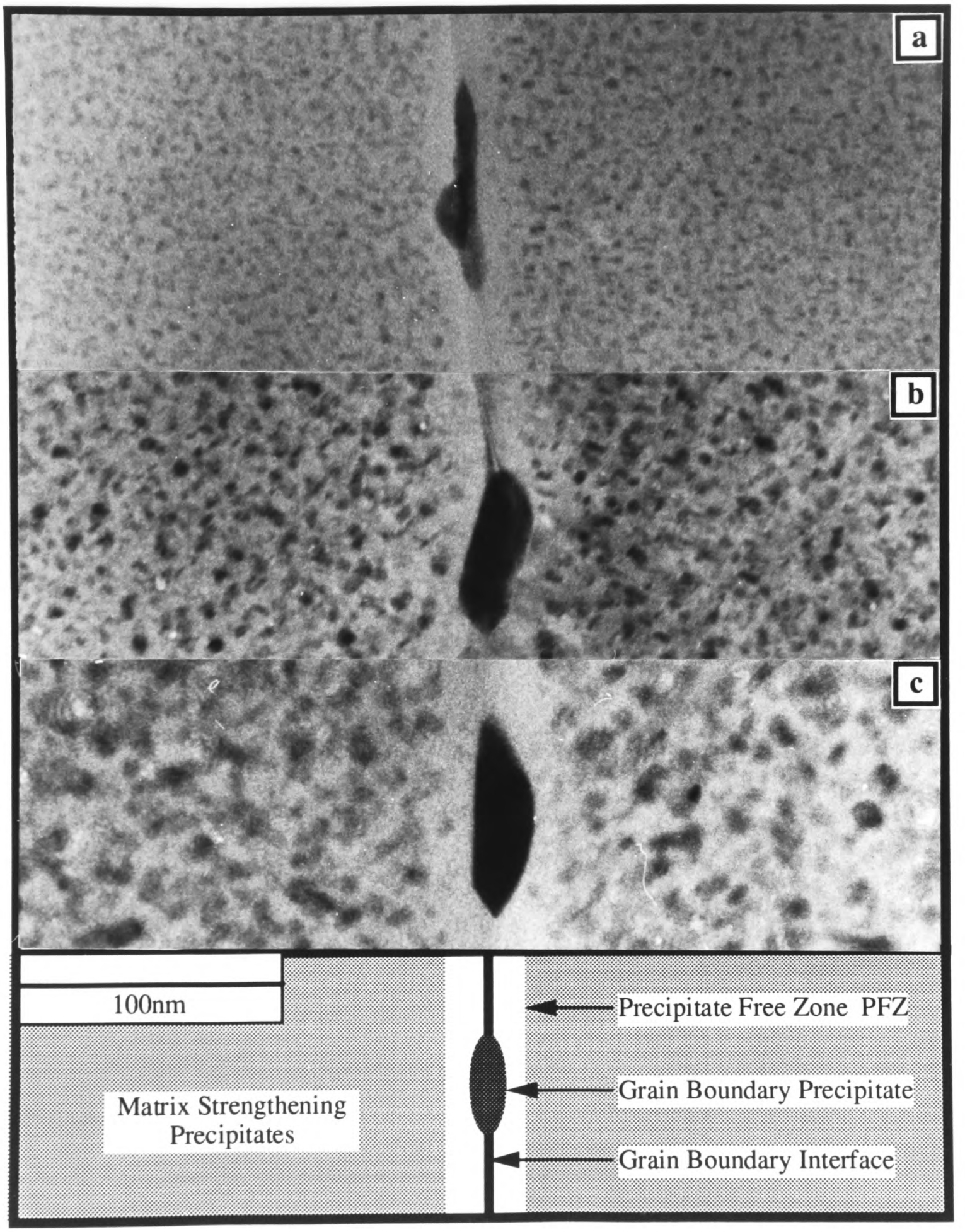
a
b
c
100nm
Precipitate Free Zone PFZ
Grain Boundary Precipitate
Grain Boundary Interface
Matrix Strengthening
Precipitates

however, provide information which should be used as a guide to the future direction of research having the long term goal of combating SCC.

Both high resolution STEM X-ray analysis and atom probe analysis have been used to investigate the chemistry of the grain boundaries in Al-7150 material. The applicability of each technique for interfacial analysis and the reliability of the data obtained will be considered in detail below.

6.2. Comparison of methods for grain boundary analysis.

In order to compare the suitability of STEM and atom probe methods for the analysis of grain boundary chemistry, an example grain boundary analysis, from material aged at 120°C, is presented for each of the two techniques. (All data given in atomic %.)

6.2.1. STEM X-ray analysis.

Since grain boundary precipitation is very dense, especially after this heat treatment, finding a suitable region of precipitate-free interface was often difficult. Any analysis is thus partially self-selected from the distribution of boundary structures present. In order to maximise the fraction of interface material contained in the volume of analysis the plane of the boundary was aligned to the incident probe direction. With this geometry, alignment of the probe over the boundary then becomes difficult, so a linescan mode was used, which optimised alignment and also provided a graphical representation of segregation to the interface. The maximum number of counts per spot in the linescan analysis is less than the number of counts possible in a normal spot analysis, due to specimen drift, thus the composition determined will be statistically less accurate. A linescan, and the corresponding spot analysis data, from the same boundary are compared in Figure 6.2. Both methods clearly show the presence of solute segregation to the interface. The segregants are primarily magnesium and copper, with slight enhancement of the zinc. Comparison of the linescan values and the spot analysis values shows very good agreement. The scatter due to inaccuracies in the positioning of the spot analyses outweighs any improvement in the counting statistics; thus, the

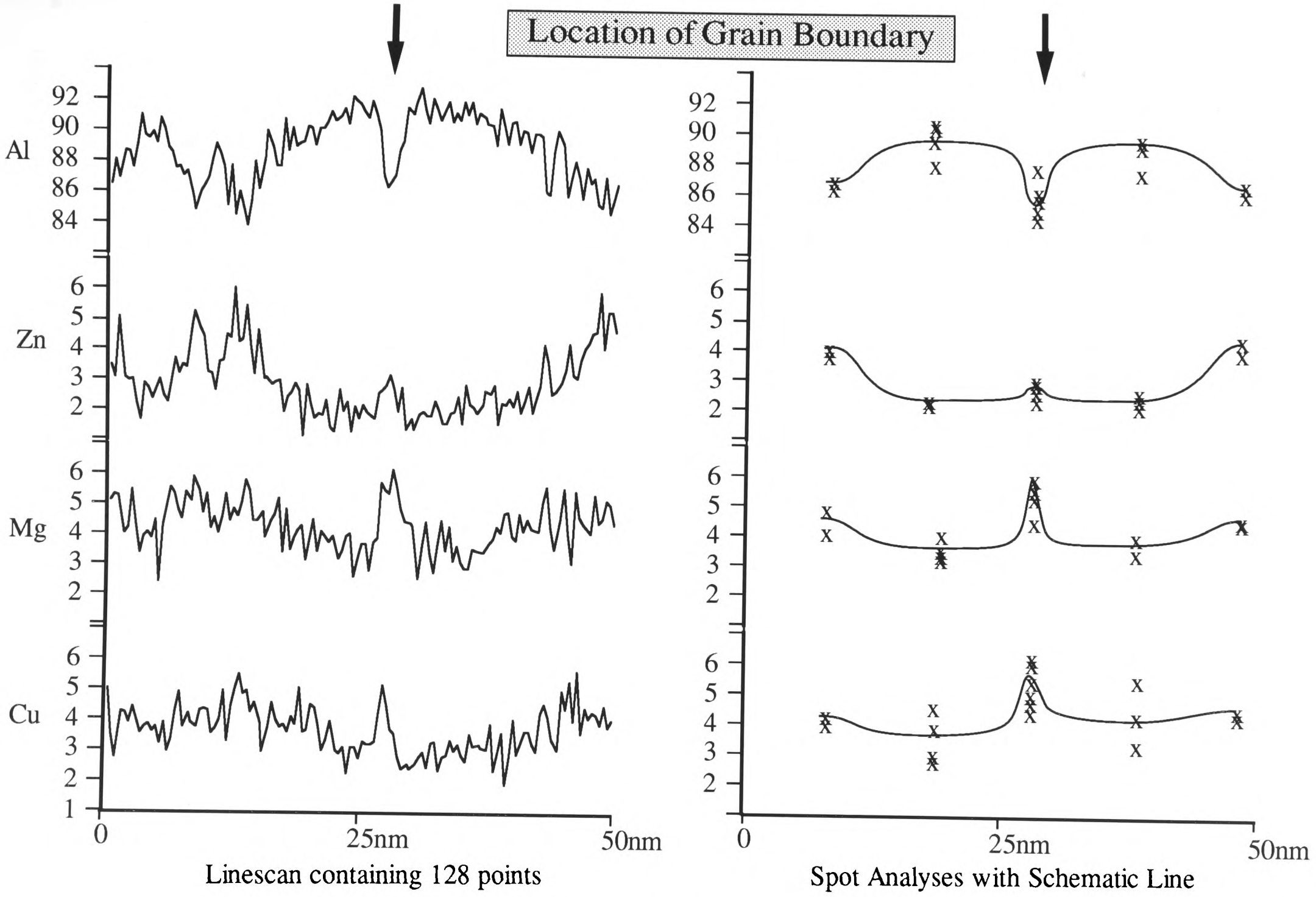

Figure 6.2 Comparison of the detection of grain boundary segregation by a linescan method and by a spot sampling method.The levels of segregation detected are very similar.

linescan with a graphical representation of the interface segregation is statistically preferable. Quantification of the chemistry of this alloy has already been shown to be inappropriate (Chapter 2), but a method of elucidating an approximate level of segregation is needed if different linescans are to be compared. The level of segregation has therefore been calculated as a percentage enhancement, over the solute levels detected in the matrix, on each side of the grain boundary

6.2.2. Atom Probe analysis.

AP analysis of an interface is always complicated by the difficulty of preparing a specimen which contains a boundary within the very small region of analysis. Since there is very little chemical information obtainable from the image alone, the grain boundary may be only faintly visible. It is therefore hard to select a region of the boundary which does not include grain boundary precipitates. Typically, a grain boundary analysis starts in the matrix of one grain and probes through into the other grain. For a heavily decorated grain boundary, most analyses will touch upon a precipitate; and because the technique averages the composition across the small area of analysis, if both precipitate and boundary are present within the area of analysis, the contribution of the precipitate will mask any contribution from the boundary. Also, since this analysis technique is destructive, only a few analyses across each boundary are possible. Figure 6.3 shows an example of an analysis across a boundary, with a clear zinc contribution from a precipitate and an indeterminable contribution from the boundary interface itself.

6.2.3. POSAP analysis.

POSAP analysis is better suited to the analysis of interfaces, due to the ability to select the data corresponding to the segregated boundary from a 3-D volume of analysis, which contains matrix, grain boundary and grain boundary precipitates. However, detecting the location of the boundary, if segregation levels are very low, can be difficult. Precise boundary location showed up most clearly due to the effect of the local field variations upon the charge of the ion species detected. Figure 6.4 shows images of the distribution of several ion species within a volume of analysis containing a

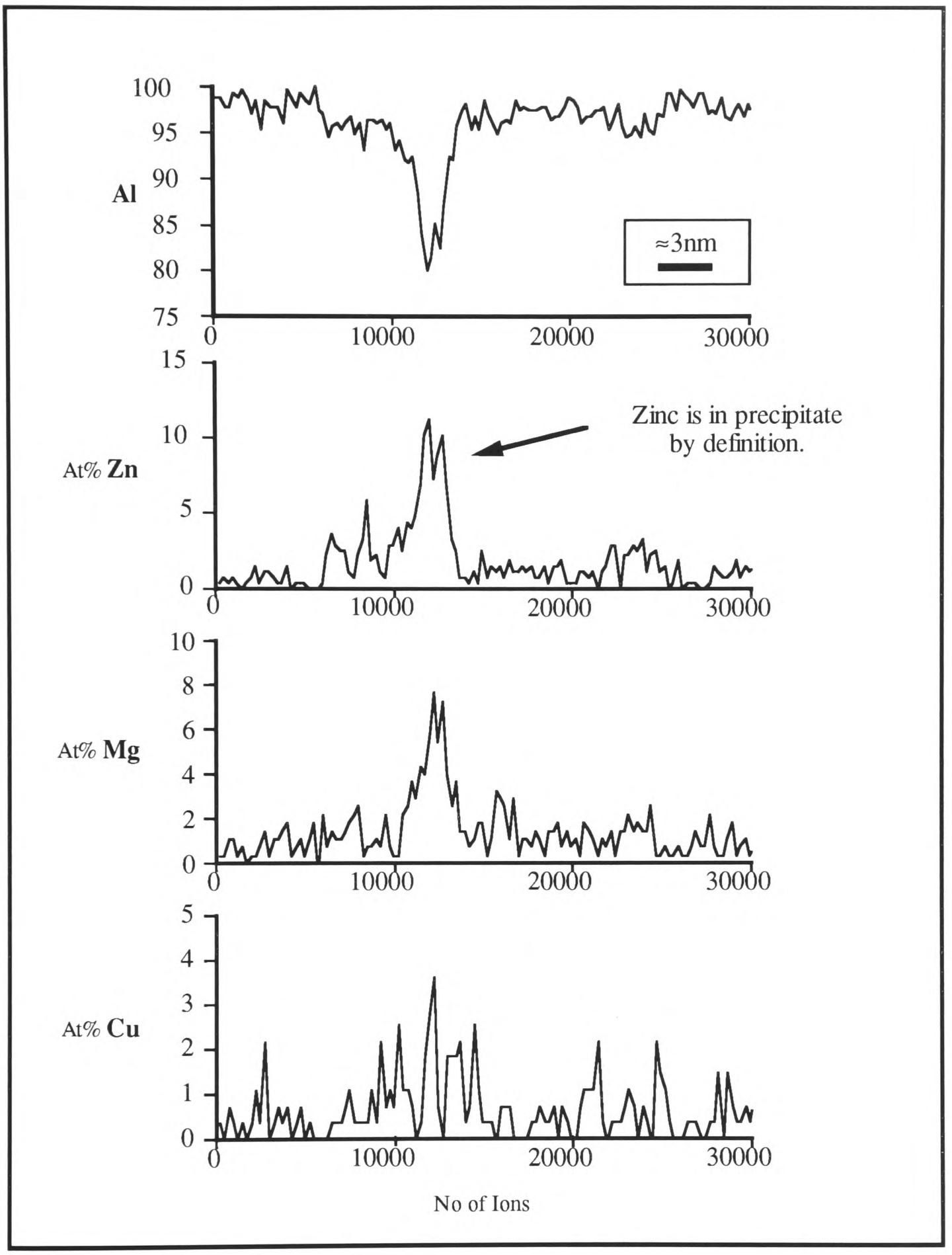

Figure 6.3. showing an AP composition profile across a grain boundary. Due to the presence of the zinc peak there must be a precipitate on the boundary. The solute content of the precipitate will mask any boundary solute.

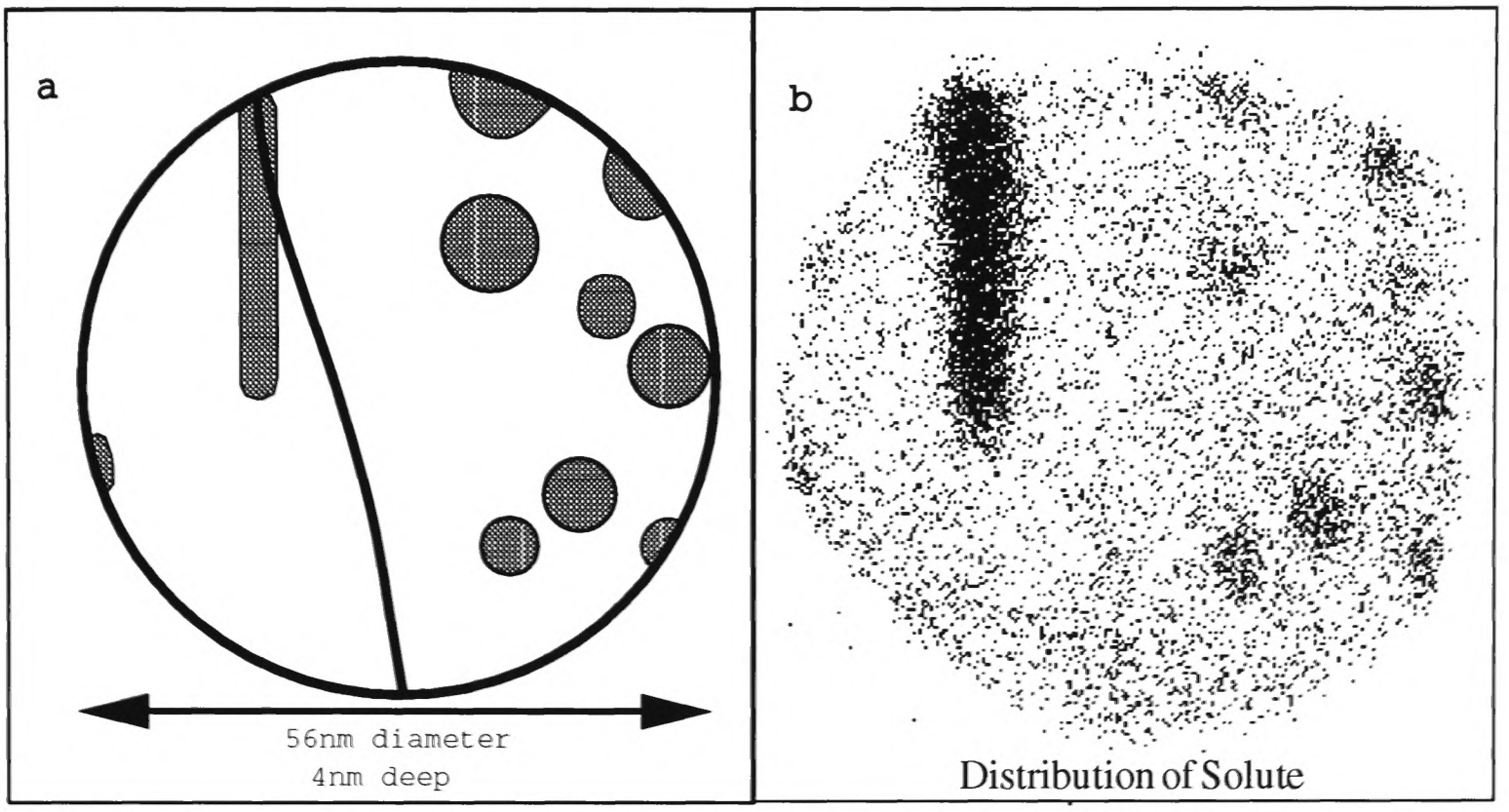

a) diagram of the microstructure analysed showing a large platelet precipitate on a boundary and smaller precipitates in the matrix.

b) image of solute ion species detected (Mg,Cu/Zn) shows the precipitates however the boundary is not easily visible due to the low solute levels and the inclination to the analysis direction.

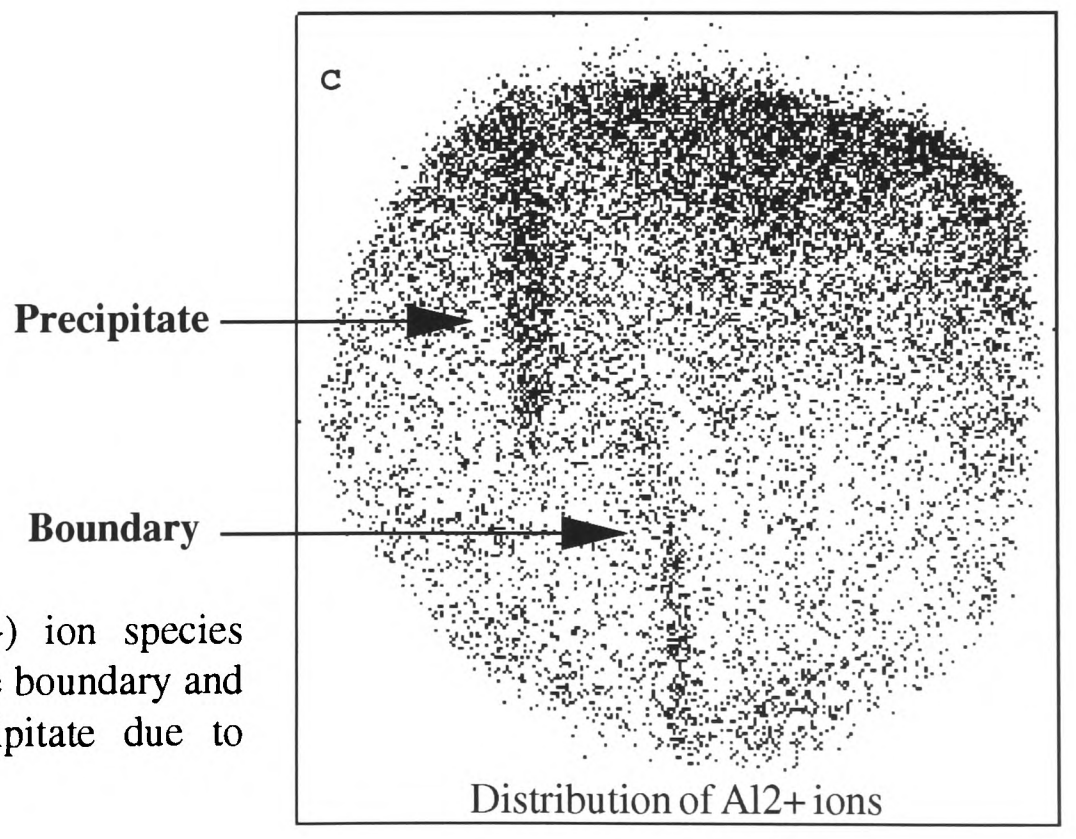

c) image of the Al(2+) ion species shows the location of the boundary and the large platelet precipitate due to local field effects.

Figure 6.4

boundary. The large grain boundary precipitate is clearly visible in the solute species (b), however the location of the segregated grain boundary is unclear. However, viewing the Al^{2+} species, (c), shows the location of both the grain boundary precipitate and the precipitate-free region of the boundary. Once the location of the boundary is identified, the region around the boundary may be selected and a composition profile formed, similar to that used in AP analysis. With POSAP data, however, it is possible to optimise the orientation of the boundary with respect to the profile direction, and also control the area of boundary selected, such that contributions from precipitates are avoided. Due to the large width of analysis, the depth of material analysed is usually small, and the number of solute atoms associated with the interface, at such low concentrations, is also small. This causes a large scatter in the composition profile formed. The accuracy of the compositional information obtained is further reduced by the lower mass resolution of the detector, as discussed in section 4.5.

6.2.4. Summary.

Both STEM and atom probe methods can detect interface segregation, even on densely precipitated boundaries. Both techniques have detected magnesium and copper segregation.

STEM enables clear qualitative detection of the presence of segregation, however attempts at quantification are inappropriate for this alloy. AP analysis can give good quantification of the interface region, however solute segregation is usually masked by the presence of the precipitates. POSAP analysis enables visualisation of the precipitates and boundary microstructure. This allows accurate selection of the grain boundary region, giving more precise identification of the location of the segregation, but less accurate compositional information.

6.3. STEM Grain Boundary Analysis.

The aims of interface analysis are: firstly, to be able to detect the presence of segregants to the interface; and secondly, to quantify this segregation, either by relative comparison for many interfaces, or by calculation of an absolute composition (given in atomic %.).

The geometry of interface analysis is shown in Figure 6.5. This shows the interface to be much narrower than the probe size. FIM investigations of equilibrium grain boundary segregation have shown that the segregants are contained on the boundary plane, which is of the order of single atom in width. For the purpose of any subsequent calculations, the width of the interface will be taken as 0.5nm. The unit cell of aluminium is face centred cubic, with a=0.4nm, and thus 0.5nm is slightly less than two atoms in width. Since the incident probe size is approximately 2nm, and subsequent beam broadening may increase this beyond 5nm, the fraction of boundary material contained in the excited volume is small. The boundary should be oriented parallel to the probe direction to maximise the fraction of boundary atoms excited.

The detectability of segregation at an interface is determined by the combined effects of beam broadening and counting statistics[98]. Decreasing the probe size, decreasing the foil thickness and increasing the accelerating voltage, all improve detectability. However, acting against this is the statistical limit of detection. The significance of any measurement is related to the spectrum counting statistics; in terms of the ratio of peak counts to background counts and the errors associated with each of these.

Quantification of grain boundary segregation from a stationary spot is limited by several factors. The detection of a peak in the spectrum must be clear, enabling removal of the background with good statistical accuracy. To obtain good statistics the number of counts detected must be high; thus the level of segregation must be high, the counting time long and the probe size small. Alignment of the probe over the boundary is difficult; thus repeated sampling of the boundary is necessary to ensure optimum detection of the segregation. Both Hall[99] (Fe in MgO) and Michael[100] (Bi in Cu) used stationary spot analyses to show grain boundary segregation, however in both these

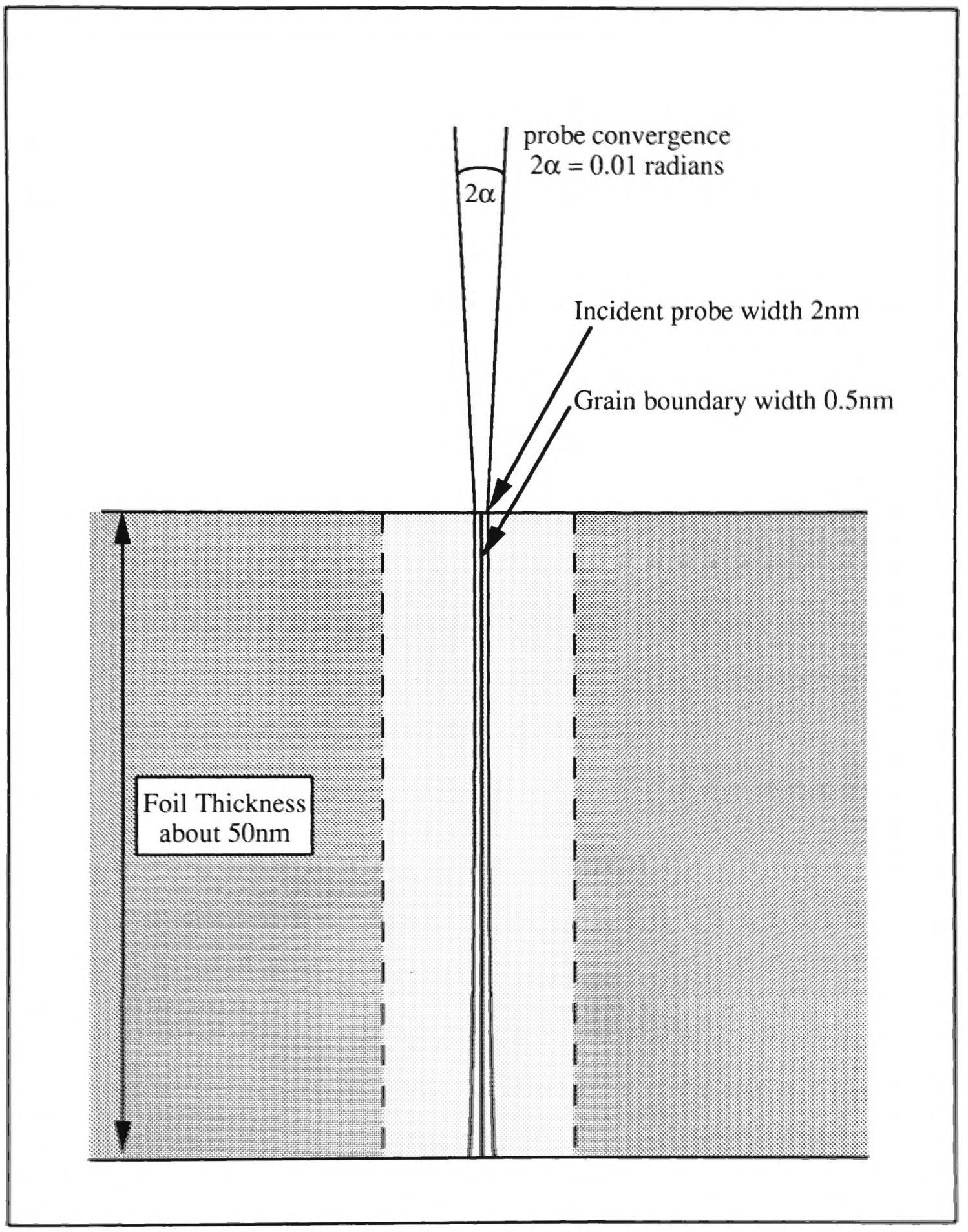

Figure 6.5 Schematic of the optimum alignment of a grain boundary for STEM X-ray analysis

examples the matrix solute levels are negligible (≈5360ppm Fe and 0.002% Cu). Sampling of the boundary was therefore relatively simple, and the solute enhancement detected was very high. In order to quantify the segregation, it is then necessary to estimate the probe size, the boundary width and the geometry of the excited volume after beam broadening. In these examples the matrix solute content was so small that all the solute detected could be attributed to the interface.

In work by Grovenor[101] (As in Si), the levels of solute were so low that extremely long counting times were required and drift of the specimen became limiting. Since alignment of a stationary probe is visual, repeated correction for drift is tedious and results in repeated alignment errors. A method for drift correction was developed using a linescan method. A line of 38 points was used, and the bright field intensity of the interface image was monitored and aligned to one spot in the linescan. The use of a linescan gave clear graphical representation of the segregation and ensured optimum alignment of the probe over the interface. Integration of the area of the segregation peak gives the total excess solute contained within the boundary, and by making a suitable estimation of the width of the boundary, the composition of the boundary may be determined.

In this work the matrix solute content is quite high, thus repeated spot sampling of the interface (to ensure optimum alignment of the probe) introduces real positional variations in solute content, which reduce the statistical benefits of sampling. The linescan maintains spatial correspondence between the spots; clearly showing the location of the boundary. On the microscope used in this work, drift correction was not possible, thus the statistics of each spot of the linescan was fairly poor, being limited by the specimen drift (and also the specimen contamination). However, the graphical representation of the segregation, and the guarantee of optimum alignment, meant that the linescan was preferred.

The linescan used in this work consisted of a sequence of 128 spot analyses with a linear separation of less than the probe diameter. (x2M magnification gives a spot separation of <2nm between analysis points). The probe was stopped for 100ms at each

point, and the total window counts for each element were recorded. This was repeated, for each linescan, typically 50 times, to improve the counting statistics of each separate point before specimen drift and contamination were deemed too severe to continue analysis on that area. Figure 6.6 shows an untypically clear example of a linescan obtained by this method.

Attempts at absolute quantification in this system are not appropriate, as discussed previously, thus it is the relative enhancement of solute at the interface that is of interest. This is calculated, as shown in Figure 6.7, by integration of the area under the linescan peak, and then attributing all of the excess solute to the width of one linescan step. Knowing the magnification (usually x2M), and the length of line on the screen (10cm), gives the actual step width. Correcting to an assumed boundary width of 0.5nm then gives a measure for the actual solute levels on the boundary.

Since most of the data for 120°C material was collected by stationary spot analyses, a method of comparison of the spot analysis measurements and the linescan measurements is needed. In the previous section on comparison of GB analysis techniques, it was shown that there was quite good agreement between linescan and spot analysis values. The calculation of the enhancement values for a spot analysis requires an estimate of the probe size. In analysis a wider probe results in a lower measured peak value. Using a probe size estimate of 2nm on a boundary of 0.5nm gave lower segregation enhancement than the corresponding linescan data of the same boundary, thus a probe size of 2.5nm was used to give very similar enhancements for the linescan and spot analysis data from this boundary. This factor was then applied to the other GB spot analyses data.

Figures 6.8-6.10 show the actual composition levels detected for each boundary plus the two PFZ regions either side of the boundary. The levels of zinc detected in the PFZ (Figure 6.8) are quite variable, and also show some correlation with the copper levels, due to slight peak overlap between ZnKα and CuKβ. Certain boundaries show strong segregation of zinc, indicating the presence of a very thin precipitated layer at the boundary. The levels of magnesium detected in the PFZ (Figure 6.9), are extremely

STEM Linescan of material aged at 180°C

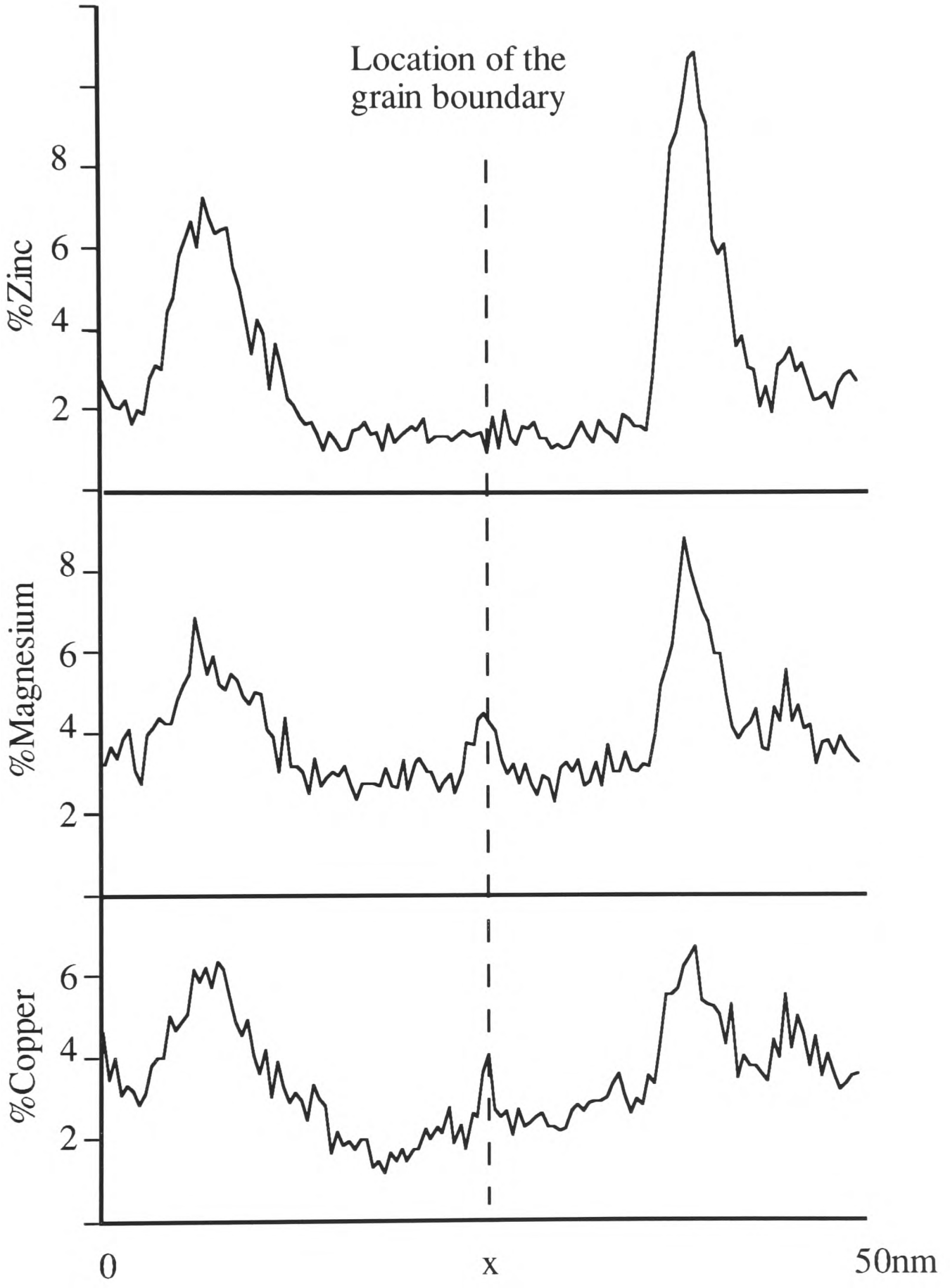

Figure 6.6 A good example of a linescan showing the segregation of magneisum and copper at the grain boundary while the matrix strengthening precipitates either side of the PFZ contain Zinc, Magnesium and Copper.

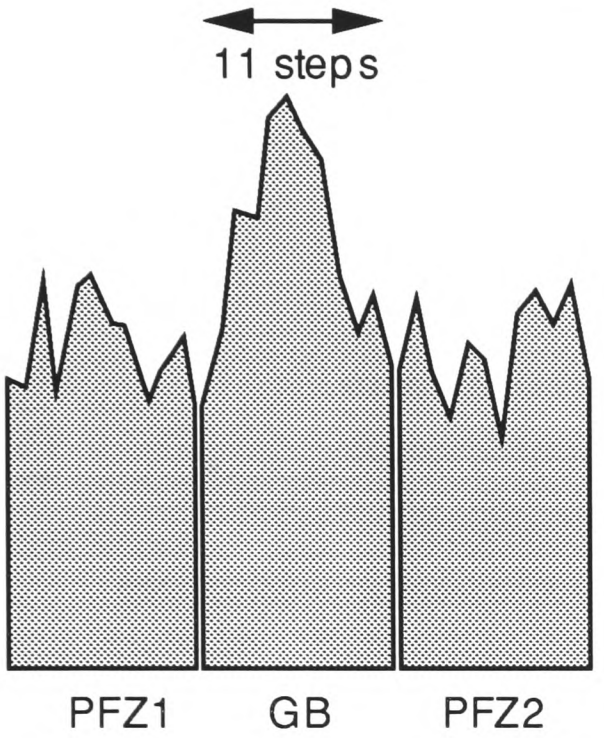

Counts	PFZ1	GB	PFZ2
Al	2534	2344.5	2325.4
Zn	40.5	36.5	33.6
Mg	82.4	94.5	76.5
Cu	45.1	67.3	66.1

%	PFZ1	GB	PFZ2
Al	93.8	92.2	92.9
Zn	1.5	1.4	1.3
Mg	3.0	3.7	3.0
Cu	1.7	2.6	2.6

Background = average of either side of GB

Excess = no of steps x (GB composition - Background composition)

Magnification = x2M Width of step = 0.39nm Estimated GB Width = 0.5nm

%GB = Excess x (0.39 / 0.5) + Background

	Background	Excess	%GB
Al	93.4	-12.8	83.3
Zn	1.4	0	1.5
Mg	3.0	7.3	8.7
Cu	2.1	5.4	6.4

Figure 6.7 Example calculation of the grain boundary composition .

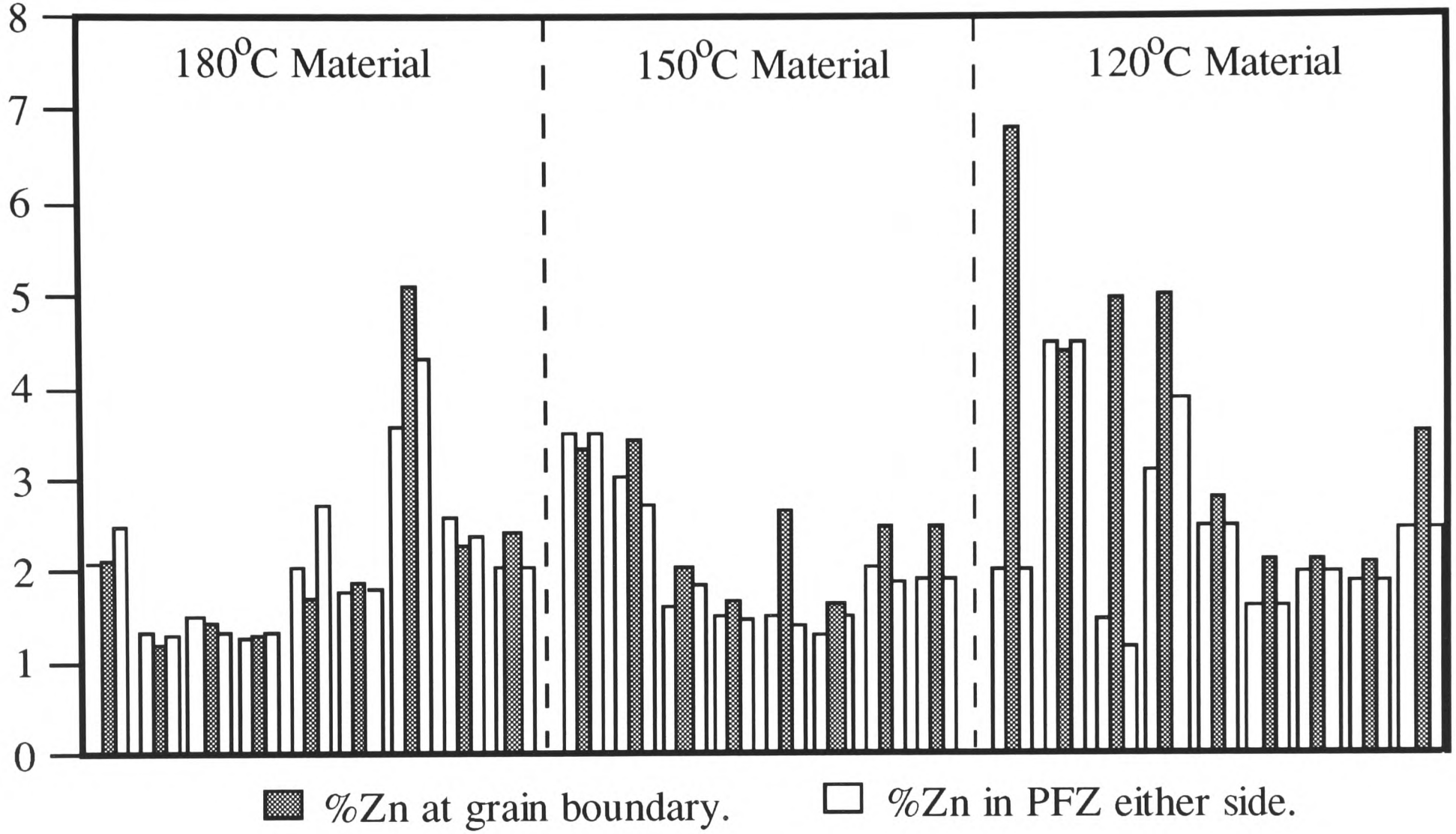

Certain grain boundaries show high levels of zinc indicating the presence of precipitates on the boundary not visible in the image. The levels of zinc in the PFZ are quite variable partly due to peak overlap with the copper.

Figure 6.8. Plot of the %Zinc levels detected at the grain boundaries analysed for each material.

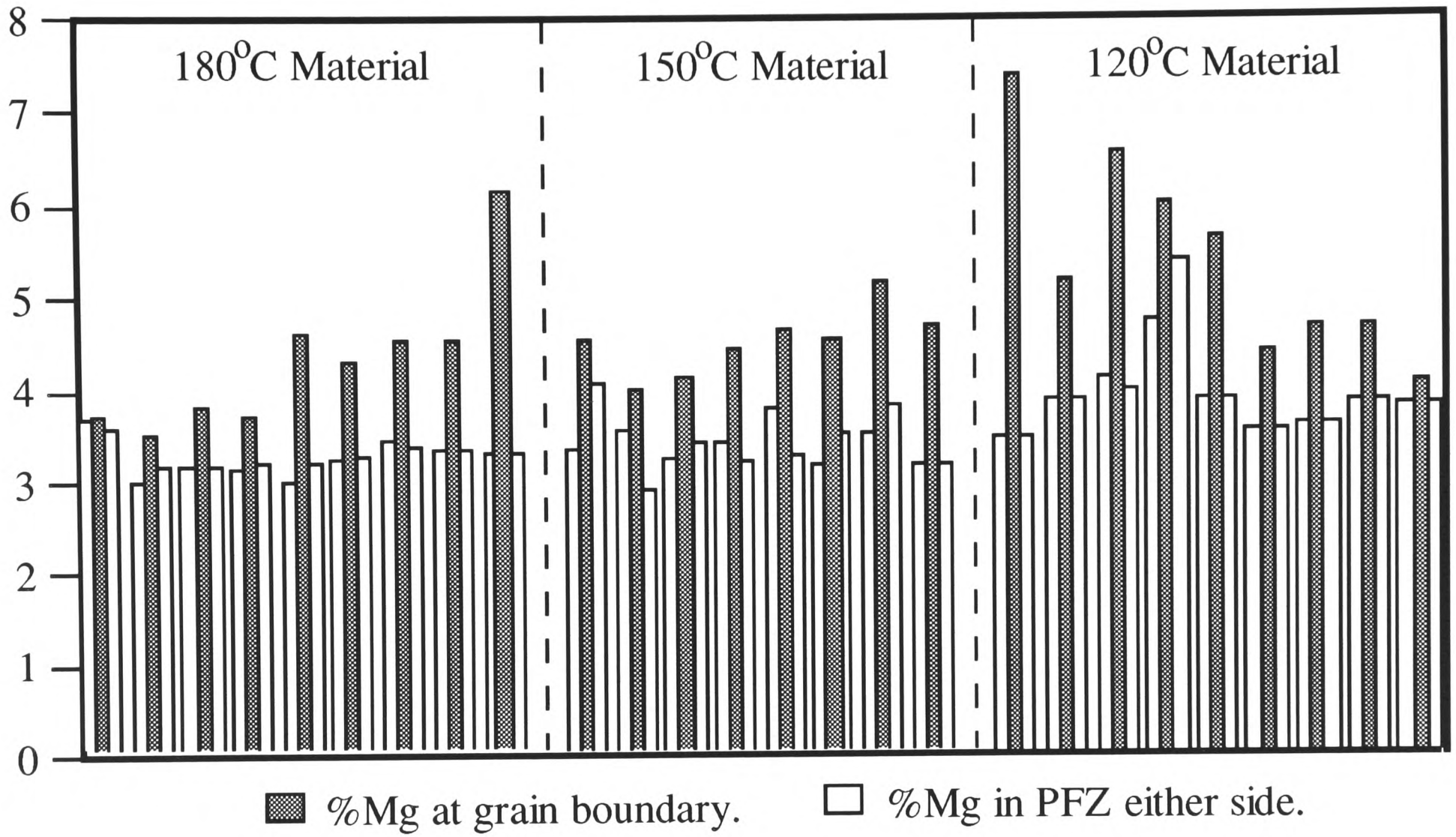

All grain boundaries show magnesium segregation. The levels of magnesium in the PFZ are very uniform and consistently too high due to peak overlap with the aluminium.

Figure 6.9. Plot of the %Magnesium levels detected at the grain boundaries analysed for each material.

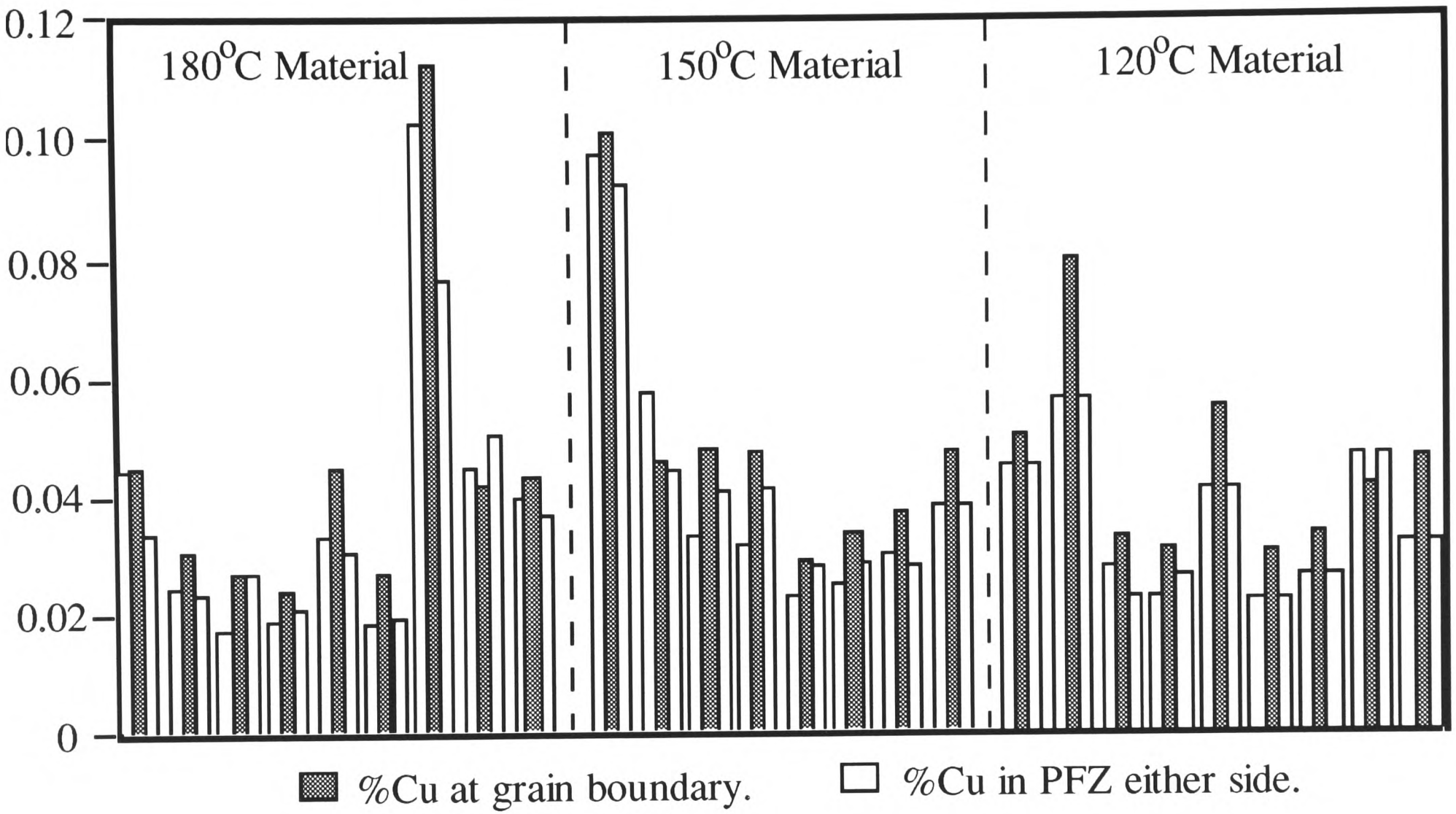

The copper levels detected show wide variability between boundaries due to the contributions of surface deposited copper.

Figure 6.10. Plot of the %Copper levels detected at the grain boundaries analysed for each material.

similar, with a slight reduction with increasing ageing temperature. The absolute levels detected still contain all the background counts, and are thus too high. In addition, the statistical variations are smoothed by the more constant contributions from the aluminium peak. All of the grain boundaries analysed showed signs of magnesium segregation. The copper levels detected in the PFZ (Figure 6.10), show wide variability due to uncontrollable contributions from surface deposition. Most of the boundaries analysed showed signs of copper segregation, although differences in surface deposition between the two grains on either side of the boundary often confused matters.

Figures 6.11-6.13 show plots of the estimated grain boundary enhancement levels, compared to the PFZ levels, for each boundary. Certain boundary analyses show very strong enhancement of the zinc which can be attributed to grain boundary precipitates. However, the other boundaries show a gradual reduction in enhancement of zinc with increasing ageing temperature. Due to the depletion profile in the PFZ leading up to the boundary, and the lack of boundary enhancement due to the precipitation, depletion of the boundary was sometimes observed, leading to the possibility of negative corrected compositions. The grain boundary enhancement levels of the magnesium show a wide variability between boundaries and no particular trend between different ageing temperatures. One particular analysis shows very strong magnesium enhancement with more than 30% magnesium at the grain boundary plane. This could be a magnesium rich interface phase as suggested by Scamens[45]. This was the only such Mg rich boundary observed, and only became notable during data analysis, so no further information is available. The levels of copper enhancement are generally lower than the levels of magnesium enhancement. The copper enhancement shows wide variability between boundaries and does not necessarily correlate with the degree of magnesium enhancement.

Investigation of the variation of the segregation levels along the grain boundary was attempted by simple spot analysis and also by a more sophisticated sequential linescan technique[102]. The results of each of these showed that segregation along the boundary

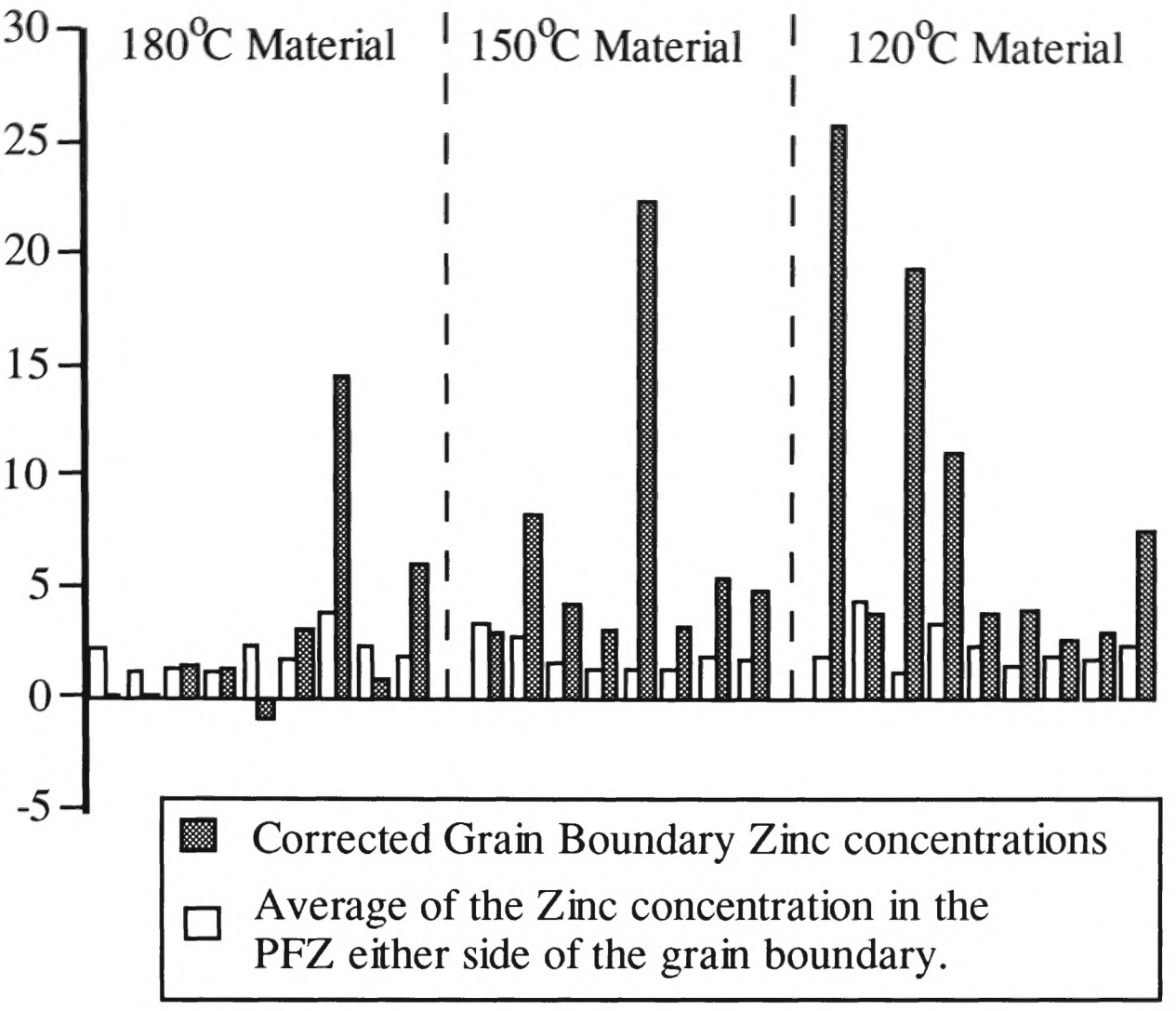

Certain boundaries show high levels of zinc which correlate with high levels of magnesium and thus are precipitates.

There is a reduction in the levels of zinc detected with increasing ageing temperature.

Depletion profiles in the PFZ leading up to the grain boundary mean that the grain boundary concentration can be sufficiently lower than the PFZ concentrations that correction results in negative concentrations. This just shows the limitations of the statistical accuracy for such low concentration levels.

Figure 6.11

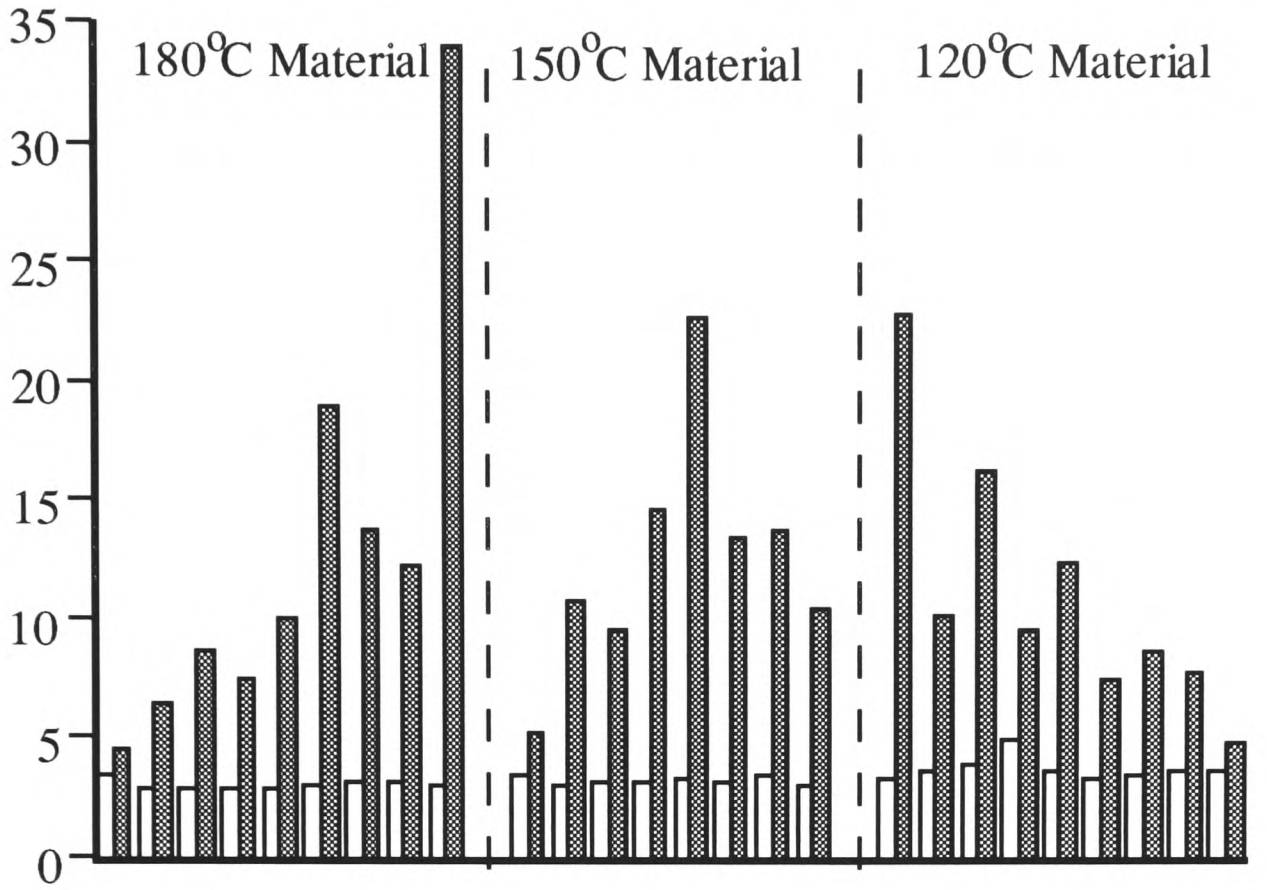

All grain boundaries show segregation of magnesium.

There is no clear trend between heat treatments except a slight reduction levels of magnesium in the PFZ with increasing ageing temperature.

One particular analysis shows extremely strong segregation of magnesium with no correlation with zinc or copper segregation.

Figure 6.12

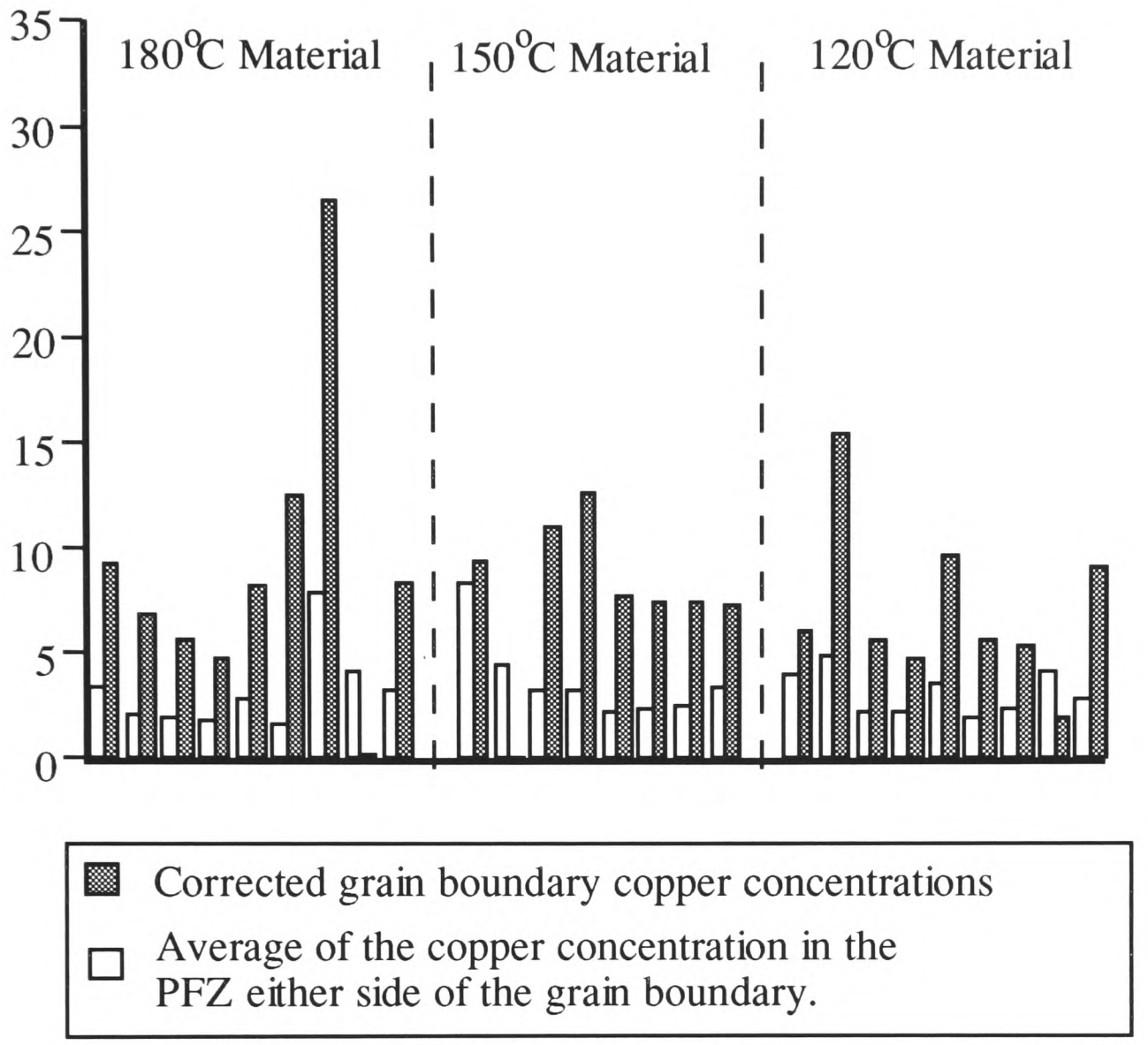

Most grain boundaries show segregation of copper.

There is a wide variability in both the grain boundary segregation levels and the PFZ levels, with no clear trend between heat treatments.

There is correlation between the copper and zinc PFZ levels due to peak overlap and the variability in copper PFZ levels is due mainly to surface deposition of copper.

Figure 6.13

was continuous along the boundary interface between precipitates. However, no diffusion profile of solute along a grain boundary was determined by this method; primarily due to limited accuracy at these levels of solute, and also due to the through foil thickness integration of the technique. Figure 6.14 shows a profile along a grain boundary moving from a precipitate onto the boundary.

Summary

STEM grain boundary analysis of material aged at 120°C, 150°C and 180°C showed grain boundary segregation of copper and magnesium in all treatments. Some boundaries showed high enhancements of both zinc and magnesium which were interpreted as being precipitates although there was no visible sign of precipitation. Most boundaries showed variable amounts of segregation of just magnesium and copper. There was no clear correlation of the magnesium segregation with the copper segregation. There was no trend in the levels of segregant detected between the different heat treatments. Quantification of the levels of enhancement assuming a boundary width of 0.5nm showed total solute levels of approximately 20%.

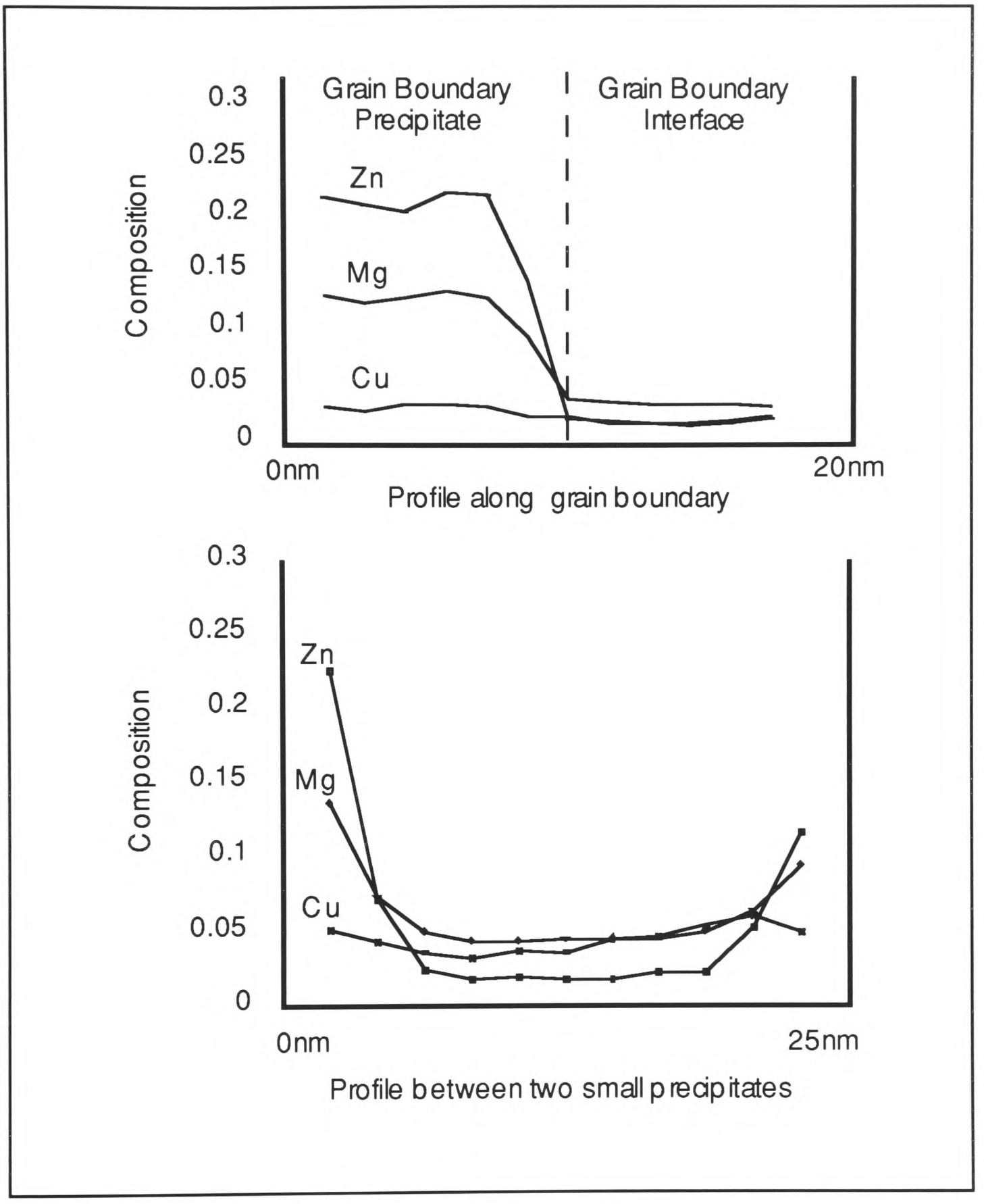

Figure 6.14 Two spot analysis profiles along grain boundaries

6.4. POSAP Grain Boundary Analysis.

The experimental difficulties of obtaining POSAP data from a grain boundary have been described earlier in Section 2.2.2. Due to these problems, only 5 analyses were obtained. These were:

i) pjw013 Solution treated material;

ii) pgb0101&2 Solution treated material;

iii) paul15/3/93 Solution treated material;

iv) pgb12010 120C material; and

v) paul3/6/93 120C material.

Due to the small number of boundaries analysed, each analysis will be presented separately, with a brief discussion of the salient features illustrated by the analysis. At the end of this section a more general discussion of grain boundary analysis, by this method, will be presented.

6.4.1. pjw013 Solution treated material.

Figure 6.15 shows TEM micrographs of the various stages of analysis of this specimen. After initial polishing a high angle grain boundary was observed, perpendicular to the tip but about 2μm from the end region, and thus outside the analysis range (Figure 6.15.a). A single electopolishing pulse of 15ms in 10% perchloric acid in acetic acid was applied which removed a large amount of material, so bring the boundary to within 500nm of the specimen tip (Figure 6.15.b). However, it also coated the tip in a deposit that was resistant to washing, and to further electropolishing (Figure 6.15.c). Analysis was attempted anyway, realising that a large amount of evaporation would be necessary to reach the boundary. The location of the boundary with respect to the specimen surface was checked again after imaging to 7kV (Figure 6.15.d). After further imaging the boundary became visible as a bright line in

a) shows a TEM dark field micrograph showing a brightly imaging end grain of a FIM specimen after initial back-polishing. The grain boundary is perpendicular to the axis of the specimen and is too far away from the end of the specimen to be suitable for atom probe analysis.

b) shows a TEM dark field micrograph of the same specimen as shown above but after a single electropolishing pulse of 15ms in 10% perchloric acid in acetic acid. This has brought the grain boundary about 1.5μm closer to the end of the specimen. The boundary is still about 400nm from the end of the specimen and ideally should be brought closer to the end of the specimen by applying another pulse however the surface proved resistant to electropolishing using a 4ms pulse.

c) shows a TEM dark field micrograph of the same grain as above at a higher magnification showing the presence of a surface deposit resistant to further electropolishing. Although the boundary is rather far from the specimen tip atom probe analysis was attempted anyway.

d) shows a TEM dark field micrograph of the specimen after field evaporation to 7kV. The specimen still requires much evaporation to bring the grain boundary to the surface of the specimen.

Figure 6.15

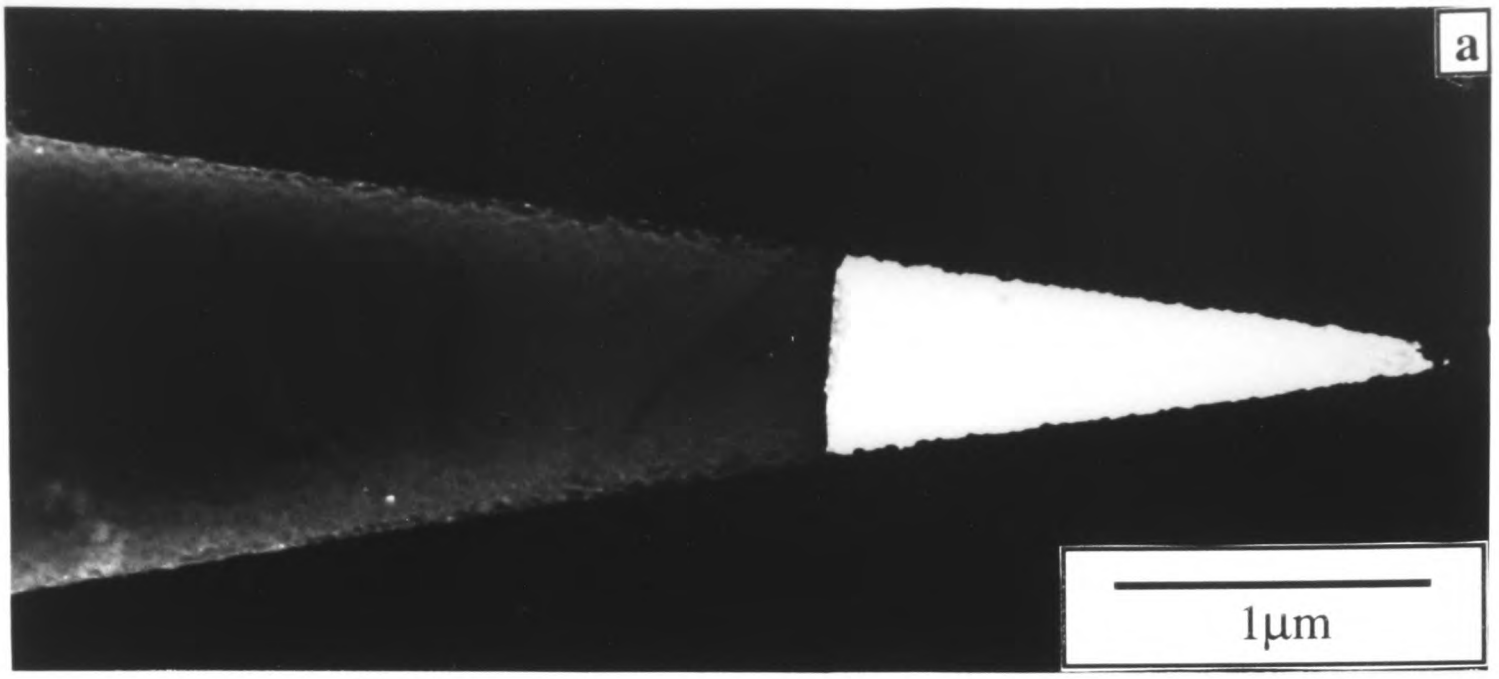
a
1μm

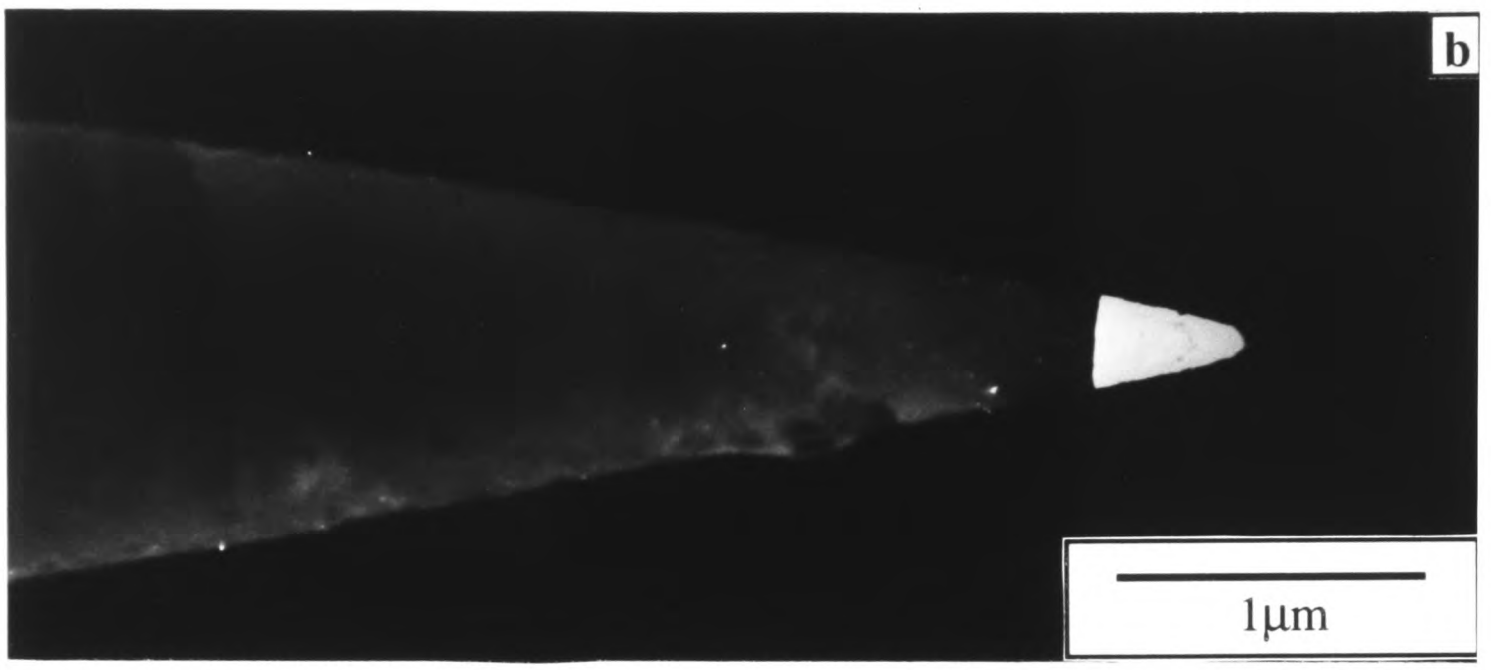
b
1μm

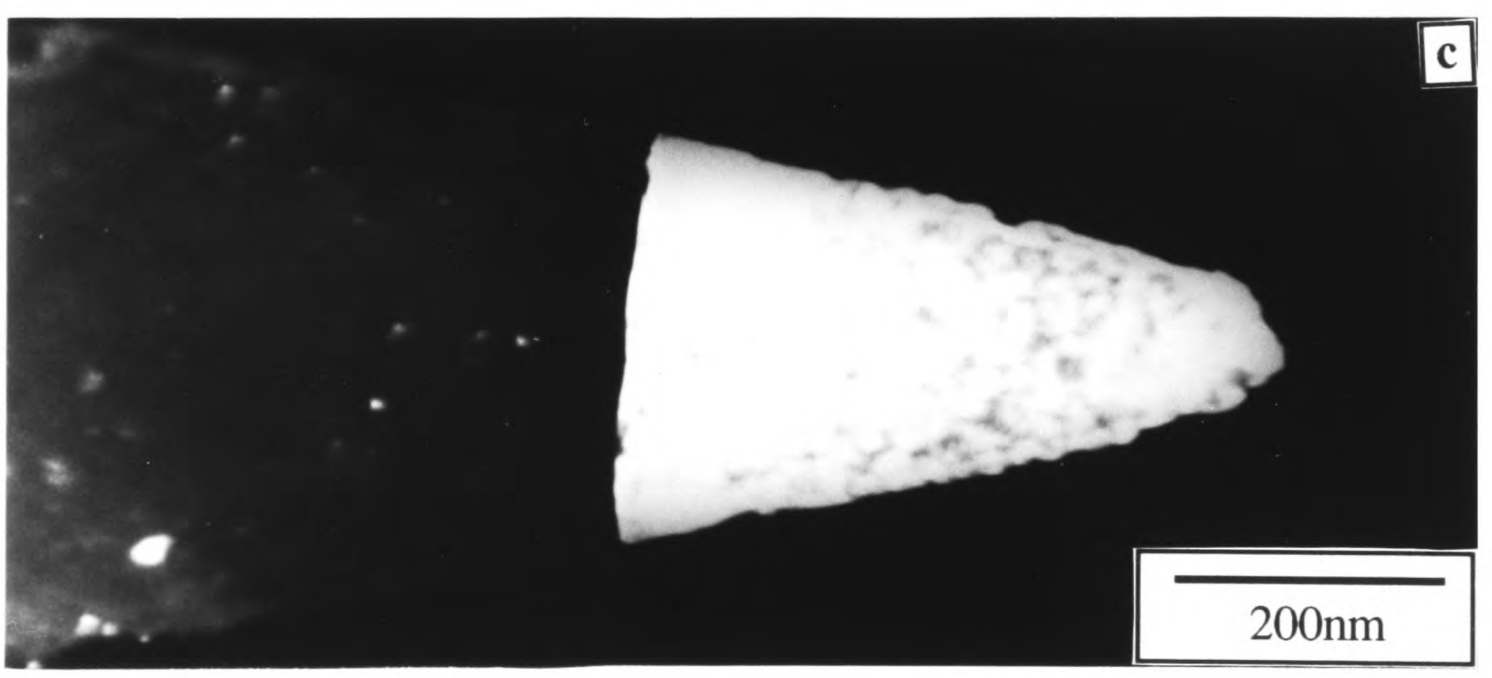
c
200nm

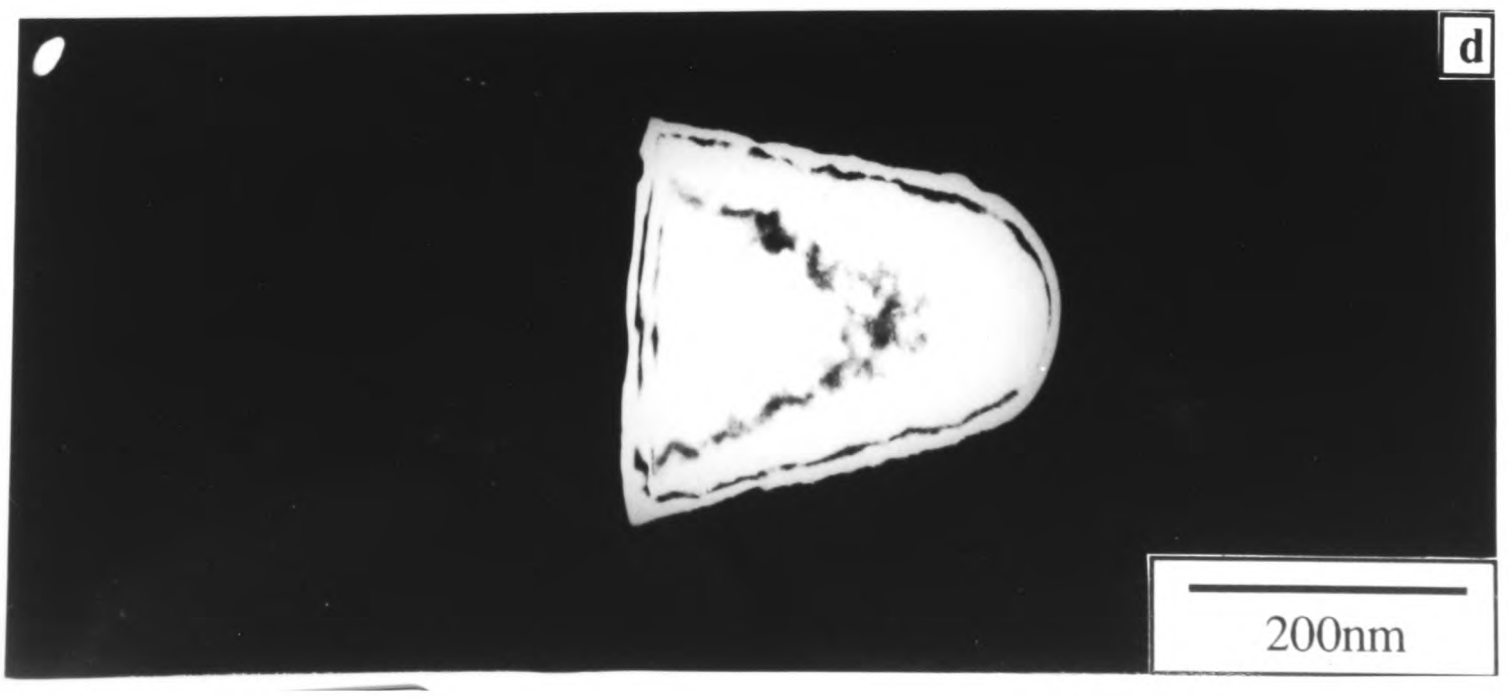
d
200nm

the FIM image (Figure 6.16.a). The brightly imaging spots could be due to segregated copper atoms or to adsorbed argon image gas at the boundary groove, but zinc and magnesium segregant is not expected to image brightly[66]. Further evaporation caused motion of the boundary across the image, as expected from the known geometry of the grain boundary with respect to the tip, and the crystallographic misorientation across the boundary was visible in the misalignment of the brightly imaging (110) poles (Figure 6.16.b).

Analysis by POSAP initially proved confusing, since the boundary was not visible in the image of the solute species being collected (Figure 6.17). However, checking the alignment of the boundary image with the detector confirmed that the boundary was being analysed. The boundary only became visible during subsequent analysis of the data, when the orientation of the volume of analysis could be altered to view the 3-D distribution of each ion species from different directions. Careful choice of the orientation of the data and the size of marker used to represent each atom was required to optimise the contrast between the grain boundary region and the surrounding matrix. It was also found that effective visualisation required the correct calibration of the diameter and depth of analysis, to ensure the correct spatial correspondence between data points. Figure 6.18 shows the side view of the volume of analysis. The location of the boundary is clearly visible in each of the windowed solute ion species, and notably it is also visible in the Al^{2+} ions, showing that there is a local variation in field at the boundary. Figure 6.19 shows ion distributions in a selected volume containing the grain boundary and showing the curvature of the boundary across the area of analysis. A profile of the composition across the boundary in this orientation (Figure 6.20) showed the clear presence of magnesium segregation at the boundary with less clear evidence of what is happening with the combined zinc/copper species. The profile was calculated using a 250 atom block size. It can also be seen that there is a large variation in the number of atoms positioned per unit volume around the grain boundary. The apparent variability of atom density across the image is caused by both ion trajectory aberrations and variations in frequency of occurrence of multiple evaporation events.

a) shows a FIM image of the grain boundary as a brightly imaging arc due to the geometry of the specimen surface. In the background a (110) pole is visible at the centre of a diffuse rectangle of brightly imaging material.

b) shows a FIM image of the same grain boundary after POSAP analysis. The grain boundary has swept across the image as evaporation has proceeded. The image of the grain boundary now almost intersects the image of the (110) pole.

Figure 6.16.

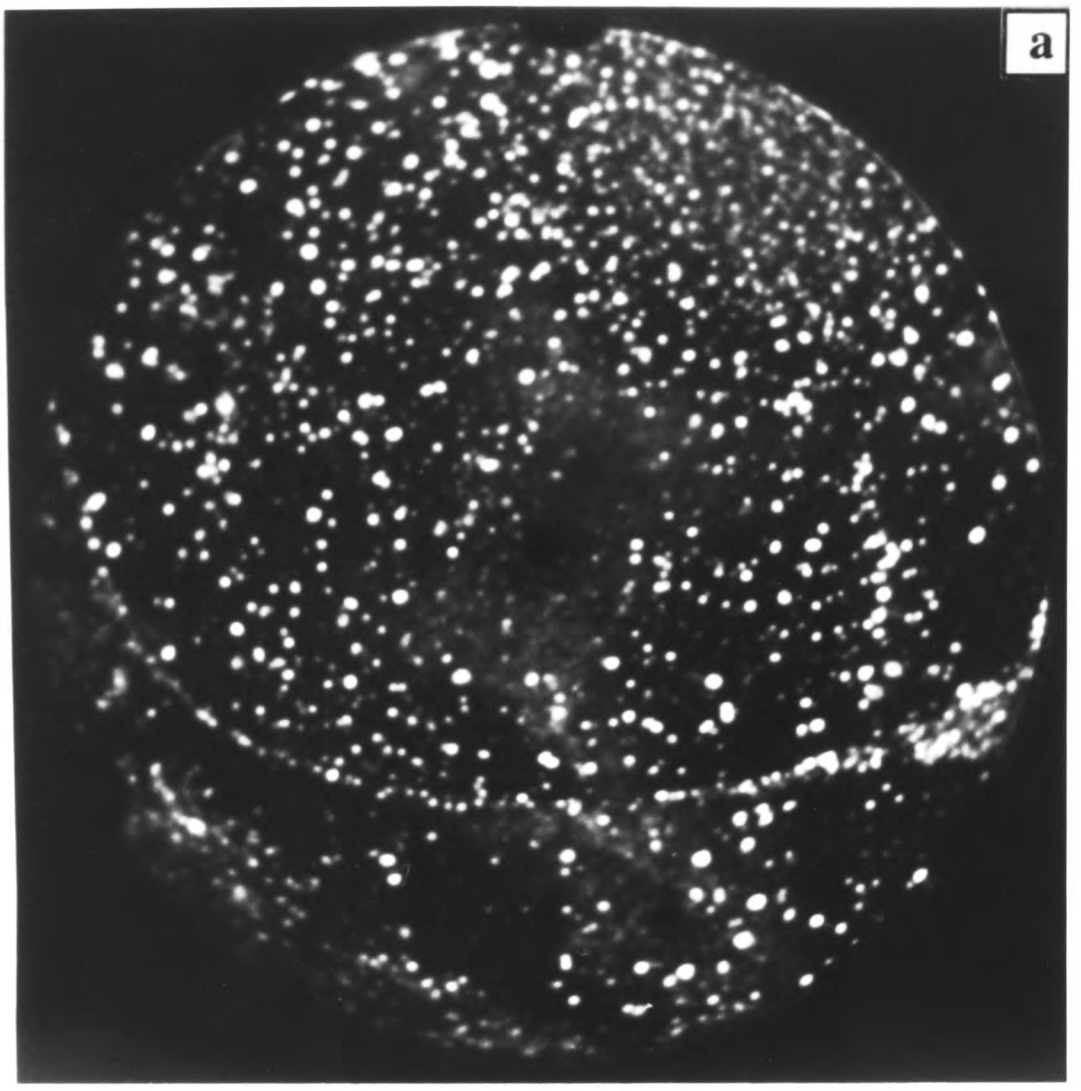
a

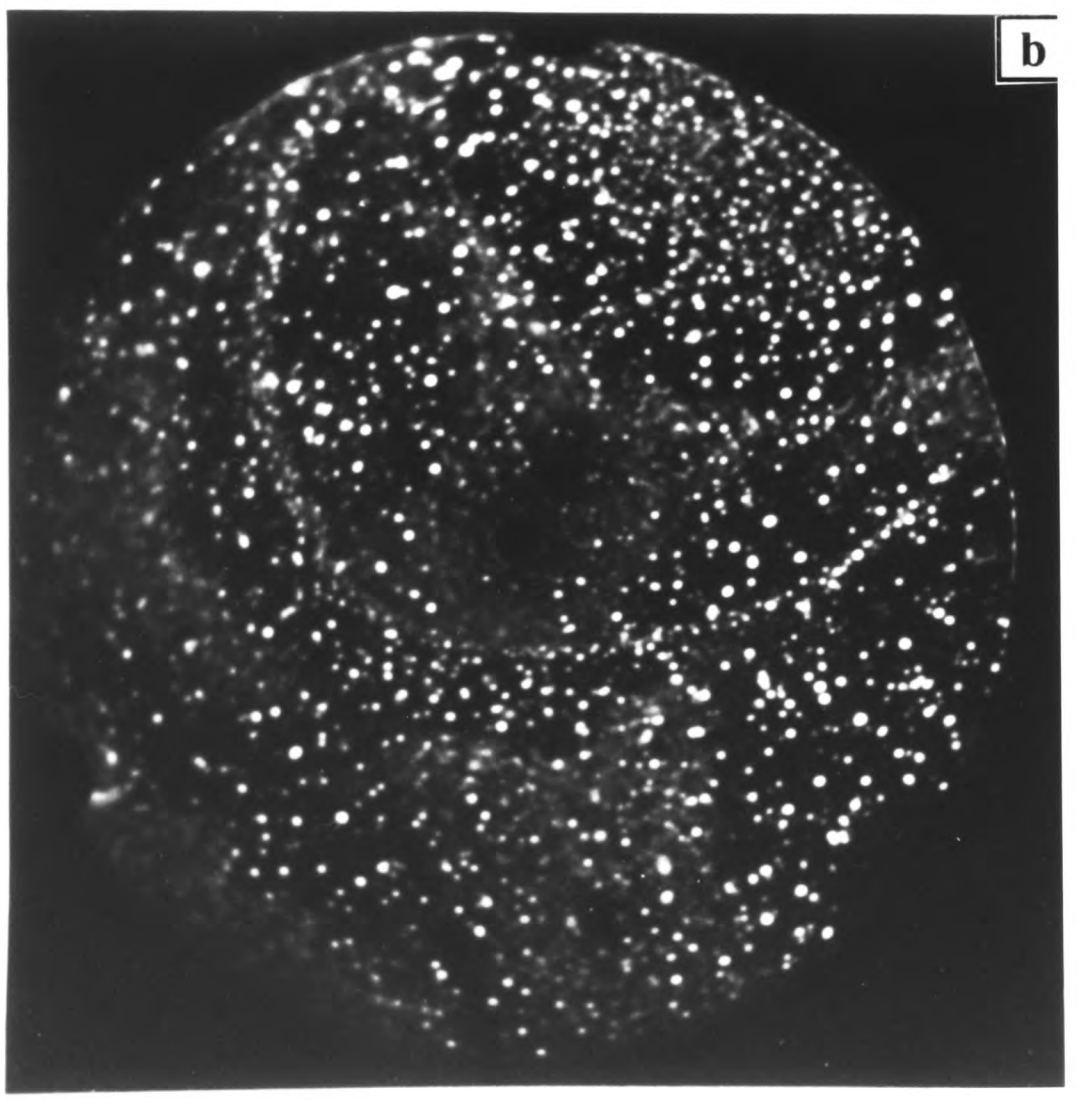
b

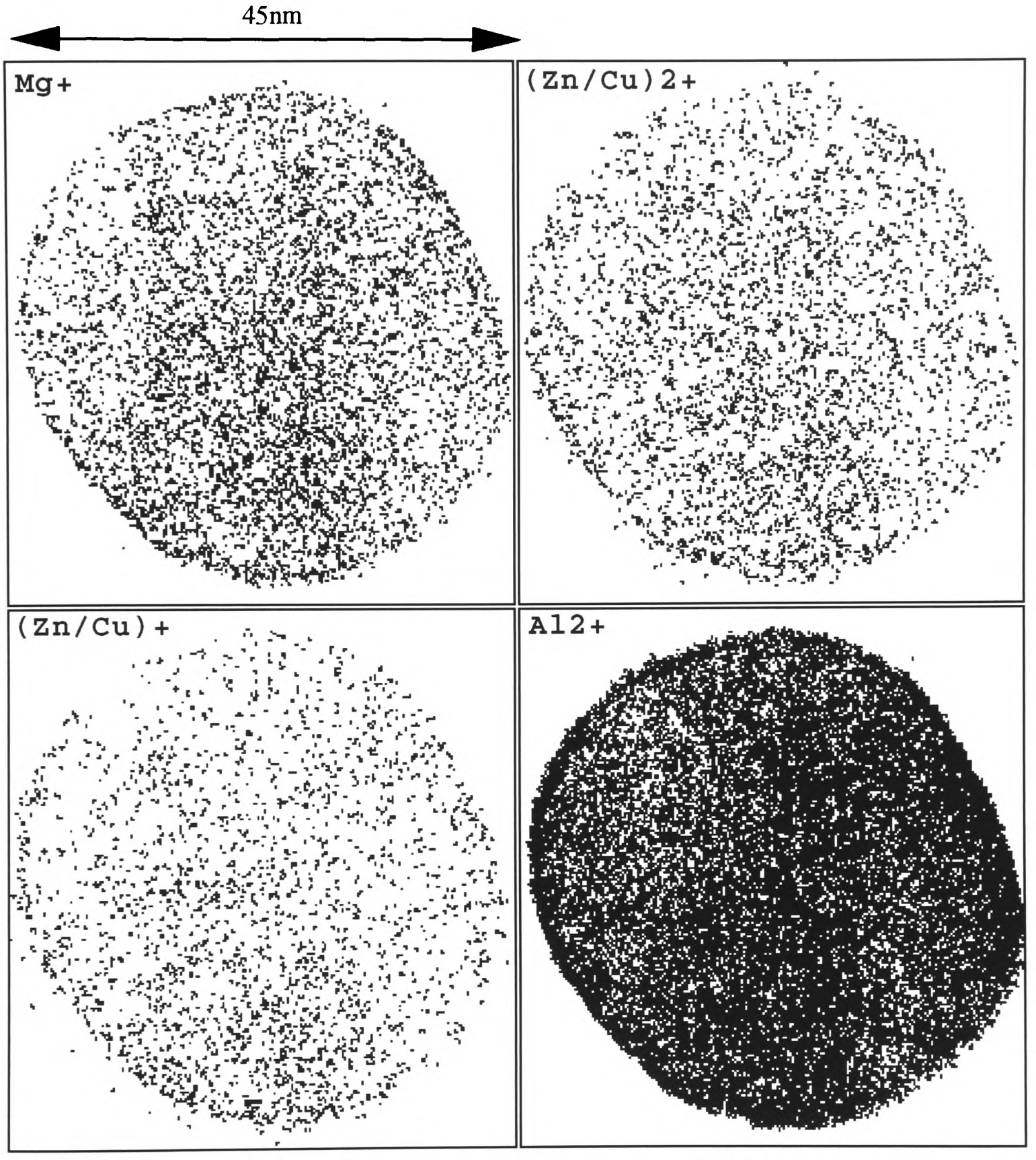

Images of the distribution of different ion species a viewed looking along the cylinder of analysis do not show the position of the grain boundary being analysed.

Figure 6.17

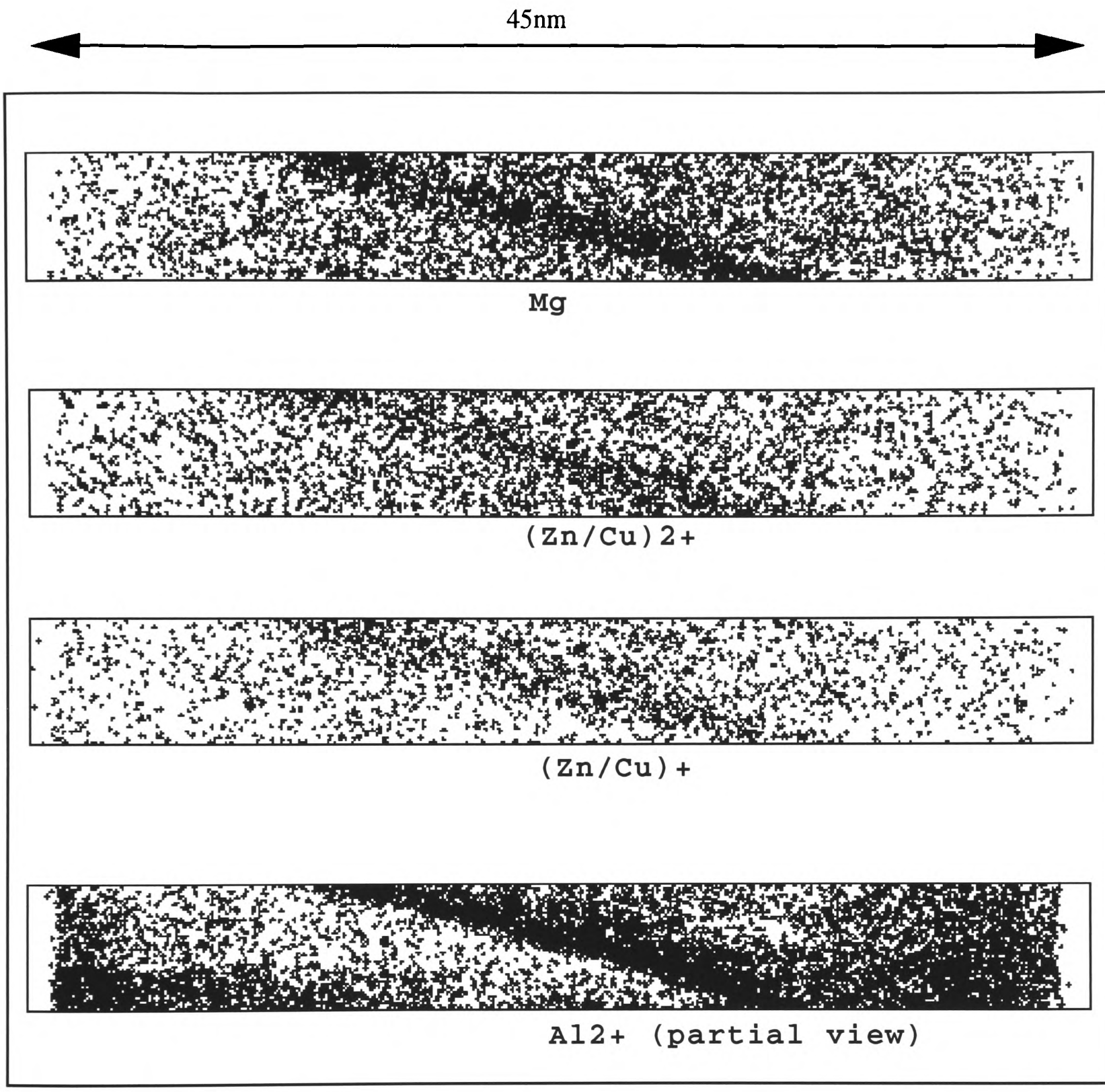

Side view images of the distribution of different ion species clearly show the location of the grain boundary. Each solute ion species shows enhancement at the boundary and the Al2+ ion species also show the location of the boundary due to variations in the local field at the boundary.

Figure 6.18

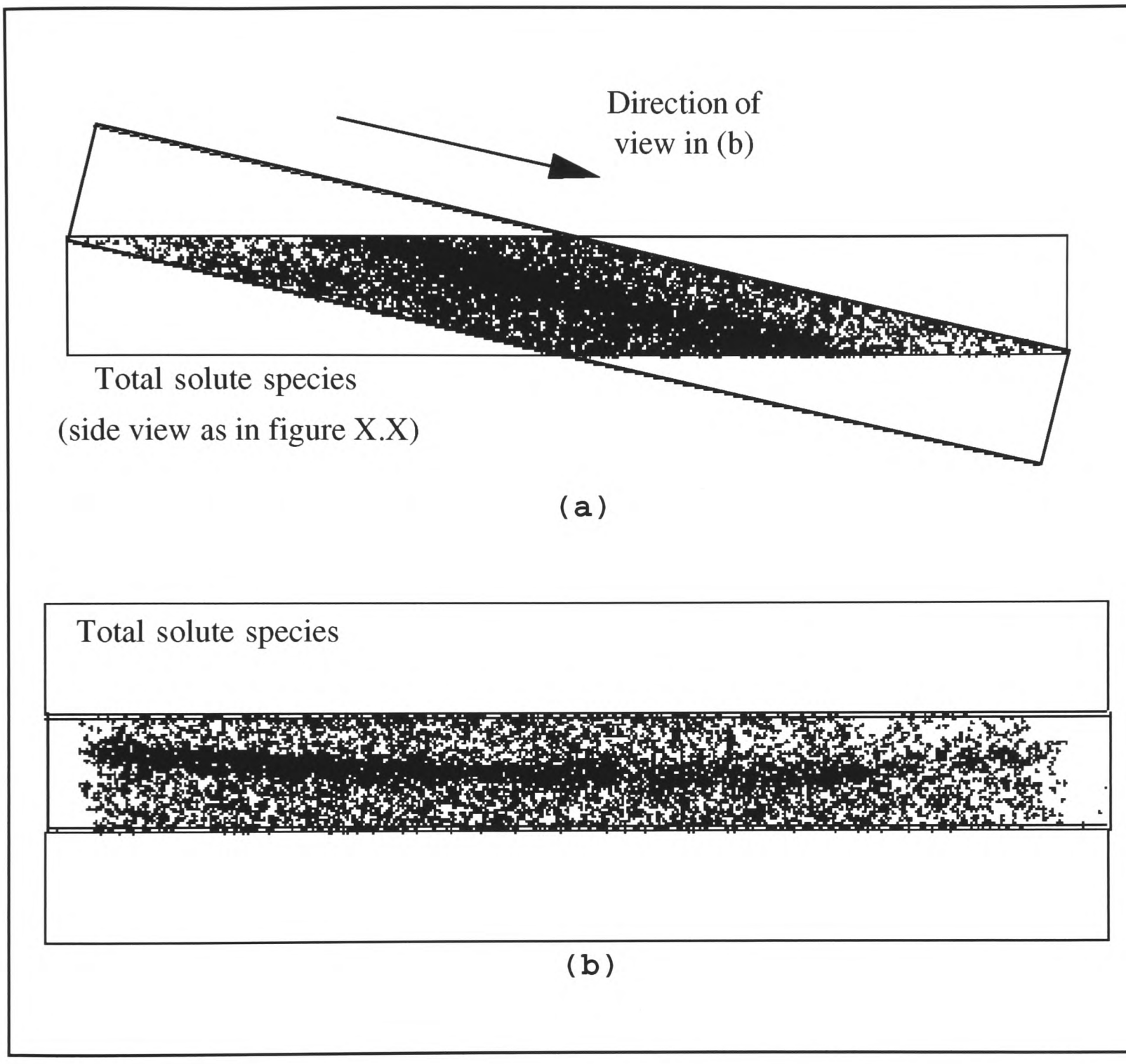

(a) This shows how the volume of data containing the boundary may be selected.

(b) Viewing just the selected volume in another direction shows up clearly the curvature of the boundary due to the geometry of analysis.

Figure 6.19

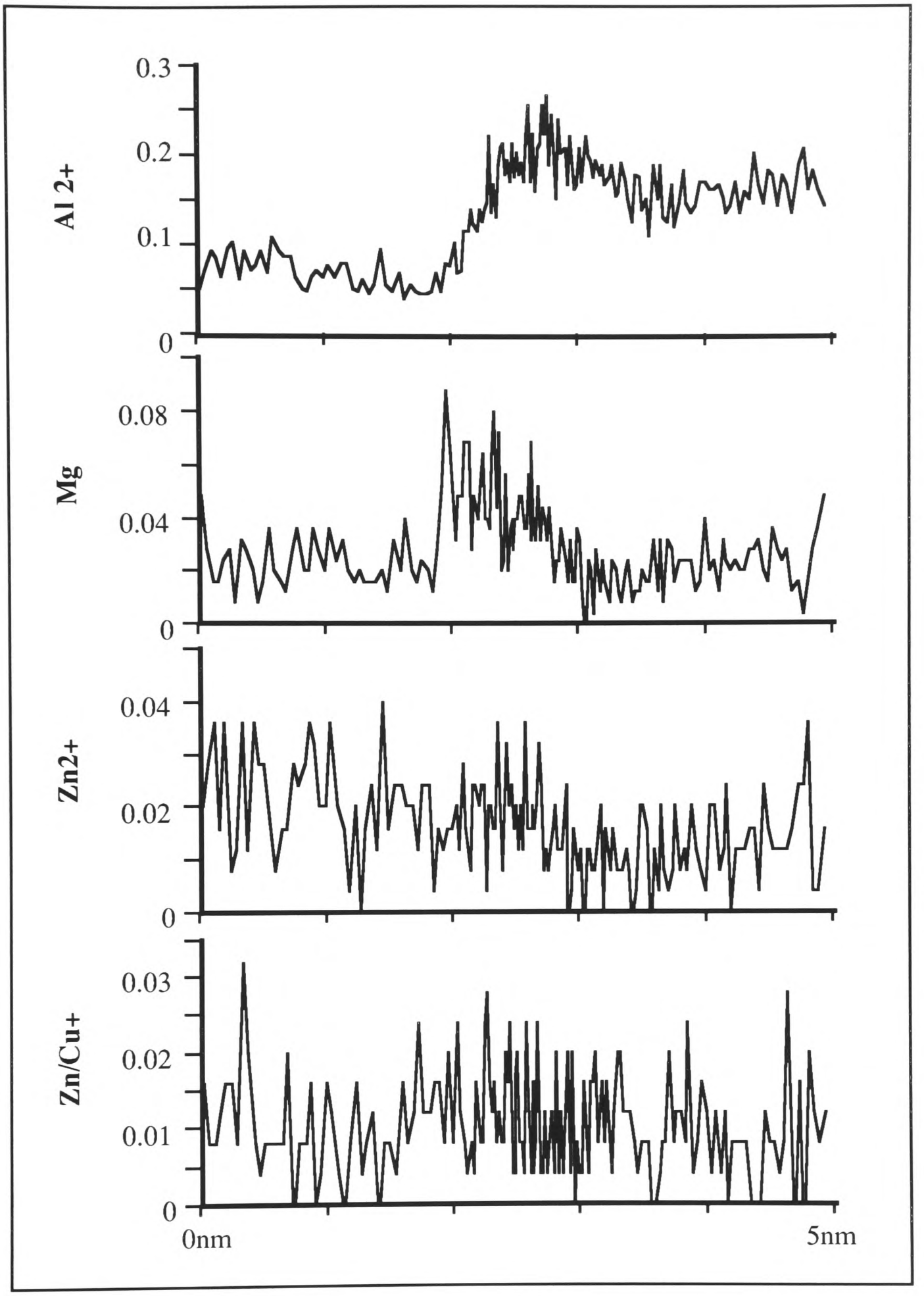

Composition profile formed across the grain boundary shown in figure 6.19. Each compositional point was calculated from 250atoms thus the scatter of compositions is large due to the low solute levels.

Figure 6.20

These must be considered when using the representation of atom distributions to signify compositional variations.

Compositional information obtained from this grain boundary will be considered later.

6.4.2. pgb0101&2 Solution treated material.

Figure 6.21 shows a TEM micrograph of a grain boundary close to the end of a solution treated specimen that had been naturally aged for 23 months. This boundary was close to the end of the tip and easily within range of analysis. The boundary is aligned almost perpendicular to the direction of analysis; a particularly suitable orientation for POSAP analysis.

Figure 6.22 shows POSAP data clearly identifying the presence of solute at the boundary. The side view of the solute species in the selected boundary region shows that some very early stage precipitates have formed during natural ageing. Viewing the data along the direction of the boundary plane shows the largest precipitate to have a plate-like morphology oriented at an angle to the plane of the interface.

Compositional information obtained from this file will be considered later.

6.4.3. paul15/3/93 Solution treated material.

Figure 6.23 shows a TEM micrograph of a sample of solution treated material prior to analysis. POSAP analysis (Figure 6.24) clearly showed the location of a linear feature in both the total solute ion distributions and the Al^{2+} ion distributions. A profile across the boundary showed, that associated with the boundary region, there was the usual increase in ions detected due to trajectory aberrations. This specimen failed during POSAP analysis after evaporation of less than 3nm of material.

Compositional information obtained from this grain boundary will be presented later.

This bright field TEM micrograph of specimen PGB0101 uses moiré fringe contrast to show the location of the grain boundary. The boundary is close to parallel to the axis of the specimen thus there is more grain boundary material available for analysis.

Figure 6.21

This dark field TEM micrograph of specimen Paul15/3/93 shows the end grain brightly imaging and the thickness fringe contrast clearly shows the location of the boundary inclined to the axis of the specimen.

Figure 6.23


50nm

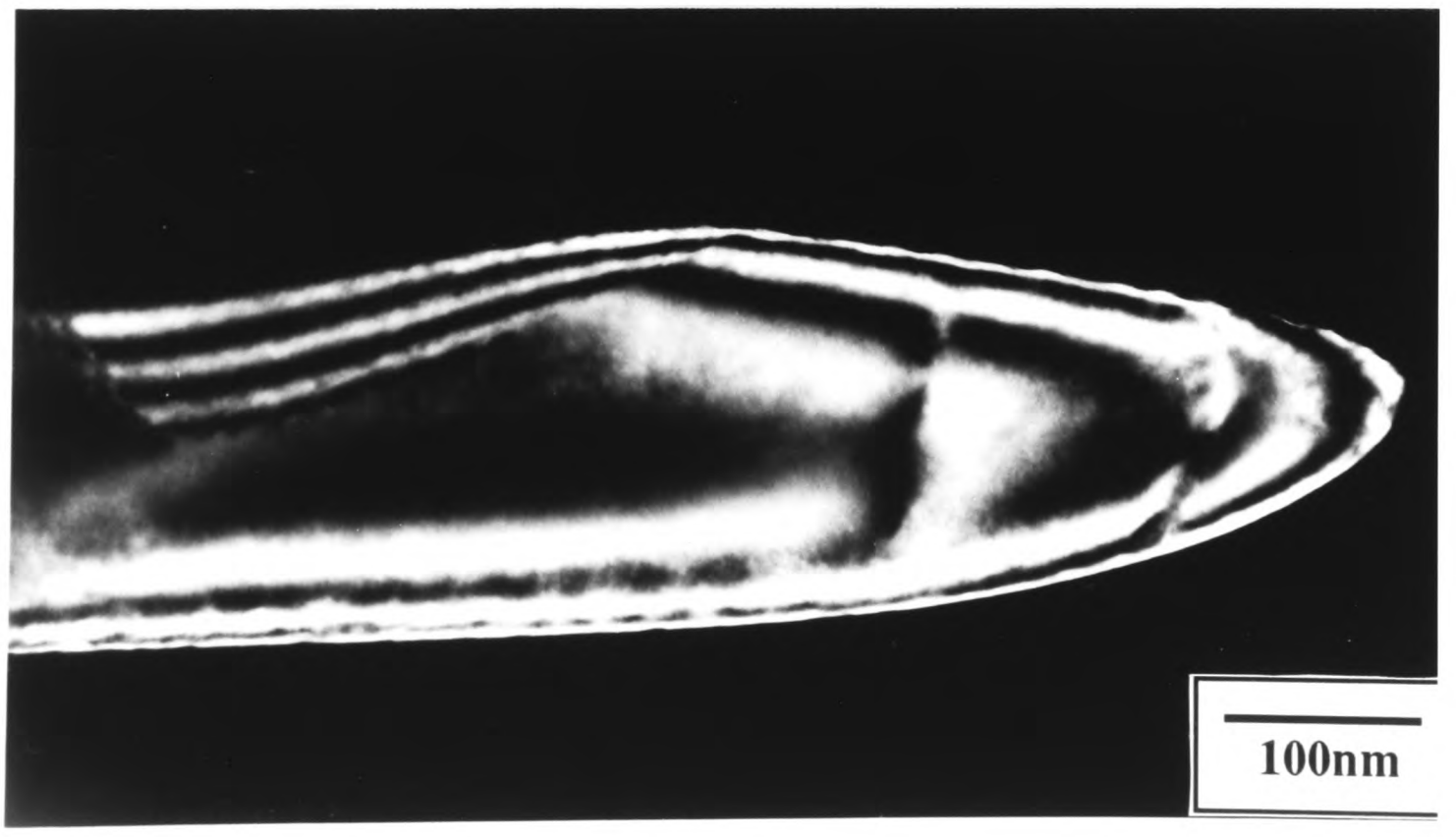
100nm

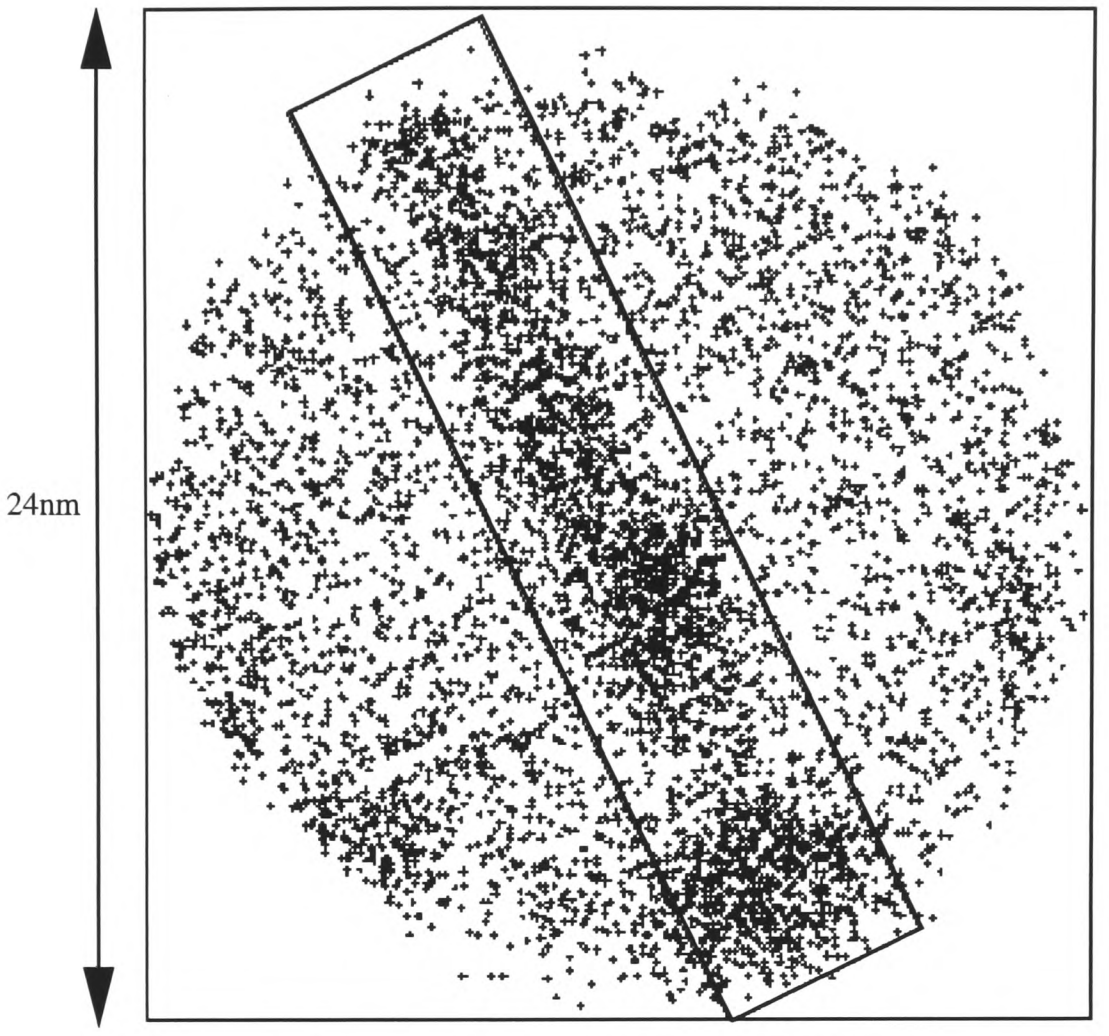

(a) Top view showing distribution of solute species. The grain boundary is clearly visible. The position of the box selecting the boundary data is shown.

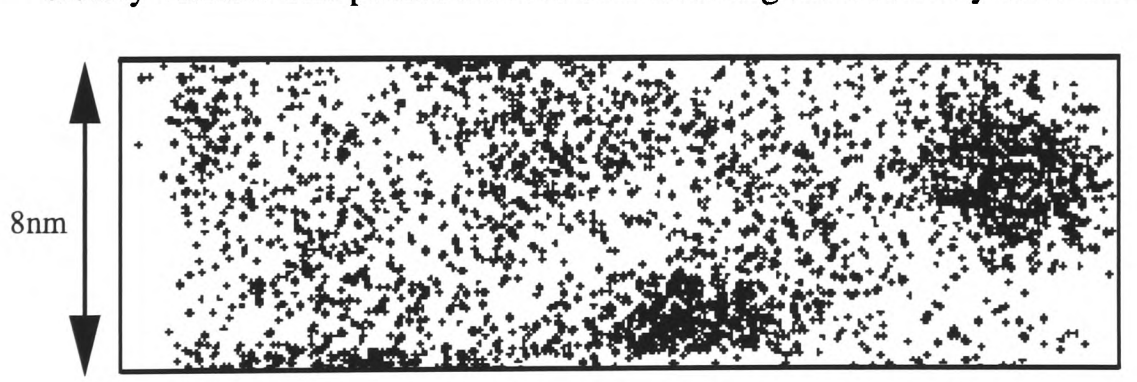

(b) Side view of the grain boundary selected data shows the presence of early stage grain boundary preciptiates.

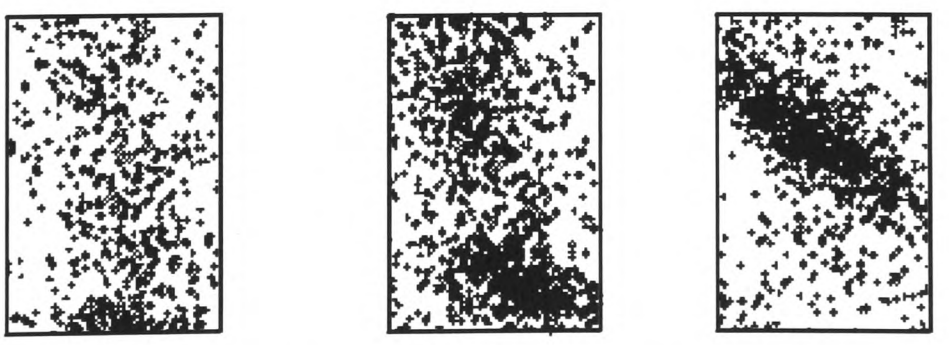

(c) Cross–sectional views of the selected boundary data showing the precipitates to be oriented at an angle to the boundary plane.

Figure 6.22

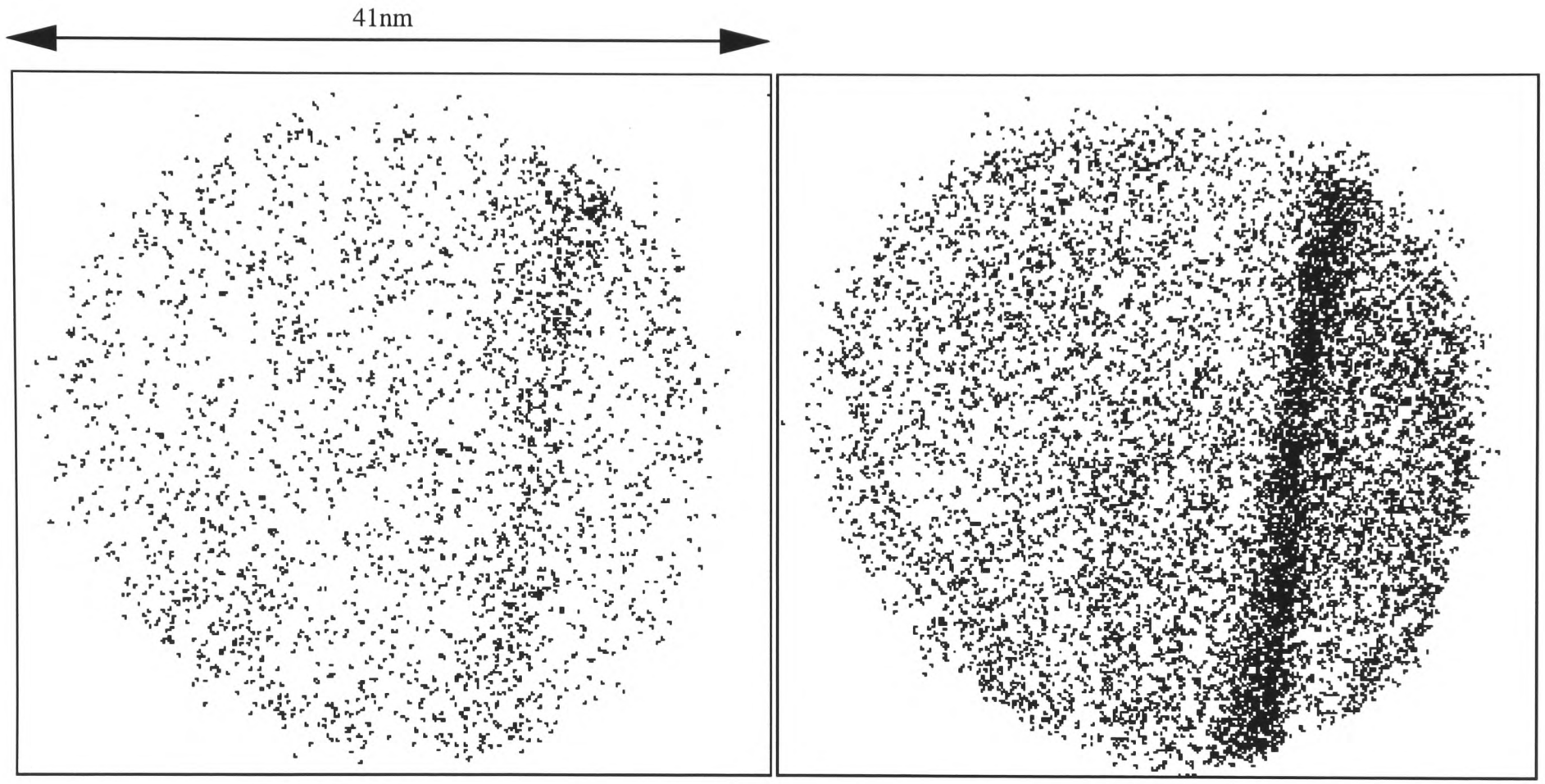

Figure 6.24 This grain boundary again shows enhancement of both the solute species and the Al2+ species at the grain boundary.

6.4.4. pgb12010 120°C material.

Figure 6.25.a shows a bright field TEM image of the precipitates in the specimen after POSAP analysis. In the TEM the precipitates show up clearly both in the matrix and along the boundary but in the FIM the boundary is barely visible, as shown in Figure 6.25.b. Increasing the applied voltage, or reducing the specimen temperature, to improve the imaging conditions tends to result in failure of the specimen. The only safe way to identify the boundary position is by the persistence of certain bright atom sites during evaporation and by the disruption of regions of brightly imaging crystallography. Figure 6.26 shows a FIM image of the bisection of a (110) pole by this boundary.

POSAP analysis of the boundary showed the presence of solute rich precipitates on the boundary. Figure 6.27 shows how the precipitates are clearly visible from the distribution of solute atoms, but the position of the boundary in the lower part of the imaged region is most easily detected from the distribution of the Al^{2+} species, as mentioned previously. Due to the large diameter of analysis (and hence limited depth of analysis, with the maximum data block size which can be visualised) the amount of boundary analysed here is small. The number of atoms associated with the interface is also small, thus it is difficult to obtain accurate compositional information about the level of segregation.

Compositional information obtained from this file will be considered later in summary.

6.4.5. paul3/6/93 120°C material.

Figure 6.28.a. shows a bright field image of the boundary region at the end of the FIM tip (after POSAP analysis), with a dense array of small precipitates decorating a stepped boundary structure. The stepped nature of the boundary is indicative of a low misorientation angle. In the FIM image, the location of the boundary was, as usual, difficult to see, however, this boundary also showed contrast only along part of its length and this contrast was observed to vary as evaporation proceeded. Thus it was not

a) shows a bright field TEM micrograph of the FIM specimen after POSAP analysis. The location of the grain boundary is clearly visible due to the grain boundary precipitates.

b) shows a FIM image of the same specimen. The location of the grain boundary in the FIM image is unclear apart from the disruption of the brightly imaging (110) pole crystallography. This is shown in more detail in Figure 6.26.

Figure 6.25

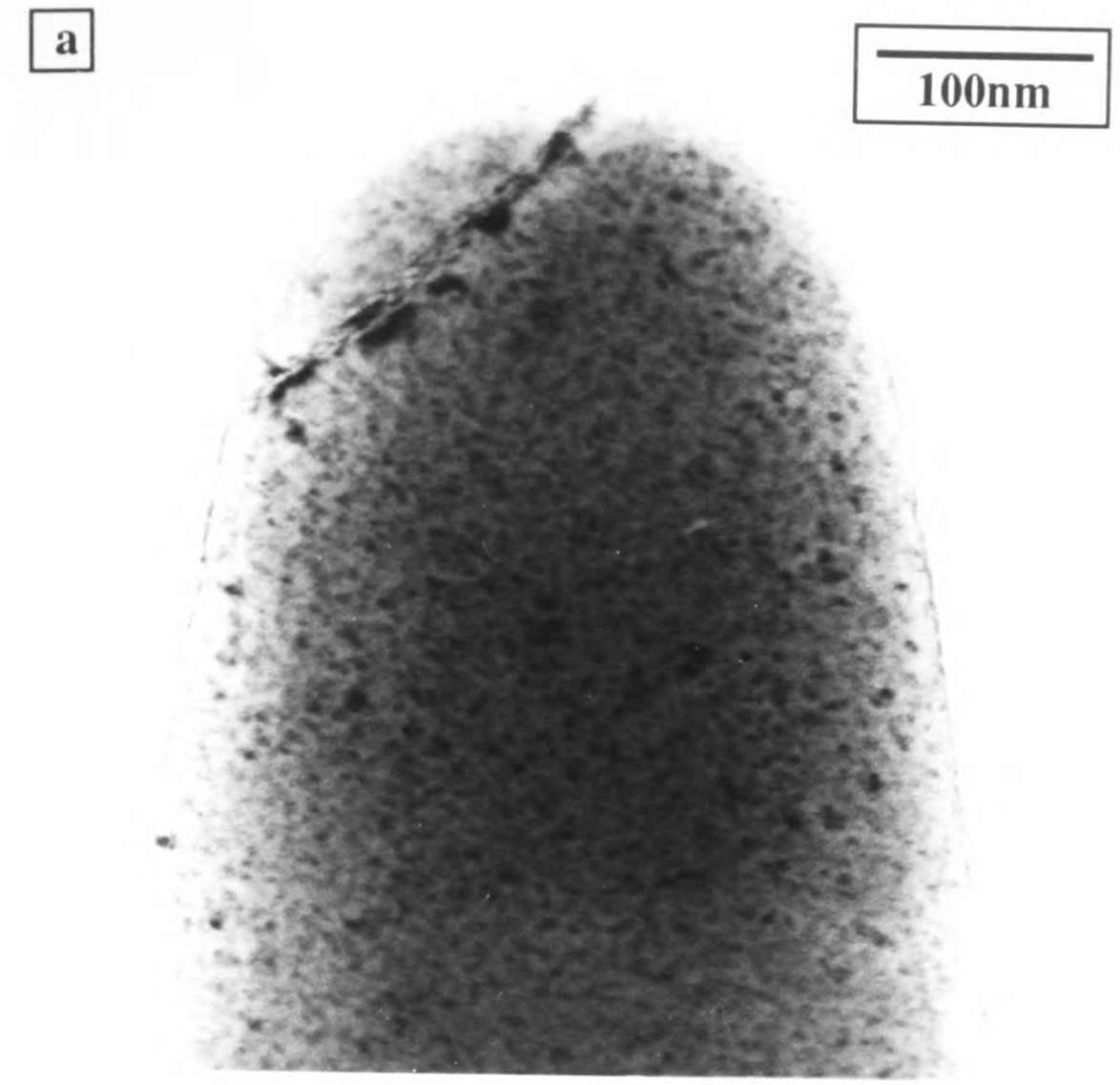
a
100nm

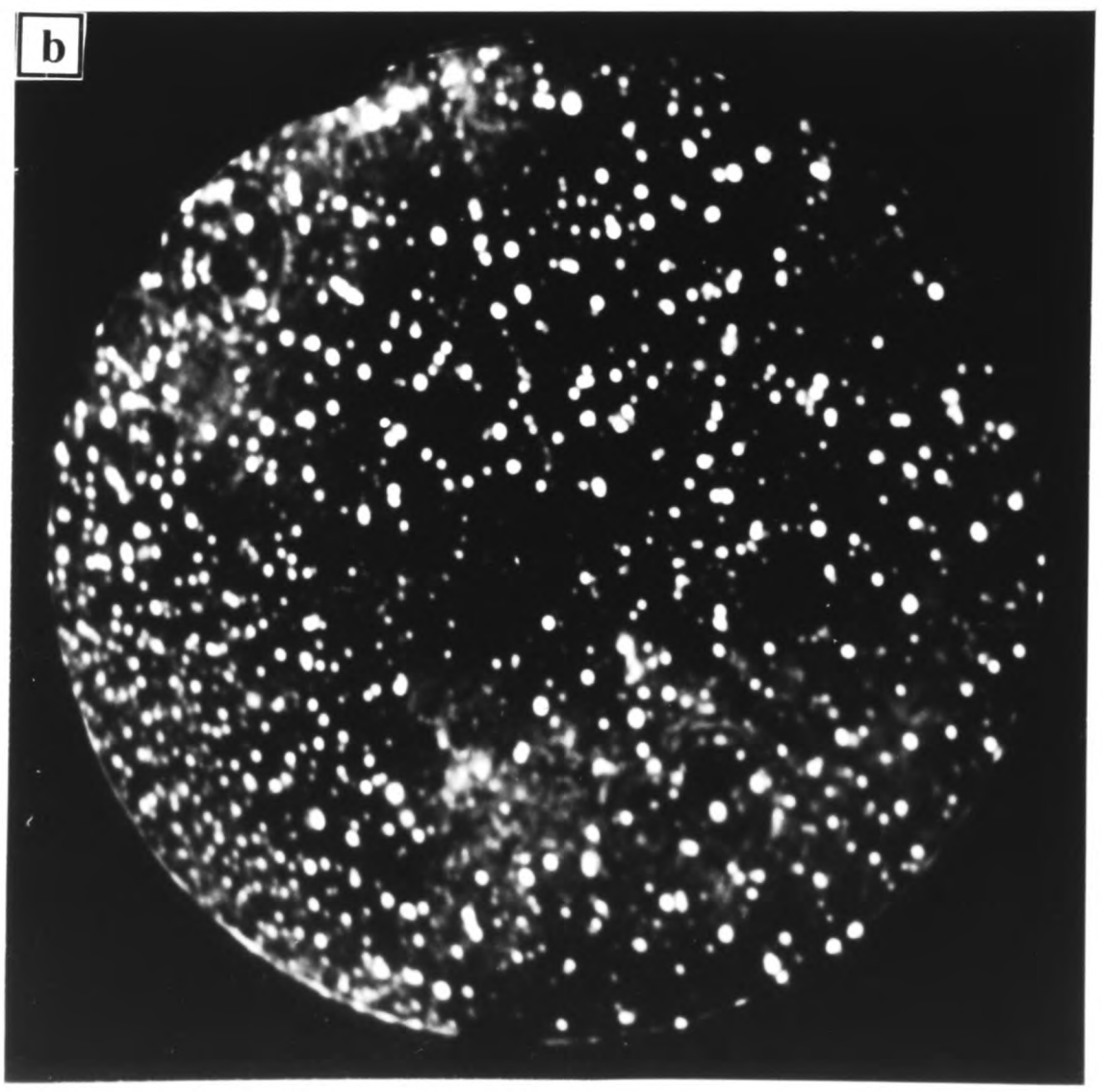
b

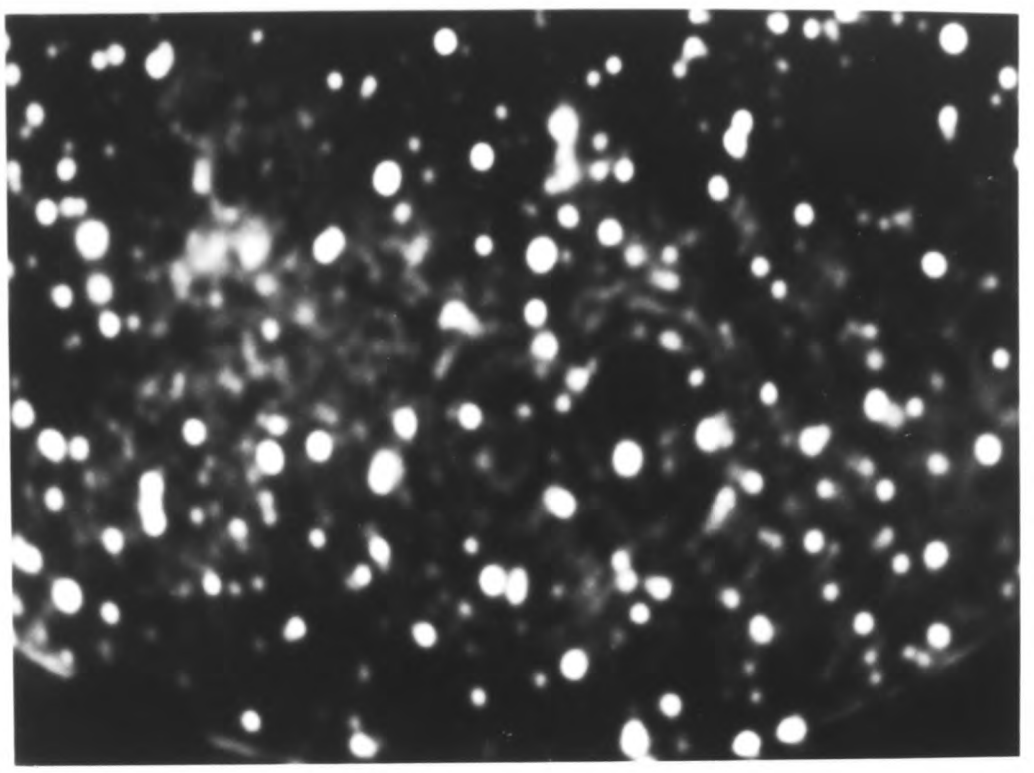

a) An enlargement of part of Figure 6.25 FIM image of the grain boundary showing the disruption of the (110) pole ring structure.

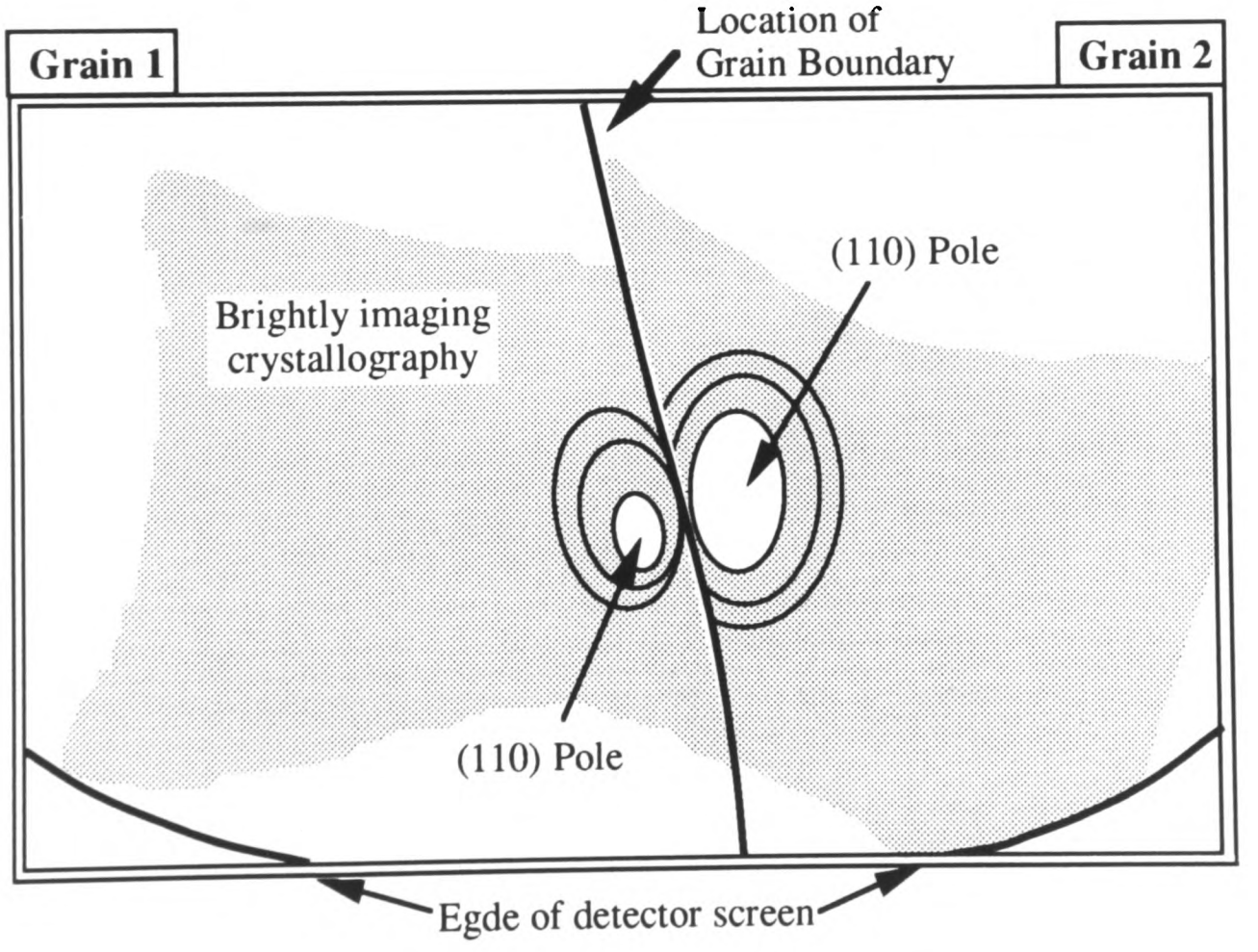

b) A schematic diagram showing the features of interest to be seen in (a).

Figure 6.26

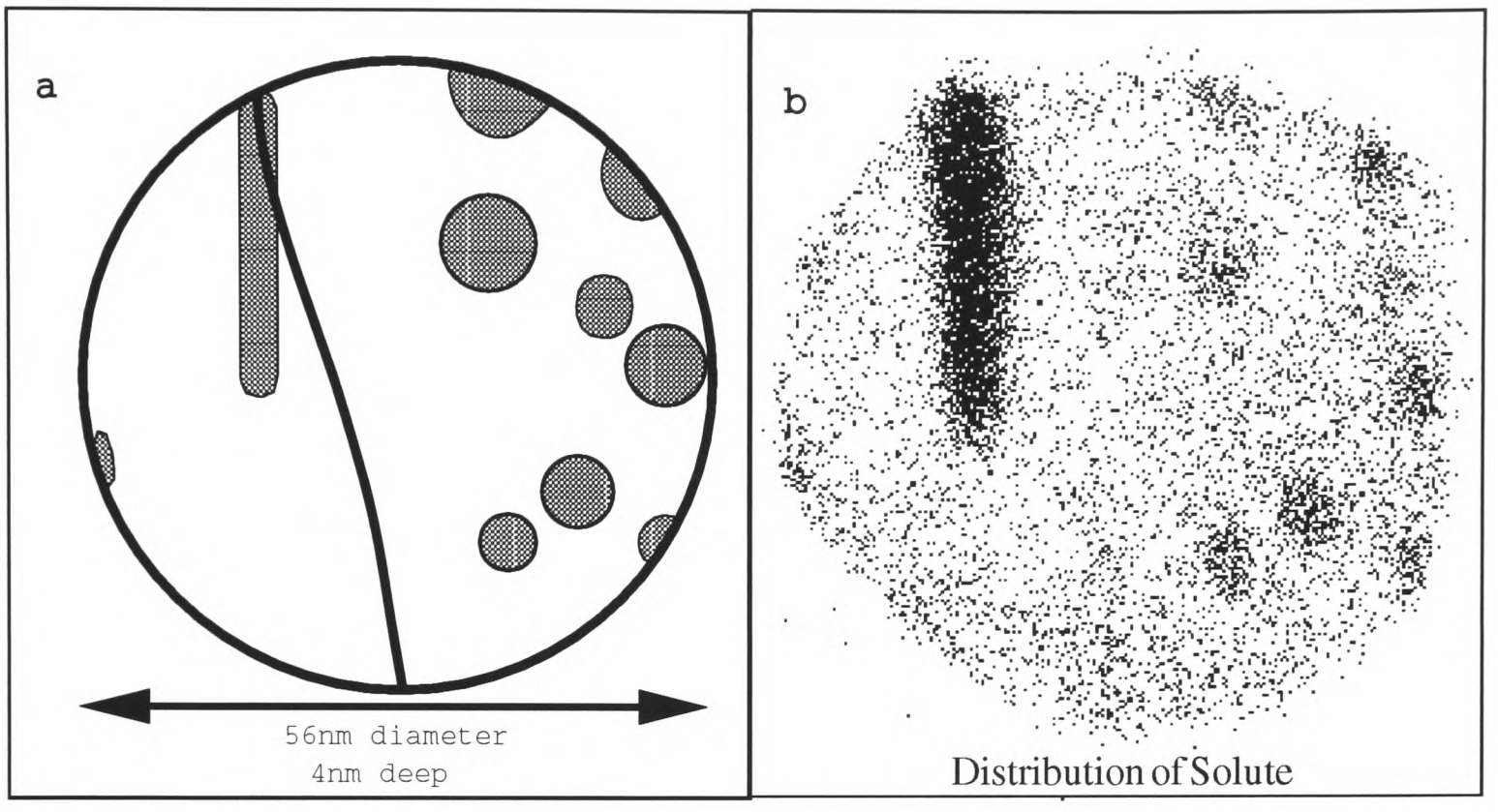

a) diagram of the microstructure analysed showing a large platelet precipitate on a boundary and smaller precipitates in the matrix.

b) image of solute ion species detected (Mg,Cu/Zn) shows the precipitates however the boundary is not easily visible due to the low solute levels and the inclination to the analysis direction.

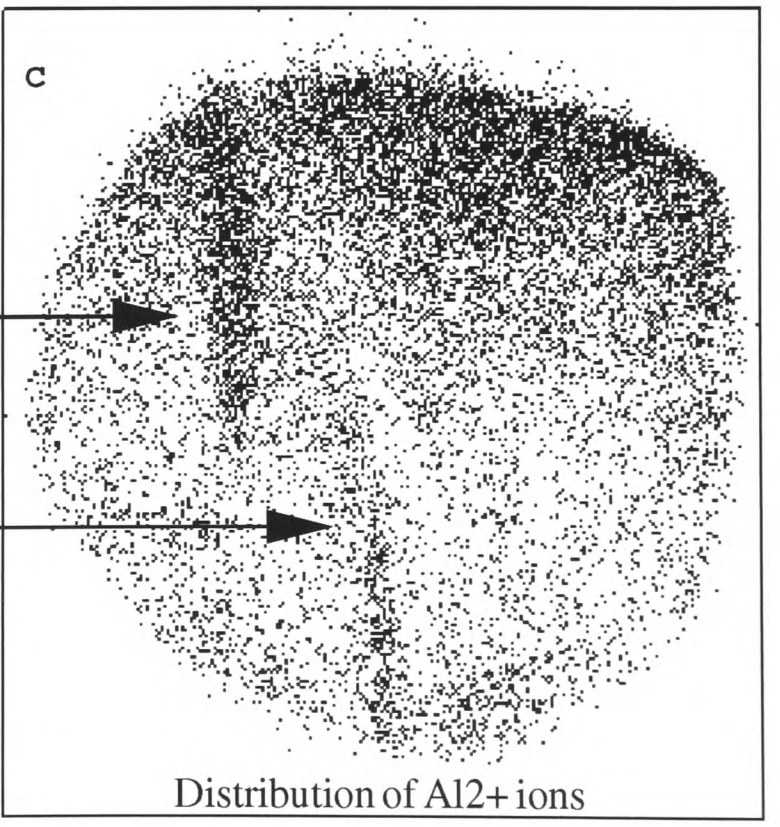

c) image of the Al(2+) ion species shows the location of the boundary and the large platelet precipitate due to local field effects.

Figure 6.27

always possible to see the location of the boundary (Figure 6.28.b). This suggests that the segregation to the boundary might not be uniform along its length; however the image is easily confused by local field effects.

Viewing the solute species showed a possible region of solute enhancement along the interface (Figure 6.29.a). Viewing the Al^{2+} species to confirm the location of the boundary faintly showed enhancement of positioning at the boundary. In addition, however, another region more obviously showed a band of depletion (Figure 6.29.b).

Continuing the analysis at 40K instead of 70K gave an image of the aluminium species that showed this region of depletion more clearly as being a faint cross pattern centred on a hole (Figure 6.29.c). Selecting the depleted region and viewing from the side (Figure 6.29.d) showed that the depletion was due to the crystallography of a pole (probably (110)). As the pole evaporated the top plane became increasingly prominent; thus as evaporation proceeded multiple evaporation events occurred more frequently, resulting in reduced positioning towards the centre of the pole. The cross pattern can therefore be explained in terms of crystallographic trajectory aberrations similar to those observed in Field Desorption Microscopy of aluminium[103]. Being able to see the ring structure down the pole allows direct checking of the depth calibration.

6.4.6. Compositional information.

As shown above, that grain boundary analysis is complicated by local variations in the evaporation field. This results in; ion trajectory aberrations, adsorption and desorption of vacuum contaminant species (possibly by surface migration along the boundary from the specimen shank), unquantifiable multiple evaporation effects and positioning problems (see Section 4.5) similar to the crystallographic effects observed at a low index pole.

Due to the ion trajectory aberrations the absolute dimensions of the boundary are not accurately preserved in the data. Ignoring the inaccuracies of scale, it is possible to deal with the solute segregation in the same manner as that of STEM segregation data and to

a) shows a bright field TEM micrograph of the FIM specimen Paul3/6/93 after POSAP analysis of the grain boundary. This shows that the grain boundary is heavily decorated with precipitates. It also has a stepped morphology possibly indicative of a low angle of misorientation.

b) shows a FIM image of the specimen surface shown above. The location of the grain boundary is visible only partly along its length which may suggest that segregation is only present along part of the grain boundary interface.

Figure 6.28

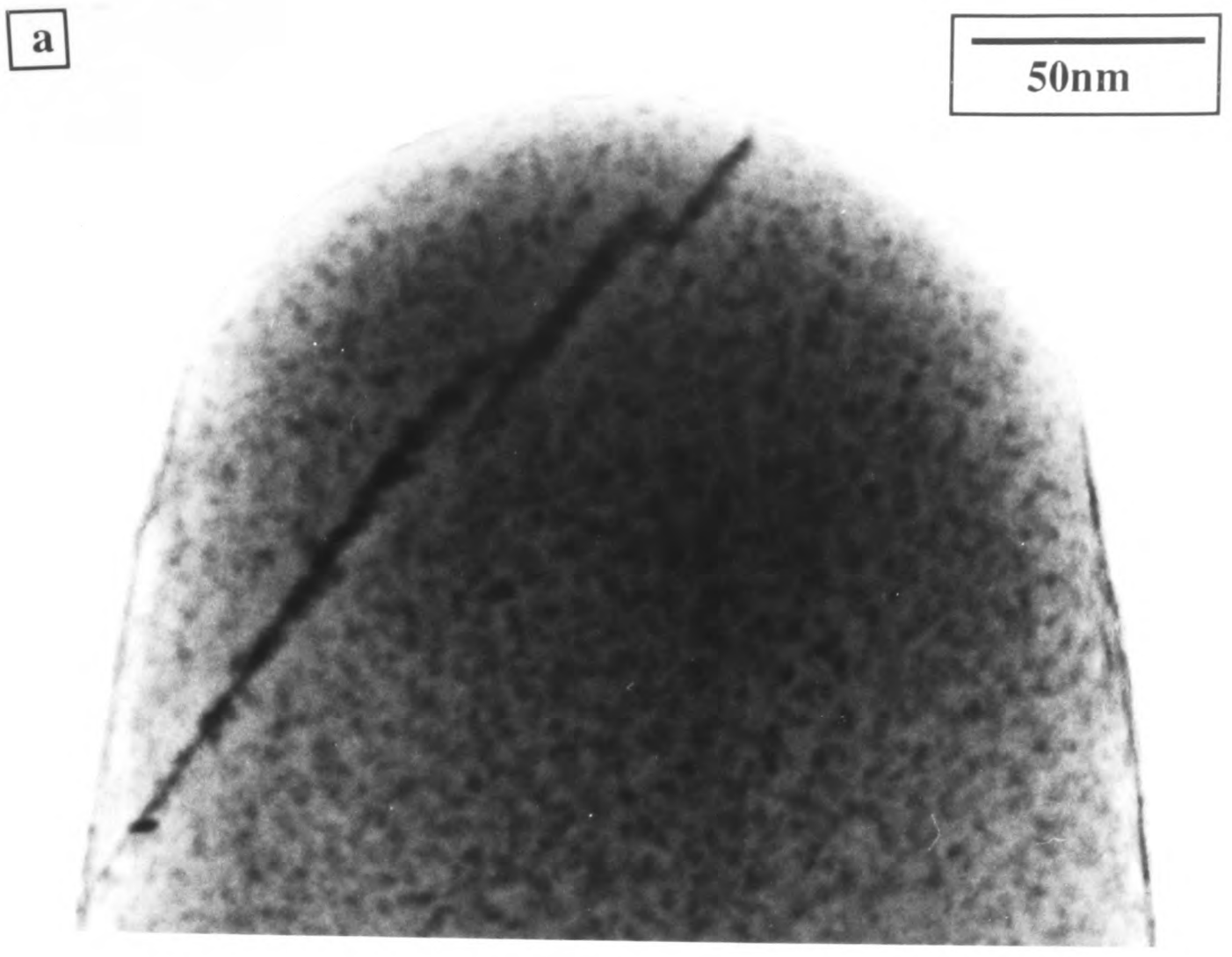
a
50nm

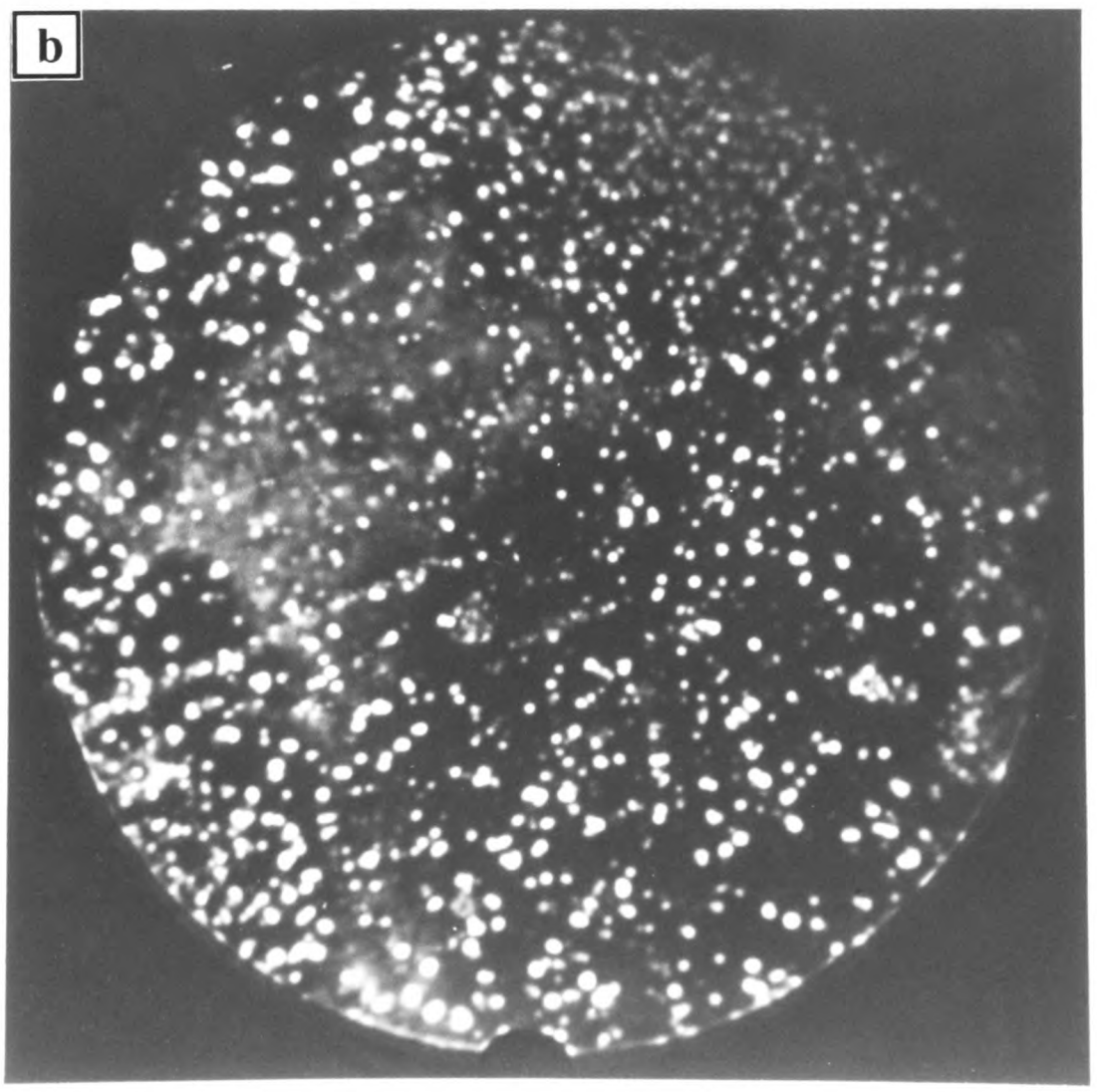
b

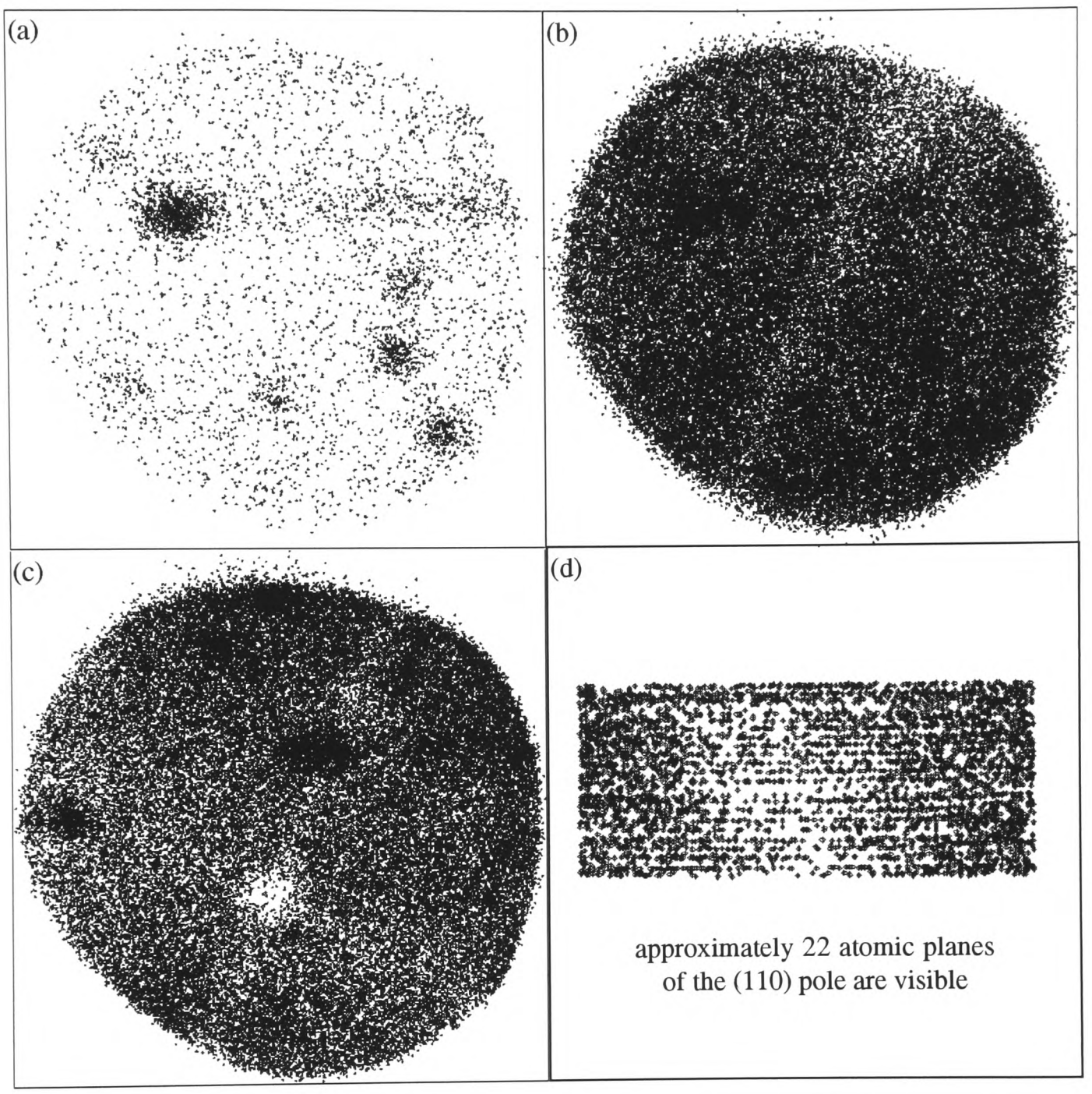

(a) shows the distribution of all the solute species. The largest precipitate lies on the boundary and to the right of the precipitate there is a more diffuse region of solute enhancement possibly due to grain boundary segregation.

(b) shows the distribution of the Al2+ species. There is a diagonal band of depletion which is more obvious than the expected line of boundary enhancement.

(c) shows the distribution of the Al2+ species after analysis at 40K instead of 70K. This shows very clearly a region of strong depletion with a cross pattern through it.

(d) shows the side view of the depleted region showing the ring structure of the pole. Multiple evaporation is more frequent at a low index pole and this results in less positioning of the ions and effectively a hole in the data.

Figure 6.29.

determine the solute enhancement levels. In order to calculate the solute enhancement of the boundary, the width of the boundary is assumed to be 0.5nm, as previously, and all of the excess solute detected is assumed to have come from the boundary.

Magnesium

As long as the possibility of peak overlap with the Al^{2+} window is very carefully avoided, then the quantification of the magnesium segregation levels provides little problem. All of the boundaries analysed have shown enhancement of magnesium at the grain boundary. Since the magnesium is the lightest species detected, except for hydrogen, a high percentage of the magnesium ions detected are positioned correctly.

Figure 6.30 shows the PFZ levels of magnesium and also the calculated grain boundary levels for each boundary analysed. All of the grain boundaries analysed show enhancement of magnesium at the boundary. The level of enhancement for analysis Paul 15/3/93 is rather low and statistically poor due to the small depth of analysis and low solute levels detected.

Zinc/Copper

As discussed in detail previously, quantification of the zinc and copper is virtually impossible due to peak overlap and the low efficiency of positioning of the zinc species. The lack of positioning is particularly difficult to correct for, since it can clearly be seen that there are local variations in the field at a boundary. Considering zinc and copper species together, in a combined window, can be used to look for the presence of solute enhancement. Using the information obtained from the binary alloys, that zinc species occur as 70% Zn^{2+} and 30% Zn^{+} while copper species occur as mostly Cu^{+}, we can qualitatively check the profile of the selected positioned atoms at the interface to see whether there is enhancement of either $(Zn/Cu)^{2+}$ or $(Zn/Cu)^{+}$ species.

Figure 6.30 shows the PFZ levels of each of $(Zn/Cu)^{2+}$ and $(Zn/Cu)^{+}$ and the calculated grain boundary levels for each boundary analysed.

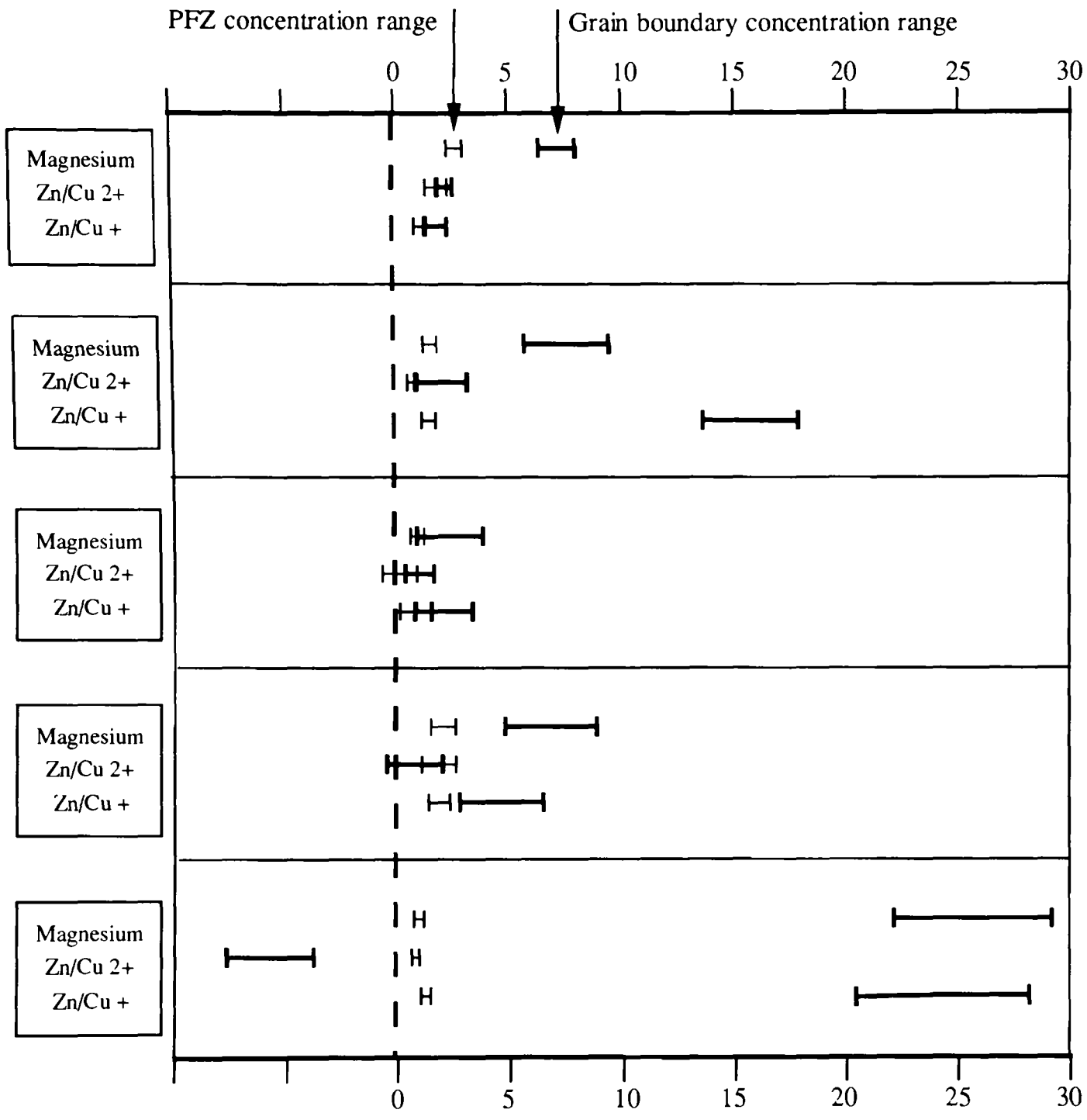

PJW013 shows grain boundary segregation of magnesium but no significant enhancement of either of the Zn/Cu species.

PGB0101 shows grain boundary segregation of both magnesium and both the Zn/Cu species. The segregation of Zn/Cu+ is more significant than the segregation of Zn/Cu2+ species.

Paul15/3/93 shows slight enhancement of the magnesium and the Zn/Cu+ species however all the enhancement levels are insignificant as shown by the error bars marked.

PGB12010 shows grain boundary segregation of both magnesium and Zn/Cu+ species and depletion of Zn/Cu2+ species.

Paul3/6/93 shows strong segregation of the magnesium and the Zn/Cu+ species. The height of the enhancement observed is possibly excessive since the actual width of the segregation was large as shown in Figure 6.29.

Figure 6.30 Plot showing the levels of Mg , Zn/Cu2+ and Zn/Cu+ in both the PFZ and on the grain boundary for each grain boundary analysed.

From STEM investigations of the solute distributions in this material, it seems that the zinc is virtually all contained in the precipitates, whilst the copper can be present on the boundary interface. If zinc is absent, then it is possible to confirm the presence of copper by checking the spectrum of the selected $(Zn/Cu)^+$ species. However, if both elements are present then it may not possible to separate them. Figure 6.31 compares the selected spectra of boundary and matrix regions for the (Zn/Cu)+ species.

In summary, magnesium segregation was detected at all the boundaries analysed, while copper segregation was difficult to confirm accurately due to the low mass resolution of the POSAP. Each boundary had particular experimental problems associated with it which affected the quality of the information obtained, and thus comparison of the solute levels between analyses is not accurate. The best analysis was PGB0101 which clearly showed the presence of early stage precipitation at the grain boundary and selection of a precipitate free region of boundary showed the presence of copper at the interface. An overview discussion of the benefits of using this technique to investigate grain boundary chemistry will be presented in Chapter 7.

6.4.7. Grain boundary precipitate compositions.

As can be seen from the images of the solute distributions for the POSAP grain boundary analyses presented above, only three of these analyses contain signs of grain boundary precipitation. The compositional information from these precipitates is presented here rather than in Chapter 5 (which contains most precipitate compositional information) because these precipitates are not strictly comparable, due to the small number of analyses from different heat treatments and also due to the added complexities of POSAP analysis of grain boundary regions, as have been described above. Each boundary showing signs of precipitation will be considered separately.

PGB0101 solution treated material.

This is solution treated material which, immediately after quenching, showed no signs of precipitation. However, the material was then naturally aged for the whole duration

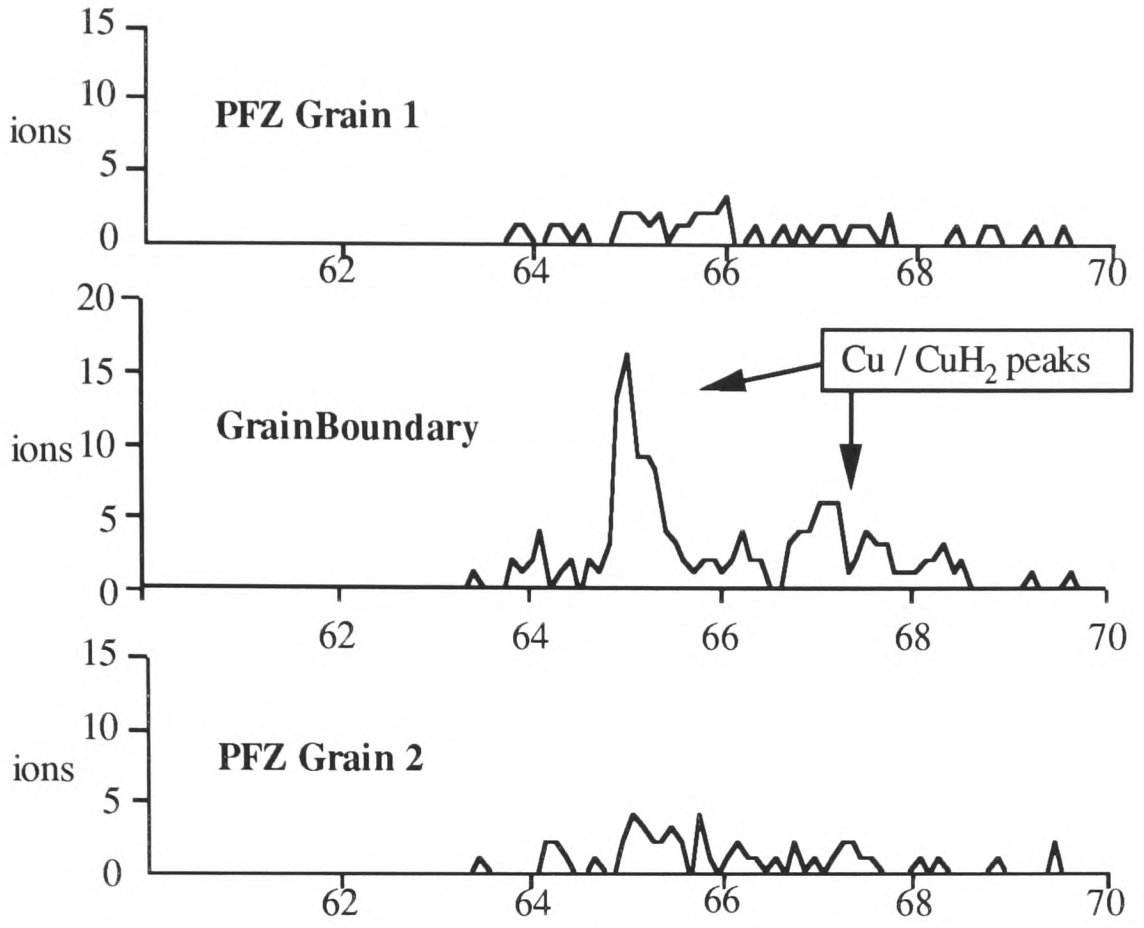

Grain boundary PGB0101 selected spectra showing copper at the grain boundary as opposed to zinc species.

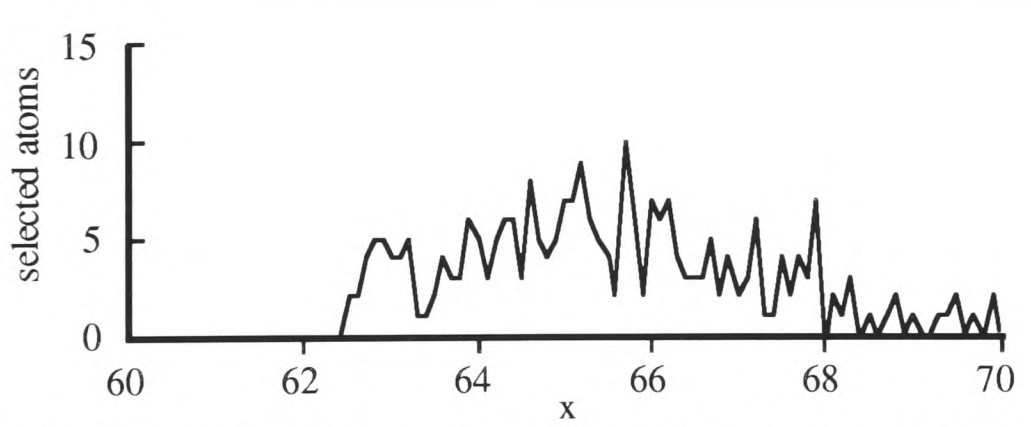

PJW013 Selected spectrum of grain boundary segregation. Due to the lower mass resolution of the POSAP mk1 the peaks are unclear.

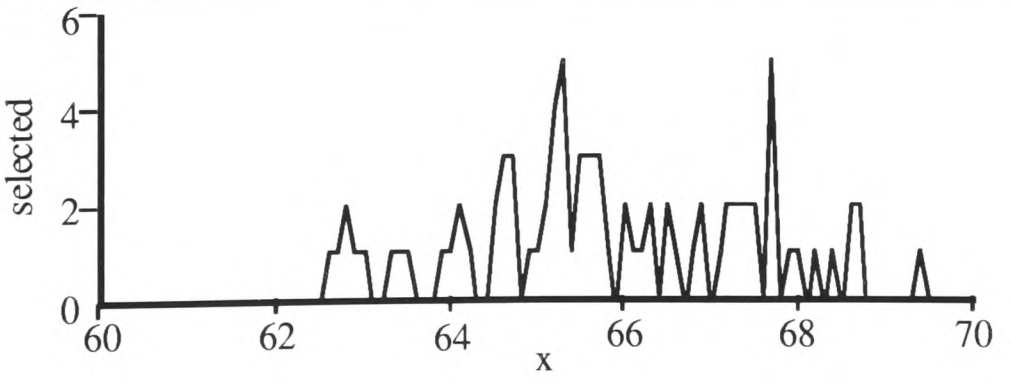

PGB12010 selected spectrum of grain boundary region. Due the small number of atoms the spectrum is unclear.

Figure 6.31

of this research and checked periodically for initial signs of precipitation. This grain boundary analysis (as shown in Figure 6.22) clearly showed signs of precipitation. The main precipitate was plate-like, oriented at an angle to the boundary plane and about 5nm in diameter and 1nm in depth. The composition of the precipitate is ≈72%Al 16%Zn/Cu 12%Mg. Calculation of the composition was done as in Chapter 5, combining the minimum aluminium concentration with the total solute content ratio. The precipitate appears zinc rich, although this lies within the scatter of Zn/Cu : Mg ratios for the matrix strengthening precipitates in material aged at 120°C. The precipitate is much more solute rich than the matrix strengthening precipitates observed in material aged at 120°C, but this is to be expected since the solute concentration at the grain boundary is high, due to segregation and solute drag to the boundary during quenching.

PGB12010 material aged for 100hrs at 120°C.

The POSAP analysis of this boundary (as shown in Figure 6.27) shows a very large plate-like precipitate on the grain boundary oriented at an angle to the boundary; although the grain boundary itself is indistinct and appears non-planar. The precipitate is approximately 5-6nm wide and at least 25nm in diameter (it extended outside the region of analysis). This is very large in comparison with the matrix strengthening precipitates and compares fairly well with the average precipitate sizes measured from TEM micrographs from this heat treatment. The composition of this precipitate is ≈47%Al 24%Zn 29% Mg (calculated in the same way as previously). This is much more solute rich that the matrix strengthening precipitates in the same datafile, which were only 10-15% total solute. The precipitate appears more magnesium rich, as did the larger matrix strengthening precipitates, however as stated above, the scatter of solute ratios observed in this heat treatment is high.

Paul3/6/93 material aged for 100 hrs at 120°C.

This POSAP analysis (Figure 6.29a) shows a grain boundary precipitate very similar to the surrounding matrix strengthening precipitates, both in size and morphology. The composition of the grain boundary precipitate is ≈65%Al 16%Zn/Cu 18%Mg

(calculated in the same way as previously). This is compared to the total solute content of the matrix strengthening precipitates, in the same file, of about 8-14%. The grain boundary precipitate is slightly magnesium rich compared to the matrix strengthening precipitates, however this is well within the statistical scatter of observed solute ratios for this heat treatment. The TEM micrograph of the grain boundary in Figure 6.28 shows the boundary to have a stepped structure, indicative of a low angle of misorientation. Also the precipitation appears very dense, with grain boundary precipitates not much larger than the matrix strengthening precipitates. A low angle of misorientation results in less solute segregation during quenching and less diffusion along the grain boundary, thus inhibiting the formation of large grain boundary precipitates. There is solute enhancement of the grain boundary precipitate due to the presence of the boundary; however, the precipitate still looks similar to the matrix strengthening precipitates and is probably η' structure rather than η structure.

To summarise:- it has been possible to detect increased solute enhancement of the precipitates due to the diffusion pathway of the grain boundary. However, insufficient analyses were achieved to be able to compare the grain boundary precipitate compositions from different heat treatments. Analysis PGB0101 showed that, even at the earliest stages of grain boundary precipitation, the precipitates can have a distinctive morphology if the misorientation of the boundary is suitable. The differences between grain boundaries due to the different boundary misorientations will always remain the major problem in linking grain boundary structure and chemistry to the macroscopically observed intergranular failure.

6.4.8. POSAP detection of hydrogen.

The existence of hydrogen detected by POSAP analysis has been carefully omitted from the previous discussion of grain boundary analysis. The ability to detect hydrogen, and the possible implications for investigation of hydrogen with respect to SCC resistance, are dealt with separately in this section.

Hydrogen may be detected by atom probe methods, just as efficiently as any other element. The problem arises in determining the real source of the hydrogen. Hydrogen may be present in the material; this is known to strongly influence SCC resistance. However, hydrogen is always going to be present in the vacuum chamber, since it is not removed very effectively by diffusion pumps; although the Titanium sublimation pumps are quite effective. Hydrogen has been used as an image gas for FIM and is known to affect the local evaporation field. In this work, hydrogen is detected as a H^+ species generated by dissociative field ionisation of molecular hydrogen or hydride species. The literature reports that gated desorption images of hydrogen on tungsten have showed no obvious crystallographic specificity of absorption sites[104]. It was suggested that hydrogen was absorbed at the surface interstitial sites, and the amount of hydrogen at any particular region was in part controlled by the gas supply function. In this work it was found that images of the distribution of hydrogen species showed very strong correlation with both the grain boundaries and also the larger precipitates.

Figure 6.32 shows the distribution of the hydrogen species for the boundary PGB0101. This clearly shows the correlation of the hydrogen with the boundary region. Comparison of the distribution of hydrogen on the interface with Figure 6.22 shows that the hydrogen also correlates with the early stage precipitates.

Since the temperature and pulse fraction calibration experiments showed that there was a dramatic increase in the detection of hydrogen when the temperature was reduced below about 50K, the analysis of PGB0101 was continued at a temperature of 40K.

Figure 6.33 shows the distribution of hydrogen in PGB0101 at 40K. Comparing the profiles of hydrogen segregation detected, shows that as expected, the level of hydrogen detected at the boundary increases (Figure 6.34).

Since the hydrogen content of the boundary increases so significantly upon reduction of the temperature, it is likely that the majority of the hydrogen detected is actually desorbed vacuum hydrogen rather than real internal hydrogen. Having determined that the hydrogen is likely to be vacuum hydrogen, the correlation with the grain boundary

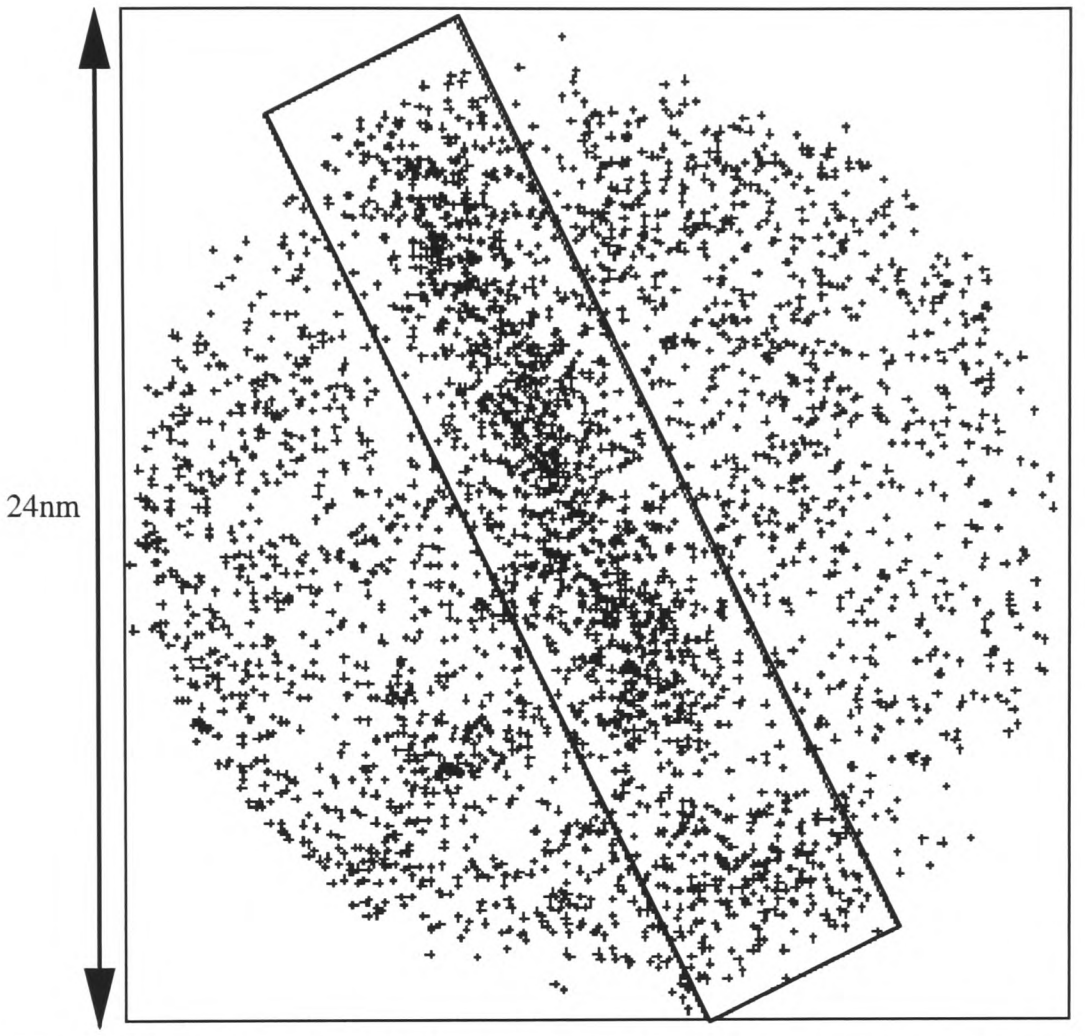

(a) Top view showing distribution of hydrogen species. The hydrogen is associated with the grain boundary. Compare with Figure 6.22.

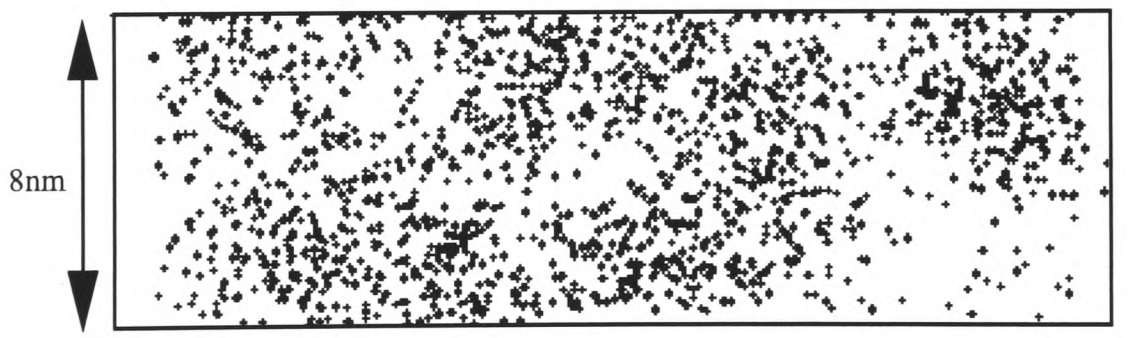

(b) Side view shows the hydrogen is weakly associated with the early stage grain boundary preciptiates.

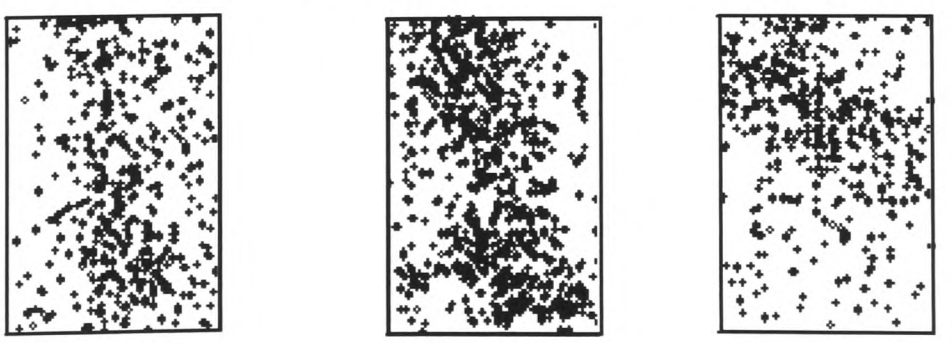

(c) Cross–sectional views of the selected boundary data showing the hydrogen distribution.

Figure 6.32

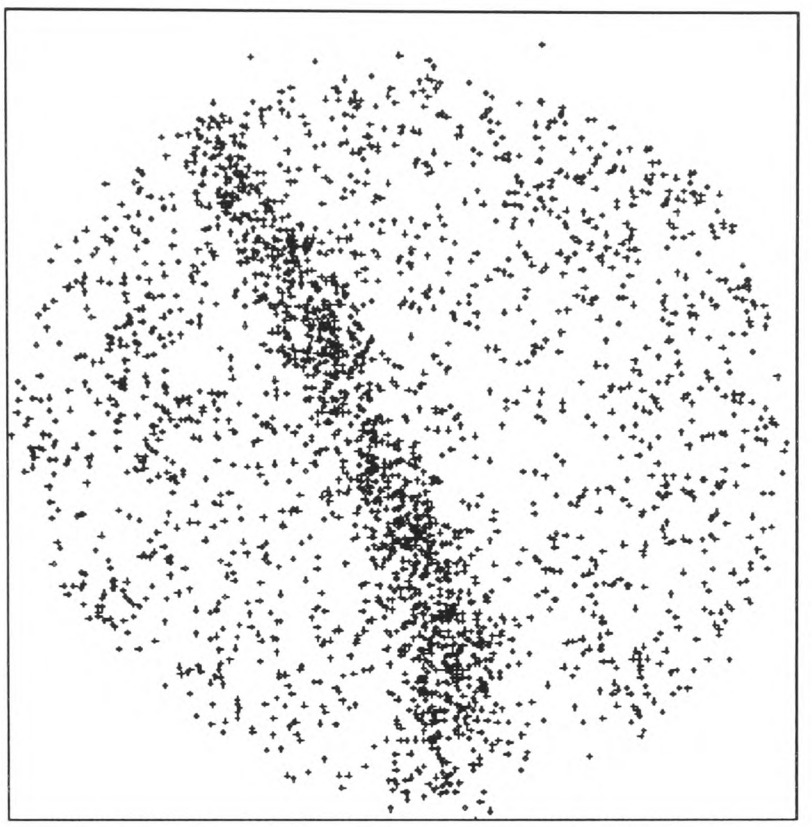

Distribution of hydrogen species in analysis at 40K.

Figure 6.33

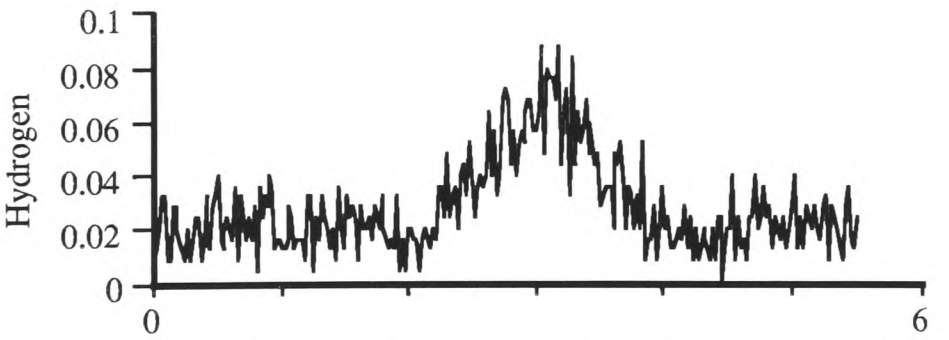

(a) Composition profile across grain boundary analysed at 70K.

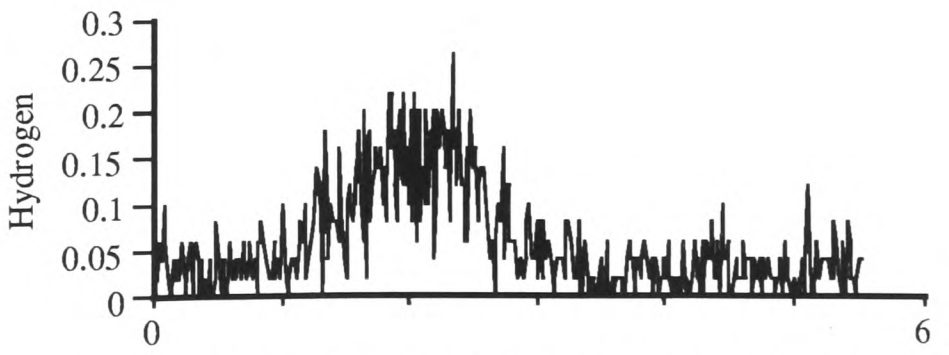

(b) Composition profile across grain boundary analysed at 40K.

Figure 6.34

region must be some sort of local field effect. The amount of hydrogen detected would be dependant upon the gas supply, the temperature, and the local field ionisation efficiency. It is possible that the boundary surface groove acts as a surface migration pathway from the specimen shank, thus enhancing the gas supply. The gas supply will of course also be dependent upon the vacuum, which varies from experiment to experiment, and also during the experiment, as the argon image gas is slowly removed.

It might be possible to determine the presence of internal hydrogen by charging the specimen with ^{2}H (deuterium). This was attempted by using deuterated electropolishing chemicals (acetic and perchloric acids). The electropolishing procedure is likely to be very effective at introducing hydrogen into the specimen (This a possible reason for the high specimen failure rate.) Analysis of a grain boundary was not achieved while using the deuterated chemicals, so the effectiveness of this experiment has not been tested. It will be difficult to confirm the presence of internal hydrogen, as opposed to the vacuum species, due to the possibility of peak overlap of the hydride isotope species. The internal hydrogen is likely to occur mostly as hydride species with the aluminium and the copper, rather than dissociated $^{2}H^{+}$ species; thus detection will be further confused due to the formation of AlH_2^{+} and CuH_2^{+} species.

The possible metallurgical benefits of being able to detect the presence and location of grain boundary hydrogen are very high; however, the experimental difficulties are severe. See the Chapter 1 for a discussion of the effects of hydrogen on SCC resistance.

Chapter 7. Summary and Conclusions.

7.1. Introduction.

This project has used two of the highest resolution techniques available for the chemical analysis of solid materials, to investigate the phase chemistry of precipitation in a commercially important aerospace aluminium alloy. The motivation for this research was the need to increase our understanding of the chemical processes occurring at grain boundaries during age-hardening precipitation. It is thought that local changes in the chemistry of grain boundary microstructures during ageing strongly correlate with the more macroscopic changes in intergranular Stress Corrosion Cracking susceptibility. To date, no clear dependence of SCC upon any one particular microscopic feature has been proven, due to the inability to independently vary the many microscopic parameters.

This project has had no impact upon the problem of SCC for this alloy system. However, it does provide a large amount of information about the microstructural phase chemistry of this alloy, and has described in detail the experimental difficulties associated with this alloy system in particular, and the two techniques in general.

7.2. Summary of techniques.

The VG-HB501 STEM used in this research has a lateral chemical resolution of below 2nm. The ultra high vacuum enables the use of a windowless detector, which can detect magnesium and it also reduces specimen contamination. The accuracy of the chemical data obtainable from a dedicated STEM is far superior to that obtainable from a TEM/STEM, especially for nanometre scale analysis as required in this investigation. With a STEM, it is easy to identify and select features of interest from the relatively large field of view. Unfortunately, in this alloy system, there are several insurmountable problems associated with accurate quantification. Magnesium Kα X-rays have a very similar energy to the aluminium Kα X-rays; thus there is significant inaccuracy in the separate identification of these elements. There is also slight overlap in

identification of zinc and copper X-rays; however, this effect is minimal compared to the effect of surface deposition of copper. Due to this surface layer of copper, the level of copper detected is dependent upon the thickness of the specimen at the point of analysis. Absolute quantification of precipitate chemistry was therefore not attempted. All of the results presented above were considered relatively rather than absolutely.

The VG-FIM100 Atom Probe used in this research has an extremely high mass resolution enabling clear elemental identification of all ion species detected. This analysis technique uses single atom identification, therefore the volume of analysis is very limited. The main limitation of the technique was the difficulty of selection of a specific feature. Atom probe analysis (AP) has a 3-7nm probe diameter, limiting lateral resolution. The development of position sensitive atom probe analysis (POSAP), which has a lateral resolution of below 0.5nm with a lateral field of view of up to 60nm diameter, greatly improves the spatial resolution, but at the expense of lower chemical resolution, and thus lower compositional accuracy. These two techniques must therefore be regarded as complementary. Again, this alloy imposes further experimental difficulties. The formation of copper hydride species affects the chemical accuracy of both AP and POSAP. Co-existing zinc and copper are too similar for separate chemical identification by POSAP. Both magnesium and zinc were found to be affected by preferential evaporation effects leading to loss of solute species, and both elements were also found to evaporate as multiple events, resulting in loss of POSAP positional accuracy, especially for zinc. Absolute quantification was not possible, however relative variations in the atomic scale chemistry were clearly observed.

7.3. Summary of Results.

Matrix Regions

Material aged for 100hours at 120°C contained a fine dispersion of matrix strengthening precipitates. These precipitates were observed to have a distribution of sizes approximately 2-5nm. The precipitates at this stage did not have a clearly defined surface interface or morphology. These precipitates were mainly η' precipitates as

identified by previous electron diffraction investigation. The precipitates were found to be only 5-20% total solute (Zn+Mg+Cu). The solute content at this stage was predominantly zinc and magnesium with very little copper. The ratio of solute species in each precipitate was found to vary around 50% magnesium and 50% zinc plus copper.

In material aged for 20hours at 150°C the size of the matrix strengthening precipitates was observed to be about 3-8nm: larger than those in the material aged at 120°C. There were also relatively fewer precipitates, and they were observed to have a more clearly defined morphology. These precipitates were identified as mainly η precipitates. The precipitates were found to contain about 20-50% total solute. The precipitates were enriched in all three solute elements (Zn, Mg, Cu) with a variety of solute ratios distributed around the total alloy content ratio of 3:3:1.

In material aged for 8hours at 180°C, the size of the matrix strengthening precipitates was observed to be about 5-15nm: larger again than the lower temperature treatments. The precipitates had clear morphologies of crystallographically oriented plates and rods. These precipitates were identified as predominantly η precipitates. They were found to contain a distribution of total solute contents up to 75%. This is to be expected if Ostwald ripening is occurring as some precipitates shrink, while others grow. Again a variety of solute ratios were observed, very similar to the precipitates in material aged at lower temperatures.

Comparing the three materials showed an increase in precipitate size, a decrease in precipitate number density and increase in precipitate definition. The η' precipitates were found to be enriched in both zinc and magnesium up to about 20% solute, whereas the η precipitates were enriched in zinc, magnesium and also copper. The change in precipitate type and increase in copper segregation was observed to occur between 120°C and 150°C.

Grain Boundary Regions

The material was supplied as $2^1/_2$" rolled plate which showed a typical rolled grain structure of elongated grains separated in layers by higher angle grain boundaries and segmented by lower angle grain boundaries. All of the grain boundaries in aged material showed dense arrays of precipitates, although the range of precipitate sizes, shapes and separations varied widely between boundaries, as did the boundary misorientations.

All of the boundaries were surrounded by a precipitate free zone. Quenching resulted in a vacancy depletion profile around the grain boundary, and solute-vacancy clustering was necessary for precipitate nucleation. The width of the PFZ was observed to be fairly consistently 35-45nm for all ageing treatments except extreme overageing, in which the width increased to more than 150nm due to solute depletion.

Comparison of the solute ratios of the grain boundary precipitates analysed in material aged at 120°C, 150°C and 180°C showed no discernible change in the solute ratios. Considering the many different precipitates, on the many different boundaries, in each of the different materials, the precipitate solute ratios were remarkably similar.

Comparison of the chemistry of the grain boundary precipitates with the chemistry of the matrix strengthening precipitates was only possible in the extremely overaged material, due to the different limitations of each of the analytical techniques. This showed the grain boundary precipitates to be relatively depleted in copper and magnesium. This can be explained by the presence of both the grain boundary and also a distribution of copper and magnesium rich precipitates, which act as alternative sinks for copper and magnesium. Neither of these sites are available in the matrix, thus all the solute in must be located in the η precipitates.

Both STEM and atom probe methods were used to detect grain boundary segregation in all of the materials analysed. Both techniques detected magnesium and copper segregation. Due to the small number of grain boundaries analysed by atom probe methods, a comparison of the segregation levels detected was only possible by STEM analysis. Almost all of the grain boundaries showed signs of segregation of copper and

magnesium. No correlation between the levels of copper and magnesium was observed. No differences between different heat treatments was observed.

One of the POSAP grain boundary analyses showed signs of grain boundary precipitation in naturally aged material. The main precipitate analysed was found to be a plate, 5nm in diameter and only 1nm in thickness, oriented at an angle to the grain boundary. Even at this early stage, the grain boundary precipitates can have a distinctive morphology if the misorientation of the grain boundary is suitable. The differences between grain boundaries, due to the different boundary misorientations, will always remain the major problem in linking grain boundary structure and chemistry to the macroscopically observed intergranular failure.

7.4. Suggestions for further work.

Suggestion for further work can be broadly categorised as: suggestions concerning future investigations of this alloy; suggestions concerning future atom probe method investigations; and suggestions concerning future STEM investigations.

This alloy is currently in widespread use. For any real changes to be made to the alloy, substantial improvements in properties must be proven. The aluminium industry is currently depressed, both due to the western economic climate, ,and the opening up of large sources of supply of aluminium from the eastern block with the demise of the USSR. The benefits for Alcan International in pursuing further research in this alloy appear minimal.

As regards the need for future investigations into the local chemistry of grain boundary regions and their effect on the macroscopic SCC susceptibility of the material, this problem is clearly not restricted to Al-7150. SCC affects the vast majority of high strength aluminium alloys, and still poses just as much of a problem as before. The main problem seems to be relating the failure of a susceptible boundary to the observed distribution of grain boundary chemistries, and structures, present in the whole material.

The two techniques used in this investigation have the highest spatial resolutions currently available for chemical analysis of grain boundary structures. STEM X-ray microanalysis was mainly limited by experimental difficulties associated with this specific alloy. Without surface deposition of copper, or peak overlap of magnesium the accuracy of the compositional information would have been much greater. A different alloy could be used for an investigation of the dependence of SCC upon grain boundary chemistry but this moves the emphasis away from commercial profit onto academic interest. Given a suitable system, it would then be of interest to carry out a detailed investigation of the dependence of grain boundary segregation upon the grain boundary misorientation. There is a clear lack of quality investigations of grain boundary segregation.

Atom probe techniques clearly have potential for the analysis of grain boundaries due to the grain boundary being an atomic scale feature. The geometry of AP analysis requires a precipitate free boundary or the means to select a region of boundary to avoid the precipitates. This was not possible in this alloy due to the imaging characteristics of the boundary solute species. The development of three dimensional atom probes, of which the POSAP was the first example, greatly increases the potential for atomic scale chemical analysis of grain boundaries. The instrument developers are already addressing the problems of multiple events and poor mass resolution, and the future for 3-D atomic analysis is good. The main limitation with atom probe analysis of grain boundaries is the selective specimen preparation. This research was unable to make specimen preparation reliable, and further work is essential in this area if aluminium boundaries are to be investigated by this technique. A quick check to see whether the experimental set-up used in this research can prepare a grain boundary specimen in a material other than aluminium is clearly the first experiment. Another problem with aluminium was that the solute species were found to evaporate preferentially, thus careful choice of analysis conditions is required. There is a strong suggestion that the FIM100 is not able to achieve sufficiently low temperatures for accurate compositional analysis of aluminium alloys. Future analyses of all aluminium alloys MUST address this problem from the beginning. Some other experimental problems, however, were

independent of material. Ion trajectory aberrations were possibly observed for the precipitates which all appeared to be cored in magnesium. Investigation of whether this is a real effect or an observation of ion trajectory effects would be useful. The grain boundary will also cause local variations in the field and it can act as a surface migration pathway. Further work on the inherent complexities of 3-D grain boundary analysis, although non-trivial, is guaranteed to be a fruitful area of research and is vital for the accurate interpretation of grain boundary analyses.

References

1 Holroyd N.J.H., Proc."Environment Induced Cracking of Metals", p311, NACE, (1989)*

2 Crompton J.S., Hepples W., Jarrett M.R., Holroyd H.J.H. and Titchmarsh J., "3rd Int.Conf. on Materials Architecture Risø", p313, (1989)*

3 Hunsicker H.Y., Proc. Rosenhain Cent.Conf., 359, (1975)

4 ASM Metals Handbook, **2**, (1979)

5 Vasudevan A.K. and Doherty R.D., "Al. Alloys:- Contemporary Research and Applications", Treatise on Materials Science and Technology, Vol 31, (1989)

6 Koster W. and Wolf W., Z.Metallkd., 155, **28**, (1936)

7 Mondolfo L.M., Int.Metall.Rev., 95, **153**, (1971)

8 Loffler H., Kovacs I. and Lendvai J., J.Mat.Sci., 2215, **18**, (1983)*

9 Mondolfo L.M., Gjøstein N.A. and Levinson D.W., Trans.AIME., 1378, **206**, (1956)*

10 Polmear I.J., J.Inst.Met., 24, **87**, (1958)

11 Graf R., Compt.Rend.Acad.Sci., 2834, **242**, (1956)*

12 Schmalzried H. and Gerold V., Z.Metallk., 291, **49**, (1958)

13 Graf R., Compt.Rend.Acad.Sci., 337, **244**, (1957)

14 Thomas G. and Nutting J., J.Inst.Metals, 81, **88**, (1959-60)

15 Lyman C. and Vander Sande J., Met.Trans.A, 1211, **7A**, (1976)

16 Ortner S.R., Grovenor C.R.M. and Shollock B.A., Scripta Met., 839, **22**, (1988)*

17 Graf R., J.Inst.Met., 535, **86**, (1957-58)

18 Gjønnes J.G. and Simensen C.J., Acta.Met., 881, **18**, (1970)*

19 Auld J.H. and Cousland S.McK., Scripta Met., 765, **5**, (1971)

20 Mondolfo L.M., "Al. Alloys:- Structure and Properties", pp577-90, 844-882, and 652-654, Butterworths (1976)

21 Park J.K. and Ardell A.J., Met.Trans.A, 1957, **14A**, (1983)*

22 Laves F. and Löhberg J., Nachr.Acad.Wiss., 59, **1**, (1934)

23 Lorimer G.W. and Nicholson R.B., Acta Met., 1009, **14**, (1966)*

24 Viswanadham R.K., Sun T.S. and Green J.A., Met Trans.A., 85, **11A**,(1980)*

25 Hono K., Sakurai T. and Polmear I.J., to be published in Scripta Met. (1993)

26 Pashley D.W., Rhodes J. and Sendorek A., J.Inst.Met., 41, **94**, (1966)

27 Lorimer G.W. and Nicholson R.B., "The Mechanisms of Phase Transformations in Crystalline Solids", Inst.Met., p36, (1969)

28 Pickens J.R. and Langan T.J., Met.Trans.A., 1735, **18A**, (1987)*

29 Adler P.N., DeIasi R. and Geschwind G., Met.Trans.A, 3191, **3A**, (1972)

30 DeIasi R. and Adler P.N., Met.Trans.A, 1185, **8A**, (1977)

31 Cina B.M., US patent 3856584, December 24, (1974)*

32 Rajan K., Wallace W. and Beddoes J.C., J.Mat.Sci., 2817, **17**, (1982)*

33 Dahn N.C., Rajan K. and Wallace W., Met.Trans.A, 1843, **14A**, (1983)*

34 DeArdo A.J. and Simensen JR. and CHR., Met.Trans.A, 2413, **4A**, (1973)

35 Park J.K.and Ardell A.J., Met.Trans.A, 1531, **15A**, (1984)*

36 Dahn N.C., Rajan K. and Wallace W., Met.Trans.A, 2068, **16A**, (1985)

37 Park J.K. and Ardell A.J., Scripta Met., 1115, **22**, (1988)

38 Buratti M., Russo E. and Lorenzetti M.L., Mat.Eng., 317, **1**, (1989)

39 Ohnishi T., Ibaraki Y. and Ito T., Mat.Trans. JIM, 601, **30**, (1989)

40 Swanson R.E., Bernstein I.M. and Thompson A.W., Scripta Met., 321, **16**, (1982)

41 Ward D.E and Lorimer G.W., "Proc.3rd Int.Conf. on Strength of Metals and Alloys", p488, **Vol 1**, (1973).

42 Doig P. and Edington J.W., Met.Trans., 943, **6**, (1975).

43 Raghavan M., Met.Trans.A, 993, **11A**, (1980)

44 Park J.K. and Ardell A.J., Acta Met., 591, **39**, (1991)

45 Scamens G.M., Holroyd H.J.H. and Tuck C.D.S., Corr.Sci., 329, **27**, (1985)*

46 Raghavan A., Koo J.Y., Steeds J.W. and Park B.K., Met.Trans.A, 1925, **16A**, (1985)

47 Rao B.V., Met.Trans.A, 1356, **12A**, (1981)

48 Sprowls D.O. and Brown R.H.,"Proc.Conf.Fundamental Aspects of SCC", NACE, (1969)

49 Holroyd N.J.H. and Scamens G.M.,"Environment InducedCracking of Metals", NACE, (1989)

50 Burleigh T.D., Corrosion, 89, **47 No.2**, (1991)

51 Ricker R.E. and Duquette D.J., Met.Trans.A, 1775, **19A**, (1988)

52 Ratke L. and Gruhl W., Werkst.u.Korro., 768, **31**, (1980)

53 Kim H-P., Song R-H. and Pyun S-I., Br. Corr. J., 254, **23**, (1988)

54 Smiyan O.D., Sov.Mater.Sci., 457, **22**, (1986)

55 Bond G.M., Robertson I.M. and Birnbaum H.K., Acta Met., 2289, **35**, (1987)

56 Gruhl W., Z.Metall., 819, **75**, (1984)

57 Polyanskii V.M., Sov.Mater.Sci., 301, **21**, (1985)

58 Warren P.J., Part II Thesis, University of Oxford, (1990)*

59 Miller M.K., and Smith G.D.W., "Atom Probe Microanalysis: Principles and Applications to Materials Problems", M.R.S., p46, (1989)

60 Mackenzie R.A.D. and Smith G.D.W., IFES Bibliography, University of Oxford

61 Fasth J.E., Loberg B. and Norden H., J.Sci.Instrum., 1044, **44**, (1967)

62 Henjered A. and Norden H., J. de Phys.E., 617, **16**, (1983)*

63 Rolander U., J. de Phys., 391, **45-C9**, (1983)

64 Seidman D.N., Mat.Sci.Eng., 57, **A137**, (1991)

65 Krakauer B.W., Hu J.G., Kuo S.M., Mallick R.L., Seki A., Seidman D.N., Baker J.P. and Loyd R.J., Rev.Sci.Instrum., 3390, **61**, (1990)*

66 Brenner S.S., Kowalik J. and Hua Ming-Jian, Surface Science, 210, **246**, (1991)*

67 Jones I.P. and Loretto M.H., J. of Microscopy, 3, **124**, (1981)*

68 Hren J.J., Goldstein J.I. and Joy D.C. Eds., "Introduction to Analytical Electron Microscopy", Plenum Press, New York, (1979)

69 Cliff G. and Lorimer G.W., J.Microscopy, 203, **103**, (1975)

70 Lee P.J., "Analytical Electron Microscopy", p69, Eds. Williams D.B. and Joy D.C., San Francisco Press, (1984)

71 Park J.K. and Ardell A.J., J.Microscopy, 301, **165**, (1991)

72 Muller E.W. and Tsong T.T., "Field Ion Microscopy -Principles and Applications", Elsevier NY, (1969)

73 Miller M.K. and Smith G.D.W., "Principles of atom probe microanalysis", MRS, (1989)*

74 Tsong T.T., "Atom Probe Field Ion Microscopy", Cambridge Univ.Press, (1990)

75 "Field Ion Microscopy and Atom Probe Microanalysis", in "Metals Handbook", Vol 10, p583, (1986)

76 Poschenrieder W.P., Int.J.Mass Spectrom.Ion Phys., 413, **6**, (1972)

77 Poschenrieder W.P., Int.J.Mass Spectrom.Ion Phys., 357, **9**, (1972)

78 Cerezo A., Godfrey T.J., Grovenor C.R.M., Hetherington M.G., Hoyle R.M., Jacubovics J.P., Liddle J.A., Smith G.D.W. and Worrall G.M., J. of Microscopy, 215, **154**, (1989)

79 Hyde J.M., Cerezo A., Stena R.P., Warren P.J. and Smith G.D.W., to be published in Surface Science*

80 Hyde J.M., D.Phil Thesis, University of Oxford, (1993)*

81 Cerezo A., Hyde J.M., Miller M.K., Petts S.C., Setna R.P. and Smith G.D.W., Phil.Trans.R.Soc.Lond.A., 313, **341**, (1992)

82 Mackenzie R.A.D., Cerezo A., Conyers J.S., Petford-Long A.K., Sijbrandij S.Y. and Smith G.D.W., "Mat.Res.Soc.Symp.Proc.", **286**, (1993)

83 Boyes E.D.,"Proc. 9th Int. Conf. Electron Microscopy", Ed.Sturgess, 104, **1**, (1978)

84 Hirano K. and Hono K., Ann.Rev.Mater.Sci., 351, **18**, (1988)

85 Hono K., Surface Science, 350, **266**, (1992)

86 Ortner S.R. and Grovenor C.R.M., Scripta Met., 843, **22**, (1988)

87 Miller M.K. and Smith G.D.W., "Atom Probe Microanalysis", p141, MRS, (1989)*

88 Menand A., al Kassab T., Chambreland S. and Sarrau J.M., J. de Phys., 353, **49-C6**, (1988)*

89 Kreyszig E., "Advanced Engineering Mathematics", 5th Edition, p951, Wiley, (1983)

90 Hono K., Hashizume T. and Sakurai T., Surface Science, 506, **266**, (1991)

91 Dreschler M. and Wolf D., "Proc. 4th Int. Conf. on Electron Microscopy", Berlin, p835, Springer-Verlag, (1960)

92 Wilkes T.J., Smith G.D.W. and Smith D.A., Metallography, 403, **7**, (1974)

93 Edington J.W.,"Practical Electron Microscopy in Material Science, Monograph 4: Typical Electron Microscope Investigations", p18, Philips Technical Library, (1976).

94 Hepples W., Jarrett M.R., Crompton J.S. and Holroyd N.J.H., "Enviroment-Induced Cracking of Metals: Proceedings", p383, National Association of Corrosion Engineers, (1989)

95 Lorimer G.W., Graham C., Champness P.E., Dickinson C., Hasan F. and Kenway P., "Analytical Electron Microscopy", p153, Ed. Joy D.C., San Francisco Press, (1984)

96 Warren P.J., Grovenor C.R.M. and Crompton J.S., Surface Science, 342, **266**, (1992)*

97 Ryum N., Acta Met., 269, **17**, (1969)

98 Doig P. and Flewitt P.E.J., Met.Trans.A, 1397, **13A**, (1982)

99 Hall E.L., J. de Phys., 239, **43-C6**, (1982)

100 Michael J.R. and Williams D.B., Met.Trans.A, 99, **A15**, (1984)

101 Grovenor C.R.M., Batson P.E., Smith D.A. and Wong C., Phil.Mag.A, 409, **50**, (1984)

102 Long N.J., unpublished work

103 Miller M.K. and Smith G.D.W., "Atom Probe Microanalysis", p63, MRS, (1989)

104 Panitz J.A., J.Vac.Sci.Tech., 206, **11**,(1974)

105 Lorretto M.H., "Electron Beam Analysis of Materials", Chapman and Hall, (1984)

* denoted multiply referenced in the text.